Methodology and application of cryo-electron tomography to vitrified plant tissue: Insights into plasmodesmata architecture, composition and gating.

Inaugural-Dissertation

zur Erlangung des Doktorgrades

der Mathematisch-Naturwissenschaftlichen Fakultät

der Heinrich-Heine-Universität Düsseldorf

vorgelegt von

Marcel Dickmanns

aus Dülken, Viersen

Düsseldorf, 03.02.2026

aus dem Institut für Molekulare Physiologie

der Heinrich-Heine-Universität Düsseldorf

Gedruckt mit der Genehmigung der

Mathematisch-Naturwissenschaftlichen Fakultät der

Heinrich-Heine-Universität Düsseldorf

Berichterstatter:

1. Prof. Dr. Wolf B. Frommer
2. Prof. Dr. Wolfgang Baumeister

Tag der mündlichen Prüfung: 07.10.2026

Eidesstattliche Erklärung

Ich versichere an Eides Statt, dass die Dissertation von mir selbständig und ohne unzulässige fremde Hilfe unter Beachtung der „Grundsätze zur Sicherung guter wissenschaftlicher Praxis an der Heinrich-Heine-Universität Düsseldorf“ erstellt worden ist.

_____

Düsseldorf, 03.02.2026 Marcel Dickmanns

Summary

Multicellular organisms rely on intercellular communication and exchange of resources. In plants, direct molecular exchange is mediated by plasmodesmata: nanoscopic pores that traverse the cell wall and establish continuity between the plasma membrane, cytosol, and endoplasmic reticulum of adjacent cells. Despite their essential role in plant development and physiology, the molecular composition, internal organization, and mechanisms controlling plasmodesmal permeability remain poorly defined. Proteomic studies have identified hundreds of putative plasmodesmal proteins, but such datasets are inherently noisy and likely include many false positives. Systematic mapping of the molecular inventory within plasmodesmata is further complicated by their nanometer-scale dimensions, placing them below the resolution limit of most light microscopy techniques, while preparation artifacts in classical electron microscopy prevent reliable analysis of the fine molecular detail.

Here, we applied a combination of methods to advance the characterization of plasmodesmal organization and function, focusing on the model plant *Physcomitrium patens*. We established a proteome of plasmodesmata-enriched cell wall fractions and analyze multiple uncharacterized candidate proteins. Among them, we found several cell wall-modifying enzymes including a clade of glycosyl hydrolase family 17 (GHL17) proteins that localize to plasmodesmata and identified a homolog modulating plasmodesmal permeability.

In addition, several nucleoporins (NUPs) were identified in the proteome. Intrigued by the similarities between nuclear and plasmodesmal pores, we examined their subcellular localization and assessed plasmodesmal permeability in NUP mutants. As multiple NUPs show dual localization to nuclei and plasmodesmata and plasmodesmal permeability is altered in NUP mutants, we probed the possibility of a NUP-containing plasmodesmal pore complex.

To visualize plasmodesmata components in the native context, we developed cryo-electron tomography workflows for imaging multicellular plant samples and assessed them on a set of tissues from *Physcomitrium patens*, *Arabidopsis thaliana* and *Limonium bicolor*. Applying these workflows, we resolved the in situ architecture of plasmodesmata in *Physcomitrium patens*. By comparing wild-type with overexpression of the previously identified glycosyl hydrolase GHL17, as well as abscisic acid-treated wild-type tissue, we could link architectural changes of plasmodesmal pores to permeability phenotypes. Under GHL17 overexpression associated with increased intercellular flux, plasmodesmata were shorter and wider. In contrast, abscisic acid treatment, known to reduce solute flux between cells, induced excessive deposition of cell wall material around plasmodesmal apertures. Unexpectedly, this deposition resulted in complete channel sealing in the majority of imaged plasmodesmata, abolishing membrane and cytosolic continuity between cells.

Beyond this cell wall-sided gating mechanism, we resolved the structure of a protein assembly, present within all imaged plasmodesmata where it coats the central, ER-derived desmotubule membrane. Through integration of subtomogram averaging with proteomics and structure predictions, we could identify Multiple C2 domain and Transmembrane Proteins (MCTPs) as the constituents of the assembly. Bioinformatic analysis further revealed that MCTPs contain extended intrinsically disordered linker regions with electrostatic sticker-spacer characteristics. As mapping back MCTPs into the tomographic representations of plasmodesmata indicated these disordered linker domains populate the cytosolic route within plasmodesmata, we hypothesized they may constitute a charge-selective permeability barrier.

In summary, our observations define molecular and architectural features of plasmodesmata and provide a structural framework for how membrane, protein, and cell wall components coordinate intercellular connectivity in plants.

Table of Contents

Summary 4
Chapter 1 7
1.1 Introduction 7
1.1.1 Multicellularity & intercellular exchange 7
1.1.2 Plasmodesmata – Architecture & composition 8
1.1.3 Plasmodesmata – Molecular trafficking and permeability control 12
1.1.4 Cryo-Electron Tomography – Structural biology in situ 14
1.2 Outline of the thesis 17
Chapter 2 20
Taking inventory – The protein landscape in and around plasmodesmata 20
2.1 Summary 20
2.2 Results 22
Chapter 3 39
Probing novel candidates – Potential roles of nucleoporins at plasmodesmata? 39
3.1 Summary 39
3.2 Results 41
Chapter 4 98
Methodology – Making plant tissue accessible for cryo-electron tomography 98
4.1 Summary 98
4.2 Results 100
Chapter 5 141
Application – Imaging native plasmodesmata in 3D 141
5.1 Summary 141
5.2 Introduction 143
5.3 Results 145
5.4 Discussion 153
5.5 Methods 158
5.6 Supplementary Materials 164
Chapter 6 174
Methodology – Preparation of moss tissue for cryo-electron tomography 174
6.1 Summary 174
6.2 Results 175
Chapter 7 232
7.1 Concluding discussion 232
Acknowledgements 237
References 238

Chapter 1

1.1 Introduction

1.1.1 Multicellularity & intercellular exchange

Over the course of biological evolution on earth, multicellularity evolved at least 50 times independently (Bingham and Ratcliff 2024), with the earliest known emergence in cyanobacteria over 3 billion years ago (Hammerschmidt et al. 2021). Multicellular communities may emerge from unicellular ancestors through two distinct routes: (1) aggregation, in which free-living cells come together to form a collective, and (2) clonal development with incomplete cell abscission, where daughter cells remain physically connected after division (Abedin and King 2010). Aggregation, prominent in dictyostelid slime molds and myxobacteria, involves facultative cooperation among otherwise independent cells (Claessen et al. 2014; Penesyan et al. 2021). In contrast, clonal development through incomplete abscission establishes permanent connections between genetically identical cells, bypassing the unicellular stage. This mode underlies most eukaryotic multicellularity and is universal in the five lineages with complex body plans – animals, fungi, red algae, brown algae, and plants (Bingham and Ratcliff 2024).

Both aggregation and clonal development provide adaptive advantages, such as increased sampling of environmental information, size-dependent predator avoidance or partitioning of labor between specialized cells, tissues and organs. However, the evolutionary incentives differ. Aggregative behavior provides short-term benefits for the community, but selection continues to act at the level of individual cells (Pentz et al. 2023). In clonal multicellularity with little in-group genetic variance, selection acts primarily on the collective rather than the individual cell level, allowing the evolution of complex body plans and capabilities for intra-organismal cooperation (Michod 2007; Pentz et al. 2023). Such complex multicellular lineages converge on three fundamental cell-biological innovations: mechanisms for stable cell-cell adhesion, differentiation with partitioning of labor, and specialized pathways for communication and molecular exchange (Knoll 2011). Cell-cell communication occurs indirectly through secretion of messenger molecules and receptor-mediated signaling, or directly via cytoplasmic connections transmitting electrical, hydraulic, and chemical signals from one cell to another. Likewise, exchange of resources, e.g. the distribution of metabolites produced by specialized cells, may rely on secretion into and reuptake from the extracellular milieu, or on direct passage through intercellular bridges (Chaigne and Brunet 2022).

In animals, direct cytoplasmic connections in somatic cells occur at specialized cell-cell contact sites termed gap junctions, where protein channels formed by connexin subunits in vertebrates or innexin subunits in invertebrates are inserted into the plasma membranes of two coupled cells (Söhl and Willecke 2004; Skerrett and Williams 2017). Docking of two such hemichannels creates complexes with central pores of 8 – 16 Å diameter, connecting the cytosol of both cells and allowing passive diffusion of ions and

small soluble molecules up to molecular masses of about 1 kDa with connexin isoform-dependent solute selectivity (Weber et al. 2004; Maeda et al. 2009; Kwon et al. 2011). While membrane interfaces at gap junction plaques are maintained, individual channels within have short half-lives of ~1.5 – 5 h before turnover (Musil et al. 2000; Gaietta et al. 2002) and are dynamically gated by voltage, post-translational modifications and changes in intracellular calcium levels and pH (Lampe and Lau 2004; Su and Lau 2014; Bennett et al. 2016).

Apart from gap junctions, which are limited to membrane interfaces of immediately adjacent cells, tunneling nanotubes (TNTs) are transient, F-actin stabilized membrane protrusions which can connect distant cells without the need for permanent adhesion. TNTs typically measure ~50 – 250 nm in diameter permitting exchange of larger cargo, including vesicles and even entire organelles (Rustom et al. 2004; Sartori-Rupp et al. 2019; Chakraborty et al. 2023; Miao et al. 2025). Stable cytoplasmic connections, however, are rare in animals and mostly limited to the germline (Dym and Fawcett 1971). Such germline bridges, termed ring canals in insects, are formed by incomplete cytokinesis, where the contractile ring halts before abscission leaving the cytosol of the two daughter cells connected (Greenbaum et al. 2007). Rarely ring canals may occur in somatic tissues, for example in Drosophila epithelia, where they permit protein equilibration between cells (McLean and Cooley 2013; Nandakumar and Vasudevan 2025).

In non-animal lineages with features of complex multicellularity, intercellular exchange is complicated by the presence of cell walls. Each lineage, often in several independent events, has evolved intercellular bridges, directly linking membranes and cytosol across cell walls: septal pores in fungi (Beckett 1981; Lai et al. 2012), pit connections in red algae (Ramus 1969), plasmodesmata-like pores in brown algae (Terauchi et al. 2014), and plasmodesmata in green algae and plants. This thesis focuses on plasmodesmata in land plants, with emphasis on investigating their ultrastructure, composition and physiology.

1.1.2 Plasmodesmata – Architecture & composition

Intercellular connections between adjacent plant cells were described independently by multiple botanists in the late 19th century, with the first illustrations published by Eduard Tangl in 1880 (Tangl 1880; Köhler and Carr 2006; Peters et al. 2021). By staining plant tissues with different iodine solutions, Tangl observed connecting channels (*“Verbindungskanäle”*) across cell walls in light microscopy which were traversed by protoplasmic extensions (*“Protoplasmafortsätze”*). In his 1901 essay, Eduard Strasburger coined the term *“Plasmodesmen”*, later anglicized to plasmodesmata (singular: plasmodesma) (Strasburger 1901). Both Tangl and Strasburger recognized the implications of intercellular connectivity, introducing the concept of symplasmic continuity throughout the plant body.

At this stage, due to the limited resolution of light microscopy, it remained unclear whether plasmodesmata are simple wall pores or contain more intricate internal organization. With the advent of electron microscopy in the 1950s, however, their dimensions and structural features started to be revealed (Strugger 1957; Welling 1965; López-Sáez et al. 1966, Fig. 1). Early transmission electron micrographs indicated that each plasmodesmal pore is lined by the plasma membrane and contains a central dense core, later termed the desmotubule, which connects to the cortical ER (Robards 1968). While some authors hypothesized that the desmotubule represents an ER-derived membrane strand (López-Sáez et al. 1966), others questioned whether such extreme membrane tubulation was physically feasible and proposed that the dense core might either not consist of lipid bilayers or must be scaffolded by a proteinaceous 'desmotubule wall'. Robards e.g. suggested that the desmotubule wall could have a similar composition to the microtubule fibers of the mitotic spindle ("*nuclear spindle fibres*", Robards 1968).

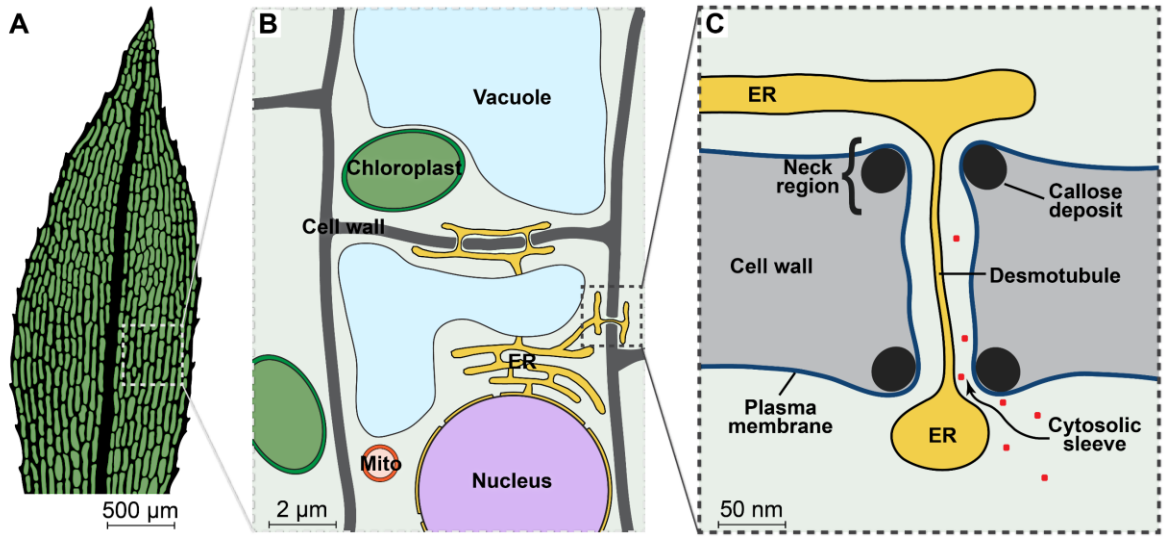


Fig. 1: Schematic overview of plasmodesmata architecture. (**A**) Representation of a *P. patens* gametophore leaflet. (**B**) Adjacent cells are connected via multiple plasmodesmata per cell-cell interface. (**C**) Plasmodesmata are cell wall pores, lined by the plasma membrane, with a central ER-derived desmotubule. The cytosolic sleeve between both membranes allows translocation of soluble molecules. Deposition or degradation of the cell wall polymer callose at neck regions can modulate aperture diameter.

Besides tubulin, other cytoskeletal components were also proposed to constitute the desmotubule wall. In the 1990s, immunolabeling with antibodies against actin was interpreted as evidence for its presence within plasmodesmata in cell sections (White et al. 1994; Blackman and Overall 1998) and cell wall protein extracts (Blackman and Overall 1998). Experiments using actin polymerization inhibitors or stabilizers appeared to support this view, as these treatments altered intercellular movement of tracer molecules (Ding et al. 1996; Su et al. 2010). Consequently, the idea that desmotubules are wrapped in filamentous actin persists in several schematic models of plasmodesmata until today (Overall et al. 2000; Benitez-Alfonso et al. 2010; Heinlein

2015; Sager and Lee 2018; Reagan and Burch-Smith 2020; Choudhary et al. 2020; Chen et al. 2021).

When Ding et al. described the desmotubule wall as consisting of individual particles, approximately 3 nm in diameter and embedded within the outer leaflet of the lipid bilayer (Ding et al. 1992), they also noted that similar particles are coating the plasma membrane within the plasmodesmal channel but did not speculate on the molecular identity of either particle type. Another ultrastructural feature described early on and repeatedly observed in later studies are spoke-like filaments (Dolzmann 1965). Extending from the desmotubule to the plasma membrane, they span the cytosol-filled intermembrane space or cytosolic sleeve. Based on immunolabeling data, it was put forward that these tethers might consist of myosin attached to an actin-coated desmotubule (Radford and White 1998; Reichelt et al. 1999; Baluška et al. 2001; Dong et al. 2011). The implicated class VIII myosins were later found to function in cell division and phragmoplast formation (Wu et al. 2011; Olatunji et al. 2023) – a process during which primary plasmodesmata are formed, which could explain co-localization. Although a structural role for actin and myosin within plasmodesmata cannot be ruled out, their widespread functions in plant cell physiology may account for both the observed localization and the physiological effects seen in perturbation experiments. Using electron tomography on high-pressure-frozen, freeze-substituted samples, Nicolas et al. reconstructed plasmodesmata in 3D with improved ultrastructural preservation (Nicolas et al. 2017). This work revealed cell type-specific differences in cytosolic sleeve diameter, which, intriguingly, did not correlate with expected effects on molecular movement – thinner sleeves permitted increased intercellular diffusion. Notably, the resolved spoke-like tethers were insensitive to actin polymerization inhibitors, challenging the previous actin- and myosin-centered models. Despite these advances in imaging methodology, the molecular identity of the desmotubule-associated particles, plasma membrane particles, and tethering elements remained unresolved.

In parallel, proteomic analyses of plasmodesmata-enriched cellular fractions provided new insights into their molecular composition (Fernandez-Calvino et al. 2011; Park et al. 2017; Kraner et al. 2017; Leijon et al. 2018; Brault et al. 2019; Gombos et al. 2023; Johnston et al. 2023; Schladt et al. 2025). While such datasets are inherently noisy, cross-comparison among studies has led to the proposal of a core plasmodesmal proteome and indicated novel structural and functional components. Chapter 2 and Chapter 3 of this work present proteomics datasets from plasmodesmata-enriched cell wall fractions of *Physcomitrium patens* and *Arabidopsis thaliana* and further discusses individual candidate proteins. One consistently identified protein family are the Multiple C2 Domains and Transmembrane Region Proteins (MCTPs). Fluorescently tagged MCTPs co-localize with known plasmodesmata markers across multiple species (Vaddepalli et al. 2014; Brault et al. 2019; Gombos et al. 2023; Johnston et al. 2023). Their N-terminal C2 domains can bind phospholipids at the plasma membrane, while

their C-terminal reticulon homology domains insert into ER membranes, rendering them compelling candidates for the spoke-like membrane tethers spanning the cytosolic sleeve (Brault et al. 2019; Li et al. 2024; Pérez-Sancho et al. 2025). Chapter 5 of this work presents in situ structures of the desmotubule coat which, in conjunction with proteomics and protein structure predictions, support a role for MCTPs as building blocks of both the desmotubule particles and the spoke-like tethers (Dickmanns et al. 2025, Fig. 2).

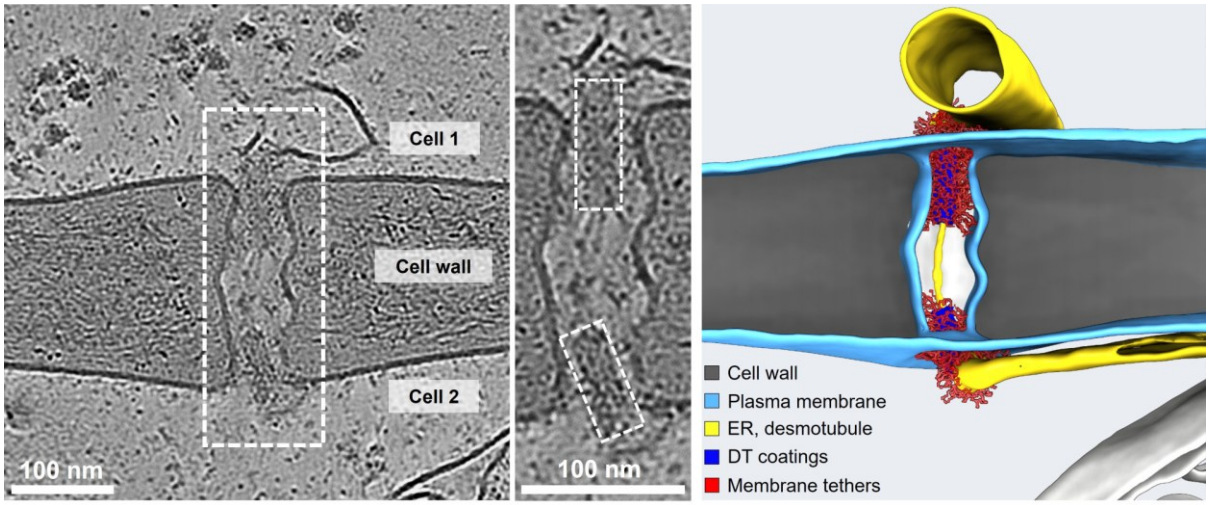


Fig. 2: A plasmodesma connecting two cells of *Physcomitrium patens* across the shared cell wall resolved by cryo-electron tomography. The plasmodesmal pore traversing the cell wall is lined by the plasma membrane (light blue), with a central desmotubule connecting to the cellular ER (yellow). The desmotubule is coated by protein assemblies (dark blue) at neck regions which are connected to the plasma membrane by proteinaceous tethers (red). Data presented in Chapter 5.

Besides internal membrane and protein structures, the surrounding cell wall also plays a major role in shaping plasmodesmata. While initially only unbranched plasmodesmata were described, broader sampling across tissues, developmental stages, and species eventually uncovered a range of pore architectures, including funnel-shaped and branched forms (Franceschi et al. 1994; Ehlers and Kollmann 2001; Ostermeyer et al. 2022). In addition to the diversity in overall pore architecture, cell walls around plasmodesmata also display dynamic reshaping. Synthesis and degradation of callose, a β-1,3-glucan polymer, are known to regulate the diameter of the plasmodesmal aperture and thus modulate permeability (Bayer and Benitez-Alfonso 2024). Callose has been recognized in plant cell walls since the 19th century (Mangin 1892) and, using fluorescent dyes like aniline blue, was later shown to accumulate at plasmodesmata (Currier and Strugger 1956). In classic electron micrographs, electron-lucent halos around plasmodesmata were suspected to represent callose (Esau and Thorsch 1985; Schnepf and Sawidis 1991), which was later confirmed by immunolabeling (Northcote et al. 1989; Vatén et al. 2011). While the function of callose at plasmodesmata remained unclear initially, Gunning had hypothesized a structural gating mechanism in 1976, suggesting that “electron microscopists should be looking for ultrastructural equivalents of sphincters” (Gunning and Robards 1976). Shortly after,

electron-dense structures surrounding the desmotubule and occupying the cytosolic sleeve at neck regions were observed in *Zea mays* and referred to as “sphincters” (Evert et al. 1977; Gao et al. 2022). In the following years, several other authors described ring-like arrangements of likely proteinaceous particles at the apoplasmic side of the neck, likewise adopting the term “sphincters” (Olesen 1979; Badelt et al. 1994). However, it should be emphasized that both of these structures initially named "sphincters" are distinct. They are spatially separated by the plasma membrane - the one surrounding the desmotubule being cytoplasmic, the other ring-like arrangement apoplasmic - and therefore they likely differ in composition and function. Based on current evidence, including data presented in this thesis, we hypothesize that cytoplasmic structures may consist of a disordered protein meshwork populating the cytosolic sleeve, potentially mediating selective filtering of diffusing solutes and/or contributing to the enrichment of specific proteins at plasmodesmata (Chapters 3 and 5). Apoplasmic particles, also referred to as “ring-like wall specializations” (Cook et al. 1997), could be either proteinaceous or consist of cell wall material. More recently, the presence of apoplasmic “callosic dormancy sphincters”, which correlate with regulation of callose-related genes, has been shown to control bud dormancy (Tylewicz et al. 2018). While not resolving ring-like apoplasmic particles, we present tomographic reconstructions of opened and closed plasmodesmata states related to callose and associated with increased and decreased intercellular flow (Chapter 5).

1.1.3 Plasmodesmata – Molecular trafficking and permeability control

A variety of molecules including hormones, metabolites, proteins and RNAs travel from cell to cell through plasmodesmata. Some phytohormones like auxin (Coudert et al. 2015; Mellor et al. 2020; Gao et al. 2020; Mehra et al. 2022) and gibberellin (Kwiatkowska 1991) have been shown to move symplasmically in addition to apoplasmic routes using transporter proteins. In non-vascular plants, metabolites such as photosynthesis-derived sugars are translocated over short and long distances involving symplasmic routes (Raven 2003). In vascular plants, sucrose is primarily synthesized in the photosynthetically active leaf mesophyll cells and moves across multiple cell-cell interfaces towards companion cells, where it is subsequently loaded into phloem sieve elements for long-range distribution in the vasculature. Depending on the species, transfer at each cell-cell interface, including unloading at the destination, may occur symplasmically through plasmodesmata or apoplasmically via SWEET and SUC sucrose transporters (Miras et al. 2022). For these relatively small molecules, passive mechanisms of symplasmic translocation, namely diffusion along a concentration gradient or bulk flow along a pressure gradient, are assumed (Dölger et al. 2014; Tee and Faulkner 2024).

Another notable case involving the phloem is that of the mobile protein signal *Flowering Locus T* (FT). The FT gene is transcribed and translated in phloem companion cells of

mature leaves. Resulting FT proteins are loaded into the phloem sieve elements via plasmodesmata and transported through the vasculature to the shoot apical meristem, where they eventually induce flowering (Corbesier et al. 2007; Liu et al. 2012). The distribution of FT in the shoot apex is impaired at low ambient temperatures, where plasmodesmal closure is triggered via callose deposition (Murata et al. 2025). While the FT protein is regarded as the primary mobile signal, FT mRNA mobility has been reported as well (Li et al. 2011; Lu et al. 2012; Luo et al. 2024). The distribution of certain transcription factors like SHORTROOT (SHR; Nakajima et al. 2001), KNOTTED 1 (KN1; Jackson et al. 1994; Lucas et al. 1995; Vatén et al. 2011), WUSCHEL (WUS; Daum et al. 2014) and LEAFY (LFY; Sessions et al. 2000; Wu et al. 2003) during development and tissue remodeling also involves plasmodesmata. As with FT, the mobility of transcription factors became evident when promoter activity was found to be confined to specific source cells, while the corresponding translated proteins can be detected in distant non-expressing tissues. In many cases it is still unclear whether mobility is conferred by travelling of the transcription factors themselves, their respective mRNAs, or both. Further, if these larger molecules are distributed purely by diffusion, enriched at plasmodesmata by specific targeting, or require facilitated transport remains to be determined.

Apart from endogenous proteins and RNAs, plant viruses also hijack plasmodesmata to spread from initial infection sites and establish systemic infection. To facilitate this, viruses express movement proteins (MPs) that modify plasmodesmal structure and permeability (Alazem et al. 2025). MPs can promote callose degradation, expanding pore size, or in some cases replace the desmotubule with virus-derived protein tubules large enough to shuttling entire virions between cells (van Lent et al. 1990; Ritzenthaler et al. 1995; Cheng et al. 1998). While certain MPs are targeted to plasmodesmata, it also remains unclear whether they actively facilitate transport of genetic information or solely remodel plasmodesmata to enhance passive movement.

The cell-to-cell mobile molecules described here are soluble and expected to use the cytosolic route when travelling symplasmically. Therefore, the diameter of the cytosolic sleeve is thought to determine the plasmodesmal size exclusion limit (SEL); i.e. the maximum size of a solute able to pass through. Ultrastructural modifications to plasmodesmal pore dimensions, such as neck constriction via callose accumulation, have been experimentally linked to changes in permeability (Vatén et al. 2011; Kitagawa et al. 2019), and in some cases the size of investigated solutes seems to correlate with their ability to pass through (Terry and Robards 1987). However, ‘size’ is an ambiguous parameter. Usually expressed as molecular mass (in Dalton) or Stokes radius (in Å or nm), neither fully captures a solute’s biochemical and biophysical properties affecting translocation. Further, plasmodesmata themselves are dynamic structures. Their components undergo Brownian motion, interact transiently with other molecules, and are subject to remodeling and turnover. In such a highly confined and fluctuating environment, other molecular properties like charge, oligomerization state and

conformational flexibility can all be expected to influence solute translocation in addition to size. Recent data support this view, demonstrating that small cationic dyes failed to move cell-to-cell, where interfaces remained permeable for larger anionic fluorophores (Howell et al. 2024). The authors propose that membrane-anchored tethering proteins may shield negative charges on membrane surfaces and thus modulate the electrostatic properties of the cytosol-filled sleeve to allow charge-dependent filtering of solutes. This interpretation aligns with the structure-grounded model presented in Chapter 5 of this thesis, where C2 domain-containing tether proteins with distinct charge patterning (the previously mentioned MCTPs) are proposed to populate cytosolic sleeves. As Howell et al. note, differential expression of variants of such proteins could confer genetically encoded, tissue-specific control of plasmodesmal solute selectivity (Howell et al. 2024).

As discussed, many aspects of plasmodesmata permeability control remain unresolved, but are attributed to a combination of ultrastructural alteration of the pore and the functions of associated protein components. This thesis therefore applies an integrated structural and cell biology approach to investigate structure-function relationships underlying permeability control.

1.1.4 Cryo-Electron Tomography – Structural biology in situ

Since the mid-20th century, structural biology has provided unprecedented insights into the molecular architecture of life. Landmark achievements such as the discovery of the DNA double helix from X-ray diffraction patterns in 1953 (Franklin and Gosling 1953; Watson and Crick 1953; Wilkins et al. 1953) demonstrate the power of molecular structure to reveal biological function. In the following decades, the application of X-ray crystallography, nuclear magnetic resonance (NMR) spectroscopy, and later single-particle analysis by cryo-electron microscopy (SPA cryo-EM) greatly expanded the catalog of available biomolecular structures (Dobson 2019). However, these techniques require the isolation of molecules of interest, removing them from their native cellular environment. As a result, much of the functional and spatial context that defines biological processes in vivo is lost (Baumeister 2022).

In contrast, cryogenic electron tomography (cryo-ET) can be applied in situ, revealing biological structures preserved within their native cellular environment (Plitzko and Baumeister 2019). In cryo-ET, a series of two-dimensional projection images is acquired at different tilt angles from vitrified, electron-transparent samples using a high-voltage (usually 300 keV) cryogenic transmission electron microscope (cryo-TEM). These projections are computationally reconstructed into a three-dimensional representation of the imaged volume. Further computational processing steps like subtomogram averaging allow the extraction of macromolecular structures of protein complexes (Wan and Briggs 2016), while template matching (Böhm et al. 2000; Cruz-León et al. 2024) and membrane segmentation (Lamm et al. 2025) facilitate analysis of the spatial

organization within cells. Through continual advances in hardware and software development, cryo-ET has become increasingly routine. Yet, proper sample preparation remains the principal bottleneck for structural biology in situ, limiting its application to a small range of accessible specimens (Ansell et al. 2025).

Unlike photons, electrons are charged particles carrying mass. Thus, electron beams strongly interact with matter and scatter in gas. Therefore, TEM columns operate under high vacuum, a condition that would dehydrate biological specimens and lead to structural collapse, unless fixed. Classical TEM approaches, therefore also nicknamed "in-plastic" electron microscopy, address this technical challenge by chemical crosslinking and resin embedding to immobilize cellular components prior to imaging (Peters et al. 2021). While sufficient for preserving ultrastructural features such as the relative positions of membranes and organelles, the accompanying treatments denature biomolecules and destroy the fine structural details underpinning their biological functions. In addition, cellular components are impregnated with heavy metals to improve image contrast via amplitude modulation. Classical TEM imaging thus primarily visualizes the metal coatings rather than the actual biomolecules. As a result, samples are altered in ways that preclude high-resolution structural analysis of molecular components within.

In cryo-ET, biological samples are rapidly frozen, preserving them in a fully hydrated state without the need for chemical fixation or staining. Cryo-preservation, however, comes with its own set of challenges. Water, the most abundant molecule in biological samples, readily crystallizes when frozen. Resulting ice crystals expand, deforming surrounding biological structures and altering the distribution of cellular components as some are excluded from the crystal lattice (Huebinger et al. 2016). Moreover, crystalline ice diffracts electrons, producing Bragg reflections leading to imaging artifacts. To avoid these effects, samples must be vitrified; i.e. the water within is converted into an amorphous, glass-like solid devoid of crystalline ice. For samples up to a thickness of 5 to 10 µm – which includes isolated proteins, small procaryotes and some mostly single-celled eukaryotes – vitrification is routinely achieved by plunging samples into a cryogen at liquid nitrogen temperatures (Klumpe et al. 2022). For thicker samples like tissues, the cooling rates achieved by plunge-freezing are not sufficient to suppress ice nucleation, effectively excluding most multicellular organisms from being properly preserved for cryo-ET imaging.

To vitrify thicker specimens, cryoprotecting agents or increased pressure during cooling must be used (Moor 1987). An applied pressure of 2100 bar lowers the melting point of water to around -22°C. This reduces the rates of ice nucleation and crystal growth, providing a longer time window to cool the sample below the critical vitrification temperature (Kanno et al. 1975). Cryoprotectants reduce ice formation by depressing the freezing point through colligative effects, disrupting water-water hydrogen bonding, and increasing solution viscosity, but must be selected carefully to avoid perturbing cellular physiology (Wowk 2010). For thick biological material such as tissues, effective

vitrification may require a combination of high-pressure freezing and addition of cryoprotectants, potentially allowing a vitrification depth of up to 700 µm (Sartori et al. 1993). Notably, plant tissues contain high water contents, particularly within their large vacuoles, and are thus especially difficult to vitrify (Moor 1987; Raven 1987).

Besides its relevance for vitrification, the thickness of a given sample also determines if and how it must be processed before imaging. Electrons must traverse the specimen with limited inelastic scattering so that they still carry interpretable structural signal to the detector, as inelastic scattering leads to energy loss, reduced phase contrast, and ultimately loss of high-resolution information. In practice, adequate contrast at acceptable signal-to-noise ratios is achieved in cryo-ET when samples are thinned to about 200 nm or less (Tuijtel et al. 2024). Thinning is achieved by cryo-focused ion beam (FIB) milling, where a beam of gallium ions or a plasma source is used to ablate excess material and produce electron-transparent lamellae (Schaffer et al. 2017; Berger et al. 2023). In plunge-frozen samples, where individual cells are exposed on the surface of a thin electron microscopy grid, milling down to 200 nm is reasonably fast and can now even be automated to some extent (Klumpe et al. 2021). Samples requiring high pressure freezing for vitrification, however, are housed in several hundred µm thick metal carriers and surrounded by a thick ice layer, drastically increasing the amount of material that needs to be removed to reach electron transparency. Several FIB-based approaches that enable efficient thinning of high-pressure frozen material have been developed in recent years (Kelley et al. 2022; Schiøtz et al. 2024; Nguyen et al. 2024). In this work, we evaluated and adapted these workflows for plant material (Chapter 4 and 6), which allowed us to resolve plant plasmodesmata in situ (Chapter 5).

1.2 Outline of the thesis

Despite being investigated for over a century, plasmodesmata remain enigmatic. Their molecular inventory is incomplete, many putative components are still uncharacterized, and mechanistic understanding is limited. This cumulative work is organized as a sequence of interdependent research chapters, all centered around the question of how intercellular connectivity in plants is mediated by plasmodesmata.

Chapter 1 reviews the current state of plasmodesmata research, from early ultrastructural descriptions to the more recent studies focusing on composition and function. This historic account highlights how advances in the field have repeatedly been facilitated by the adaptation of newly emerging methodologies, as has work presented in the following chapters of this thesis.

Chapter 2 defines a high-confidence plasmodesmata proteome in *Physcomitrium patens*. Defining the molecular context within plasmodesmata is essential for interpreting their function, yet proteomic data sets are inherently noisy and contain many false positives. This chapter aims to refine the candidate list by combining comparative proteomics with sequence feature analysis and systematic in vivo localization.

The resulting high-confidence proteome served as an essential reference for hypothesis generation and integration of downstream data, as described further in Chapters 3 and 5. In parallel, we made use of the emergence of transformer-based protein structure prediction models and developed bioinformatic pipelines for proteome-scale structure prediction and analysis. The developed pipelines are applied throughout the following chapters where they support the characterization of candidate proteins and aid the identification of proteins resolved by cryo-electron tomography (Chapters 4 and 5).

Chapter 3 examines the potential involvement of nucleoporins at plasmodesmata. A central unresolved question in plasmodesmata research is how pore permeability is regulated and, as some solutes readily travel cell-to-cell while others are restricted, how molecular selectivity is achieved. Addressing this gap, the chapter explores parallels between plasmodesmata and other cellular nanopores, namely the nuclear and ciliary pores and their nucleoporin protein components. Nucleoporins were identified in plasmodesmata-enriched proteomic fractions (including Chapter 2), several nucleoporins co-localizing with plasmodesmal markers in vivo, and selected mutants show reduced intercellular solute mobility.

The chapter evaluates whether components of the nuclear pore complex could contribute to permeability regulation at plasmodesmata. While the observations support a functional association, how nucleoporins would be organized within the plasmodesmal pore or whether they form a dedicated plasmodesmal pore complex remains unresolved. This conclusion illustrates the limitations of compositional and

localization data alone and the need for high-resolution approaches to directly resolve molecular organization at plasmodesmata, as pursued in the following chapters.

Chapter 4 describes the development of cryo-electron tomography (cryo-ET) approaches applicable to multicellular plant tissue. While proteomic and genetic studies of plasmodesmata have generated extensive candidate lists, the lack of direct structural information has limited the integration of these findings into a molecular framework. Cryo-ET is uniquely suited to resolve macromolecular organization in situ, but its application has been largely restricted to unicellular systems due to technical constraints. Vitrification, an essential requirement for near-native sample preservation and high-resolution imaging, becomes increasingly difficult to achieve in thick samples like those derived from tissue. In plants, high cellular water content, large cell size, and plant-specific histological features have so far precluded successful application of cryo-ET in the plant sciences.

In this chapter, workflows for sample vitrification, thinning, and data acquisition were developed and assessed, establishing the application of cryo-ET in planta. These methodological advances provide the foundation for the structural analyses of plasmodesmata presented in Chapter 5.

Chapter 5 applies cryo-ET to resolve the architecture of plasmodesmata. Previous imaging of plasmodesmata has largely relied on conventional electron microscopy approaches that revealed general ultrastructural features but do not allow to resolve molecular detail. As a result, how membrane, cell wall and protein components are arranged in native plasmodesmata has remained unresolved.

Applying the workflows developed in Chapter 4, this chapter examines plasmodesmata in *Physcomitrium patens* and resolves their native membrane and pore architecture. In addition, the structure of consistently present protein assemblies coating desmotubule membranes is determined and its constituents are identified. The interpretation of these observations is closely integrated with prior work. Mutant lines characterized in Chapter 2 are used to link architectural pore features to permeability phenotypes. Identification of the proteins forming the desmotubule-coating assembly was aided by filtering of the *Physcomitrium patens* proteome and use of the structure prediction pipelines established earlier (Chapter 2). Further, conceptual considerations on permeability regulation at cellular nanopores, explored in Chapter 3, guided new hypotheses about potential functions of the resolved assembly.

This chapter demonstrates the discovery potential of in situ cryo-ET in the context of plasmodesmata, especially when integrated with findings from complementary approaches. However, in situ cryo-ET remains a technically demanding, low throughput approach that requires substantial user experience. These challenges motivated the following chapter.

Chapter 6 presents a step-by-step protocol for cryo-ET in planta, aimed at lowering the technical entry barrier and facilitating broader adaptation in the plant sciences.

Chapter 7 discusses the findings of previous chapters, their limitations and implications for future work.

Taken together, the research presented here advances the understanding of plasmodesmata biology by integrating compositional, functional, and structural data across complementary experimental approaches. The adaptation of cryo-electron tomography to plants has been a challenging endeavor but ultimately succeeded in visualizing native plasmodesmal organization in situ and, in doing so, revises current models and stimulates new hypotheses to be addressed in the future.

Chapter 2

Taking inventory – The protein landscape in and around plasmodesmata

A high-confidence *Physcomitrium patens* plasmodesmata proteome by iterative scoring and validation reveals diversification of cell wall proteins during evolution

Status: Published, Peer-reviewed.

DOI: https://doi.org/10.1111/nph.18730

2.1 Summary

Background and research question

As proteomics datasets are inherently noisy, existing molecular inventories of plasmodesmata are likely incomplete and contain false positives. This study aimed to establish a comparative, quantitative proteomics strategy combined with in vivo candidate localization to define a high-confidence plasmodesmata proteome.

Experimental approach

The moss *Physcomitrium patens* was used as a model system, for which at the time no plasmodesmata proteome had been established. Plasmodesmata-enriched fractions were obtained from cell wall fractions through enzymatic digestion of the cell wall to release embedded membranes and proteins, including those of the cell wall-enclosed plasmodesmata. Enrichment scores were calculated based on comparison between whole-cell, microsomal, cell wall and plasmodesmata-enriched fractions. In addition, a feature score was derived based on protein and domain annotations in PFAM. Datasets were filtered and compared to published plasmodesmata proteomes from other plant species to assess interspecies conservation and specificity of plasmodesmal association. By fluorescent tagging and microscopy, candidate proteins were scored based on their in vivo co-localization with the plasmodesmal callose markers aniline blue. These experimental results were integrated with feature and enrichment scores to define the threshold for a high-confidence proteome list. Selected high-confidence candidate proteins were further analyzed using experimental and bioinformatic approaches.

Key findings

The study defined a high confidence proteome comprising several hundred candidates and demonstrated that confidence increases substantially when enrichment and cross-species conservation are considered in candidate scoring. Known plasmodesmata-associated protein families (e.g. callose-related enzymes, PDLPs, MCTPs) were recovered, while also identifying and localizing new candidates. Further analysis of selected candidates revealed orthologs of glycosyl hydrolase family 17 (GHL17) proteins and their function in callose degradation and permeability regulation at plasmodesmata. The resulting proteome and characterization of individual proteins formed the basis for subsequent experiments and hypotheses. For example, the in situ architecture of plasmodesmata was later analyzed in the GHL17-overexpressing line, revealing reduced callose levels and wider plasmodesmata, consistent with the increased permeability measured here (see Chapter 5).

Contributions to this chapter

I contributed to the analysis of multiple candidate proteins identified in the high-confidence plasmodesmata proteome. I established structure prediction and sequence analysis pipelines used to predict structures for the majority of high-confidence candidates in the proteome and analyzed their domain architecture and sequence features. Focusing on the identified GHL17 cell wall-modifying enzymes, this included the identification of signaling peptides, GPI-anchor attachment sites and predicted substrate binding sites, which contributed to their overall characterization and classification. With PX, I imaged samples of cell wall and plasmodesmata-enriched cell wall fractions used in the comparative proteomics analysis by cryo-transmission electron microscopy. These experiments confirmed digestion of cell walls and release of membranes and protein components in the plasmodesmata-enriched fraction, in contrast to the undigested cell wall fraction.

Check for updates

New Phytologist

Research

A high-confidence *Physcomitrium patens* plasmodesmata proteome by iterative scoring and validation reveals diversification of cell wall proteins during evolution

Sven Gombos[1]*, Manuel Miras[2]*, Vicky Howe[3]*, Lin Xi[1], Mathieu Pottier[2], Neda S. Kazemein Jasemi[3], Moritz Schladt[2], J. Obinna Ejike[2], Ulla Neumann[4], Sebastian Hänsch[5], Franziska Kuttig[3], Zhaoxia Zhang[1], Marcel Dickmanns[2,6], Peng Xu[6], Thorsten Stefan[1], Wolfgang Baumeister[6], Wolf B. Frommer[2,7], Rüdiger Simon[3] and Waltraud X. Schulze[1]

[1]Department of Plant Systems Biology, University of Hohenheim, 70593 Stuttgart, Germany; [2]Department of Molecular Physiology, Heinrich Heine University of Düsseldorf, 40225 Düsseldorf, Germany; [3]Department of Developmental Genetics, Heinrich Heine University of Düsseldorf, 40225 Düsseldorf, Germany; [4]Central Microscopy, Max Planck Institute for Plant Breeding Research, 50829 Cologne, Germany; [5]Center for Advanced Imaging, Heinrich Heine University of Düsseldorf, 40225 Düsseldorf, Germany; [6]Department of Molecular Structural Biology, Max Planck Institute of Biochemistry, 82152 Martinsried, Germany; [7]Institute for Transformative Biomolecules, Nagoya University, Nagoya 464-0813, Japan

Author for correspondence:
Waltraud X. Schulze
Email: wschulze@uni-hohenheim.de

Received: *4 November 2022*
Accepted: *27 December 2022*

New Phytologist (2023) **238:** 637–653
doi: 10.1111/nph.18730

Key words: cell wall-modifying enzymes, cell-to-cell communication, evolution of multicellularity, plasmodesmata proteome, *Physcomitrium patens*.

Summary

- Plasmodesmata (PD) facilitate movement of molecules between plant cells. Regulation of this movement is still not understood. Plasmodesmata are hard to study, being deeply embedded within cell walls and incorporating several membrane types. Thus, structure and protein composition of PD remain enigmatic. Previous studies of PD protein composition identified protein lists with few validations, making functional conclusions difficult.
- We developed a PD scoring approach in iteration with large-scale systematic localization, defining a high-confidence PD proteome of *Physcomitrium patens* (HC300). HC300, together with *bona fide* PD proteins from literature, were placed in PDDB. About 65% of proteins in HC300 were not previously PD-localized.
- Callose-degrading glycolyl hydrolase family 17 (GHL17) is an abundant protein family with representatives across evolutionary scale. Among GHL17s, we exclusively found members of one phylogenetic clade with PD localization and orthologs occur only in species with developed PD. Phylogenetic comparison was expanded to xyloglucan endotransglucosylases/hydrolases and Exordium-like proteins, which also diversified into PD-localized and non-PD-localized members on distinct phylogenetic clades.
- Our high-confidence PD proteome HC300 provides insights into diversification of large protein families. Iterative and systematic large-scale localization across plant species strengthens the reliability of HC300 as basis for exploring structure, function, and evolution of this important organelle.

Introduction

Plasmodesmata (PD) are important and complex structures present in all land plants, providing connections between plant cells that are otherwise separated by a thick cell wall. During the evolution of multicellular life forms, the exchange of nutrients and information was required to coordinate development and distinct cellular differentiation. The cellular structures and mechanisms facilitating intercellular communication evolved along different paths. In animals, different types of gap junctions mediate the exchange of small molecules between cells, while primary cilia coordinate cell-to-cell signaling (Bangs & Anderson, 2017; Song *et al.*, 2018; Anvarian *et al.*, 2019). In plants, PD evolved to facilitate translocation of both nutrients and signaling molecules in the presence of a cell wall. While the structure and function of gap junctions and primary cilia are rather well understood, PD structure and function remain somewhat enigmatic.

Plasmodesmata were serendipitously discovered in the 1800s by the botanist Eduard Tangl while staining cell wall cellulose using organic pigments. To his surprise, he observed cytoplasmic connections between plant cells in the endosperm (Tangle, 1879). Similar structures were subsequently identified in many other plant species. Notably, analogous structures likely evolved independently at least six times, underlining their necessity for multicellularity (Raven, 2007).

*These authors contributed equally to this work.

© 2023 The Authors
New Phytologist © 2023 New Phytologist Foundation
This is an open access article under the terms of the Creative Commons Attribution-NonCommercial License, which permits use, distribution and reproduction in any medium, provided the original work is properly cited and is not used for commercial purposes

Plasmodesmata connect neighboring cells by forming sophisticated channels lined by a contiguous plasma membrane. A special feature of land plant PD is the desmotubule, a strand of apparently tightly appressed ER that extends through the cytoplasmic sleeve (Ding *et al.*, 1992a,b, 1996). Since their discovery, PD are considered as pores between cells, enabling diffusion of small molecules below a certain size (Wolf *et al.*, 1989). They also seem to enable passage of macromolecules, such as RNAs, peptides, and proteins that are vital for plant development and physiological processes (Lucas *et al.*, 1995, 2009; Kim *et al.*, 2005). Recently, tethering between the plasma membrane and the desmotubule was suggested as a mechanism to control PD pore size and multiple C2 domains and transmembrane region proteins (MCTP) were shown to play a major role in this process (Brault *et al.*, 2019). However, mechanisms of transport through PD are still unclear, as is their precise structural composition.

Proteomic analyses of PD enrichments provide a glimpse of the protein composition of these complex channels. To date, PD proteomes have largely been derived through biochemical enrichment of cell wall preparations, for example in Arabidopsis (Bayer *et al.*, 2006; Fernandez-Calvino *et al.*, 2011; Kraner *et al.*, 2017), *Populus trichocarpa* (Leijon *et al.*, 2018), or *Nicotiana benthamiana* (Park *et al.*, 2017). Some of these proposed PD proteins were also found enriched in detergent-resistant membrane fractions. This may be due to the plasma membrane in PD being characterized by a distinct lipid and sterol composition (Grison *et al.*, 2015a; Yan *et al.*, 2019). Out of several thousand candidates identified in such proteomics analyses, only a small subset has actually been validated with PD localization *in planta*, and the fraction of false positives and contaminants in such lists is expected rather high.

Biochemical preparations of PD obtained, for example, through cell wall enrichment or differential centrifugations contain a large proportion of copurifying proteins from cellular domains other than PD. Therefore, quantitative methods distinguishing PD proteins from non-PD proteins are required. In previous studies, comparative quantitative assessments of PD proteomes were performed, for example, by determining an enrichment ratio of proteins identified in PD compared with cell walls to define a 'core PD proteome' (Brault *et al.*, 2019). In another study, a reduced abundance of PD proteins was observed in the loss of function mutant of Choline Transporter 1 (*cher1-1*) and this observation was used to rank PD components (Kraner *et al.*, 2017). A further approach characterizing PD proteomes explored protein recruitment to PD in response to viral infection (Park *et al.*, 2017). Viral movement between cells occurs through PD and thus proteins recruited or depleted from PD in response to viral infection were considered as candidate PD proteins. However, due to limited validation and limited number of species that have been used in PD studies, a reliable PD proteome with the probabilistic classification of core PD components and copurifying proteins remains to be resolved.

Here, we used the bryophyte *Physcomitrium patens* as a model organism to establish a PD proteome by an iterative discovery-verification workflow using experimental protein enrichment and a feature scoring algorithm in iteration with *in planta* localization. Bryophytes were among the first evolving land plants (Coudert *et al.*, 2019), thus requiring transport and communication between cells despite rigid cell walls. Our results give insights into the large PD protein families, such as cell-wall-modifying enzymes and Exordium (EXO) proteins. These protein families are evolutionarily conserved across species, indicating their importance in the evolution of multicellularity.

Materials and Methods

Plant material and culture conditions

Physcomitrium patens (Hedw.) ecotype Gransden cultures were obtained from the International Moss Stock Center (IMSC, Freiburg, Germany). *Physcomitrium patens* was cultured on modified BCD medium containing 5 mM diammonium tartrate (Cove *et al.*, 2009; Supporting Information Methods S1). *Nicotiana benthamiana* seeds were soaked in water for 24 h at 20°C and then grown on peat moss substrate in a glasshouse for 3 wk under long-day conditions (Methods S1).

Preparation of plasmodesmata

The PD preparation workflow (Fig. S1A) was based on two previously published methods (Faulkner & Bayer, 2017; Kraner *et al.*, 2017) and optimized for *P. patens* tissue. First step in PD (Fig. S1B) preparation workflow was disruption of plant tissue with a Potter-Elvehjem Homogenizer in presence of high detergent concentrations (150 mM NaCl, 10 mM EDTA, 1 mM DTT, 1% (v/v) Triton X-100, 0.5% (v/v) sodium deoxycholate, 0.1% (w/v) SDS, 10% (v/v) glycerol, and 100 mM Tris–HCl, pH 8). This gently perforated cell walls and removed organelles while leaving cell walls mostly intact to preserve PD structures (Fig. S1C). Two subsequent rounds of grinding cell wall fractions in liquid nitrogen efficiently removed additional soluble protein contaminants and prepared cell walls for digestion by breaking up cell clusters (Fig. S1D). Washing with lower concentrations of detergents (150 mM NaCl, 10 mM EDTA, 0.1% (v/v) Triton X-100, 10% (v/v) glycerol, and 100 mM Tris–HCl, pH 8) prevented premature solubilization of PD membranes at this point. Cell wall fragments were digested using driselase. After ultracentrifugation, the resulting PD pellet contained small membranous components and protein aggregates with very little remains of cell walls (Fig. S1E). Along the PD preparation workflow, four protein fractions were collected as input for later PD scoring: cell wall proteins (CW), total of microsomal membranes (Mic), final pellet of PD-enriched proteins (PD), and a total cell extract (TC).

Protein isolation from other sources

Total protein was extracted in a urea thiourea environment (He *et al.*, 2021). Microsomal fraction isolation followed established protocols (Pertl *et al.*, 2001). Cell wall extracts were obtained after cell homogenization with a Potter-Elvehjem PTFE tissue grinder in a high-detergent environment and centrifugation at 1000 ***g*** (Kraner *et al.*, 2017).

© 2023 The Authors
New Phytologist © 2023 New Phytologist Foundation

14698137, 2023, 2, Downloaded from https://nph.onlinelibrary.wiley.com/doi/10.1111/nph.18750 by MPI 386 Biochemistry, Wiley Online Library on [08/01/2026]. See the Terms and Conditions (https://onlinelibrary.wiley.com/terms-and-conditions) on Wiley Online Library for rules of use; OA articles are governed by the applicable Creative Commons License

14698137, 2023, 2, Downloaded from https://nph.onlinelibrary.wiley.com/doi/10.1111/nph.18730 by MPI 386 Biochemistry, Wiley Online Library on [08/01/2026]. See the Terms and Conditions (https://onlinelibrary.wiley.com/terms-and-conditions) on Wiley Online Library for rules of use; OA articles are governed by the applicable Creative Commons License

LC–MS/MS analysis of peptides

Proteins were trypsin-digested and desalted (Hughes *et al.*, 2019), and peptide mixtures were analyzed on a nanoflow UPLC-coupled Orbitrap hybrid mass spectrometer (Q-Exactive HF; Thermo Scientific, Waltham, MA, USA; Methods S1). Spectra were matched against *P. patens* proteome (Ppatens_318_v.3.3.-protein.fasta, 87 533 entries) using MaxQuant v.2.0.3.0 (Cox & Mann, 2008). Mass spectrometry proteomics data were deposited to ProteomeXchange Consortium via the PRIDE partner repository (Deutsch *et al.*, 2017) with identifier PXD032820.

PD score

The PD score is the sum of two components, enrichment score (Eqn 1) and feature score (Eqns 2, 3; Fig. S2A). LFQ values from the TC, MIC, CW, and PD fractions derived from MaxQuant (Tyanova *et al.*, 2016) were $\log_2$-transformed before further calculations. Fraction means were calculated and normalized using *z*-score (Fig. S2B):

$$\text{Enrichment Score}: \sum_{x \in X} z\,\text{Score}\big(\log_2(\text{LFQ intensity PD})\big) - z\,\text{Score}\big(\log_2(\text{LFQ intensity } x)\big) \quad \text{Eqn 1}$$

$X = \{\text{MIC, TC, CW}\}$.

Feature scores were based on frequency of protein functions, and Pfam domains (https://pfam.xfam.org/) found in the reference data set and validated PD candidates. The feature score is the sum of feature frequencies of PD protein-associated features found in the scored protein (Fig. S2C):

$$\text{Feature Frequency}: \sum_{i=1}^{n} \frac{\text{count}(\text{feature}_i)}{\max(\text{count}(\text{feature}_i))} \quad \text{Eqn 2}$$

$$\text{Feature Score}: \sum_{i=1}^{n} \text{feature}_i \text{ frequency} \quad \text{Eqn 3}$$

Quantification of PD candidate localization

Confocal images were screened visually for colocalization of proteins of interest and aniline blue. Candidates showing colocalization with aniline blue were quantitatively scored by the so-called PD index (Grison *et al.*, 2019). To minimize bias in quantification, we used a semi-automated approach of an in-house-generated macro for Fiji software package (Schindelin *et al.*, 2012; Methods S1).

Phylogenetic analysis

GHL17s, XTHs, and EXOs protein sequences were retrieved from Phytozome, Ensembl, Phycocosm, and http://genome.microbedb.jp/klebsormidium databases (Goodstein *et al.*, 2012; Hori *et al.*, 2014; Howe *et al.*, 2020; Grigoriev *et al.*, 2021). All protein sequences were subjected to protein domain prediction at InterPro server (Hunter *et al.*, 2009). Maximum likelihood trees were generated using the NGPhylogeny.fr tool (Lemoine *et al.*, 2019) and visualized and edited in iTol (Letunic & Bork, 2019).

Results

Detection of PD in *P. patens*

To evaluate the presence and type of PD in *Physcomitrium*, transmission electron micrographs of longitudinal and cross sections were generated from protonemata, in which PD were randomly distributed along the cell-to-cell interface (Fig. 1a,b). Simple PD morphotypes were found at interfaces between protonema cells at a relatively high density of 11.3 (±1.4) PD μm^{-2} (Fig. 1c) compared with PD densities in Arabidopsis roots, which ranged from 2.5 to 12.5 PD μm^{-2}, depending on the cell-type interface (Zhu & Lucas, 1998). Plasmodesmata averaged to 362.6 nm (±119.2 nm) in length and 29.7 nm (±4.9) in diameter. *Physcomitrium* protonema PD were clearly longer than what has been published for Arabidopsis suspension cells or roots (Grison *et al.*, 2015b; Nicolas *et al.*, 2017) because of thicker cell walls in measured *Physcomitrium* protonema. The diameter was in a similar range as described previously for Arabidopsis. (Fig. 1d) We achieved an enrichment of common PD proteins from *Physcomitrium* with concurrent depletion of typical contaminants. Proteins expected in PD, such as C2-domain-containing proteins (Brault *et al.*, 2019), were found with increased abundance in PD fractions compared with TC or CW fractions (Fig. 1e). Photosynthetic proteins in PD pellets were found in reduced abundance, while non-PD membrane proteins, such as plasma membrane ATPases, were most abundant in the microsomal fraction (Fig. 1e), and not in PD.

Our PD preparation workflow (Fig. S1) identified a total of 870 proteins in the final PD pellet. A comparison of published PD pellet proteomes from Arabidopsis (Bayer *et al.*, 2006; Fernandez-Calvino *et al.*, 2011; Kraner *et al.*, 2017; Brault *et al.*, 2019), *P. trichocarpa* (Leijon *et al.*, 2018), and *N. benthamiana* (Park *et al.*, 2017) revealed large overlap of 422 Arabidopsis orthologs in PD pellets of *Physcomitrium* and Arabidopsis (Fig. 1f). Besides typical PD protein functions in cell wall modification or C2-domain-containing proteins, there was a high fraction (22%; $n = 38$) of typical contaminants, such as ribosomes and photosynthetic proteins from light-harvesting complexes and Calvin-Benson Cycle among orthologs found in at least three species. The fact that such nontarget proteins made up of a high percentage of the overlap in PD protein lists, suggesting that definition of PD proteins, solely based on discovery in multiple proteomics data sets, lacks specificity and requires additional criteria for a robust definition of PD composition. Therefore, to identify high-confidence PD protein candidates, a data-driven proteomics-based approach was used in iteration with systematic verification of PD localization.

© 2023 The Authors
New Phytologist © 2023 New Phytologist Foundation

New Phytologist

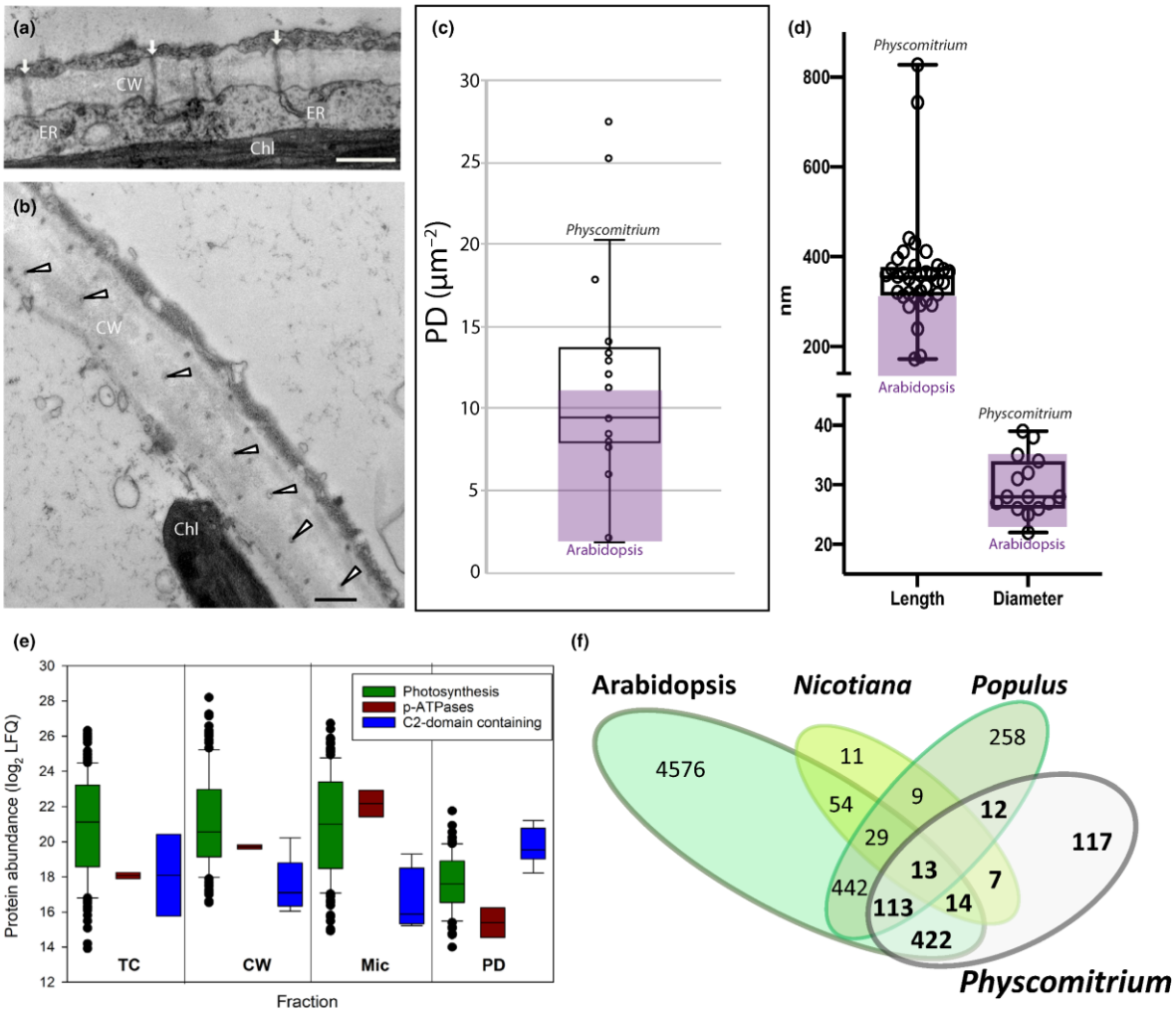


Fig. 1 Plasmodesmata (PD) from *Physcomitrium patens*. (a) Longitudinal section through simple PD between two protonema cells. Desmotubule (pointed with arrows) is visible in the central part of the lumen as a higher electron density. Bar, 500 nm. (b) Cross-section through PD between two protonema cells. Desmotubule (pointed with arrowheads) is visible in the central part of the lumen as a higher electron density. Bar, 500 nm. (c) PD density in protonema cell-to-cell interface as determined by TEM analysis. (d) Measurements of PD length and density based on TEM images. In (c) and (d), purple boxes indicate the ranges of respective values as found in the literature for Arabidopsis. The boxes and whiskers represent the 25th to 75th percentiles and minimum–maximum distributions of the data, respectively. Horizontal lines represent the median and open circles represent individual values. (e) Depletion of nontarget proteins (e.g. photosynthetic proteins) and enrichment of target proteins (e.g. C2-domain-containing proteins) in PD preparations. The family of plasma membrane H^+-ATPases (p-ATPases) was used as control for non-PD plasma membrane. The boxes and whiskers represent the 25th to 75th percentiles and minimum–maximum distributions of the data, respectively. Horizontal lines represent the median and open circles represent individual values. CW, cell wall; Mic, microsomal membranes; PD, plasmodesmata pellet; TC, total cell extract. (f) Overlap of identified protein in PD pellets from *Physcomitrium* and published data sets from *Arabidopsis* (Bayer *et al.*, 2006; Fernandez-Calvino *et al.*, 2011; Kraner *et al.*, 2017; Brault *et al.*, 2019), *Populus trichocarpa* (Leijon *et al.*, 2018) and *Nicotiana benthamiana* (Park *et al.*, 2017). For Arabidopsis, the protein lists from four different studies were combined. For this comparison, Arabidopsis orthologs from respective species were used based on mappings available from PHYTOZOME (Goodstein *et al.*, 2012).

Definition of a high-confidence PD proteome using an iterative scoring system

To reliably distinguish actual PD proteins from non-PD proteins in biochemical PD preparations, we developed a PD score (Fig. S2), which is based on protein abundance data along the PD preparation workflow and on annotated features of a reference data set containing confirmed PD proteins from public sources. We compiled published proteome data sets in a relational database (PDDB http://pddb.uni-hohenheim.de, Fig. S3)

© 2023 The Authors
New Phytologist © 2023 New Phytologist Foundation

14698137, 2023, 2, Downloaded from https://nph.onlinelibrary.wiley.com/doi/10.1111/nph.18730 by MPI 386 Biochemistry, Wiley Online Library on [08/01/2026]. See the Terms and Conditions (https://onlinelibrary.wiley.com/terms-and-conditions) on Wiley Online Library for rules of use; OA articles are governed by the applicable Creative Commons License

14698137, 2023, 2, Downloaded from https://nph.onlinelibrary.wiley.com/doi/10.1111/nph.18730 by MPI 386 Biochemistry, Wiley Online Library on [08/01/2026]. See the Terms and Conditions (https://onlinelibrary.wiley.com/terms-and-conditions) on Wiley Online Library for rules of use; OA articles are governed by the applicable Creative Commons License

and complemented this with 70 individual protein entries with literature evidence of experimental PD localization (Table S1). These proteins were used as *bona fide* confirmed PD proteins and were further expanded by 115 proteins published as the PD core proteome (Brault *et al.*, 2019) based on their high enrichment in PD fractions compared with cell wall or membrane fractions. Additional reliable PD proteins from published sources included 152 proteins with greater than twofold depletion in the *cher1-1* mutant (Kraner *et al.*, 2017), and 56 proteins (52 unique Arabidopsis orthologs) with more than fivefold enrichment or depletion in PD in response to viral infection (Park *et al.*, 2017). Respective threshold values were chosen upon re-evaluation and by applying a two-standard deviation width to histograms of published quantitative data (Table S1). The list of 201 proteins published as PD-enriched from *P. trichocarpa* (Leijon *et al.*, 2018) was not included, since no enrichment ratios were published, making a quantitative re-evaluation difficult. Thus, the first PD scoring training data set comprised 338 unique Arabidopsis orthologs (Table S1) coming from complementary data sources (Fig. 2a).

The PD score was then calculated for each identified protein as the sum of an enrichment score and a feature score (Fig. S2). The enrichment score was derived from the abundance of proteins identified in PD fractions compared with the corresponding abundance in CW, MIC, and TC. The feature score was calculated from frequencies of PFAM domains (http://www.pantherdb.org) and functional classifications by MAPMAN (Thimm *et al.*, 2004) in the reference data set of 338 *bona fide* PD proteins. Consequently, proteins received higher PD scores when they were enriched in the PD fraction and in addition shared features with reference PD proteins.

For 863 proteins found in the *Physcomitrium* PD pellet, we were able to calculate an enrichment score, and for 200 proteins the enrichment score was > 1 (Fig. 2b). The full PD score was calculated for 2053 out of the 4996 identified proteins (Table S2). There were more proteins with a PD score (Fig. 2c) than with an enrichment score because also proteins not quantified by an enrichment score were awarded a PD score based on their features, and thus potentially qualified as part of the PD proteome. Out of this first PD score distribution, 147 proteins were selected and the corresponding cDNAs were cloned to validate PD localization by transient expression in *N. benthamiana* (Fig. 2d). Proteins which localized to PD were added to the reference data set in PDDB for PD scoring. As a result of an iterative second PD scoring based on the updated PD protein list, most of the experimentally localized PD proteins increased in PD score, as did other proteins with similar features (Fig. 2e). This visualizes the key concept of iterative PD scoring consisting of (1) protein abundance enrichment in PD fractions, (2) identification of proteins with similar features as known reference proteins, and (3) re-evaluating their PD score based on features of experimentally validated new PD-localized proteins.

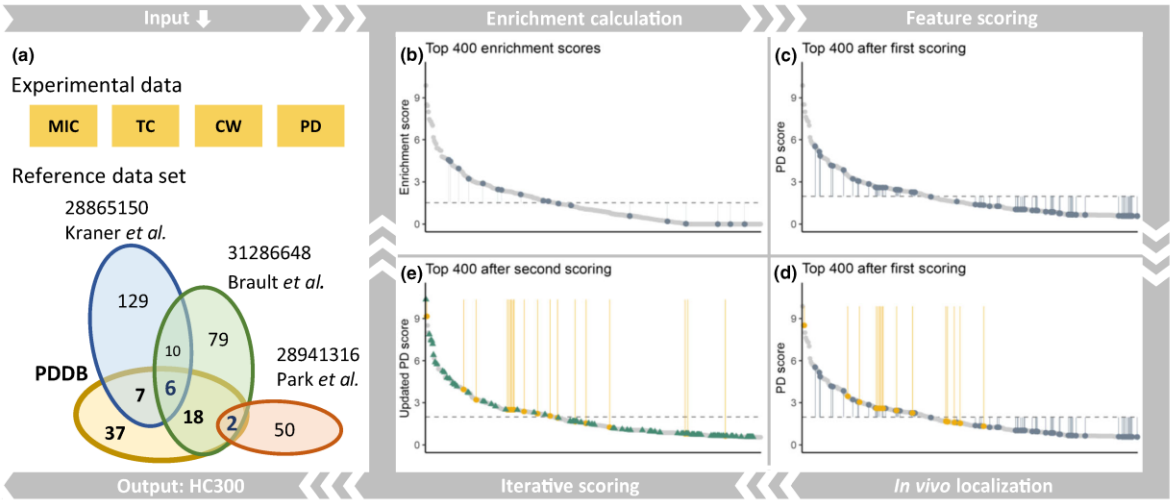


Fig. 2 Plasmodesmata (PD) scoring process visualized with the top 400 best-scoring proteins. (a) Input data consisting of protein abundances in microsomal (MIC), total cell (TC), cell wall (CW), and PD fractions and the *bona fide* PD reference data set of PD proteins characterized by quantitative proteomics (Kraner *et al.*, 2017; Park *et al.*, 2017; Brault *et al.*, 2019) (blue, green, red) and the additional PD-localized proteins in PDDB from different literature sources (yellow). This data set was used as a PD positive set in the first round of PD scoring. (b–e) The components of the PD scoring process. The *y*-axes show enrichment score or PD score. Each of the top 400 scoring proteins is represented by a light gray dot. Proteins are ordered by score in descending order from left to right. Dark gray dots and vertical lines mark the scores of proteins from the reference data set. Yellow dots and vertical lines mark the scores of proteins that have been verified by *in vivo* localization. Gray dashed lines show mean scores. (b) Calculation of the enrichment score that is solely based on proteomics data. (c) PD scores after including a first round of feature scoring. Higher values represent higher likelihood for PD presence. (d) Scores of newly PD-localized proteins are highlighted (yellow dots with vertical yellow lines) before iterative scoring. (e) Iterative second PD scoring including proteins experimentally localized to PD across the full range of PD candidate proteins. Green triangles indicate proteins which were not part of the reference data set but increased in score after iterative scoring.

© 2023 The Authors
New Phytologist © 2023 New Phytologist Foundation

New Phytologist

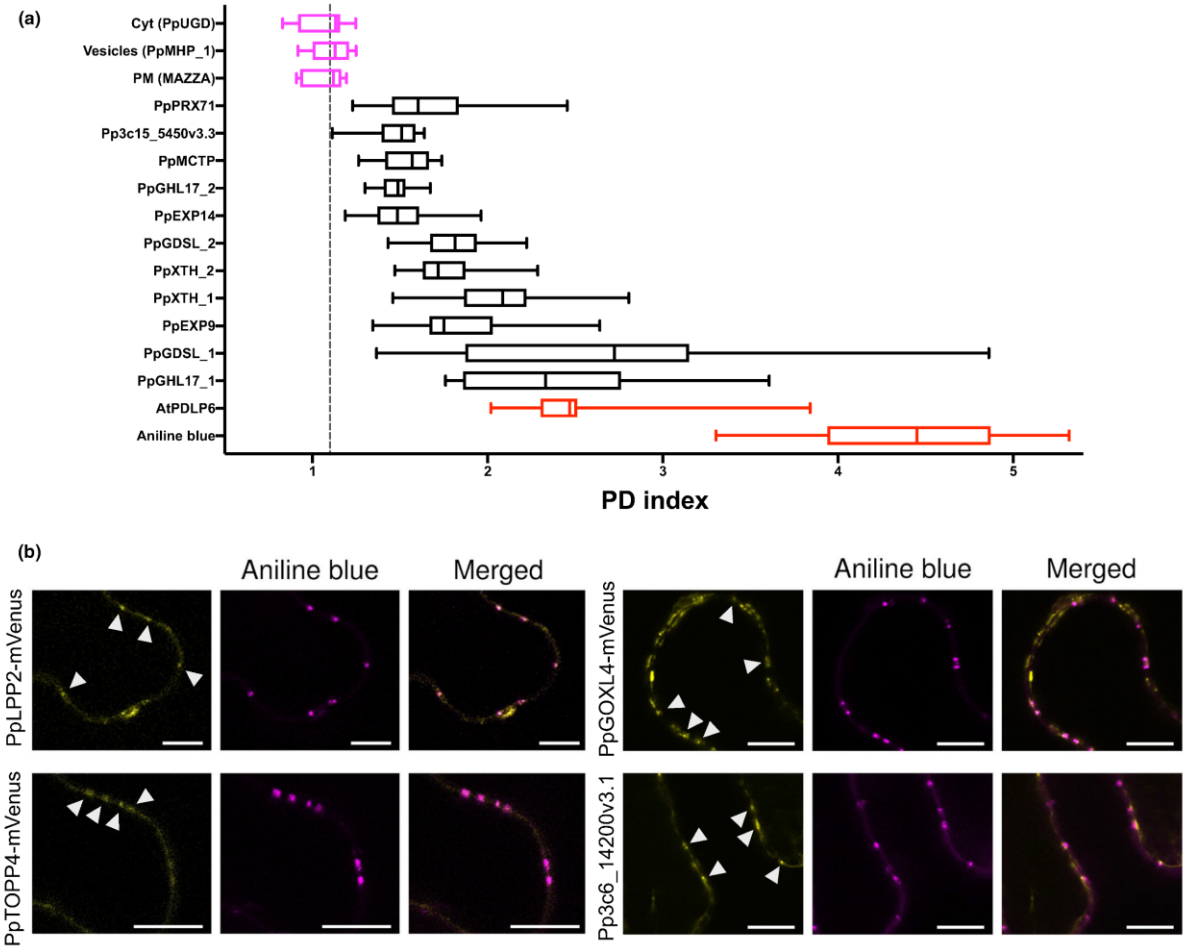


Fig. 3 Selected candidate proteins from *Physcomitrium patens* plasmodesmata (PD) proteome located at PD. Proteins were C-terminally fused to mVenus and transiently expressed under a β-estradiol inducible promoter. Subcellular localization was observed in epidermal cells of *Nicotiana benthamiana* at the confocal microscope. (a) Plasmodesmata index (PD index) of selected candidates, mainly known PD proteins, showed an enrichment at PD similar to well-established PD marker Arabidopsis Plasmodesmata Located Protein 6 (PDLP6). Plasmodesmata markers aniline blue and PDLP6, and non-PD-localized proteins Arabidopsis MAZZA (PM), PpMHP_1 (Pp3c16_460v3.7; vesicles), and PpUGD (cytoplasm) are shown as red and magenta boxplots, respectively. In the boxplots, the median value is denoted by a line and the boxes and whiskers represent the 25th to 75th percentiles, and minimum to maximum distribution. Dashed lines represent the threshold at which a protein is considered PD-enriched and was set at 1.1 corresponding to the highest mean score of the non-PD-localized proteins PpMHP_1. (b) Examples of single optical sections at cell-to-cell interface showing the colocalization of four novel PD protein candidates with PD marker aniline blue (white arrowheads). Bars, 10 μm.

Validation of PD localization using confocal microscopy

Putative PD-localized proteins were systematically screened for colocalization with the callose-staining dye aniline blue as a marker of PD pit fields. Candidates were initially screened for PD localization and given a preliminary validation score (Table S3). Proteins not colocalizing with aniline blue (112 candidates) were considered non-PD proteins for the purpose of PD scoring iteration. For the 36 proteins colocalizing with aniline blue, the degree of enrichment at PD compared with PM was calculated using a semi-automated PD indexing script. Proteins with a PD index > 1.1 (the highest mean score of the negative controls, Figs 3a, S4) were considered enriched at PD compared with bulk PM. For comparison, aniline blue and the Arabidopsis protein Plasmodesmata Located Protein 6 (PDLP6), a protein known to localize exclusively to PD (Thomas *et al.*, 2008), were used as positive controls (Fig. S4). Aniline blue had a PD index of 4.4, while PDLP6 had a PD index of 2.5. Similarly, three proteins from the initial screen that did not show any obvious colocalization with aniline blue, localizing to either PM, vesicles, or cytoplasm, were used as negative controls and had PD indices of *c.* 1.

Due to deficiencies in image quality, the PD index could not be calculated for all candidates deemed PD-localized by qualitative means. We calculated PD indices (range: 1.4–2.7) for 30 of

© 2023 The Authors
New Phytologist © 2023 New Phytologist Foundation

14698137, 2023, 2, Downloaded from https://nph.onlinelibrary.wiley.com/doi/10.1111/nph.18730 by MPI 386 Biochemistry, Wiley Online Library on [08/01/2026]. See the Terms and Conditions (https://onlinelibrary.wiley.com/terms-and-conditions) on Wiley Online Library for rules of use; OA articles are governed by the applicable Creative Commons License

14698137, 2023, 2, Downloaded from https://nph.onlinelibrary.wiley.com/doi/10.1111/nph.18750 by MPI 386 Biochemistry, Wiley Online Library on [08/01/2026]. See the Terms and Conditions (https://onlinelibrary.wiley.com/terms-and-conditions) on Wiley Online Library for rules of use; OA articles are governed by the applicable Creative Commons License

the 36 candidates that colocalized with aniline blue (Fig. 3b). For the purposes of iterating the PD scoring, all 36 candidates, including those not assigned a PD index, were treated as PD-localized proteins. Among this set of proteins were 20 proteins (56%) that had not previously been considered as PD proteins in other species (Table S4). Five members of the glyoxal oxidase family (Pp3c12_15000; Pp3c3_25264; Pp3c4_20120; Pp3c2_25840; Pp3c22_8310, and pPGOXL4, Fig. 3b), a serine–threonine phosphatase (Pp3c1_370, TOPP4, Fig. 3b), an uncharacterized transmembrane proteins (e.g. Pp3c6_14200, Fig. 3b), and members of the EXO protein family are examples of novel PD-localized proteins, which ranked among the top 10% proteins in the PD scoring (Table S2). For iterative scoring, the feature score component was modified by the contribution of these PD-localized proteins.

Refinement of a *Physcomitrium* high-confidence PD proteome

The iterative PD scores of proteins confirmed as PD localized in *N. benthamiana* clearly separated from PD scores of proteins that could not be localized to PD (Figs 4a, S5A). The PD score was then used to separate high-confidence PD proteins from other proteins (Figs 4a, S5A). A threshold PD score of 0.7 was chosen by carefully balancing the numbers of proteins not found with PD localization among the top-ranking proteins against proteins found with PD localization among lower ranking proteins. Among those 335 PD protein candidates with PD scores > 0.7 (Table S2) were 16 of the cloned and tested proteins, which did not show PD localization in *N. benthamiana*. Although there may be many valid reasons for failed PD localization of these proteins, we termed these as false positives and they made up 3.9% of the top 335 ranking PD protein subset. In turn, 28 proteins (1.6%) localizing to PD in *N. benthamiana* were found among the 1718 proteins with a calculated PD score of < 0.7, which were considered as false negatives.

The 335 PD protein candidates were further refined by considering the PD score difference between the second and the first round of PD scoring, thus taking advantage of the iterative improvement of PD scores by the contribution of novel PD protein functions after experimental localization. For protein functions expected among PD proteins, such as cell wall modifying proteins and C2-domain-containing proteins, but also for proteins with functions not thus far associated with typical PD proteins, the PD score improved throughout the iterative scoring process leading to high average PD score differences (Fig. S5B). In turn, for typical contaminant proteins, such as ribosomes, catalases, and photosynthetic proteins, the PD score was downgraded by the iterative process resulting in large negative PD score differences (Fig. S5B). By applying the PD score difference as further refinement, we excluded proteins that had a negative PD score difference (PD score difference < −0.13; Fig. 4b), resulting in *P. patens* high-confidence PD Proteome (HC300).

Arabidopsis orthologs were used to compare *Physcomitrium* PD proteomes with previously published PD proteomes of other species (Fig. 4c,d). The whole PD proteome dataset contained 1436 Arabidopsis orthologs (Fig. 4c). Of the 292 proteins contained in the HC300, 273 proteins were annotated with Arabidopsis orthologs. After exclusion of photosynthetic proteins as typical contaminants, HC300 contained 39 proteins annotated to 17 orthologs of confirmed PD proteins in other species and 249 other proteins mapping to 191 orthologous proteins which were previously not considered as high-confidence PD proteins (Fig. 4d,e). Upon stepwise refinement of the *Physcomitrium* HC300 PD proteome based on PD score and PD score difference, the overlap with other quantitative PD proteomes (Kraner *et al.*, 2017; Park *et al.*, 2017; Brault *et al.*, 2019) became smaller at each refinement step (Fig. 4c,d). The refinement steps efficiently removed typical contaminants, such as photosynthetic proteins and ribosomes. The proportion of contaminant proteins was rather high (25%) among the proteins not considered high-confidence PD proteins while in HC300 the fraction of putative contaminants was reduced to 16% (Fig. 4e). Among the novel proteins in HC300 were five out of 17 EXO/Exordium-Like (EXL) proteins, whose Arabidopsis orthologs were previously shown to be located in cell walls (Schröder *et al.*, 2009). HC300 contained five out of seven MCTP protein family members (Pp3c27_520, Pp3c14_25200, and Pp3c10_11080 in Fig. S4, Pp3c16_9250 and Pp3c27_540) as well as two other C2-domain-containing proteins (Pp3c9_16970 and Pp3c9_12510). Three receptor kinases (Pp3c25_12800, Pp3c1_10970, and Pp3c19_8660), a phosphatase (Pp3c1_370), and a transmembrane scaffold protein (Pp3c4_1550) were further top-ranking proteins of HC300 (Table S2).

Within HC300, 62% of the proteins were found to have a signal peptide, 76% had at least one transmembrane domain, and 57% of the proteins were predicted to have intrinsically disordered regions (IDR). Cell wall proteins (84 proteins; bins 10; $P = 5.5 \times 10^{-26}$) were highly over-represented, as were glyoxal oxidases (bin 24; $P = 8.9 \times 10^{-13}$; Fig. S5C). In agreement with the overall high content of cell wall-related proteins, HC300 was significantly enriched with PFAM domains of glycosyl hydrolase family 17 (GHL17) proteins (PF00332 and GHL17s), xyloglucan endotransglucosylases/hydrolases (PF06955, XTHs), and pectin esterase (PF1095). The PFAM X8 domain (PF07983), proposed with a role in protein targeting to PD through its signal sequences for a glycosylphosphatidylinositol (GPI) linkage, was found 14 times (5%; Fig. S5D; Simpson *et al.*, 2009).

Phylogenetic distribution of glycosyl hydrolase family 17

Cell wall proteins made up the largest functional group in HC300. We identified 16 proteins annotated as β-1,3-glucanases containing a GHL17 domain (Table S2). GHL17s are callose-degrading enzymes located at the cell wall and associated with PD (Levy *et al.*, 2007; Zavaliev *et al.*, 2013; Benitez-Alfonso, 2014). Members of the GHL17 family were previously identified in PD proteome lists from Arabidopsis, *P. trichocarpa*, and *N. benthamiana*, and 10 of them overlapped in at least two species. PpGHL17_16 (Pp3c16_16680) was the only member of the GHL17 family, for which orthologs were found in PD proteome lists of all four species. *Physcomitrium patens* HC300

© 2023 The Authors
New Phytologist © 2023 New Phytologist Foundation

New Phytologist

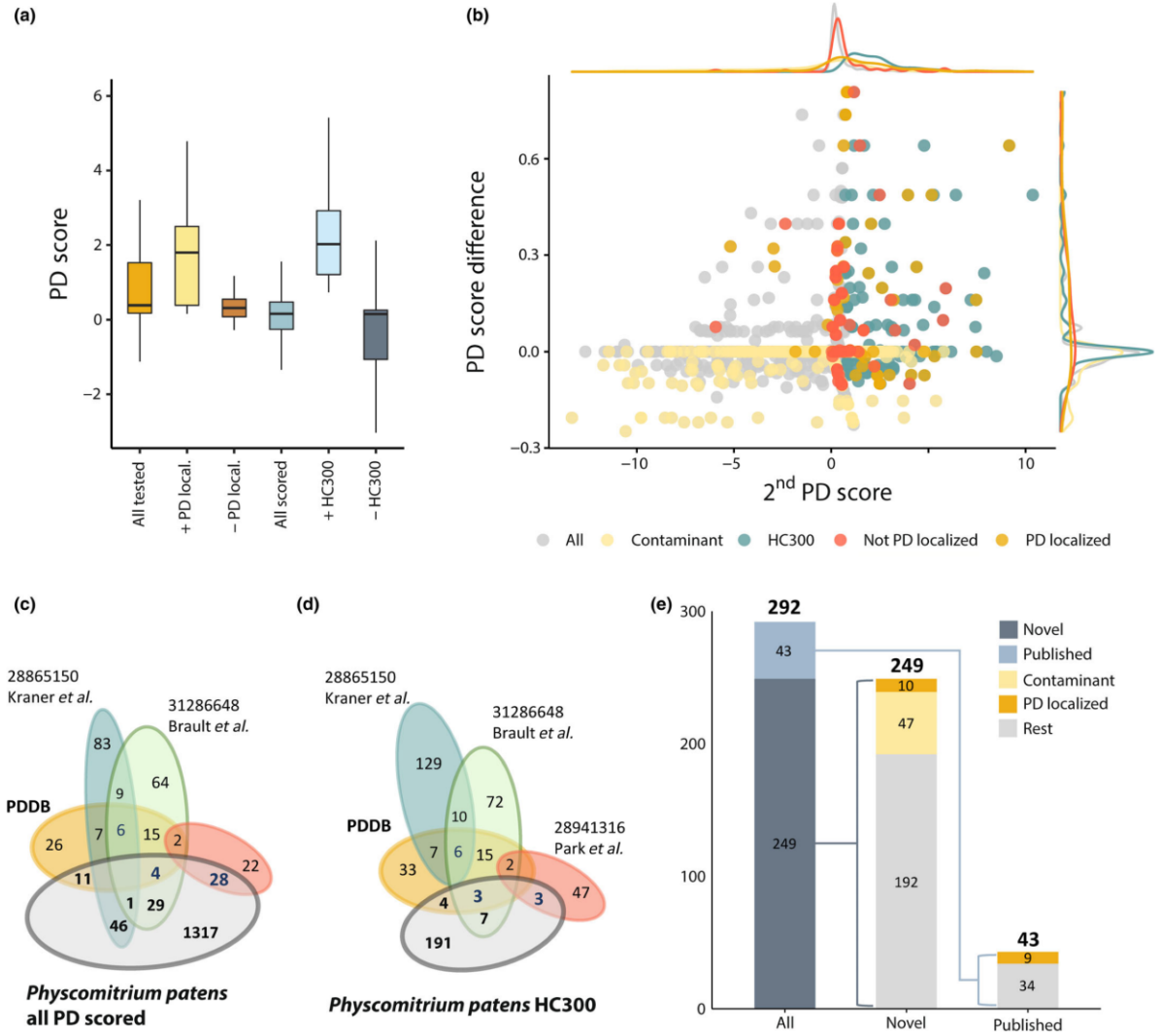


Fig. 4 Characterization of *Physcomitrium* plasmodesmata (PD) scored proteome. (a) Boxplots of PD scores (2nd scoring) of all proteins that were tested for localization at PD in *Nicotiana benthamiana* combined ('All tested') and separated into the proteins localized ('+ PD local.') and nonlocalized to PD ('– PD local.') and boxplots of PD scores (2nd scoring) of all scored proteins combined ('All scored') and separated into proteins that were included into the refined HC300 proteome ('+ HC300)') and excluded of the HC300 proteome ('- HC300'). Outliers were removed to improve clarity. See Supporting Information (Fig. S5A) for a comprehensive version of the plot. Horizontal lines represent the median value, whiskers indicate 25th and 75th percentiles. (b) PD score (> 0.7) and PD score difference (> −0.13) as criteria to define the high-confidence *Physcomitrium* PD proteome. Light gray: proteins not included in the refined HC300 proteome. Light yellow: photosynthetic proteins and ribosomal proteins as typical contaminants. Blue, refined HC300 proteome; red, proteins that did not localize at PD in *N. benthamiana*; yellow, proteins with PD localization in *N. benthamiana*. (c) Venn diagram containing the nonrefined set of Arabidopsis orthologs of all PD-scored proteins and the *bona fide* PD reference data set. (d) Venn diagram containing the Arabidopsis orthologs of the refined high-confidence PD proteome HC300 and the *bona fide* PD reference data set. (e) Overview of the HC300 based on *Physcomitrium* protein identifiers classified as 'published' and novel' proteins. For each group, contaminants (e.g. plastidial proteins) and experimentally PD-localized proteins were specifically highlighted.

contained three GHL17 orthologs (PpGHL17_2, PpGHL17_7, and PpGHL17_9; Table S5), which showed no overlap with PD proteomes from angiosperms (Fig. 5a).

Based on sequence similarity, GHL17 proteins of representative species from charophytic algae and embryophytes, including *P. patens*, were classified into three major clades (Doxey *et al.*, 2007; Gaudioso-Pedraza & Benitez-Alfonso, 2014). To get insights into their role in the evolution of multicellularity, a new phylogenetic analysis of the GHL17 family was performed including *P. patens*, Arabidopsis, *P. trichocarpa*, *Oryza sativa*, and

© 2023 The Authors
New Phytologist © 2023 New Phytologist Foundation

14698137, 2023, 2, Downloaded from https://nph.onlinelibrary.wiley.com/doi/10.1111/nph.18720 by MPI 306 Biochemistry, Wiley Online Library on [08/01/2026]. See the Terms and Conditions (https://onlinelibrary.wiley.com/terms-and-conditions) on Wiley Online Library for rules of use; OA articles are governed by the applicable Creative Commons License

14698137, 2023, 2, Downloaded from https://nph.onlinelibrary.wiley.com/doi/10.1111/nph.18750 by MPI 386 Biochemistry, Wiley Online Library on [08/01/2026]. See the Terms and Conditions (https://onlinelibrary.wiley.com/terms-and-conditions) on Wiley Online Library for rules of use; OA articles are governed by the applicable Creative Commons License

representative species from green algae (Figs 5b, S6A). Unexpectedly, no GHL17 orthologs could be identified in the unicellular algae *Mesostigma viride* and *Chlamydomonas reinhardtii*, which belong to the *Streptophyta* and *Chlorophyta* clades and thus are ancestors to embryophytes. This suggests that the GHL17 family emerged in multicellular organisms.

GHL17s from charophytic algae (*Klebsormidium nitens*, *Chara braunii*, and *Nepenthes mirabilis*) were present only near the base of the gamma clade, likely representing the ancestral type of GHL17 proteins (Fig. 5b). The alpha clade only contained GHL17s from embryophytes, suggesting that this group appeared during land colonization. Three of the Arabidopsis GHL17 proteins from the alpha clade were previously described to localize at PD, suggesting that phylogenetic distribution might correlate with the subcellular localization either at PD or apoplasm (Levy *et al.*, 2007; Benitez-Alfonso *et al.*, 2013). To further test this hypothesis, we studied the subcellular localization of six *P. patens* GHL17 representatives, four from the alpha clade and two from the beta clade by transient expression in *N. benthamiana*.

Transient expression of beta clustered PpGHL17_28-mVenus and PpGHL17_30-mVenus showed apoplasmic localization (Fig. S6B), whereas PpGHL17_1-mVenus, PpGHL17_7-mVenus, PpGHL17_8-mVenus, and PpGHL17_15-mVenus from the alpha clades were found with a punctate pattern at the cell periphery and overlaid with aniline blue (Fig. 5c). Since transient expression assays can lead to mislocalization, and PD targeting mechanisms might not be conserved between *N. benthamiana* and *P. patens*, we obtained a *P. patens* stable transgenic line expressing UBQ:PpGHL17_1-mVenus to further validate PD localization. The subcellular localization of PpGHL17_1-mVenus in the stable line confirmed PD localization found in transient expression assays (Fig. 5d,e). In addition, when overexpressing PD-localized PpGHL17_1 in *Physcomitrium*, diffusion of the PD mobile dye carboxyfluorescein diacetate (CFDA) increased compared with wild-type ecotype (Fig. 5f, g) suggesting GHL17s play a role in regulating PD opening through the degradation of callose. Interestingly, expressing beta-clade PpGHL17_30, which did not localize to PD (Fig. S6), did not enhance CFDA diffusion between neighboring protonema cells (Fig. 5f,g). This points to a functional diversification of PD and non-PD-localized members of the GHL17 family or that only PD-localized PpGHL17s can degrade callose at PD. In recent parallel work, GHL17_4 (Pp3c11_25840) and GHL17_18 (Ppc16_15860), also members of the GHL17 alpha clade, were localized to PD in *P. patens* (Johnston *et al.*, 2023), thus adding further evidence for PD localization of alpha clade GHL17s.

In search of a potential PD localization signal, we modeled structures of alpha-clade PpGHL17s (Fig. 5h). The sequence motif IFALFENE(N) was over-represented among this group of GHL17s and was absent in the members of the beta clade. However, this motif was predicted to be only partially surface-exposed as part of the 40 Å cleft of the glycosyl hydrolase domain and is therefore more likely to be related to enzyme function rather than localization (Fig. 5g). Another interesting observation was that all GHL17s from the alpha clade contained a beta tunnel and cleft domain, while the distribution of other structural features, such as an X8 domain and GPI-anchor signal, was not equally present (Table S5).

Xyloglucan endotransglucosylases/hydrolases

XTHs are enzymes involved in xyloglucan metabolism and are important for the control of cell wall strength as well as extensibility during growth and development. In Arabidopsis, XTHs were shown to be upregulated in the *ise2* mutants, which displayed an increase in cell-to-cell transport of fluorescent probes (Burch-Smith *et al.*, 2011). We found 12 members of the XTH family in HC300, six of which were confirmed as PD-localized in *N. benthamiana* (Fig. S7A). The molecular phylogeny of XTH genes was previously shown to segregate into three major groups (I, II, and III), and an isolated small group named 'ancestral' (Baumann *et al.*, 2007; Eklöf & Brumer, 2010; Shinohara & Nishitani, 2021). All *Physcomitrium* XTH genes, except Pp3c13_11910 and Pp3c3_9730, clustered in group I. The PpXTHs identified in HC300 were exclusively from group I (Fig. S7B), indicating a correlation between PD localization and phylogenetic distribution to group I.

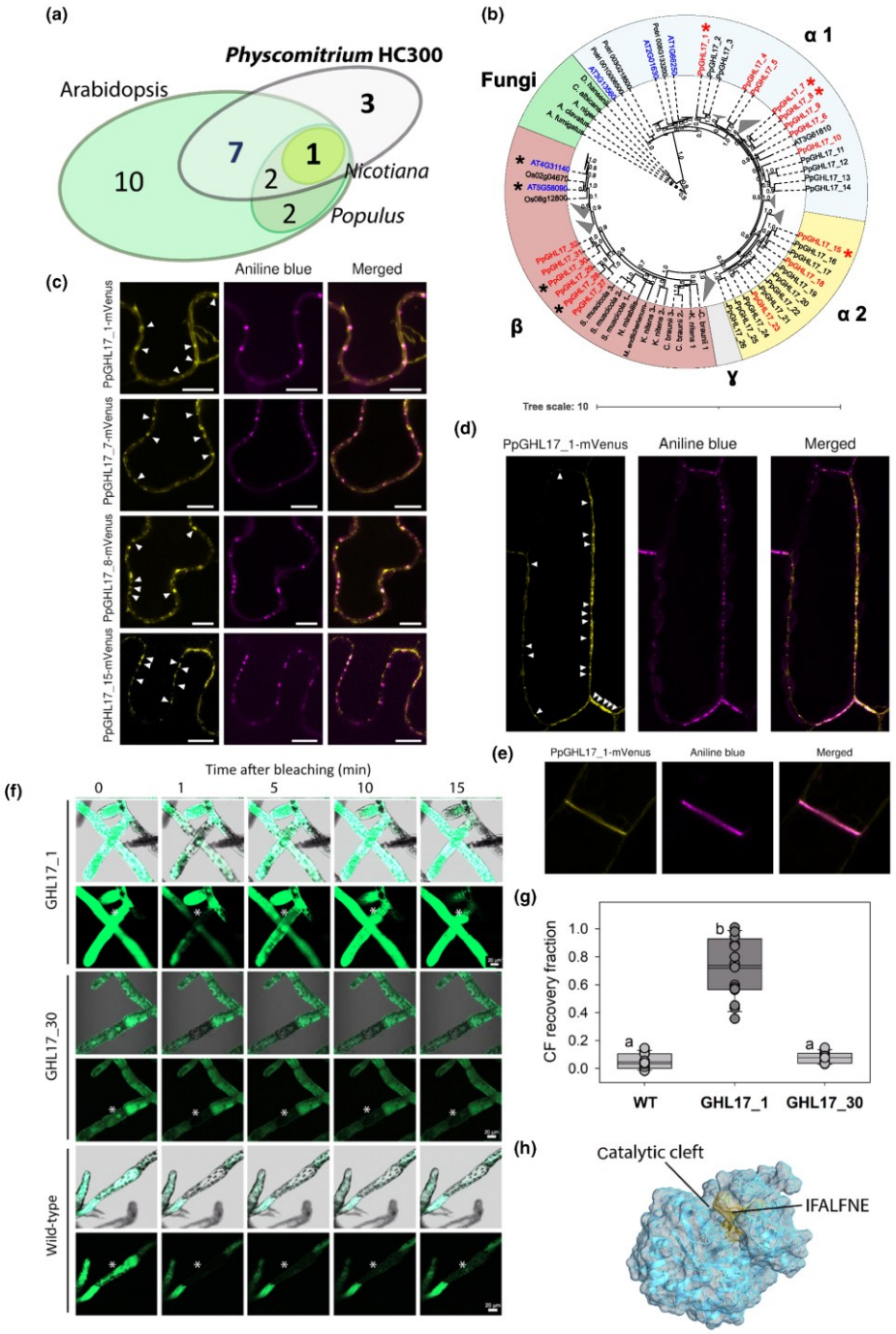
Exordium and exordium-like proteins

Five members of the Arabidopsis EXO and EXL protein family were identified in HC300: Pp3c19_8770 (PpEXO1), Pp3c10_8680, and Pp3c14_6120 (AtEXO ortholog by protein BLAST), Pp3c18_22500 (AtPHI1/EXL7 ortholog), and Pp3c22_12550 (AtEXL2 ortholog). EXL2 was previously found in Arabidopsis and *P. trichocarpa* PD proteomes, but their PD localization was not confirmed (Fernandez-Calvino *et al.*, 2011; Leijon *et al.*, 2018). Several members of this family were also found in Arabidopsis cell wall proteomes (AtEXO, AtEXL1, AtEXL2, AtEXL3, and AtEXO4) and membrane proteomes (AtEXL4) (Bayer *et al.*, 2006; Feiz *et al.*, 2006; Jamet *et al.*, 2006; Mitra *et al.*, 2007). Here, PpEXO1 and Pp3c22_12550 were found among the top 10 PD score ranks in HC300 (Table S2) and PpEXO1 localized to PD in transient expression assays in *N. benthamiana* (Fig. 6a). The members of the EXO protein family share structural similarity in an N-terminal tail with a transmembrane domain and a globular C-terminal part (Fig. 6b). The globular part of the EXO proteins contains a distinct 'nose' with two clefts, which could serve as scaffolding or binding sites (Fig. 6b).

A phylogenetic analysis was undertaken to study sequence divergence along the EXO family evolution. Exordium proteins from representative species of the embryophytes (17 from *P. patens*, 8 from Arabidopsis, 12 from *O. sativa*, and 17 from *P. trichocarpa*) as well as all EXO proteins identified in algae were therefore included in this analysis (Fig. 6b). We found that EXOs are distributed between three clades. While clade I contained only EXO sequences from algae including both Chlorophyta and Charaphyta, clade II contained EXO sequences from all the investigated species, distributed between two subclades. Subclade II-a exclusively included EXOs from the algae *Spirogloea*

© 2023 The Authors
New Phytologist © 2023 New Phytologist Foundation

muscicola, and subclade II-b contained embryophyte sequences. This clustering shows that embryophyte EXOs found in clade II are more similar to the EXOs of algae *S. muscicola* of subclade II-b than to embryophyte EXOs found in clade III. Clade III contained EXO sequences from all investigated embryophyte species but none from the investigated algae species. The four *P. patens*



© 2023 The Authors
New Phytologist © 2023 New Phytologist Foundation

14698137, 2023, 2, Downloaded from https://nph.onlinelibrary.wiley.com/doi/10.1111/nph.18730 by MPI 306 Biochemistry, Wiley Online Library on [08/01/2026]. See the Terms and Conditions (https://onlinelibrary.wiley.com/terms-and-conditions) on Wiley Online Library for rules of use; OA articles are governed by the applicable Creative Commons License

14698137, 2023, 2, Downloaded from https://nph.onlinelibrary.wiley.com/doi/10.1111/nph.18730 by MPI 386 Biochemistry, Wiley Online Library on [08/01/2026]. See the Terms and Conditions (https://onlinelibrary.wiley.com/terms-and-conditions) on Wiley Online Library for rules of use; OA articles are governed by the applicable Creative Commons License

Fig. 5 Plasmodesmata (PD) localization of glycolyl hydrolase 17 (GHL17) proteins correlates with phylogenetic distribution. (a) Members of the GHL17 family identified in PD proteomes from angiosperms (Arabidopsis, *Populus trichocarpa*, *Nicotiana benthamiana*) and the moss *Physcomitrium*. (b) Phylogenetic analysis of GHL17 sequences showed three major clades: α (yellow), β (blue), and γ (red), as defined by Gaudioso-Pedraza & Benitez-Alfonso (2014). *Physcomitrium patens* GHL17 proteins identified in the PD proteome are labeled in red and Arabidopsis orthologs previously assayed for localization colored in blue (Benitez-Alfonso, 2014; Gaudioso-Pedraza & Benitez-Alfonso, 2014). Red asterisks indicate *P. patens* and Arabidopsis PD-localized GHL17 proteins and group in clade α, whereas non-PD-localized proteins are marked with black asterisks and cluster in either β or γ clades. Charophyta green algae grouped in clade β. Fungi GHL17 sequences clustered separately (in green). The phylogenetic tree was generated with the maximum likelihood method implemented in PhyML (Lemoine *et al*., 2019). Support values from 1000 bootstrap samples are shown at the nodes. Clades which do not contain *P. patens* or Arabidopsis sequences were collapsed. (c) Subcellular localization in *N. benthamiana* epidermis cells of PpGHL17_1 (Pp3c17_13760V3.2), PpGHL17_7 (Pp3c10_5480V3.1), PpGHL17_8 (Pp3c14_5200V3.2), and PpGHL17_15 (Pp3c12_13470V3.5) mVenus fusion proteins belonging to α clades. Bars, 20 μm. (d) Localization of PpGHL17_1-mVenus at PD pit fields (white arrowheads) in *P. patens* gametophore cells (Supporting Information Methods S1). (e) Protonema cells of *P. patens* expressing PpGHL17_1-mVenus (Pp3c17_13760v3.2) showed an enrichment at the cell-to-cell interface. Due to the high density of PD at the cell–cell interface, individual PD cannot be resolved in the image. (f) Images of CFDA/FRAP transport assays of *Physcomitrium* ecotype Grandsen chloronema cells for wild-type, overexpressing PpGHL17_1 or PpGHL17_30. Bars, 20 μm. Asterisks indicate the cell which was bleached. (g) Quantification of CFDA transport rates in *P. patens* ecotype Grandsen wild-type and genotypes overexpressing GHL17_1 or GHL17_30 presented as fraction of CF recovery in the photo-bleached protonema cells within 15 min (Methods S1). Values represent the mean ± SE of 16 experiments for each line; small letters indicate significant ($P < 0.05$) differences (one-way ANOVA, Holm-Sidak correction). (h) AlphaFold model of *Pp*GHL17 α clade glycoside hydrolase domains (cyan) with the conserved IFALFNE(N) motif (yellow).

EXO proteins identified in HC300 were all found in a subclade of clade III which seems to correspond to a cluster of EXO orthologs from seedless plants previously defined by the EXO sequences of *P. patens* and *Selaginella moellendorffii* (Li *et al*., 2021). Interestingly, EXOs from Arabidopsis and *P. trichocarpa* previously identified in PD proteome lists were also found in clade III (Fig. 6b). The EXO protein family is yet the third example of a protein family in which PD-localized members group in a distinct phylogenetic clade.

Discussion

A PD scoring algorithm to define PD proteomes

Plasmodesmata are nanometer-scale structures of high complexity. They contain different types of cellular membranes, and their protein composition depends on environmental cues, tissue, and/or developmental stage. Thus, in order to understand the protein composition of PD, we require *in silico* approaches which tag likely PD-localized proteins and separate them from likely non-PD proteins. No biochemical method yields pure PD. Therefore, highly abundant proteins such as photosynthetic proteins or ribosomes will always be detected in PD preparations. We found that the overlap between unweighted PD proteome lists contains a high proportion of contaminant proteins and mere identification of a protein in biochemically enriched PD preparations is not sufficient to conclude its PD localization without additional information. We demonstrated the improvement of the scoring algorithm after extensive protein localization and used this information to refine a high-confidence PD proteome of *Physcomitrium* (HC300) (Fig. 4). A previous approach (Kirk *et al*., 2021) also applied a bioinformatic strategy to predict PD proteins based on protein features found in a subset of the published proteomes (Fernandez-Calvino *et al*., 2011; Park *et al*., 2017; Brault *et al*., 2019). However, these authors did not consider biochemical aspects (i.e. enrichment in biochemical PD fractions) and they did not benchmark the predictions against experimental protein localization.

Here, we used strict scoring thresholds to define the high-confidence set of proteins likely present in PD of *P. patens*. However, the drawback of stringent thresholding lies in accepting potential losses of loosely associated proteins or proteins dynamically associated with PD. Similar effects were discussed previously for interactome data: proteins identified with high reproducibility and high-confidence tended to make up stable protein complexes, such as ribosomes, respiratory chain, or photosynthetic complexes (Gilbert *et al*., 2021). In turn, proteins with higher variability among replicates and lower confidence values tended to contain more protein functions for which dynamic or conditional interactions are expected, such as for example signaling proteins (Gilbert *et al*., 2021).

A trade-off between accuracy and coverage has also been discussed for yeast interactome data (von Mering *et al*., 2002). In analogy, HC300 is rich in cell wall proteins and structural elements (e.g. the C2-domain-containing proteins and putative scaffolds) but contains a rather low fraction of signaling elements such as receptor kinases. We found only one member of the GDSL-motif lipase/hydrolase family proteins in HC300, while nine other identified family members were not considered part of the high-confidence proteome based on their PD score rank, although two of them were experimentally localized to PD. Similarly, dynamins and RAN-GTPases were not classified among the HC300 after PD score ranking (Table S2). However, members of these protein families also showed a PD score difference > 0.3, indicating highly improved ranking based on features of experimental localizations. We therefore considered these protein families part of an extended PD proteome (Table S2).

Besides cell wall modifying proteins, our approach identified several members of the EXO protein family (Fig. 6) and several members of the glyoxal oxidase family (Fig. 3) as prominent novel protein families with PD localization. In general, since protein composition, structure, and molecular functioning of PD still remain largely enigmatic, a high-confidence 'parts list' will be a valuable basis for future work on PD structure and function. In that sense, the HC300 defined here presents the community with a set of potentially rewarding targets for in-depth functional studies.

© 2023 The Authors
New Phytologist © 2023 New Phytologist Foundation

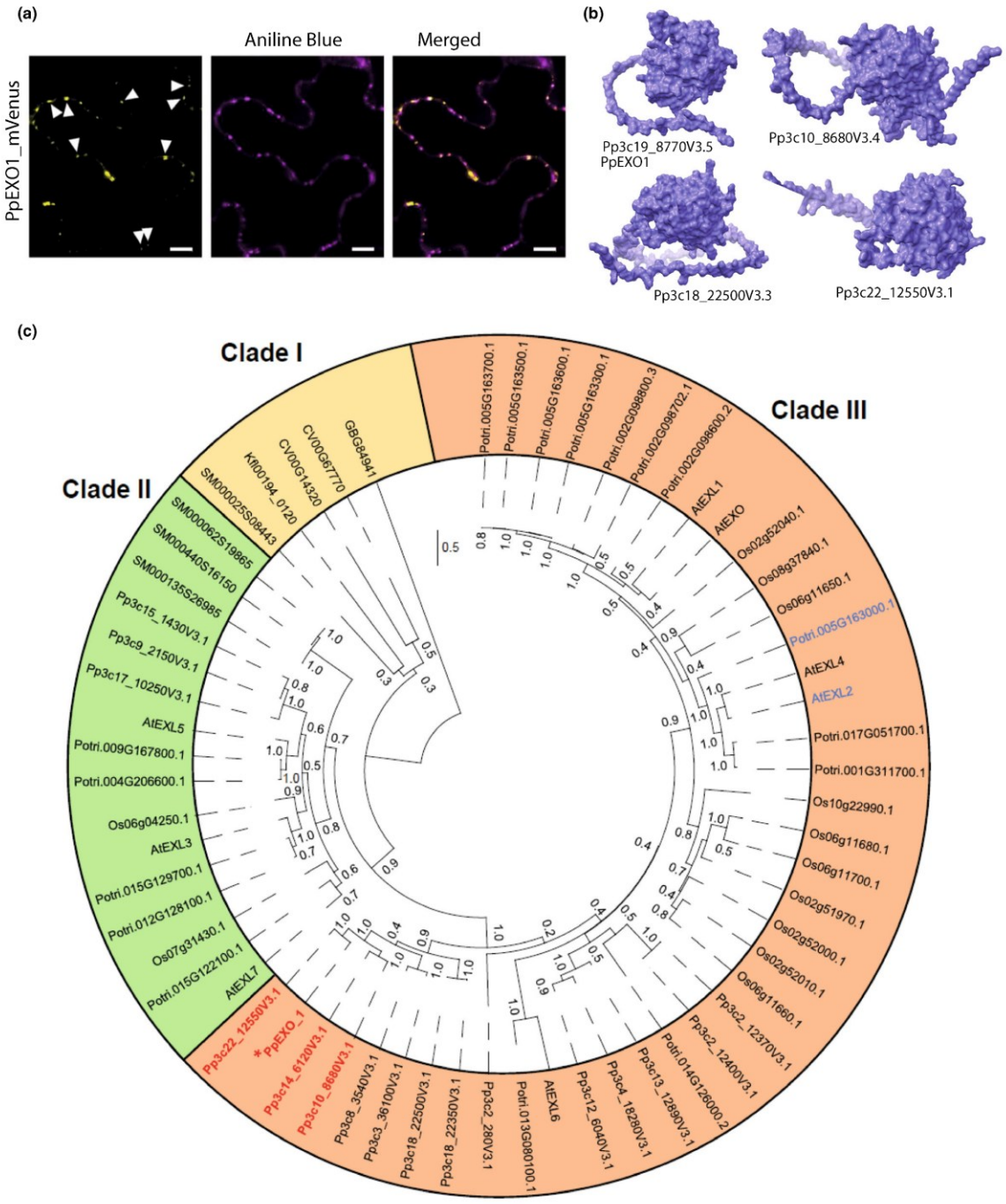


Fig. 6 Exo/Exordium-Like (EXO/EXL) family members. (a) Subcellular localization of PpEXO_1 (Pp3c19_8770V3.5) in *Nicotiana benthamiana* leaf epidermis cells showing overlay with aniline blue. Bars, 10 μm. (b) AlphaFold model of the four top-ranking EXO family members in HC300. (c) Phylogenetic tree of EXO/EXL family members from representative species of the embryophytes (17 from *Physcomitrium patens*, 8 from Arabidopsis, 12 from *Oryza sativa*, and 17 from *Populus trichocarpa*) and all algae for which EXO orthologs could be identified (*Coccomyxa subellipsoidea*, *Klebsormidium nitens*, *Chara braunii*, *Spirogloea muscicola*). *Physcomitrium patens* EXO/EXL members identified in the HC300 plasmodesmata (PD) proteome are labeled in red and clustered in clade III in which EXO identified in other PD proteomes are grouped (labeled in blue). Numbers indicate fraction of bootstrapping rounds supporting this node.

© 2023 The Authors
New Phytologist © 2023 New Phytologist Foundation

14698137, 2023, 2, Downloaded from https://nph.onlinelibrary.wiley.com/doi/10.1111/nph.18730 by MPI 386 Biochemistry, Wiley Online Library on [08/01/2026]. See the Terms and Conditions (https://onlinelibrary.wiley.com/terms-and-conditions) on Wiley Online Library for rules of use; OA articles are governed by the applicable Creative Commons License

14698137, 2023, 2, Downloaded from https://nph.onlinelibrary.wiley.com/doi/10.1111/nph.18750 by MPI 386 Biochemistry, Wiley Online Library on [08/01/2026]. See the Terms and Conditions (https://onlinelibrary.wiley.com/terms-and-conditions) on Wiley Online Library for rules of use; OA articles are governed by the applicable Creative Commons License

Large-scale PD localization in *N. benthamiana*

Despite improvement in distinguishing likely PD proteins from likely non-PD proteins by the PD scoring, experimental localization remains important. For example, we tested five members of the GHL17 family of glycosyl hydrolases from the whole PD proteome for PD localization with positive results for three proteins and no PD localization in *N. benthamiana* for two family members. Overall, the transient localization of *Physcomitrium* proteins in the *N. benthamiana* system proved efficient and applicable also on a larger scale. Most importantly, our approach showed that targeting mechanisms to PD are conserved between bryophytes and vascular plants. However, we cannot exclude the possibility that false negatives occurred, either due to the absence of required chaperones or misinterpretation of sorting signals in this heterologous system. In turn, false positives could have resulted from overexpression or mislocalization. To address such caveats, we used an inducible promoter and appropriate induction times to minimize overexpression artifacts.

Major protein families of *P. patens* PD

Plasmodesmata in land plants evolved to have more complex structures compared with their counterparts found in *Characeae* algae (Brunkard & Zambryski, 2017). This might reflect adaptations to regulate PD conductance and the emergence of specialized metabolic enzymes. Deposition of callose at the neck region of PD is one of the major modes to gate PD (Zavaliev *et al.*, 2011). The maintenance of callose associated with PD is affected mainly by callose synthases and β-1,3-glucanases. Thus, it comes as no surprise that our high-confidence subset of the *P. patens* PD proteome contains a high number ($n = 84$) of cell wall and cell wall-modifying proteins. Among these, the largest group comprised glycosyl hydrolases from the GHL17 subfamily. The GHL17 family is an excellent example of a large protein family which throughout evolution diversified in its subcellular localization, with one clade becoming PD-localized. This subfamily can also be taken as an example highlighting the two components of the PD scoring, namely biochemical enrichment in PD, and a feature scoring component. The feature scoring component alone would not have been able to differentiate proteins from the two clades of GHL17 proteins. However, the whole PD score revealed an important means to differentiate PD-localized and non-PD-localized GHL17s.

GHL17s and XTHs are considered important in controlling PD gating by affecting callose formation. GHL17s as callose-degrading enzymes are considered to be involved in keeping PD in an open state (Levy *et al.*, 2007; Zavaliev *et al.*, 2013; Benitez-Alfonso, 2014; Fig. 5e,f), while for XTHs, a role in cell wall remodeling during formation of secondary PD was proposed (Ehlers & Kollmann, 2001). Similarly, a callose synthase ortholog has been characterized with critical functions in enabling sucrose transport in rice (Wang *et al.*, 2009). The large numbers of proteins involved in cell wall synthesis and remodeling in the *Physcomitrium* PD proteome may reflect the need to dynamically modify the composition of the PD associated cell wall regions independently of other regions.

We identified four out of the 17 *P. patens* EXO/EXL proteins in HC300. The Arabidopsis ortholog to Pp3c18_22500 is Phosphate induced 1 (PHI-1) and was initially identified in tobacco BY-2 cell suspension cultures among genes induced after recovery from phosphate-induced starvation (Sano *et al.*, 1999). In Arabidopsis, EXO/EXLs were proposed as potential mediators of brassinosteroid-promoted growth (Coll-Garcia *et al.*, 2004; Schröder *et al.*, 2011). Indeed, *AtEXO* and *AtEXL1* expression is induced by brassinosteroids, and *AtEXO* regulates other brassinosteroid-responsive genes (Coll-Garcia *et al.*, 2004; Schröder *et al.*, 2011). While overexpression of *AtEXO* promotes shoot and root growth, its loss of function leads to a reduction in growth resulting from a defect in cell expansion (Schröder *et al.*, 2009). The expression of several *AtEXLs* is also controlled by carbon metabolism and energy status and is required during adaptation to carbon and energy-limiting growth conditions (Schröder *et al.*, 2011). Although physiological functions of EXO proteins are still unclear, it was proposed that AtEXO could connect extracellular carbon status to growth responses (Schröder *et al.*, 2009, 2011; Lisso *et al.*, 2013).

Bud dormancy was shown to be associated with a molecular carbon starvation response which includes an increase in *EXL2* and *EXL4* RNA levels (Tarancon *et al.*, 2017). During bud dormancy, meristematic cells are symplasmically isolated through callose-dependent PD obstruction (Rinne *et al.*, 2001; Ruonala *et al.*, 2008; Cooke *et al.*, 2012; Tylewicz *et al.*, 2018). Photoperiod and gibberellic acid mediate opening of PD by inducing the expression of GHL17s. GHL17s then promote callose hydrolysis at PD and thereby contribute to dormancy release (Rinne *et al.*, 2011). Because of increasing evidence of EXO/EXL localization at PD, the involvement of these proteins in sensing of carbon status and regulation of growth response might need to be revisited in the context of symplasmic communication. Indeed, mechanisms by which these proteins mediate their physiological functions remain to be elucidated. Structural features of the EXO proteins suggest they can interact with other proteins through their C-terminal globular domain and thus may have functions in stabilizing protein complexes as scaffolds and/or in presenting signaling components or substrates.

The Arabidopsis homolog to phosphatase Pp3c1_370, TOPP4, was shown to regulate PIN1 polarity and trafficking (Guo *et al.*, 2015). This, together with receptor kinases identified in HC300, indicates that also in *Physcomitrium* PD, posttranslational modification of proteins could be an important mechanism defining protein localization or gating of PD. Indeed, phosphorylation-dependent recruitment to PD was described for coreceptor QSK1 in Arabidopsis (Grison *et al.*, 2019).

Evolution of PD localization within large protein families

Here, we present a thorough characterization of the PD proteome of *P. patens*, a member of the bryophytes, which were among the evolutionary early land plants. It is now possible to compare PD proteomes of an early embryophyte to PD

© 2023 The Authors
New Phytologist © 2023 New Phytologist Foundation

proteomes of vascular plants to obtain insights into evolution of PD itself and also into evolution of processes that involve PD. Symplasmic transport is highly regulated and involved in numerous processes in plant development, for example, bud dormancy and meristem activity. Thus, some of the PD proteins are involved in transport of signaling molecules and resource sharing and/or regulation thereof. These functions must have evolved and diversified during evolution of multicellularity. The *P. patens* HC300 contains multiple members of larger protein families, exemplified by GHL17s, XTHs, and EXO/EXLs, each of which diverged into several phylogenetic clades. Interestingly, in all cases, PD-localized members grouped in a distinct clade, often – as in the GHL17s – separating PD-localized and non-PD-localized family members. Contrary to what has been previously reported (Li *et al.*, 2021), we also found EXO/EXL orthologs in algae. However, EXO/EXL identified in the PD proteome do not cluster with algae members, suggesting that EXO/EXL PD localization might have emerged later during evolution of embryophytes. The EXLs are not predicted to have GPI anchors, but they contain an N-terminal alpha-helix, which is predicted to contain an ER/secretory pathway targeting signal. We hypothesize that a co-evolution of PD functions and respective protein localization took place, leading to diversification in these protein families.

Acknowledgements

We thank Elmehdi Bahafid for excellent assistance during *Physcomitrium* transformation, Jan Weber for excellent assistance during protein preparations of PD fractions, and Ronja Lange for excellent assistance in cloning of *Physcomitrium* genes. pTH UbiGate plasmid was a kind gift from Prof. Bezanilla, Dartmourth, USA. This work received funding from the European Research Council (ERC) and the Marie Skłodowska-Curie under the European Union's Horizon 2020 research and innovation program (Grant agreements 'SymPore' no. 951292 to WBF, RS, WXS, and WB, 'PDgate' no. 101023981 to MM, and 'CLAVHUB' no. 101023589 to VH, respectively). This research was supported by the Deutsche Forschungsgemeinschaft (DFG, German Research Foundation) under Germany's Excellence Strategy – EXC-2048/1 – project ID 390686111 (RS, SH and WF), and the Alexander von Humboldt Professorship (WBF). Open Access funding enabled and organized by Projekt DEAL.

Author contributions

SG performed proteomics experiments, developed the PD scoring and prepared figures, and wrote the manuscript. MM contributed to cloning and localization of PD candidates in *N. benthamiana*, image analysis, figure preparation, phylogenetic analysis, and wrote the manuscript. VH contributed to cloning and localization of PD candidates in *N. benthamiana*, and image analysis, and contributed to writing of the manuscript. LX contributed to development of the PD scoring and PDDB structure and participated in writing of the manuscript. MP contributed to cloning and localization of PD candidates in *N. benthamiana*, image analysis, and phylogenetic analysis. NSKJ contributed to cloning and localization of PD candidates in *N. benthamiana*, transformation of PD-localized candidates in *P. patens*, transport assay of CFDA in *P. patens*, and figure preparation. MS contributed to cloning and localization of PD candidates in *N. benthamiana*, and image analysis. JOE contributed to cloning and localization of PD candidates in *N. benthamiana*, image analysis, and transformation of PD-localized candidates in *P. patens*. UN performed transmission electron microscopy. SH wrote PD indexing Fiji macro. FK contributed to cloning and localization of PD candidates in *N. benthamiana*. ZZ contributed to the implementation of Pddb database structure and design. MD performed Cryo transmission electron microscopy of PD fraction preparation and structural analysis of *Pp*GHL17s. PX performed Cryo transmission electron microscopy of PD fraction preparation. TS performed sequence motif analysis of the GHL17 proteins. WB developed the concept and designed experiments. WBF and RS developed the concept, designed experiments, and contributed to writing. WXS developed the concept, designed experiments, performed data analysis, and wrote the manuscript. SG, MM and VH contributed equally to this work.

ORCID

Wolfgang Baumeister https://orcid.org/0000-0001-8154-8809
Marcel Dickmanns https://orcid.org/0000-0003-4001-707X
J. Obinna Ejike https://orcid.org/0000-0002-4601-8551
Wolf B. Frommer https://orcid.org/0000-0001-6465-0115
Sven Gombos https://orcid.org/0000-0003-4177-526X
Sebastian Hänsch https://orcid.org/0000-0002-7762-2516
Vicky Howe https://orcid.org/0000-0002-7319-0664
Neda S. Kazemein Jasemi https://orcid.org/0000-0002-7842-6998
Manuel Miras https://orcid.org/0000-0002-3636-0265
Ulla Neumann https://orcid.org/0000-0001-9200-4209
Mathieu Pottier https://orcid.org/0000-0003-1551-4699
Moritz Schladt https://orcid.org/0000-0002-9160-4664
Waltraud X. Schulze https://orcid.org/0000-0001-9957-7245
Rüdiger Simon https://orcid.org/0000-0002-1317-7716
Lin Xi https://orcid.org/0000-0002-6811-9505

Data availability

Proteomics data sets: Mass spectrometry proteomics data were deposited to the ProteomeXchange Consortium via the PRIDE partner repository (Deutsch *et al.*, 2017) with the dataset identifier PXD032820.
Image data sets: Images of PD-localized proteins were made public within the Pddb (pddb.uni-hohenheim.de). In addition, confocal images and the TEM micrographs were deposited at Bioimage Archive (https://www.ebi.ac.uk/bioimage-archive/) under accession no. S-BIAD466.
PD index quantification scripts: A script was developed aiding assessment of PD localization based on the co-expression of

© 2023 The Authors
New Phytologist © 2023 New Phytologist Foundation

14698137, 2023, 2, Downloaded from https://nph.onlinelibrary.wiley.com/doi/10.1111/nph.18750 by MPI 386 Biochemistry, Wiley Online Library on [08/01/2026]. See the Terms and Conditions (https://onlinelibrary.wiley.com/terms-and-conditions) on Wiley Online Library for rules of use; OA articles are governed by the applicable Creative Commons License

14698137, 2023, 2, Downloaded from https://nph.onlinelibrary.wiley.com/doi/10.1111/nph.18730 by MPI 386 Biochemistry, Wiley Online Library on [08/01/2026]. See the Terms and Conditions (https://onlinelibrary.wiley.com/terms-and-conditions) on Wiley Online Library for rules of use; OA articles are governed by the applicable Creative Commons License

mVenus fusion proteins with aniline blue. Code of the FIJI macro can be accessed at: https://github.com/SHaensch/2022_PD-index-quantification.

PD scoring: The formulas underlying PD scoring are described in the Materials and Methods section of the manuscript.

References

Anvarian Z, Mykytyn K, Mukhopadhyay S, Pedersen LB, Christensen ST. 2019. Cellular signalling by primary cilia in development, organ function and disease. *Nature Reviews. Nephrology* **15**: 199–219.

Bangs F, Anderson KV. 2017. Primary cilia and mammalian hedgehog signaling. *Cold Spring Harbor Perspectives in Biology* **9**: a028175.

Baumann MJ, Eklof JM, Michel G, Kallas AM, Teeri TT, Czjzek M, Brumer H 3rd. 2007. Structural evidence for the evolution of xyloglucanase activity from xyloglucan endo-transglycosylases: biological implications for cell wall metabolism. *Plant Cell* **19**: 1947–1963.

Bayer EM, Bottrill AR, Walshaw J, Vigouroux M, Naldrett MJ, Thomas CL, Maule AJ. 2006. Arabidopsis cell wall proteome defined using multidimensional protein identification technology. *Proteomics* **6**: 301–311.

Benitez-Alfonso Y. 2014. Symplastic intercellular transport from a developmental perspective. *Journal of Experimental Botany* **65**: 1857–1863.

Benitez-Alfonso Y, Faulkner C, Pendle A, Miyashima S, Helariutta Y, Maule A. 2013. Symplastic intercellular connectivity regulates lateral root patterning. *Developmental Cell* **26**: 136–147.

Brault ML, Petit JD, Immel F, Nicolas WJ, Glavier M, Brocard L, Gaston A, Fouche M, Hawkins TJ, Crowet JM *et al.* 2019. Multiple C2 domains and transmembrane region proteins (MCTPs) tether membranes at plasmodesmata. *EMBO Reports* **20**: e47182.

Brunkard JO, Zambryski PC. 2017. Plasmodesmata enable multicellularity: new insights into their evolution, biogenesis, and functions in development and immunity. *Current Opinion in Plant Biology* **35**: 76–83.

Burch-Smith TM, Brunkard JO, Choi YG, Zambryski PC. 2011. Organelle-nucleus cross-talk regulates plant intercellular communication via plasmodesmata. *Proceedings of the National Academy of Sciences, USA* **108**: E1451–E1460.

Coll-Garcia D, Mazuch J, Altmann T, Müssig C. 2004. EXORDIUM regulates brassinosteroid-responsive genes. *FEBS Letters* **563**: 82–86.

Cooke JE, Eriksson ME, Junttila O. 2012. The dynamic nature of bud dormancy in trees: environmental control and molecular mechanisms. *Plant, Cell & Environment* **35**: 1707–1728.

Coudert Y, Harris S, Charrier B. 2019. Design principles of branching morphogenesis in filamentous organisms. *Current Biology* **29**: R1149–R1162.

Cove JD, Perroud P-F, Charron AJ, McDaniel SF, Khandelwal A, Quatrano RS. 2009. Culturing the moss *Physcomitrella patens. Cold Spring Harbor Protocols.* doi: 10.1101/pdb.prot5136.

Cox J, Mann M. 2008. MAXQUANT enables high peptide identification rates, individualized p.p.b.-range mass accuracies and proteome-wide protein quantification. *Nature Biotechnology* **26**: 1367–1372.

Deutsch EW, Csordas A, Sun Z, Jarnuczak A, Perez-Riverol Y, Ternent T, Campbell DS, Bernal-Llinares M, Okuda S, Kawano S *et al.* 2017. The ProteomeXchange consortium in 2017: supporting the cultural change in proteomics public data deposition. *Nucleic Acids Research* **45**: D1100–D1106.

Ding B, Haudenshield JS, Hull RJ, Wolf S, Beachy RN, Lucas WJ. 1992a. Secondary plasmodesmata are specific sites of localization of the tobacco mosaic virus movement protein in transgenic tobacco plants. *Plant Cell* **4**: 915–928.

Ding B, Kwon MO, Warnberg L. 1996. Evidence that actin filaments are involved in controlling the permeability of plasmodesmata in tobacco mesophyll. *The Plant Journal* **10**: 157–164.

Ding B, Turgeon R, Parthasarathy MV. 1992b. Substructure of freeze-substituted plasmodesmata. *Protoplasma* **169**: 28–41.

Doxey AC, Yaish MW, Moffatt BA, Griffith M, McConkey BJ. 2007. Functional divergence in the *Arabidopsis* β-1,3-glucanase gene family inferred by phylogenetic reconstruction of expression states. *Molecular Biology and Evolution* **24**: 1045–1055.

Ehlers K, Kollmann R. 2001. Primary and secondary plasmodesmata: structure, origin, and functioning. *Protoplasma* **216**: 1–30.

Eklöf JM, Brumer H. 2010. The *XTH* gene family: an update on enzyme structure, function, and phylogeny in xyloglucan remodeling. *Plant Physiology* **153**: 456–466.

Faulkner C, Bayer EM. 2017. Isolation of plasmodesmata. *Methods in Molecular Biology* **1511**: 187–198.

Feiz L, Irshad M, Pont-Lezica RF, Canut H, Jamet E. 2006. Evaluation of cell wall preparations for proteomics: a new procedure for purifying cell walls from Arabidopsis hypocotyls. *Plant Methods* **2**: 10.

Fernandez-Calvino L, Faulkner C, Walshaw J, Saalbach G, Bayer E, Benitez-Alfonso Y, Maule A. 2011. Arabidopsis plasmodesmal proteome. *PLoS ONE* **6**: e18880.

Gaudioso-Pedraza R, Benitez-Alfonso Y. 2014. A phylogenetic approach to study the origin and evolution of plasmodesmata-localized glycosyl hydrolases family 17. *Frontiers in Plant Science* **5**: 212.

Gilbert M, Li Z, Wu XN, Rohr L, Gombos S, Harter K, Schulze WX. 2021. Comparison of path-based centrality measures in protein–protein interaction networks revealed proteins with phenotypic relevance during adaptation to changing nitrogen environments. *Journal of Proteomics* **235**: 104114.

Goodstein DM, Shu S, Howson R, Neupane R, Hayes RD, Fazo J, Mitros T, Dirks W, Hellsten U, Putnam N *et al.* 2012. PHYTOZOME: a comparative platform for green plant genomics. *Nucleic Acids Research* **40**: D1178–D1186.

Grigoriev IV, Hayes RD, Calhoun S, Kamel B, Wang A, Ahrendt S, Dusheyko S, Nikitin R, Mondo SJ, Salamov A *et al.* 2021. PHYCOCOSM, a comparative algal genomics resource. *Nucleic Acids Research* **49**: D1004–D1011.

Grison MS, Brocard L, Fouillen L, Nicolas W, Wewer V, Dormann P, Nacir H, Benitez-Alfonso Y, Claverol S, Germain V *et al.* 2015a. Specific membrane lipid composition is important for plasmodesmata function in Arabidopsis. *Plant Cell* **27**: 1228–1250.

Grison MS, Fernandez-Calvino L, Mongrand S, Bayer EM. 2015b. Isolation of plasmodesmata from Arabidopsis suspension culture cells. *Methods in Molecular Biology* **1217**: 83–93.

Grison MS, Kirk P, Brault M, Wu XN, Schulze WX, Benitez-Alfonso Y, Immel F, Bayer EMF. 2019. Plasma membrane-associated receptor like kinases relocalize to plasmodesmata in response to osmotic stress. *Plant Physiology* **181**: 142–160.

Guo X, Qin Q, Yan J, Niu Y, Huang B, Guan L, Li Y, Ren D, Li J, Hou S. 2015. TYPE-ONE PROTEIN PHOSPHATASE4 regulates pavement cell interdigitation by modulating PIN-FORMED1 polarity and trafficking in Arabidopsis. *Plant Physiology* **167**: 1058–1075.

He M, Li X, Mang M, Li Z, Ludewig U, Schulze WX. 2021. A systems-biology approach identifies co-expression modules in response to low phosphate supply in maize lines of different breeding history. *The Plant Journal* **109**: 1249–1270.

Hori K, Maruyama F, Fujisawa T, Togashi T, Yamamoto N, Seo M, Sato S, Yamada T, Mori H, Tajima N *et al.* 2014. *Klebsormidium flaccidum* genome reveals primary factors for plant terrestrial adaptation. *Nature Communications* **5**: 3978.

Howe KL, Contreras-Moreira B, De Silva N, Maslen G, Akanni W, Allen J, Alvarez-Jarreta J, Barba M, Bolser DM, Cambell L *et al.* 2020. Ensembl Genomes 2020-enabling non-vertebrate genomic research. *Nucleic Acids Research* **48**: D689–D695.

Hughes CS, Moggridge S, Muller T, Sorensen PH, Morin GB, Krijgsveld J. 2019. Single-pot, solid-phase-enhanced sample preparation for proteomics experiments. *Nature Protocols* **14**: 68–85.

Hunter S, Apweiler R, Attwood TK, Bairoch A, Bateman A, Binns D, Bork P, Das U, Daugherty L, Duquenne L *et al.* 2009. INTERPRO: the integrative protein signature database. *Nucleic Acids Research* **37**: D211–D215.

Jamet E, Canut H, Boudart G, Pont-Lezica RF. 2006. Cell wall proteins: a new insight through proteomics. *Trends in Plant Science* **11**: 33–39.

Johnston MG, Breakspear A, Samwald S, Zhang D, Papp D, Faulkner C, de Keijzer J. 2023. Comparative phyloproteomics identifies conserved plasmodesmal proteins. *Journal of Experimental Botany.* doi: 10.1093/jxb/erad022.

Kim I, Kobayashi K, Cho E, Zambryski PC. 2005. Subdomains for transport via plasmodesmata corresponding to the apical-basal axis are established during

© 2023 The Authors
New Phytologist © 2023 New Phytologist Foundation

Arabidopsis embryogenesis. *Proceedings of the National Academy of Sciences, USA* **102**: 11945–11950.

Kirk P, Amsbury S, German L, Gaudioso-Peraza R, Benitez-Alfonso Y. 2021. Comparative meta-proteomic analysis for the identification of novel plasmodesmata proteins and regulatory cues. *bioRxiv*. doi: 10.1101/2021.05.04.442592.

Kraner ME, Muller C, Sonnewald U. 2017. Comparative proteomic profiling of the choline transporter-like1 (CHER1) mutant provides insights into plasmodesmata composition of fully developed *Arabidopsis thaliana* leaves. *The Plant Journal* **92**: 696–709.

Leijon F, Melzer M, Zhou Q, Srivastava V, Bulone V. 2018. Proteomic analysis of plasmodesmata from *Populus* cell suspension cultures in relation with callose biosynthesis. *Frontiers in Plant Science* **9**: 1681.

Lemoine F, Correia D, Lefort V, Doppelt-Azeroual O, Mareuil F, Cohen-Boulakia S, Gascuel O. 2019. NGPhylogeny.fr: new generation phylogenetic services for non-specialists. *Nucleic Acids Research* **47**: W260–W265.

Letunic I, Bork P. 2019. Interactive Tree Of Life (iTol) v.4: recent updates and new developments. *Nucleic Acids Research* **47**: W256–W259.

Levy A, Erlanger M, Rosenthal M, Epel BL. 2007. A plasmodesmata-associated beta-1,3-glucanase in Arabidopsis. *The Plant Journal* **49**: 669–682.

Li S, Liu Z, Chen G, Qanmber G, Lu L, Zhang J, Ma S, Yang Z, Li F. 2021. Identification and analysis of GhEXO gene family indicated that GhEXO7_At promotes plant growth and development through brassinosteroid signaling in cotton (*Gossypium hirsutum* L.). *Frontiers in Plant Science* **12**: 719889.

Lisso J, Schröder F, Müssig C. 2013. EXO modifies sucrose and trehalose responses and connects the extracellular carbon status to growth. *Frontiers in Plant Science* **4**: 219.

Lucas WJ, Bouche P-S, Jackson DP, Nguyen L, Baker L, Ding B, Hake S. 1995. Selective trafficking of KNOTTED1 homeodomain protein and its mRNA through plasmodesmata. *Science* **270**: 1980–1983.

Lucas WJ, Ham BK, Kim JY. 2009. Plasmodesmata – bridging the gap between neighboring plant cells. *Trends in Cell Biology* **19**: 495–503.

von Mering C, Krause R, Snel B, Cornell M, Oliver SG, Fields S, Bork P. 2002. Comparative assessment of large-scale data sets of protein–protein interactions. *Nature* **417**: 339–403.

Mitra SK, Gantt JA, Ruby JF, Clouse SD, Goshe MB. 2007. Membrane proteomic analysis of *Arabidopsis thaliana* using alternative solubilization techniques. *Journal of Proteome Research* **6**: 1933–1950.

Nicolas WJ, Grison MS, Trepout S, Gaston A, Fouche M, Cordelieres FP, Oparka K, Tilsner J, Brocard L, Bayer EM. 2017. Architecture and permeability of post-cytokinesis plasmodesmata lacking cytoplasmic sleeves. *Nature Plants* **3**: 17082.

Park SH, Li F, Renaud J, Shen W, Li Y, Guo L, Cui H, Sumarah M, Wang A. 2017. NbEXPA1, an alpha-expansin, is plasmodesmata-specific and a novel host factor for potyviral infection. *The Plant Journal* **92**: 846–861.

Pertl H, Himly M, Gehwolf R, Kriechbaumer R, Strasser D, Michalke W, Richter K, Ferreira F, Obermeyer G. 2001. Molecular and physiological characterisation of a 14-3-3 protein from lily pollen grains regulating the activity of the plasma membrane H+ ATPase during pollen grain germination and tube growth. *Planta* **213**: 132–141.

Raven JA. 2007. *Evolution of plasmodesmata*. Hoboken, NJ, USA: John Wiley and Sons.

Rinne PL, Kaikuranta PM, van der Schoot C. 2001. The shoot apical meristem restores its symplasmic organization during chilling-induced release from dormancy. *The Plant Journal* **26**: 249–264.

Rinne PL, Welling A, Vahala J, Ripel L, Ruonala R, Kangasjarvi J, van der Schoot C. 2011. Chilling of dormant buds hyperinduces FLOWERING LOCUS T and recruits GA-inducible 1,3-beta-glucanases to reopen signal conduits and release dormancy in *Populus*. *Plant Cell* **23**: 130–146.

Ruonala R, Rinne PL, Kangasjarvi J, van der Schoot C. 2008. CENL1 expression in the rib meristem affects stem elongation and the transition to dormancy in *Populus*. *Plant Cell* **20**: 59–74.

Sano T, Kuraya Y, Amino S, Nagata T. 1999. Phosphate as a limiting factor for the cell division of tobacco BY-2 cells. *Plant & Cell Physiology* **40**: 1–8.

Schindelin J, Arganda-Carreras I, Frise E, Kaynig V, Longair M, Pietzsch T, Preibisch S, Rueden C, Saalfeld S, Schmid B *et al.* 2012. Fiji: an open-source platform for biological-image analysis. *Nature Methods* **9**: 676–682.

Schröder F, Lisso J, Lange P, Müssig C. 2009. The extracellular EXO protein mediates cell expansion in Arabidopsis leaves. *BMC Plant Biology* **9**: 20.

Schröder F, Lisso J, Müssig C. 2011. EXORDIUM-LIKE1 promotes growth during low carbon availability in Arabidopsis. *Plant Physiology* **156**: 1620–1630.

Shinohara N, Nishitani K. 2021. Cryogenian origin and subsequent diversification of the plant cell-wall enzyme XTH family. *Plant & Cell Physiology* **62**: 1874–1889.

Simpson C, Thomas C, Findlay K, Bayer E, Maule AJ. 2009. An Arabidopsis GPI-anchor plasmodesmal neck protein with callose binding activity and potential to regulate cell-to-cell trafficking. *Plant Cell* **21**: 581–594.

Song DK, Choi JH, Kim MS. 2018. Primary cilia as a signaling platform for control of energy metabolism. *Diabetes and Metabolism Journal* **42**: 117–127.

Tangle E. 1879. Über offene Communicationen zwischen den Zellen des Endosperms einiger Samen. *Jahrbücher für Wissenschafliche Botanik* **12**: 170–190.

Tarancon C, Gonzalez-Grandio E, Oliveros JC, Nicolas M, Cubas P. 2017. A conserved carbon starvation response underlies bud dormancy in woody and herbaceous species. *Frontiers in Plant Science* **8**: 788.

Thimm O, Bläsing O, Gibon Y, Nagel A, Meyer S, Kruger P, Selbig J, Muller LA, Rhee SY, Stitt M. 2004. Mapman: a user-driven tool to display genomics data sets onto diagrams of metabolic pathways and other biological processes. *The Plant Journal* **37**: 914–939.

Thomas CL, Bayer E, Ritzenthaler C, Fernandez-Calvino L, Maule AJ. 2008. Specific targeting of a plasmodesmal protein affecting cell-to-cell communication. *PLoS Biology* **6**: e7.

Tyanova S, Temu T, Sinitcyn P, Carlson A, Hein MY, Geiger T, Mann M, Cox J. 2016. The Perseus computational platform for comprehensive analysis of (prote)omics data. *Nature Methods* **13**: 731–740.

Tylewicz S, Petterle A, Marttila S, Miskolczi P, Azeez A, Singh RK, Immanen J, Mahler N, Hvidsten TR, Eklund DM *et al.* 2018. Photoperiodic control of seasonal growth is mediated by ABA acting on cell-cell communication. *Science* **360**: 212–215.

Wang R, Xing X, Wang Y, Tran A, Crawford NM. 2009. A genetic screen for nitrate regulatory mutants captures the nitrate transporter gene NRT1.1. *Plant Physiology* **151**: 472–478.

Wolf S, Deom CM, Beachy RN, Lucas WJ. 1989. Movement protein of tobacco mosaic virus modifies plasmodesmatal size exclusion limit. *Science* **246**: 377–379.

Yan D, Yadav SR, Paterlini A, Nicolas WJ, Petit JD, Brocard L, Belevich I, Grison MS, Vaten A, Karami L *et al.* 2019. Sphingolipid biosynthesis modulates plasmodesmal ultrastructure and phloem unloading. *Nature Plants* **5**: 604–615.

Zavaliev R, Levy A, Gera A, Epel BL. 2013. Subcellular dynamics and role of Arabidopsis β-1,3-glucanases in cell-to-cell movement of tobamoviruses. *Molecular Plant–Microbe Interactions* **26**: 1016–1030.

Zavaliev R, Ueki S, Epel BL, Citovsky V. 2011. Biology of callose (beta-1,3-glucan) turnover at plasmodesmata. *Protoplasma* **248**: 117–130.

Zhu T, Lucas WJ. 1998. Directional cell-to-cell communication in the Arabidopsis root apical meristem. I. An ultrastructural and functional analysis. *Protoplasma* **203**: 35–47.

Supporting Information

Additional Supporting Information may be found online in the Supporting Information section at the end of the article.

Fig. S1 Enrichment protocol of plasmodesmata from *Physcomitrium patens*.

Fig. S2 Details on the plasmodesmata score.

Fig. S3 Structure of the core PDDB database.

© 2023 The Authors
New Phytologist © 2023 New Phytologist Foundation

14698137, 2023, 2, Downloaded from https://nph.onlinelibrary.wiley.com/doi/10.1111/nph.18750 by MPI 386 Biochemistry, Wiley Online Library on [08/01/2026]. See the Terms and Conditions (https://onlinelibrary.wiley.com/terms-and-conditions) on Wiley Online Library for rules of use; OA articles are governed by the applicable Creative Commons License

Fig. S4 Subcellular localization of control proteins from *Physcomitrium patens* plasmodesmata proteome in *Nicotiana benthamiana* leaf epidermis cells.

Fig. S5 Refinement of the *Physcomitrium* plasmodesmata proteome.

Fig. S6 Plasmodesmata localization of glycosyl hydrolase family 17 (GHL17) proteins correlates with phylogenetic distribution.

Fig. S7 Plasmodesmata-localized *Physcomitrium patens* XTHs grouped in cluster I.

Methods S1 Additional details of experimental procedures.

Table S1 Published plasmodesmata data sets.

Table S2 Plasmodesmata (PD) proteome list with PD scores.

Table S3 Plasmodesmata index validation scale.

Table S4 Verified proteins.

Table S5 List of protein family members GHLs, XTHs, and EXOs.

Please note: Wiley is not responsible for the content or functionality of any Supporting Information supplied by the authors. Any queries (other than missing material) should be directed to the *New Phytologist* Central Office.

© 2023 The Authors
New Phytologist © 2023 New Phytologist Foundation

14698137, 2023, 2, Downloaded from https://nph.onlinelibrary.wiley.com/doi/10.1111/nph.18750 by MPI 386 Biochemistry, Wiley Online Library on [08/01/2026]. See the Terms and Conditions (https://onlinelibrary.wiley.com/terms-and-conditions) on Wiley Online Library for rules of use; OA articles are governed by the applicable Creative Commons License

Chapter 3

Probing novel candidates – Potential roles of nucleoporins at plasmodesmata?

Identification of nuclear pore proteins at plasmodesmata: potential role in intercellular transport?

Status: Peer-reviewed preprint.

DOI: https://doi.org/10.7554/eLife.108676.1.sa3

3.1 Summary

Background and research question

Plasmodesmata and nuclear pores are cellular nanopores that enable selective molecular exchange between otherwise separated compartments. While nuclear pores and their constituting nuclear pore complexes (NPCs) are structurally and mechanistically well characterized, plasmodesmata remain poorly understood. Shared transport properties between the two pore types, together with the identification of nucleoporins (NUPs) in plasmodesmata-enriched proteomic fractions from *Physcomitrium patens* (Chapter 2) and *Arabidopsis thaliana* (Chapter 3), raised the question of whether plasmodesmata could involve protein-based permeability barriers similar to those of NPCs.

Experimental approach

To test whether nucleoporins contribute to plasmodesmal permeability, NUPs identified in plasmodesmata-enriched proteomic fractions were selected for further analysis. Their subcellular localization was examined by fluorescence microscopy to assess association with plasmodesmata. Plasmodesmal permeability was analyzed using intercellular tracer movement assays in NUP mutant backgrounds. The data was evaluated based on potential roles of NUPs involved in NPC-like permeability barriers at plasmodesmata.

Key findings

Seven nucleoporins showed dual localization to nuclei and plasmodesmata. Mutants of the putative transmembrane NUP CPR5 showed reduced intercellular movement of tracer dyes independent of callose. These observations indicated a potential function of CPR5 and other NUPs at plasmodesmata, with a conclusive mechanism yet to be determined.

Contributions to this chapter

I performed structure prediction and analysis of plant nuclear pore proteins and generated Figure 4 – figure supplement 1.

3.2 Results

Reviewed Preprint
v1 • September 26, 2025
Not revised

Cell Biology

Identification of nuclear pore proteins at plasmodesmata: potential role in intercellular transport?

T Moritz Schladt, Manuel Miras, Jona Obinna Ejike, Mathieu Pottier, Lin Xi, Andrea Restrepo-Escobar, Masayoshi Nakamura, Niklas Pütz, Sebastian Hänsch, Chen Gao, Julia Engelhorn, Marcel Dickmanns, Gwendolyn V Davis, Ahan Dalal, Sven Gombos, Ronja Lange, Rüdiger Simon, Waltraud X Schulze, Wolf B Frommer

Heinrich Heine University Düsseldorf, Faculty of Mathematics and Natural Sciences, Institute for Molecular Physiology, Düsseldorf, Germany • Cluster of Excellence on Plant Sciences, Heinrich Heine University Düsseldorf, Düsseldorf, Germany • Department of Plant Systems Biology, University of Hohenheim, Stuttgart, Germany • Institute for Transformative Biomolecules (WPI-ITbM), Nagoya University, Nagoya, Japan • New address: Department of Biochemistry and Molecular Biology, Saitama University, Saitama, Japan • Center for Advanced Imaging; Heinrich Heine University Düsseldorf, Düsseldorf, Germany • Department of Molecular Structural Biology, Max Planck Institute of Biochemistry, Martinsried, Germany

https://en.wikipedia.org/wiki/Open_access
Copyright information

eLife Assessment

Plasmodesmata are channels that allow cell-cell communication in plants; based on the functional similarities between facilitated transport within plasmodesmata and into the nucleus, the authors speculate that nuclear pore complex proteins might be involved in plasmodesmata function. If supported, this would transform our understanding of cell-to-cell communication in plants. The authors localize nuclear pore complex proteins to plasmodesmata using proteomics and heterologous overexpression; however, the data are **incomplete** since key controls for localization, functionality, and expression level of fluorescent protein fusions are absent.

https://doi.org/10.7554/eLife.108676.1.sa3

Abstract

Plasmodesmata (PD) mediate intercellular exchange of small molecules, RNAs and proteins between plant cells with an apparent exclusion limit for passive non-specific transport, and transport of specific cargo mediated by mediators. PD and nuclear pore complexes (NPC) are nanometer sized micropores with strikingly similar properties. Cargo translocation through NPC is mediated by phase separating FG-nucleoporins (FG-NUP). Here, bioinformatics, proteomics and fluorescence imaging identified FG-NUPs at PD. Transient expression of GFP fusions at low and intermediate expression levels supported dual localization of 12 NUPs to NPC and PD. Structured illumination microscopy detected the transmembrane anchor NUP CPR5 close to orifices of PD. *cpr5* mutants showed reduced intercellular short-root (SHR) transport. However, transport defects cannot be excluded due to indirect effects in the mutants. Identification of FG-NUPs at PD is consistent with the recruitment of NUPs to form a

PD pore gating complex consistent with phase separation domains as diffusion barriers at PD. Further analyses will be required to determine whether NUPs are *bona fide* PD components, or accumulate at PD in certain conditions, or may serve intermediate NPC storage.

Introduction

Nutrient exchange and communication between cells are essential for multicellular organisms. Besides membrane transporters and cell surface receptors, metazoa, fungi and plants independently evolved cell-cell bridges. The green lineage developed unique structures, called plasmodesmata (PD), composed of modified cell wall domains that form plasma membrane-lined channels and that contain an ER-derived desmotubule providing continuity between the cytoplasm of neighboring cells (symplasm). Since PD are embedded into the cell wall and contain diverse membrane and soluble proteins, PD pose a major challenge for biochemical and cell biological analyses. Several studies obtained PD proteomes by enriching membrane proteins in cell wall fractions (Bayer et al., 2006; Brault et al., 2019; Fernandez-Calvino et al., 2011; Gombos et al., 2023). Genetic approaches failed so far to identify proteins that could fully explain the transport mechanism, possibly due to redundancy or lethality of mutants. Intercellular transport studies are also challenging since intact at minimum, a functional two cell system is required. Current models for PD translocation implicate a simple filter mechanism generated by spoke-like structures connecting the peripheral plasma membrane with the desmotubule, however the complex transport properties as well as inconsistencies such as the finding that sleeveless PD lacking an obvious path may put these models in question.

Key features of PD transport include the ability to translocate highly diverse cargo (from ions to macromolecules), an apparent size exclusion limit (which, depending of the type of PD, can reach 70 kDa, in funnel PD up to 120 kDa), and the ability to translocate specific cargo (Paultre et al., 2016; Ross-Elliott et al., 2017). Translocation through PD and the nuclear pore complex (NPC) share common features, namely both NPC and PD transport a similar spectrum of cargo species (ions, metabolites, proteins, and ribonucleoprotein complexes)(Ejike et al., 2025; Lee et al., 2000). For both NPC and PD, the ability for pore dilation has been described (Kragler et al., 1998; Zimmerli et al., 2021). Both NPC and PD constitute selective barriers, allowing '*passive passage of molecules*' with an apparent size exclusion limit (term used in animal literature; named '*non-targeted movement*' for PD) and '*facilitated translocation of specific macromolecules*' ('*targeted movement*' for PD)(Crawford and Zambryski, 2001; Frey et al., 2018). Notably, the surface properties of cargo proteins play an important role for translocation, allowing even tetrameric GFP variants with compatible surface properties to pass (Frey et al., 2018). The core of the permeability barrier of the NPC appears to be a separated phase / condensate formed by disordered phenylalanine–glycine (FG) repeat-containing proteins, the FG-nucleoporins (Frey et al., 2018; Hoogenboom et al., 2021; Ng et al., 2021; Yu et al., 2023). These smart sieves mediate passage of smaller molecules without interaction with the FG repeats, while larger molecules or specific cargo can pass with the help of nuclear transport receptors that specifically interact with the FG repeats (Kehlenbach et al., 2023). As a shared structure among eukaryotes, the ultrastructure, function and transport mechanism of the NPC is well understood (Ejike et al., 2025; Mosalaganti et al., 2022). The human NPC, with about 1000 polypeptides, has an approx. diameter of 120 nm, a pore size of ~43 nm and a height of 80 nm generated by membrane-anchors, three stacked rings (a sandwich of two outer and one inner ring), cytoplasmic filaments, and a nucleocytoplasmic basket (Lin and Hoelz, 2019). The human genome encodes twelve FG-nucleoporins (NUPs): NUP42, NUP50, NUP54, NUP58 (aka NUP45), NUP62, NUP98, NUP153, NUP214, POM121, POM121B, POM121C, and NUP358(Terry and Wente, 2009), while plant genomes encode ten FG-NUPs: NUP42 (aka CG1), NUP50a & NUP50b, NUP54, NUP58, NUP62, NUP98a & NUP98b, NUP136 and NUP214 (Chopra et al., 2019; Makarov et al., 2021). The majority of the FG-NUPs were conserved, with only three FG-NUPs lost in the green lineage (NUP153, POM121, NUP358).

FG-NUPs and other NUPs in PD fractions of *Physcomitrium patens* and localization to PD

Based on the striking similarities in transport properties, we hypothesized that PD transport may use permeability barriers similar as the NPC, that is, phase-separation generated by FG-repeat proteins. We thus explored whether the green lineage evolved a distinct set of FG-repeat containing proteins. A bioinformatic search for FG repeat-containing proteins in the genome of the moss *P. patens* revealed that 12 out of the 15 top-ranked FG-containing proteins were NUPs; the other three proteins were not considered candidates for a transport function (**table S1**; file S1; file S2 for Arabidopsis FG-containing proteins). An alternative hypothesis was that the PD permeability barrier is generated by NUPs derived by tandem gene duplications followed by differentiation into NPC and PD functions. However, phylogenetic analyses of Arabidopsis *NUPs* showed that the majority of NUPs are encoded by single genes (see also **table S2** for overview of Arabidopsis *NUPs*)(Makarov et al., 2021; Zhang et al., 2020). Interestingly, however, the PD proteome from *P. patens* contained FG-NUP50a and two other NUPs, SEC13 and NUA (Gombos et al., 2023). Since PD cannot be purified to homogeneity, we cannot exclude that these NUPs represent contaminations. Previous work had indicated that *bona-fide* moss PD proteins can be targeted to PD when expressed in tobacco leaves (Gombos et al., 2023). To test whether FG-NUPs localize exclusively to the NPC or can also be targeted to PD, the subcellular localization of fluorescent protein (FP) fusions of three *P. patens* FG-NUPs (NUP58, NUP62 and NUP98) was analyzed by confocal microscopy after β-estradiol-controlled transient expression in *Nicotiana benthamiana*. A substantial number of fluorescent puncta derived from C-terminal mVenus fusions of the three FG-NUPs overlaid with fluorescent puncta of aniline blue marking callose at PD (**Figure 1A**; **Figure1-figure supplement 1**). PD localization did not appear to be due to an FG-NUPs-specific mis-localization, since the inner ring linker NUP35, which connects the transmembrane interaction hub with the ALADIN-NDC1 core to NUP155, also localized to PD (**Figure 1A**). Of note, the fluorescent puncta derived from mVenus fusions in the periphery did not exclusively localize to aniline blue labeled PD pit fields. Fluorescent mVenus and aniline blue derived puncta were also separately detected in locations without overlay. It is known that aniline blue does not detect all pit fields (Huang et al., 2022). Notably, transient expression in *N. benthamiana*, even though controlled by use of an estrogen-inducible system, can lead to overexpression; thus, the observed localization could either represent a physiologically relevant site for accumulation when under conditions of excess, or be due to accumulation in the vicinity of PD orifices.

FG-NUPs and other NUPs in PD fractions of Arabidopsis

To explore whether FG-NUPs may also be present in PD fractions from a vascular plant, we utilized established PD enrichment and data analysis pipelines to generate a PD proteome from Arabidopsis shoots (Gombos et al., 2023). This shoot PD proteome had an overlap of 80% with published PD proteomes and included ~43% of known high-confidence PD proteins, e.g., the well-established plasmodesmata-located proteins (PDLP) and multiple C2 domains and transmembrane region proteins (MCTP) PD markers (table S3, **Figure 1-figure supplement 2** and **3**, file S3) (Brault et al., 2019; Thomas et al., 2008). The Arabidopsis PD-enriched fraction included seven Arabidopsis FG-NUPs (**Figure 1B**). Moreover, inner and outer ring and basket NUPs were found in the high-confidence PD protein list (**Figure 1B**). In total, 20 proteins from different NPC domains were identified. 15 proteins were enriched in PD fractions compared to cell wall and total Arabidopsis protein fractions (**Figure 1B, C**, **Figure 1-figure supplement 2** and **3**). Several of the identified nuclear pore components passed the threshold for consideration as high-confidence PD proteins, in particular proteins of the inner and outer rings, core and basket. High-confidence PD scoring was based on enrichment in biochemical PD fractions as well as on an iterative weighting process which factors in features of known PD-localized proteins (Gombos et al. 2023). Separation of PD scores of “likely PD proteins” and likely contaminants (here: plastidic

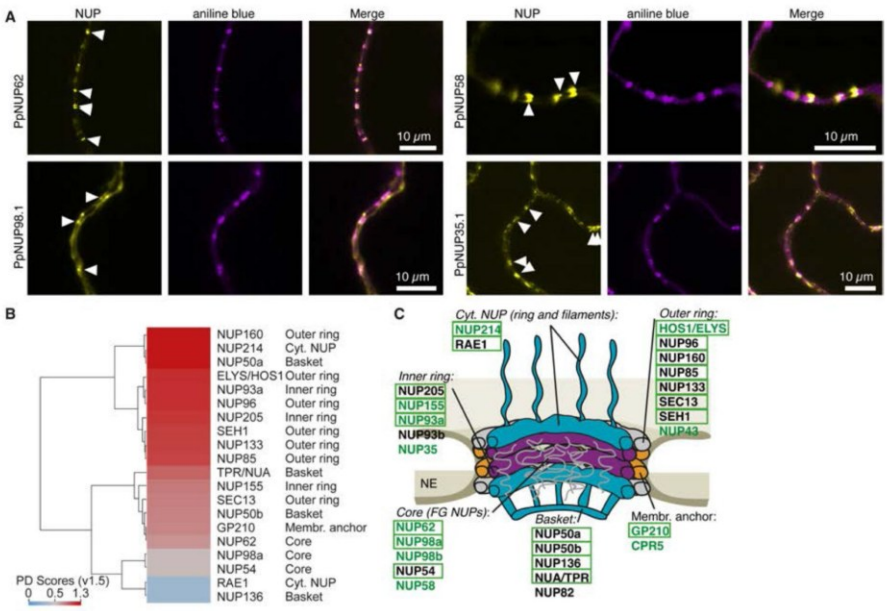


Figure 1.

Identification of NUPs at PD

(**A**) Localization of NUPs from *Physcomitrium patens* at PD.
(B) Hierarchical clustering of PD scores of Arabidopsis NPC components found in PD proteome preparations from 5-week-old Arabidopsis shoot tissues. Clustering based on Euclidean distance of PD scores (v1.5), which were averages of at least three replicate scores from separate tissue preparations. Color scale represents PD score values. PD scores above the high-confidence threshold of 0.5 are indicated in shades of red. (**C**) Scheme of an NPC embedded in the nuclear envelope with all NUPs studied in this work. NUPs listed in B are green boxed. Green letters: NUPs significantly enriched at PD in transient localization assays (**Figure 2B**, **3B**). Green boxed black letters: NUP was identified in the proteome, but was not enriched at PD in transient localization assays. Corresponding AGI locus identifiers in **table S2**. Cytoplasmic NUP is abbreviated as Cyt. NUP, and membrane anchor as Membr. anchor.

and mitochondrial proteins)(Fernandez-Calvino et al., 2011; Gombos et al., 2023) was significant, allowing to define confidence scores. NUP proteins were also previously identified in PD proteome preparation (**Figure 1-figure supplement 2E**). In particular NUPs such as FG-NUPs NUP62, NUP214, NUP50a, as well as CPR5, GP210, NUP35, NUP93a, NUP155, NUP205, NUP43, HOS1 (aka HOS1/ELYS), SEC13, and NUP82 were found in proteomics data of cell wall/PD protein fractions from other studies (**table S4**)(Bayer et al., 2006; Fernandez-Calvino et al., 2011; Gombos et al., 2023; Kirk et al., 2022; Kraner et al., 2017). Biochemical enrichment of PD resulted in enrichment of well-established PD proteins, such as PDLPs and MCTPs (**Figure 1-figure supplement 4**). As expected, likely contaminants, such as plastidic and mitochondrial proteins were depleted during PD preparation. Very highly abundant proteins, such as cytosolic ribosomal proteins, as well as histones remained high in all fractions. Ribosomal proteins did not show significant differences in abundance between fractions, while histones seemed enriched in cell wall preparations. The abundance of nuclear proteins of the nucleus showed distinct patterns: NUPs were enriched in cell wall and PD fractions compared to total cell extract, while the abundance of other nuclear envelope proteins was unaffected by the PD purification and showed no enrichment in PD fractions (**Figure 1-figure supplement 4**). Of note, grouping of the proteins provides an average; individual proteins within each group may deviate from the average pattern. While the detection of a large number of NUPs including FG-NUPs in the PD fractions, even with enrichment, may support a possible role in PD functions, we can not fully exclude that they represent contaminants.

Localization of Arabidopsis FG-NUPs and other NUPs to PD

To explore whether Arabidopsis FG-NUP-mVenus fusions can be detected at PD, candidates were expressed from an β-estradiol-inducible promoter in *N. benthamiana* leaves, which can be used to limit overexpression. Fluorescence derived from FP-fusions of the FG-NUP58, FG-NUP62 and FG-NUP98b overlaid with aniline blue fluorescent puncta (with a significantly higher PD index relative to that for the non-specific cell wall dye propidium iodide, **Figure 2**, **Figure 2-figure supplement 1**, **table S2**), indicating that Arabidopsis FG-NUPs can be targeted to PD. Notably, 12 out of a total of the 16 NUPs tested here localized to puncta in the cell periphery that overlaid with aniline blue fluorescence at pit fields (**Figure 2**, **Figure 3A, B**; **Figure 2-figure supplement 1**)(Zavaliev and Epel, 2015). Overall, 12 NUPs showed significant enrichment at PD compared to the cell wall marker (**Figure 2B**, **Figure 3B**, **table S2**), including two outer ring NUPs (NUP43, HOS1/ELYS) and two transmembrane NUPs (GP210, CPR5) (**Figure 1C**, **3B**). Ten NUP fusions for various inner and outer ring and membrane anchor NUPs were also detected in nuclei (**Figure 2-figure supplement 1**, list of 16 tested NUPs: **table S2**). Fluorescent puncta of aniline blue and FP-fusions of PD protein typically do not provide a perfect colocalization since aniline blue staining does not mark all PD and typically, the overlay is partial since FP-fusions are not detected at all PD even for high confidence PD proteins (Pendle and Benitez-Alfonso, 2015). As an independent line of evidence we observed overlay of the PD marker PDLP5-mScarlet3 and an mCitrine fusion of the putative NUP107-160 complex recruitment factor HOS1/ELYS at PD (**Figure 3G**). To test for potential artifacts, caused possibly by mistargeting due to overexpression, the concentration of the inducer β-estradiol and the induction time were reduced. In plants expressing NUP43-mCitrine or CPR5-FP fusions, the fluorescence intensity was reduced (**Figure 3D,E**), without negatively affecting dual NUP localization at NPC and PD (example for NUP43-mCitrine in **Figure 3C**). The fluorescence ratio between periphery and nucleus did not differ significantly after expression induction by 2 µM compared to 20 µM β-estradiol (**Figure 3F**). The resolution of confocal imaging is insufficient to conclude that the NUPs localize inside PD or accumulate in the vicinity. We also cannot exclude that expression of the NUP fusions leads to mis-targeting to PD. Different from data obtained for NUP98a (Gallemí et al., 2016), a C-terminal mVenus fusion to the auto-cleavable NUP98b was fluorescent and localized to PD (**Figure 2**, **Figure 2-figure supplement 1**), indicating that either under the condition used in our experiments, the main fraction of NUP98b was unprocessed, or that the C-terminal peptide reassociated with the N-terminal domain of NUP98b, as previously described for the two splice forms of the human NUP98 (Hodel et al., 2002). Out of 16 NUPs tested, four NUPs did not localize

at PD, as indicated by non-significant PD indices over the cell wall marker (p-values > 0.08, **table S2**). Out of 35 currently known Arabidopsis NUPs, 19 NUPs were not yet tested here (**table S2**).

Single copy insertions of GFP-fusions in stable transformants reduce the potential for artifacts caused by overexpression. Analysis of nine independent stably transformed homozygous single insertion Arabidopsis lines expressing a full-length genomic FG-NUP62-GFP fusion under the control of the native NUP62 promoter showed dual localization of the protein to the nuclei and PD. However, PD-specific localization was only detected in mature cotyledons older than 10 days (**Figure 2C, D**). Notably, the peripheral localization of NUP62-GFP was not restricted solely to PDs, as punctate fluorescence was detected at the cell surface, outside of PD regions (**Figure 2E**). Importantly, these punctate fluorescent signals at the cell periphery, encompassing both PD-associated and non-PD-associated localization, were absent in roots and in young leaves approximately 4 days old (**Figure 2D**). Although the single insertion Arabidopsis lines tested here should have FG-NUP62-GFP levels closer to native conditions than the heterologous overexpression of FG-NUP62-mVenus in *N. benthamiana*, it cannot be excluded that the levels in tested lines are still higher than the native levels, or that the fluorescence protein fused to the NUP affects localization.

Components of the inner ring, NUP93a and NUP155, and the basket, NUP82, were also detected at PD when heterologously overexpressed in *N. benthamiana*, although with lower confidence compared to, e.g., CPR5. Analysis of published data from other groups, who had localized NUPs to nuclei also showed peripheral puncta, which had not been analyzed further (**table S5**). As of now, we cannot exclude that the localization in the periphery is an overexpression artifact due to accumulation in the ER at the orifices of PD since the complexes are too large for translocation (Giordano et al., 2013). Alternatively, the puncta in the periphery could be the consequence of an accumulation, when biotic or abiotic conditions lead to elevated production of NUPs that cannot replace existing NUPs, similar to annulate lamellae (AL). In such conditions, the peripheral accumulation might serve as cellular storage of excessive NUPs. Interestingly, in mammalian cells, depletion of NUP98 led to FG-NUP accumulation sites in the periphery at ER junctions. Such sites of accumulation may serve as NUP storage depots rather than sites of degradation (Pletan et al., 2025).

Topology of CPR5, a potential membrane anchor at both NPC and PD

Since the phase separation domain in the nuclear pore is produced by ten FG-NUPs and PD appear to contain multiple FG-NUPs, it may be necessary to mutate multiple *FG-NUP* genes before it is possible to observe intercellular transport defects (Xiao et al., 2020). It is also conceivable that *knock-out* mutants in multiple *FG-NUPs* may be lethal. We thus rather focused on the green lineage-specific membrane anchor CPR5, a nuclear pore component with a high PD index of 1.48 (**Figure 3**, **table S2**). Four potential membrane proteins that anchor the human NPC in the nuclear membrane had been identified: GP210, POM121, NDC1 and TMEM33. Arabidopsis encodes genes for three anchors GP210, NDC1 and PNET1 (homolog of human TMEM209; **table S6**), while CPR5 had been proposed to serve as an anchor in the equatorial plane of the NPC (Apelt et al., 2016; Gu et al., 2016). Since CPR5 was among the top 5 candidates based on the PD index, one may hypothesize that it may serve as an anchor for an NPC-like structure at PD (**Figure 3A, B**, **Figure 2-figure supplement 1**). CPR5, a polytopic membrane protein, is predicted to form a globular helix bundle domain at its N-terminus, flanked by disordered regions and connected to a 105 amino acid α-helix (**Figure 4-figure supplement 1**). The central helix contains a hydrophobic region, which, together with four shorter hydrophobic helices, forms an approximately 35 Å long transmembrane domain, consistent with the expected thickness of ER membranes. The C-terminus possibly extends into the ER lumen. While it has been considered that CPR5 may play specialized roles, e.g., in defense reactions, it is also conceivable that the

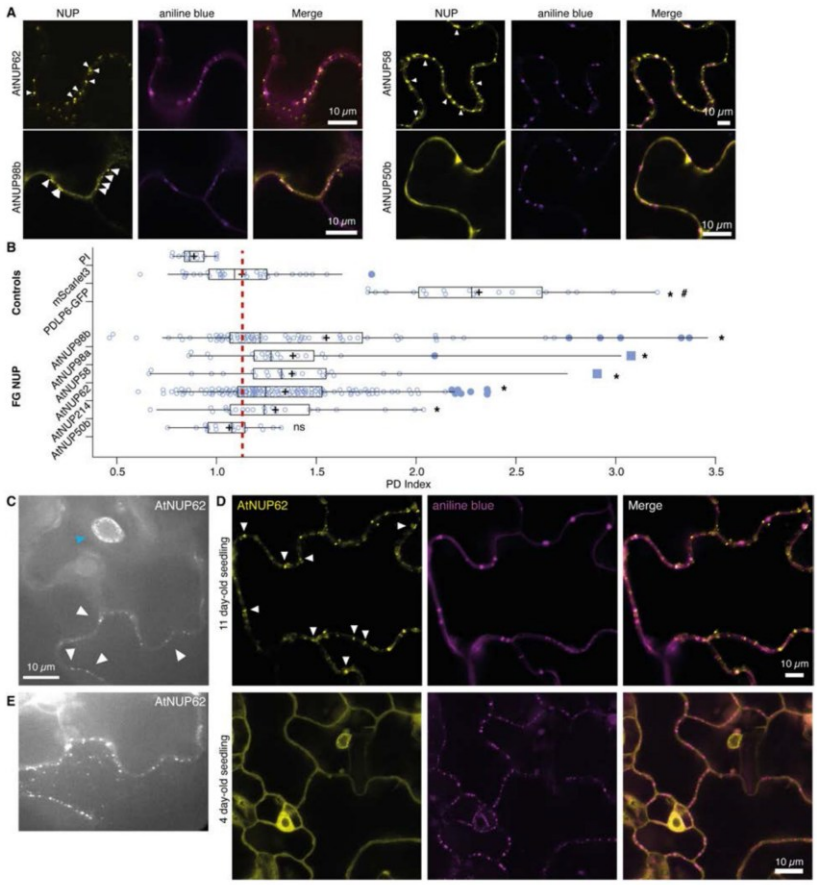


Figure 2.

Dual localization of Arabidopsis FG NUPs

(A) Localization of selected Arabidopsis FG-NUPs after transient expression under the control of the β-estradiol-inducible XVE promotor in *N. benthamiana* epidermal cells using confocal microscopy. mVenus was fused to the C-terminus of different NUPs, except for NUP98a for which GFP was fused both N- and C-terminally (GFP-NUP98a-GFP). Aniline blue was infiltrated to detect callose in pit fields as a PD marker. Localization was repeated in three independent experiments with similar results. (**B**) Quantification of the PD localization by PD index. Red dashed line indicates the mean PD index of mScarlet3 (cytoplasmic control). PI, propidium iodide ('membrane impermeant dye'). Significantly ($p < 0.05$) increased PD indices compared to the cell wall or cytoplasmic controls are indicated by * and #, respectively. Kruskal-Wallis Test $p < 0.001$, p-values of Bonferroni corrected pairwise test are summarized in **table S2**. Median is represented by vertical line inside the box, mean is represented by the bold +. Values between quartiles 1 and 3 are represented by box ranges, and 5^{th} and 95^{th} percentile are represented by error bars. At least 15 images from 3 biological replicates were analyzed for each NUP. Independent localization data are shown in **Figure 1-figure supplement 3**. (**C-E**) Arabidopsis NUP62-GFP plants expressing NUP62 fused to GFP under its own promoter. (**C**) The localization of NUP62-GFP in 11-day-old cotyledon epidermal cells was visualized by confocal microscopy (CSU10; 100x oil-immersion objective). Arrowhead: blue nucleus, white peripheral NUP62-GFP. **(D)** Localization of NUP62-GFP in cotyledonar epidermal cells of stably transformed 11-day-old (*top*) and 4-day-old (*bottom*) Arabidopsis lines. Cotyledons were immersed in aniline blue to detect callose in pit fields as PD markers. White arrowheads in D indicate overlay of NUPs and aniline blue. Scale bar: 10 µm. **(E)** Maximum intensity projection of 20 optical cross-sections taken at 1µm intervals of epidermal cotyledon cells expressing NUP62 fused to GFP under its own promoter (11-day-old seedling). Punctate localization of NUP62-GFP can also be found at the epidermis cell surface on the adaxial side of the cell.

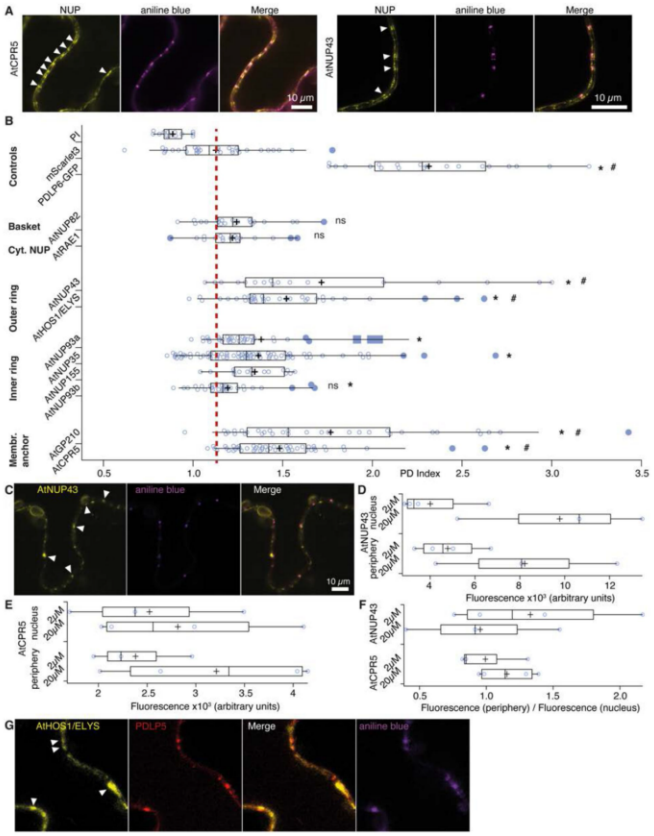


Figure 3.

Dual localization of Arabidopsis scaffold and transmembrane NUPs

(A) Localization of Arabidopsis transmembrane (CPR5) and scaffold (NUP43) NUPs after transient expression under the control of the β-estradiol-inducible XVE promotor in *N. benthamiana* epidermal cells using confocal microscopy. mVenus was fused to the C-terminus of different NUPs. Aniline blue was infiltrated to detect callose in pit fields as PD marker. White arrowheads indicate overlay with aniline blue. Localization was repeated in three independent experiments with similar results. (**B**) Quantification of the PD localization by PD index. Red dashed line indicates the mean PD index of mScarlet3 (cytoplasmic control). PI, propidium iodide ('membrane impermeant dye'). Significantly ($p < 0.05$) increased PD indices compared to cell wall or cytoplasmic controls indicated by * and #, respectively. Kruskal-Wallis Test $p < 0.001$, p-values of Bonferroni corrected pairwise test are summarized in **table S2**. Median: vertical line inside box, mean: +. Values between quartiles 1 and 3: box ranges, and 5th and 95th percentile are represented by error bars. At least 15 images from 3 biological replicates were analyzed for each NUP. Independent data in **Figure 1-figure supplement 3**. Control identical to **Figure 2B**. **(C)** NUP43-mCitrine localization at PD at 1/10 β-estradiol concentration and shortened induction time (not exceeding 10h). White arrowheads: overlay with aniline blue. **(D and E)** Quantification of the fluorescence intensity of NUP43-mCitrine (D) and CPR5-FP fusions (mVenus and mCitrine) (E) in the periphery and the nucleus after induction by 20μM or 2μM β-estradiol. **(F)** Periphery/nucleus fluorescence ratios in plants expressing NUP43-mCitrine or CPR5-FP fusions after expression is induced by 2 or 20μM β-estradiol. Box plots in (D-F) are based on a smaller subset of confocal images that show nucleus and peripheral fluorescence in one image; for individual conditions: n ≥ 3 images from at least 2 independent repeats. Student's t-test in (F) 2μM vs. 20μM estradiol: for NUP43, p = 0.26 and for CPR5, p = 0.45. (**G**) Localization of HOS1/ELYS-mCitrine and PDLP5-mScarlet3 co-expressed transiently under the control of the inducible XVE promoter in *N. benthamiana* epidermal cells. Aniline blue was infiltrated to stain callose that accumulates in pit fields. White arrowheads: overlay of HOS1/ELYS-mCitrine and PDLP5-mScarlet3 channels. Localization repeated in three independent experiments with comparable results.

phenotypes are secondary defects (Arra et al., 2024; Gu et al., 2016; Ma et al., 2023; Peng et al., 2022), caused by the missing anchoring activity (Apelt et al., 2016; Gu et al., 2016). CPR5 is encoded by a single gene in Arabidopsis and two in rice (**Figure 4-figure supplement 2**, **table S6**, **table S7**)(Arra et al., 2024). In PD, CPR5 could either be embedded into the plasma membrane near or at PD, with the C-terminus facing the apoplasm, or into the ER/desmotubule membrane, with its C-terminus facing the desmotubule lumen (or ER lumen in the vicinity of PD) and the long N-terminal domain pointing into the intermembrane space of PD/cytosol, analogous to the CPR5 topology in the ER-derived nuclear membrane at the NPC. A split-GFP system for topology studies of membrane proteins was used to determine whether the C-terminus of CPR5 faces the luminal side of the ER (Xie et al., 2017). When an N-terminal GFP11 fusion to CPR5 was co-expressed with a free cytosolic GFP1-10, fluorescence was reconstituted, consistent with the N-terminus being located in the cytosol or the cytosolic sleeve of PD (**Figure 4A**; **Figure 4-figure supplement 3**). A control using a GFP1-10 domain targeted to and retained in the ER lumen (GFP1-10-HDEL) did not show detectable fluorescence reconstitution (**Figure 4B**). The complementary fusion of GFP11 to the C-terminus of CPR5 led to reconstitution of fluorescence when co-expressed with an ER lumen targeted GFP1-10-HDEL, but not when co-expressed with a cytosolic GFP1-10 (**Figure 4A, B**; **Figure 4-figure supplement 3**). The topological data are consistent with a model in which the C-terminal five-helix-bundle of CPR5 traverses the ER/desmotubule membrane with the C-terminus inside the lumen of the ER/desmotubule, while the extended central α-helix, the predicted unstructured domains, and the smaller helical bundle of CPR5 are located in the intermembrane space between the ER/desmotubule and the plasma membrane (**Figure 4-figure supplement 1**).

Localization of CPR5 at the orifices of PD

A hypothetical NPC-like structure could serve as a micropore in the PD channel, or be present close to the PD entrance. To determine CPR5 localization in the PD at higher resolution, we performed structured illumination microscopy (SIM) with a CPR5-mCitrine fusion. CPR5 was found to localize adjacent to aniline blue labeled callose deposition at PD. Therefore, CPR5 may localize to or near the neck region of PD, but not in the central cavity of the PD, where a PDLP5-mScarlet3 was localized (**Figure 4C, D**; **Figure 4-figure supplement 4**)(Fitzgibbon et al., 2010). These findings are consistent with a model in which NUPs are present at or close to the PD orifices. We did not observe puncta at both paired neck regions in all cases (**Figure 4-figure supplement 4B**, top), possibly due to mosaic-like expression in *N. benthamiana*, in which only one of the adjacent cells expressed the fusion protein (model: **Figure 4D**). CPR5-mCitrine localization was absent at some PD (**Figure 4-figure supplement 4B**, *bottom*): in 10 images from 3 independent repeats, CPR5-mCitrine and PDLP5-mScarlet3 localized to 76 ± 6% and 81 ± 10% of the aniline blue labeled pit fields, respectively, while CPR5-mCitrine localized to 79 ± 9% of the PDLP5-mScarlet3 puncta (**Figure 4-figure supplement 4D**). Note that CPR5-mCitrine also localized in the periphery outside PD (**Figure 4-figure supplement 4D**).

Intercellular transport defects in *cpr5* mutants

If indeed NUPs form phase-separated barriers at PD to control cell-to-cell transport, and given the defects of *cpr5* mutants in nuclear transport, one may expect that interference with CPR5 function might impair *facilitated and non-facilitated cell-to-cell translocation of specific macromolecules*. Particle bombardment of Arabidopsis leaves was performed to transiently express a tandem-GFP fusion (2xmEGFP; 54 kDa) in two independent *cpr5* loss-of-function mutants (EMS mutant *cpr5-1* (G420D) and T-DNA insertion mutant *cpr5-T3*; **Figure 5-figure supplement 1C, D**)(Bowling et al., 1997; Crawford and Zambryski, 2000; Faulkner et al., 2013; Gu et al., 2016; Otero et al., 2016; Sakulkoo et al., 2018; Wang et al., 2017). Cell-to-cell movement of 2xmEGFP was significantly reduced in the *cpr5* mutants relative to wild type (WT) (**Figure 5A, B**; **Figure 5-figure supplement 1A, B**). Originally named for its *constitutive pathogen response* phenotype,

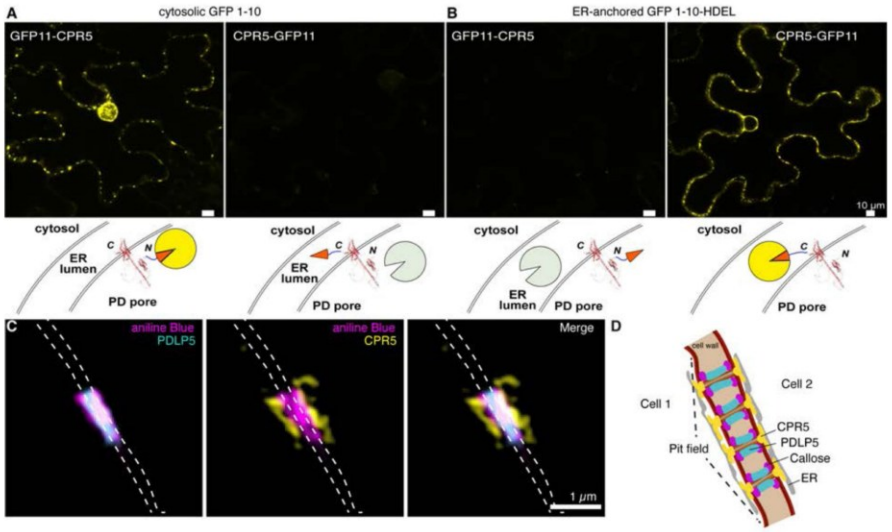


Figure 4.

CPR5 topology and localization of CPR5 near PD orifices

Split-GFP membrane topology to test for the orientation of CPR5 in the nuclear pore membrane and the ER at PD. (**A**) *(left)* Fluorescence reconstitution at PD between a cytosolic non-fluorescent GFP domain lacking β-sheet 11 (GFP1-10; the circle missing a wedge) and a fusion of the GFP11 to the N-terminus of CPR5 (the red wedge). Since reconstitution occurs at PD, each cartoon indicates reconstitution in the intermembrane space between ER/desmotubule and plasma membrane. *(right)* Cytosolic GFP1-10 and GFP11fusion to C-terminus of CPR5. (**B**) *(left)* ER-retained GFP1-10-HDEL and GFP11 fused to N-terminus of CPR5. *(right)* ER-retained GFP1-10-HDEL and fusion of GFP11 to C-terminus of CPR5. Repeated independently 3 times with comparable results. (**C**) CPR5-mCitrine close to the orifices of PD by Structured Illumination Microscopy in *N. benthamiana* leaves co-infiltrated with XVE:PDLP5-mScarlet3 and XVE:CPR5-mCitrine. Prior to imaging, leaves were infiltrated with aniline blue. PDLP5-mScarlet3: turquoise, CPR5-mCitrine: yellow, aniline blue: magenta. Repeated independently four times with comparable results. **(D)** Cartoon approximately to scale, illustrating PD in pit field between adjacent cells with callose marked magenta, PDLP5 turquoise, CPR5 yellow.

loss of CPR5 activity can trigger constitutive defense responses that could cause callose deposition and closure of PD (Kohler et al., 2002), however, callose levels were not significantly different (**Figure 5C**).

The transcription factor SHORT-ROOT (SHR), produced in cells of the stele, migrates into the endodermis by *facilitated cell-to-cell translocation*, followed by nuclear import (Nakajima et al., 2001). Intercellular transport of SHR is crucial for tissue patterning (Koizumi et al., 2012; Nakajima et al., 2001; Winter et al., 2024). To explore whether SHR-GFP (86.6 kDa) movement was impacted in a *cpr5* loss-of-function mutant, we compared the endodermis-to-stele ratio (E:S ratio) of GFP fluorescence intensity in roots of homozygous *shr* mutants expressing pSHR:SHR–GFP in WT, as well as in the *cpr5-1* mutant background. The E:S ratio was significantly reduced in *cpr5-1* compared to WT, consistent with a defect in facilitated SHR transport across PD (**Figure 5D, E**). Fluorescence recovery after photobleaching (FRAP) of nuclei in the root endodermis of homozygous *shr*/pSHR:SHR lines in *cpr5-1* was significantly lower compared to WT, further supporting that targeted transport across PD is reduced in *cpr5-1* (**Figure 5F,G**, **Figure 5-figure supplement 1F**). Notably, no significant difference in SHR–GFP fluorescence intensity was observed in the steles of WT when compared to *cpr5-1* lines (**Figure 5-figure supplement 1E**). The *cpr5* mutants showed no detectable defect in small molecule transport indicative of WT-like PD density and preservation of the capability to mediate small molecule transport as shown by 'Drop-ANd-See' *trans*-leaf diffusion assays (DANS, carboxyfluorescein: 376 Da; control CaMV*35S:PDLP5*; **Figure 5H, I**)(Lee et al., 2011). In summary, the intercellular transport assay results indicate that a callose-independent transport mechanism for macromolecules is defective in *cpr5* mutants. While consistent with a possible contribution of NUPs to intercellular transport, we cannot exclude that the reduced transport is due to secondary effects in the *cpr5* mutants, which show rather severe phenotypic defects (**Figure 5-figure supplement 1C, D**).

Discussion

Based on the observations that (i) a substantial number of NUPs were identified in PD-enriched cell wall fractions, (ii) 12/35 known plant NUPs, including multiple FG-NUPs, localized to PD, and (iii) intercellular tandem-GFP and SHR transport was reduced in *cpr5* mutants could indicate that components of the NPC may generate a complex that can sustain a similar phase separation domain at PD as found in the NPC, and that phase separation generated by FG-NUPs may play a role in intercellular translocation (Kehlenbach et al., 2023). Previous studies had shown that cargo size cannot be the only criterion for cell-to-cell transport efficiency through PD (Alazem et al., 2025; Campbell et al., 2025; Howell et al., 2024; Kragler et al., 1998; Lee et al., 2003). The evidence for PD localization of NUPs obtained here is intriguing, as it may provide new potential explanations for the underlying mechanism of transport of certain mobile molecules (e.g. RNA-protein complexes) that are larger than the expected size exclusion limit (Tee and Faulkner, 2024). In this context the discovery of a new function of the nuclear transport receptor importin α4 as a PD-associated protein in mediating systemic infection of a plant virus in rice may further support the hypothesis of NPC-like transport functions (Lu et al., 2025).

Nuclear transport experiments using surface modified GFPs and analysis of the properties of nuclear transport receptors indicate that the phase separated domain generated by FG-NUPs in the permeation pathway of the NPC facilitates the transit of cargo that carry arginines, cysteines, histidines, and hydrophobic amino acids at their surface (Ejike et al., 2025; Frey et al., 2018). It will be very informative to test whether similar cargo surface properties are important for the transport through PD. Transport assays combined with pharmacological approaches using compounds such as hexanediol, which disrupt phase-separated domains, and systematic analyses of transport using surface-modified FPs of the same size (Frey et al., 2018; Ng et al., 2023) might help identifying phase separated domains at PD.

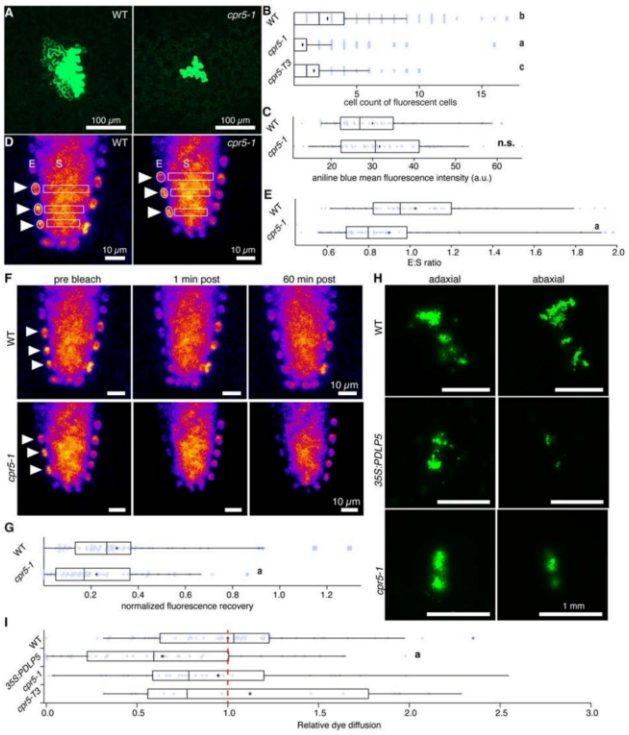


Figure 5.

Defects in cell-to-cell transport of kDa-sized cargo in *cpr5* mutants

(A) Example images of intercellular 2xmEGFP movement in wild type (WT, *left*) and *cpr5-1* (*right*) Arabidopsis leaves. Leaves were bombarded with gold particles coated with p35S:mEGFP-mEGFP DNA plasmids 24 h prior to the analysis by confocal microscopy (fusion protein abbreviated as 2xmEGFP). **(B)** Quantification of the intercellular spread of mEGFP by counting fluorescent cells in the GFP channel. $n_{(WT)}$ = 594 bombarded cells, 17 independent biological replicates: $n_{(cpr5\text{-}1)}$ = 278 bombarded cells, 6 independent biological replicates. $n_{(cpr5\text{-}T3)}$ = 99 bombarded cells, four independent biological replicates. **a** indicates significant difference to WT with $p_{(cpr5\text{-}T3)}$ = 0.0004; **b** indicates significant difference to WT with $p_{(cpr5\text{-}1)} < 10^{-15}$; $p_{(cpr5\text{-}1 \text{ vs. } cpr5\text{-}T3)}$ = 0.0002 (Kruskal-Wallis test with Bonferroni correction for pairwise comparison). **(C)** Callose quantification. $n_{(WT)}$ = 4 independent experiments, $n_{(cpr5\text{-}1)}$ = 5 independent experiments, graph summarizes all experiments. Student's *t*-test p = 0.48. **(D)** Sum projections showing SHR–GFP distribution in WT (*left*) and *cpr5-1* mutant (*right*) root. White circles and boxes indicate positions of endodermis nuclei (E, arrows) and corresponding regions in the stele (S, white boxes). **(E)** Quantification of SHR–GFP endodermis:stele ratio (E:S) for WT and *cpr5-1* mutant. $n_{(WT)}$ = 62 nuclei, $n_{(cpr5\text{-}1)}$ = 62 nuclei, with 3-4 nuclei analyzed per root. **a** indicates significantly decreased E:S in *cpr5-1* mutant, based on Mann-Whitney U test with p = 0.0006. **(F)**, Sum projections showing SHR–GFP distribution in WT (*top*) and *cpr5-1* (*bottom*) background. **(G)**, Quantification of relative SHR–GFP fluorescence recovery for WT and *cpr5-1* mutant after 1 h. Fluorescence recovery was normalized to a control nucleus in the endodermis (see Methods and **Figure 5-figure supplement 1F**). n(WT) = 59 bleached nuclei, n(*cpr5-1*) = 59, per root 3-4 nuclei were bleached. Student's t-test p = 0.037 indicating significantly decreased fluorescence recovery after 60 min. **(H and I)** PD permeabilities examined by CFDA/CFSE-based DANS dye loading assays. **(H)** Epifluorescence reporting on CF diffusion in the epidermis of the adaxial (*left*) and abaxial (*right*) side of the leaf. WT *(top), 35S:PDLP5* (*middle*), and *cpr5-1* (*bottom*). Bars, 1 mm. **(I)** Quantification of CF diffusion in WT and mutant lines. $n_{(WT)}$ = 49 plants, 7 independent biological replicates; $n_{(35S:PDLP5)}$ = 38 plants, 5 independent biological replicates; $n_{(cpr5\text{-}1)}$ = 29 plants, 5 independent biological replicates; $n_{(cpr5\text{-}T3)}$ = 15 plants, 5 independent biological replicates. Fluorescent areas on the abaxial side were identified using auto threshold and Fiji YEN-algorithm with user modifications. The same threshold setting was used for the adaxial side. The extent of dye diffusion was quantified by the ratio between the areal spread of fluorescence on the abaxial side and the areal spread of fluorescence on the adaxial side. **a** indicates significantly different at the α = 0.032 level according to Bonferroni-corrected pair wise comparison following Kruskal-Wallis analysis.

In summary we found three independent lines of evidence for the presence of NUPs at or near PD in the context of this work, based on subcellular localization, proteomics, and transport. However, all three independent lines could potentially be the result of artifacts. In particular, we found NUP localization at PD in overexpression conditions and, interestingly, also in stable transgenic Arabidopsis lines with presumably lower protein levels. However, NUP localization in the Arabidopsis lines at PD has only been observed in mature cotyledons and so far not in other tissues such as younger leaves or root. We can not exclude that in the NUP62-GFP lines, PD localization of NUPs is caused by elevated protein levels. Alternatively, it might be possible that localization of NUPs at PD occurs at (natively) elevated protein levels and/or depends on factors such as growth condition, pathogen infection and hormones, which were shown to influence mRNA levels of NUPs (Ascencio-Ibanez et al., 2008; Chen et al., 2012; Narsai et al., 2011; Okuma et al., 2014; Song et al., 2009). Interestingly, dynamic changes in subcellular localization of NUPs in response to environmental stimuli were reported previously, e.g., HOS1-GFP re-localizes from the periphery to the nucleoplasm after cold treatment (Lee et al., 2001). Perhaps the PD localization of NUPs is dynamic, occurring only under certain environmental conditions. To validate the subcellular localization, additional evidence is needed from stable transgenic lines with NUP fusions expressed under the control of the native promoter and terminator, complementing the NUP mutant background, and grown in different environmental conditions. Specific antisera raised against plant NUPs that are suitable for immunolocalization may help to clarify the subcellular localization of NUPs under native conditions. New insights may also be generated by cryo-electron tomography, for which recently suitable protocols have been established (Pöge et al., 2025). An alternative hypothesis that also implicates LLPS for the PD permeability barrier is based on the finding that the linker between the N-terminal C2A and C2B domains (C2A-B linker domain) of multiple C2 domains and transmembrane region proteins (MCTP) found in PD is predicted to be disordered and show strong intrinsic propensity for liquid-liquid phase separation (Dickmanns et al., 2025). Cryo-electron microcopy of plasmodesmata identified assemblies that decorate the desmotubule, which are likely formed by MCTPs, and which could then form an extended permeability barrier in the PD pore (Dickmanns et al., 2025).

There is evidence for NUPs to constitute a permeability barrier between cytoplasm and cilia (ciliary transition zone) in animal cells (Blasius et al., 2019; del Viso et al., 2016; Gu et al., 2016; Takao et al., 2017). However, the exact composition of the proposed ciliary pore complex and its anchoring at the ciliary base remains a matter of debate, as cryo-ET structures of the ciliary base/ transition zone are not yet available (Johnson and Malicki, 2019). Similarly, the assembly of NUPs at PD must differ from that at the NPC because, as described above, desmotubules extend through the central channel of PD and the cytoplasmic sleeve width at PD is smaller than the pore width at the NPC (Ejike et al., 2025; Mosalaganti et al., 2022; Nicolas et al., 2017). The localization of the same NUPs at PD as well as nuclear pores is unexpected, given that one would rather expect gene duplication and diversification to enable independent regulation. Note that not all known NUPs were tested here, and some of those tested did not localize to the PD. The structure, function and regulation of the predicted PD pore complex (PDPC) may differ from that of the NPC.

NUPs seem to also play functional roles outside the NPC in animal cells: FG-NUPs were found in several cyto- and nucleoplasmic membrane-less organelles, such as P-bodies, P-granules, stress granules, and viral-associated organelles. In animals, annulate lamellae, preassembled NPCs in ER stacks, are characteristic for rapidly dividing cells during germ cell development, early embryogenesis and cancerogenic growth and might serve as storage place for NUPs (Kessel, 1992; Penzo and Palancade, 2023). AL have also been found in plant cells (Scheer and Franke, 1972). High NUP levels could result in accumulation within AL. Missing an organellar marker for AL, we cannot exclude that fluorescent puncta derived from NUP-FP fusions in our subcellular

localization experiments indicate NUP localization to AL. However, the arrangement of fluorescent puncta did not follow a stacking pattern, which we would expect because of the stacked ER sheets in AL.

PD are challenging research subjects due to the embedding into the cell wall, and the presence of multiple membranes. Based on the similarities between transport properties of PD and NPC, one may hypothesize that they both use similar transport mechanisms. Further characterization will be required to explore mechanisms for delivery of a diverse set of GFP-fused NUPs to PD, and to evaluate their localization and trafficking, e.g. by immunolocalization. Alternatively, accumulation could serve as transient storage of NPC complexes, or are a consequence of overaccumulation at the constriction of ER at PD entrances.

Materials and methods

Plant materials and growth conditions

Physcomitrium patens (*P. patens*) ecotype Grandsen cultures were obtained from the *International Moss Stock Center (IMSC)* (Freiburg). *P. patens* was cultured in liquid cultures of modified BCD medium as described (Gombos et al., 2023). The BCD medium consisted of the following solutions which were mixed prior to use: Solution B (0.1 mM $MgSO_4 \cdot 7H_2O$), Solution C (1.84 mM KH_2PO_4), Solution DK (1 M KNO_3), Solution DF (4.5 mM $FeSO_4 \cdot 7H_2O$), Trace Element Solution (TES) (614 mg H_3BO_3, 55 mg $CuSO_4 \cdot 5H_20$, 28 mg KBr, 110 mg $Al_2(SO_4)3 \cdot K_2SO_4 \cdot 24H_20$, 389 mg $MnCl_2 \cdot 4H_20$, 55 mg $ZnSO_4 \cdot 7H_20$, 28mg LiCl, 10 mM $CoCl_2 \cdot 6H_20$, 28 mg KI and 28 mg $SnCl_2 \cdot 2H_20$ in 1 L H_20), 500 mM diammonium tartrate and 1 M $CaCl_2$. For liquid cultures, 1% (m/v) glucose was added. For propagation of liquid cultures, moss was homogenized and then transferred to 100 ml medium in a 250 ml. Cultures were harvested after two weeks of growth at 21°C under long day conditions (16 h light/8 h dark) at ~90 µmol m^{-2} sec^{-1}, 60% humidity.

Arabidopsis *cpr5-1* (G420D) mutant and *cpr5-T3* (SALK_074631) T-DNA insertion mutant were kindly provided by Dr. Gu (University of California Berkeley) and Professor Chun-Hai Dong (Qingdao Agricultural University), respectively (Bowling et al., 1994; Wang et al., 2017). Arabidopsis Col-0 *shr*/pSHR:SHR–GFP line was described before (Cui et al., 2007) and kindly gifted by Ikram Blilou, KAUST. The pSHR:SHR–GFP/*cpr5-1* in the *shr* mutant background was generated by crossing, and identified in the F2 segregating generation by sequencing of CPR5. For quantification of the SHR-GFP endodermis-to-stele ratio, F5 seedlings of the Arabidopsis lines pSHR:SHR–GFP *cpr5-1* were grown on a glass plate coated with ½ salt strength Murashige and Skoog (MS) media agar [half-strength Murashige and Skoog basal salt mixture (Duchefa Biochemie, Haarlem, The Netherlands), 0.1 % (w/v) 2-(N-morpholino)-ethanesulfonic acid, 1.5% agar, pH 5.6] (Dyachok et al., 2010) for 6 days in short day conditions (10 h light, 14 h darkness), at 21°C with a light intensity to 130 µmol m^{-2} s^{-1}. For microparticle bombardment assays and callose quantification, Arabidopsis Col-0, *cpr5-1*, and *cpr5-T3* plants were grown on ½ MS plates in the same conditions as described above for 4 weeks. Nine independent stably transformed homozygous Arabidopsis wildtype lines with single insertions for NUP62-GFP were used for fluorescence imaging (T3 segregants; 3:1 segregation) and grown on ½ MS media supplemented with 1% (w/v) sucrose and 1% (w/v) agar in a growth chamber (16 h light/8 h darkness, 23 °C, 50 µmol m^{-2} $s^{-1}$of white light, 60% humidity). For DANS assay, Arabidopsis WT and T-DNA insertion lines were grown in soil with one plant per pot at 21°C under long day conditions (16 h light/8 h dark) for 3 weeks. For analyses of the Arabidopsis shoot proteome, plants were grown in soil at 21°C under long day conditions (16 h light/8 h dark) at ~90 µmol m^{-2} sec^{-1}, 60% humidity. Respective tissues were harvested after three or five weeks. *Nicotiana benthamiana* (*N. benthamiana*) plants were grown individually in a pot under controlled conditions (16 h light/8 h darkness, 26 °C, ~90 µmol m^{-2} s^{-1}, 60% humidity).

DNA constructs

For transient expression in *N. benthamiana*, the selected NUP open reading frames (ORFs) were cloned into the binary pAB134-mVenus plasmid (Bleckmann et al., 2010). To generate the ORFs, total RNA was extracted from Arabidopsis leaves using the RNeasy plant mini kit (Qiagen, Hilden, Germany), and DNase I treatment was performed following the manufacturer's instructions. cDNA was then synthesized using the Maxima H Minus First Strand cDNA synthesis kit (Thermo Fisher Scientific Inc., Waltham, Massachusetts, USA). The ORFs were amplified, incorporating the Gateway attB sites, and purified PCR products were cloned into pDONR221 using a BP clonase reaction (Thermo Fisher Scientific Inc., Waltham, Massachusetts, USA). *E. coli* Stellar cells (Takara Bio) were transformed with the resulting entry vectors. Plasmids with the correct sequence were isolated and then recombined by LR reaction into the binary plant expression vector pAB134-mVenus as C-terminal mVenus fusions under the control of a β-estradiol-inducible promoter (Bleckmann et al., 2010). For localization of PpNUP35.1, Pp3c6_16260V3 was amplified and cloned into the binary pAB134-mVenus plasmid. For SIM experiments, XVE:CPR5-mCitrine and XVE:PDLP5-mScarlet3 were generated using GreenGate (Lampropoulos et al., 2013). CPR5 and PDLP5 genomic sequences were amplified with primers including *Bsa*I restriction sites and ligated to pGGC000 previously digested with *Bsa*I. Resulting vectors were used to generate expression constructs using the GreenGate modules: XVE promoter (module A), CPR5 or PDLP5 (module C), C-mCitrine or mScarlet3 (module D), HSP18.2-Terminator (module E), and the pOLE1:OLE1-RFP seed coat selection marker (Shimada et al., 2010) (module F) were ligated to the linearized binary vector pGGZ003.

Monomeric enhanced GFP (mEGFP) and 2xmEGFP sequences were amplified by PCR from plasmids pENTR-R4R3-mEGFP-C (Addgene #113749) and pGGC025 (Addgene #48830), respectively, using Gateway specific primers adding the attB1 and attB2 sites and cloned into pDONR221 by BP reaction (Thermo Fisher Scientific Inc., Waltham, Massachusetts, USA). The resulting constructs, pDONR221-mEGFP and pDONR221-2xmEGFP were used for LR reaction into the destination vector pGWB502 (Addgene #74844). The p35S:3xmCherry construct was generated using GreenGate by ligating the modules Ca MV 35S promoter (Addgene #48815) (module A), 3xmCherry (Addgene #48831) (module C), HSP18.2-Terminator (module E), and the pOLE1:OLE1-RFP seed coat selection marker (module F) into the linearized binary vector pGGZ003. Topology localization of CPR5 was carried out using the split-GFP system with the vectors kindly provided by Prof. Thordal-Christensen (University of Copenhagen) (Xie et al., 2017). pDONR-CPR5 plasmid was recombined into pDest-GW-GFP11 and pDest-GFP11-GW to generate either N- and C-fusions to the GFP 11th β-sheet using LR Gateway reactions (Thermo Fisher Scientific Inc., Waltham, Massachusetts, USA). The GFP1-10 fragment was co-expressed with either cytosolic localization (GFP1-10) or with ER-luminal localization (GFP1-10-HDEL). Plasmids pEG100-35S:nYFP-CPR5, pEG100-35S:cYFP-CPR5 and pEG100-35S:NUP93a-cYFP used for homo-and hetero-oligomerization were kindly gifted by Prof. Xinnian Dong (Duke University. North Carolina, USA) (Gu et al., 2016). The nYFP fragment contains residues 1-172, and cYFP consists of residues 173-238. A translational fusion NUP62-GFP construct was generated from a genomic clone of *NUP62* (At2g45000), including a 1135-bp region 5'-upstream from the initiation ATG and a 407-bp region 3'-downstream from the stop codon. mEGFP was fused to the NUP62 separated by a GGGGSGGGGSGGGGS-linker (Shimozono and Miyawaki, 2008), just before the stop codon using NEBuilder® HiFi DNA Assembly (NEB). The fluorescent protein-fusion construct was digested by *Not*I and integrated into the pBIN40 binary vector (Miyashima et al., 2011). The final binary vectors were introduced into *Agrobacterium tumefaciens* strain GV3101:pMP90 and used to carry out the transformation of Arabidopsis. We confirmed the nucleotide sequences of all constructs using standard DNA manipulation and sequencing techniques. Primers used in this study are listed in **table S8**.

Transient expression in *N. benthamiana* leaves

The *Agrobacterium tumefaciens* strain GV3101 (pMP90, pSOUP), containing the desired construct, was cultured overnight, then diluted to 1/10 and grown until the culture reached an OD_{600} of 0.6-0.8. Cultures were pelleted by centrifuge at 4000 rpm for 10 minutes. Bacteria were subsequently re-suspended in an Infiltration Buffer comprising 0.01 M 2-(N-morpholino) ethanesulfonic acid (MES) at pH 5.6, 0.01 M $MgCl_2$, and 150 µM acetosyringone at a final OD_{600} of 0.3. The *Agrobacterium* strain containing the intended construct was then combined with an *Agrobacterium* strain containing the P19 silencing suppressor (OD_{600} 0.1) (Qu and Morris, 2002). The resulting mixture was introduced into the leaves of 4-week-old *N. benthamiana* plants through syringe infiltration. Two days after infiltration, gene expression was induced by spraying infiltrated leaves with β-estradiol solution (20 µM β-estradiol, 0.1% v/v Tween-20). Induction time was dependent on protein maturation times and ranged from 6 to 24 h. To test localization of XVE:NUP43-mCitrine or XVE:CPR5-FP fusions at lower expression levels induction was performed with 2 µM β-estradiol and induction times did not exceed 10 h (2 µM β-estradiol, 0.1% v/v Tween-20).

For split-GFP assays, agrobacterial cultures were suspended in the Infiltration Buffer at a final OD_{600} of 0.3. *Agrobacterium* strains containing constructs split-GFP were co-infiltrated with the P19 silencing suppressor (OD_{600} 0.1) into *N. benthamiana* leaves. For split-GFP assays either GFP11-CPR5 or CPR5-GFP11 and GFP1-10 or GFP1-10-HDEL were co-infiltrated. Samples were imaged 2 days post infiltration.

Microscopy

Subcellular localization of FP fusions by confocal microcopy

Confocal microscopy was performed on a Zeiss LSM 900 (Carl Zeiss, Oberkochen, Germany) equipped with Airyscan GaAsP-PMT detectors and diode lasers using a 40x/1.20 water immersion objective (C-Apochromat 40x/1.20 W Korr FCS). mCitrine or mVenus were excited with a 488 nm laser and emission was collected in a 520-579 nm window. GFP was excited at 488 nm and collected in a 500-550 nm window. mScarlet3 was excited at 561 nm and collected from 579-617 nm (Gadella et al., 2023). To visualize pit fields, *N. benthamiana* leaves expressing a protein of interest were infiltrated with 0.1% (w/v) aniline blue (Sigma Aldrich) solution and then imaged (excitation at 405 nm and 3-5% laser power, emission detected in a 440-480 nm window). Free mScarlet3 was expressed and excited to visualize cytoplasmic localization. Propidium iodide, a cell impermeant dye, stains the apoplasm when short incubation times are used. Thus, for visualization of the cell wall, shortly before the experiment, PI was pipetted on the object slide on the leaf disc (excitation 561 nm, 6% laser power, emission 574-617 nm). Pit fields in cotyledons of 8-day old transgenic NUP62-GFP Arabidopsis seedlings were stained by immersing leaves in 0.5% aniline blue in Sørensen's phosphate buffer [0.5% aniline blue (w/v) in 200 mM Sørensen's phosphate buffer prepared with Na_2HPO_4 and NaH_2PO_4 pH 8, Sigma-Aldrich, Saint Louis, Missouri, USA)]. For confocal imaging of NUP62-GFP Arabidopsis lines, an Eclipse Ti2 inverted microscope (Nikon) equipped with spinning disk confocal unit CSU-10 (Yokogawa) and a sCMOS camera PRIME 95B (Photometrics, Tuscon, AZ, USA) was used. GFP was excited with a 488-nm laser, and emission was collected with a 525/50-nm filter (Semrock, Rochester, New York). Images were taken with a 100x oil-immersion lens (CFI Plan Apo Lambda 1.45 NA, Nikon).

Structured Illumination Microscopy

For structured illumination microscopy (SIM), only pit fields that were not deeply embedded in the plant tissue and most proximal to the cover glass close to the objective, were observed. To do so, a *N. benthamiana* leaf disk (2-mm diameter) was immersed in water and pressed between an object

slide and a high-precision coverslip (1.5H, 18 x 18 mm; A. Hartenstein) using a magnet. The sample chamber was sealed with a flexible mounting adhesive (Fixo gum; Marabu). Z-stacks with a scaling of 149-nm steps were obtained using an Elyra PS1 (Zeiss Microscopy GmbH, Oberkochen, Germany) equipped with a C-Apochromat 63x/1.2 water-immersion M27 objective. Frame size was 512 x 512 pixels. PDLP5-mScarlet3, CPR5-mCitrine, and aniline blue were excited with 561 nm, 488 nm, and 405 nm laser wavelengths, respectively. Detection filters were set for the different channels: aniline blue: bandpass (BP) 420–480/LP 750; CPR5-mCitrine: BP 495–570/LP 750; PDLP5-mScarlet3: BP 570-650/LP 655. In initial control experiments with the Elyra PS1, we observed more puncta in the green channel after excitation at 488 nm, after having used the 405 nm laser to excite aniline blue. These additional puncta in the green channel precisely overlayed with the puncta observed in the aniline blue channel. The identification of fluorescent puncta in this channel in response to excitation of aniline blue might be the result of photoconversion to longer wavelengths. To exclude possible artifacts due to photoconversion of the aniline blue, which could lead to emission in the channels used for detection of mCitrine, sequential excitation was performed at 561, 488 and 405 nm. The grating periods (grid size) for structured illumination were set to 34, 34, and 28 µm, respectively, for the three different laser wavelengths. The number of grid rotations was set to 3 rotations. Camera exposure time ranged from 49-128 ms. The setup was operated using Zeiss ZEN 2.3 SP1 software. An internal deconvolution program for SIM z-stacks was used in 3D mode with maximum isotropy, zero sectioning, and the baseline shift active for all three excitation channels. The noise filter was initially run in automatic mode, but was set to a unit below the automatic setting for the actual processing.

Callose quantification in Arabidopsis seedlings

CPR5 is involved in the activation of pattern triggered immunity (PTI) and in the repression of effector-triggered immunity (ETI) (Ma et al., 2023; Wang et al., 2014). The *cpr5-1* mutant had previously been reported to show constitutive resistance to two virulent pathogens (Bowling et al., 1997). An important plant defense mechanism against pathogens is induction of callose deposition at PD. Elevated callose deposition in the *cpr5*-1 mutant after wounding has been reported (Kohler et al., 2002). To test whether callose deposition was increased relative to WT under the growth and experimental conditions used here, PD callose levels in WT and *cpr5-1* Arabidopsis seedlings were quantified. Leaf 5 of young seedlings (8-12 leaf stage) was stained to minimize variability. Leaves were detached with a forceps, immersed in 1% aniline blue diluted in water [1% aniline blue (w/v); Sigma-Aldrich, Saint Louis, Missouri, USA] and infiltrated by applying a vacuum in a 20 ml syringe. Aniline blue fluorescence was observed on a Zeiss LSM 900 (Zeiss Microscopy GmbH, Oberkochen, Germany) C-Apochromat 40x/1.20 W Korr FCS and GaAsP-Pmt1 detector with excitation at 405 nm, 5% laser power and gain at 632 V. Emission was detected from 400-500 nm. Imaging parameters were consistent across all experiments. Per experiment, 3-4 leaves were assayed per genotype, 4 images were acquired per leaf. Four independent experiments were performed for WT and 5 for *cpr5-1*. Mean aniline blue fluorescence intensity was quantified with Fiji using the calloseQuant macro (calloseQuant settings: Method A, peak prominence = 55 and measurement radius = 6) (Huang et al., 2022). Regions of Interest (ROIs) assigned to non-PD regions by the Fiji macro were removed manually. Mean aniline blue fluorescence per image was plotted.

Plasmodesmatal proteome

Preparation of *A. thaliana* plasmodesmatal (PD), cell wall (CW) and total cellular proteins (total cell extract, TC) fractions

Various Arabidopsis shoot tissues, including cauline leaves, meristem, and rosette leaves, were collected individually. Each sample pool consisted of at least six plants. PD preparation involved a minimum of three pools of the same tissue type. Tissues were freshly excised and promptly frozen in liquid nitrogen. The PD preparation protocol was based on two previously published methods

(Faulkner and Bayer, 2017; Kraner et al., 2017). Each pool of samples was ground in liquid nitrogen and incubated in PD extraction buffer [150 mM NaCl, 10 mM EDTA, 1 mM DTT, 1% (v/v) Triton X-100, 0.5% (v/v) sodium deoxycholate, 0.1% (w/v) SDS, 10% (v/v) glycerol, and 100 mM Tris-HCl, pH 8] with 0.5% Protease Inhibitor Cocktail (PIC, P9599, Sigma-Aldrich), 5 mM DTT, 1 mM PMSF, 50 mM NaF, 1 mM Na_3VO_4, 1 mM benzamidin and 4 µM leupeptin. For the cell wall fractions, two rounds of grinding in liquid nitrogen efficiently removed soluble protein contaminants and better prepared cell walls for digestion. The pellet was washed at least four times with a low concentration of detergents [150 mM NaCl, 10 mM EDTA, 0.1% (v/v) Triton X-100, 10% (v/v) glycerol, and 100 mM Tris–HCl, pH 8]. After the last washing step, the sample was centrifugated at 1500 x g at 4 °C with swing-out bucket (Sigma 3-30KS, Rotor 11390 & 13150). Cell wall fractions (CW; 100-200 µl) were collected from the final pellet. The rest of the CW pellet was digested in cell wall digestion buffer (1.4% cellulase, mannitol 300mM, 10 mM $CaCl_2$, 10 mM KCl) with 1 mM DTT and 0.5% PIC (P9599, Sigma-Aldrich) at room temperature for 1 h. After centrifugation, the supernatant was collected and ultracentrifuged for 80 min at 4 °C and 110,000 x g (Beckman XPN-80, Rotor SW41Ti). After ultracentrifugation, the resulting pellet was washed twice with TBS buffer (2.5 mM KCl, 140 mM NaCl and 20 mM Tris-HCl, pH 7.4 with 0.5% PIC). The final pellet was PD fraction (PD). Total protein (total cell extract, TC) was extracted according to He *et al.* (He et al., 2022). All fractions were dissolved in 8M UTU (6 M urea, 2 M thiourea, Tris-HCl pH 8.0) before in-solution tryptic digestion.

Protein clean-up, trypsin digestion and peptide desalting

A single-pot, solid-phase-enhanced, sample-preparation (SP3) technology (Hughes et al., 2019) with trypsin digestion was used to remove the detergent in the protein extracts. Disulfide bridges were reduced by an excess of DTT (6.5 mM), and alkylation of free cysteines was done by iodoacetamide (27 mM). SpeedBead Magnetic Carboxylate Modified Particles (SP3 beads, 45152105050250 / 65152105050250, GE Healthcare) were pre-washed by Milli-Q water. SP3 beads (50 µg/µl) were added to the protein sample in a ratio of 1:10. 50% ethanol was used for inducing protein-bead binding. After incubating 15 min at 24°C, 1,000 rpm constant shaking, the beads were washed three times with 80% ethanol and subjected to trypsin digestion [100 mM Ammonium bicarbonate, trypsin (trypsin: protein ratio 1:100, V5113, Promega)] for 12-14 h at 37 °C. Digested proteins were acidified to pH 2 using TFA and were then desalted over C18 STAGE tips (Rappsilber et al., 2003).

LC-MS/MS analysis of peptides

Peptide mixtures were analyzed by HPLC system nanoflow Easy-nLC (Thermo Scientific, Waltham, Massachusetts) and Orbitrap hybrid mass spectrometer (Q-exactive, Thermo Scientific). Peptides were eluted from a 75 µm x 25 cm analytical C18 column (PepMan, Thermo Scientific) on a linear gradient running from 5% to 90% acetonitrile over 70 min. Proteins were identified based on the information-dependent acquisition of fragmentation spectra of multiple charged peptides. Up to ten data-dependent MS/MS spectra were acquired in the linear ion trap for each full-scan spectrum acquired at 60,000 full-width half-maximum (FWHM) resolution.

Peptide and protein identification

MaxQuant version 2.2.0.0 was used for raw file peak extraction and protein identification against the Arabidopsis TAIR11 database (35,386 entries). The following parameters were applied: trypsin as cleaving enzyme; minimum peptide length of six amino acids; maximal two missed cleavages; carbamidomethylation of cysteine as a fixed modification; N-terminal protein acetylation, and oxidation of methionine as variable modifications. Peptide mass tolerance was set to 20 ppm, and 0.5 Da was used as the MS/MS tolerance. Multiplicity was set to 1. For label-free quantification, retention time matching between runs was chosen within a time window of two minutes. iBAQ quantification was selected within label-free quantification. The peptide false discovery rate (FDR) and the protein FDR were set to 0.01, while site FDR was set to 0.05. Hits to contaminants (e.g.

keratins) and reverse hits identified by MaxQuant were excluded from further analysis. The mass spectrometry proteomics data have been deposited to the ProteomeXchange Consortium via the PRIDE partner repository (Deutsch et al., 2020) with the dataset identifier PXD049466.

PD score (V1.5)

The PD scoring (v1.5) was derived from the earlier PD score equation by Gombos *et al.* (Gombos et al., 2023) with the modification that its components enrichment score and feature score were scaled between 0 and 1. The proteingroups.txt output from Maxquant was analyzed using Perseus. Protein iBAQ values were normalized using z-scores, and the values for PD, CW, and TC fractions were averaged across tissues (file S3). The ratios PD/CW and PD/TC were then calculated based on the average values obtained for each fraction. The PD enrichment score for each protein is the sum of PD/CW and PD/TC. The score was then scaled to a range of 0 to 1, based on the proportion of the distance to the minimum score. Regardless of the enrichment score, the feature score relies on the frequency of protein functions, sublocalizations and PFAM domains (available at *https://pfam.xfam.org/*) identified within the high-confidence dataset and validated PD candidates (Gombos et al., 2023; Johnston et al., 2023; Kirk et al., 2022). Similar to the enrichment score, the feature score was also normalized to a scale from 0 to 1, based on the proportion of the distance to the minimum score across all *Arabidopsis* proteins (30843 entries). For each protein, the PD score (v 1.5) is obtained by summing the transformed PD enrichment score and the feature score, resulting in a range from 0 to 2. A higher PD score (1.5) indicates a greater likelihood that the protein is a PD protein.

Intercellular Transport assays

Microparticle bombardment

To test passive diffusion of 2xEGFP, microparticle bombardment was performed to deliver DNA coated gold microcarriers into single epidermal cells. 60 mg of 1.0 µm gold microcarriers (Bio-Rad Laboratories, Hercules, CA, USA) were added into a 1.5-mL microcentrifuge tube and washed with 70% ethanol before use. After the final washing step, 1 mL of 50% glycerol was added, and the tube was sealed using Parafilm® (Amcor). The suspended gold particles (35 µL) were labelled with 2 – 2.5 µg of plasmid DNA (pGWB502-p35S:2xmEGFP) in the presence of 0.1 M spermidine and 2.5 M $CaCl_2$. Tubes were vortexed for 1 min and put on ice for 1 min. Coated gold particles were centrifuged at 1,500 x g for 30 sec. The particles were washed twice with 70% ethanol. After the second washing step, 35 µL of 100% ethanol was added and vortexed until the pellet completely dispersed. This gold suspension (10 µL) was transferred onto a macrocarrier (Bio-Rad Laboratories, Hercules, CA, USA). Bombardment was performed using the PDS-1000/He Biolistic Particle Delivery System (Bio-Rad, #1652257) as described (Tee et al., 2022). To visualize bombardments, 2xmEGFP was excited with a 488-nm laser and emission detected at 495-548 nm, while 3xmCherry was excited with a 561-nm laser and emission detected at 548-617 nm. Cells showing fluorescence in the GFP channel were counted manually on maximum projections. To identify the initially bombarded cell, Arabidopsis leaves were bombarded with gold particles coated with pGWB502-p35S:3xmCherry (84 kDa, unable to move passively through non-specific trafficking) and pGWB502-p35S:2xmEGFP. Fluorescence intensity profile plots across transects were generated using Fiji software package (Schindelin et al., 2012) to analyze the correlation of the fluorescence intensity of mCherry (bombarded cell) and mEGFP (**Figure 5-figure supplement 1**).

SHR-GFP endodermis-to-stele ratio and Fluorescence Recovery After Photobleaching (FRAP) analysis

SHR–GFP was detected in root endodermis and stele using a Zeiss LSM 900 equipped with Airyscan GaAsP-PMT detectors and diode lasers using a C-Apochromat 40x/1.20 W Korr FCS water objective. For quantification of SHR-GFP, a brief Z-stack series of up to 60 sections of short intervals (2.1 µm) around the ROI were captured, and the Sum-Projection of the volume was analyzed using ImageJ. The background fluorescence was subtracted from the average pixel intensity in the circled region in the endodermis (E) and from the average pixel intensity of the corresponding boxed region in the stele (S) (see **Figure 5D**). The ratio between endodermis and corresponding stele region was calculated (E:S). Multiple samples were taken for each root to determine the average ratio.

The SHR–GFP fluorescence was bleached in endodermal cells using the 488 nm laser at full laser power for 150 iterations, which lead to around 50-70% reduction in fluorescence. 1-3 cells in the same cell layer were bleached at the same time for each root. To acquire recovery images, laser power was set to 2% to avoid bleaching. The recovery images of the bleached areas were captured every 20 min to reduce the possibility of additional bleaching from frequent scanning. To ensure the identification of the same region of interest during the time-course imaging, a brief Z-stack series of up to 60 sections with short interval (2.1µm) around the region of interest were captured. In this way, the same region should be included in the series of images and can be re-tracked later for analysis. For each time point the Sum-Projection of the same volume was analyzed. The background subtracted fluorescence intensity ratio (endodermis bleached nucleus/endodermis control nucleus) before bleach, after bleach and after 60 minutes was determined using ImageJ (see also **Figure 5-figure supplement 1F** for positions of ROIs). Time 0 post-bleach fluorescence was set to 0 and all measurements were normalized to this point by subtracting the time 0 post-bleach fluorescence signal from all of the pre-bleach and the recovery values. The percent recovery was calculated using the normalized values. For analysis of intracellular FRAP, a frame size of 512 × 512 pixels with a scanning speed of 0.93 ms per frame (1 Hz) and bi-directional scanning was used to accelerate the scanning rate for each frame.

DANS assay

For Drop-ANd-See (DANS) assays, 1 µl of 10 mM 5-(and 6)-carboxy-fluoresceindiacetat-acetoxymethylester (CFDA) in 0.002 % Silwet® was pipetted on the adaxial side of a rosette leaf and removed after 5 min. The 4th and 24 h later also the 5th rosette leaf was used. For microscopy, the leaf was cut off, washed in water, and mounted between two cover slips. Fluorescence was observed under an Axio Zoom.V16 (Zeiss Microscopy GmbH, Oberkochen, Germany) equipped with a X-Cite Xylts (Excelitas Technologies, PA, USA) LED light source, using a GFP broad bandpass filter cube (excitation: 470/40 nm, beam splitter: FT495 nm, emission: 525/50 nm). Images of the adaxial- and abaxial side were taken using Orca-fusionBT digital camera (C15440, Hamamatsu, Japan). Imaging parameters were consistent across experiments. To identify the fluorescent area, thresholding was performed in ImageJ with the same threshold value for adaxial-and abaxial sides. The diffusion is quantified by ratio between the area above the intensity threshold on the abaxial side and the adaxial side. Experiments of the same day were normalized to the WT experiments of the same day.

Bioinformatics

FG repeat analysis

To identify FG repeat proteins, *A. thaliana* and *P. patens* peptides encoded by gene models were downloaded from Araport 11 and Phypa_V3 genomes and screened, respectively. FG occurrences were counted in a sliding window of 200 amino acids (aa), and the maximum number of FG

repeats per window was determined using a custom python script (Supplementary Script 1 and 2). Within the same script, the number of GLFG and xFxFG motifs in each peptide were counted (**table S1**).

PD index quantification

Overlay of fluorescence from NUP-FPs and aniline blue was quantitatively scored using the PD index (Grison et al., 2019). To minimize bias in quantification, we employed our recently developed PD index script (Gombos et al., 2023). Briefly, clear PD sites were cropped, and channels were separated. PD were identified using auto threshold and Fiji YEN-algorithm, with user modifications. Center coordinates of PD were determined, and square ROIs were set. The PD index was calculated by dividing mean intensity values of PD ROIs by background ROI values. Background ROIs were defined as areas of weak aniline blue fluorescence. Regions previously recognized as PD were automatically omitted from the positioning of background ROIs. Image processing was used for background ROI placement. The software Igor Pro (version 9) was used for data plotting and SPSS was used for statistical analyses.

Structure prediction for CPR5

The structure of CPR5 was predicted using Alphafold monomer version 2.3.1 (Jumper et al., 2021).

Phylogenetic analyses

The tree shown in **Figure 4-figure supplement 2** was generated from 68 amino acid sequences as listed in **table S7**. Full-length sequences were imported into the Molecular Evolutionary Genetics Analysis (MEGA) package version 11, and aligned by CLUSTALW (Tamura et al., 2021). All positions with at least 85% site coverage were used. Phylogenetic analyses were conducted using the Maximum Likelihood method. Based on the suggestions of the “find best protein model (ML)” tool in MEGA 11, the lower BIC (Bayesian Information Criterion) model was selected, which was the JTT matrix-based model (Jones et al., 1992). A discrete Gamma distribution was used to model evolutionary rate differences among sites (five categories, +G, parameter = 6.413). Initial trees for the heuristic search were obtained automatically by applying Neighbor-Joining and BioNJ algorithms to a matrix of pairwise distances estimated using the JTT model, and then selecting the topology with a superior log likelihood value. The bootstrap consensus tree inferred from 1000 replicates was taken to represent the evolutionary history of the analyzed genes. Branches corresponding to partitions reproduced in less than 50% bootstrap replicates were collapsed.

Statistics

In the PD proteome from Arabidopsis leaf tissue, we identified 5145 proteins from PD, CW, and TC fractions, with 3347 proteins having a PD score > 0.63. Among them, 3062 proteins were quantifiable in the PD fraction, constituting our Arabidopsis shoot PD proteome. Among these, 2268 proteins were categorized as high-confidence PD proteins, while 792 proteins fall into the medium-confidence category (file S3). The PD index is based on the analysis of at least 15 images from three independent repeats for each NUP and negative control. The quantification of the intercellular spread of 2xmEGFP by counting fluorescent cells in the mEGFP channel is based on the analysis of $n_{(WT)} = 17$ independent biological experiments with in total 594 bombarded cells; $n_{(cpr5\text{-}1)} = 6$ independent biological replicates with in total 278 bombarded cells; $n_{(cpr5\text{-}T3)} = 4$ independent biological replicates with in total 99 bombarded cells. Kruskal-Wallis test with Bonferroni correction for pairwise comparison was used to test for significant differences in mean cell counts between WT, *cpr5-1*, and *cpr5-T3* with $p_{(\text{WT vs. } cpr5\text{-}1)} < 1\times10^{-10}$, $p_{(\text{WT vs. } cpr5\text{-}T3)} = 0.025$, and $p_{(cpr5\text{-}1 \text{ vs. } cpr5\text{-}T3)} = 0.00005$. The *p*-values are summarized in **table S2**. The callose quantification is based on $n_{(WT)} = 4$ independent experiments, $n_{(cpr5\text{-}1)} = 5$ independent experiments. Student’s *t*-test indicated a non-significant difference with $p = 0.48$.

SHR-GFP endodermis-to-stele ratio is based on the quantification of $n_{(WT)}$ = 62 and $n_{(cpr5\text{-}1)}$ = 62 different endodermis nuclei and corresponding stele regions, while per root 3-4 different nuclei and corresponding stele regions were quantified. For endodermis-to-stele ratio, Mann-Whitney U test indicated a significant difference between WT and *cpr5-1* background with p = 0.0006. For baseline stele fluorescence, Mann-Whitney U test indicated no significant differences between s*hr* and s*hr x cpr5-1* with p = 0.074. The quantification of SHR-GFP fluorescence recovery was normalized to a control nucleus in the endodermis (see Methods and **Figure 5-figure supplement 1F**) and is based on n(WT) = 59 and n(*cpr5-1*) = 59 bleached nuclei, while per root 3-4 nuclei were bleached. Student's T-Test indicated a significant difference between WT and *cpr5-1* background with p = 0.037.

For the DANS data, Kruskal-Wallis test with Bonferroni correction for pairwise comparison was used to test for significant differences between WT and mutant lines. All statistical test were performed with SPSS. In all box plots median is represented by vertical line inside the box, mean is represented by the bold +. Values between quartiles 1 and 3 are represented by box ranges, and 5^{th} and 95^{th} percentile are represented by error bars. Data was plotted using Igor Pro (version 9).

Data availability

Source data have been assigned a DOI (*http://doi.org/10.60534/46qra-6bw98*) and are accessible via *https://git.nfdi4plants.org/projects/2188*. Materials will be made available under MTA; some materials were obtained from others as marked and require permission from the respective authors.

Figure supplements and supplementary tables

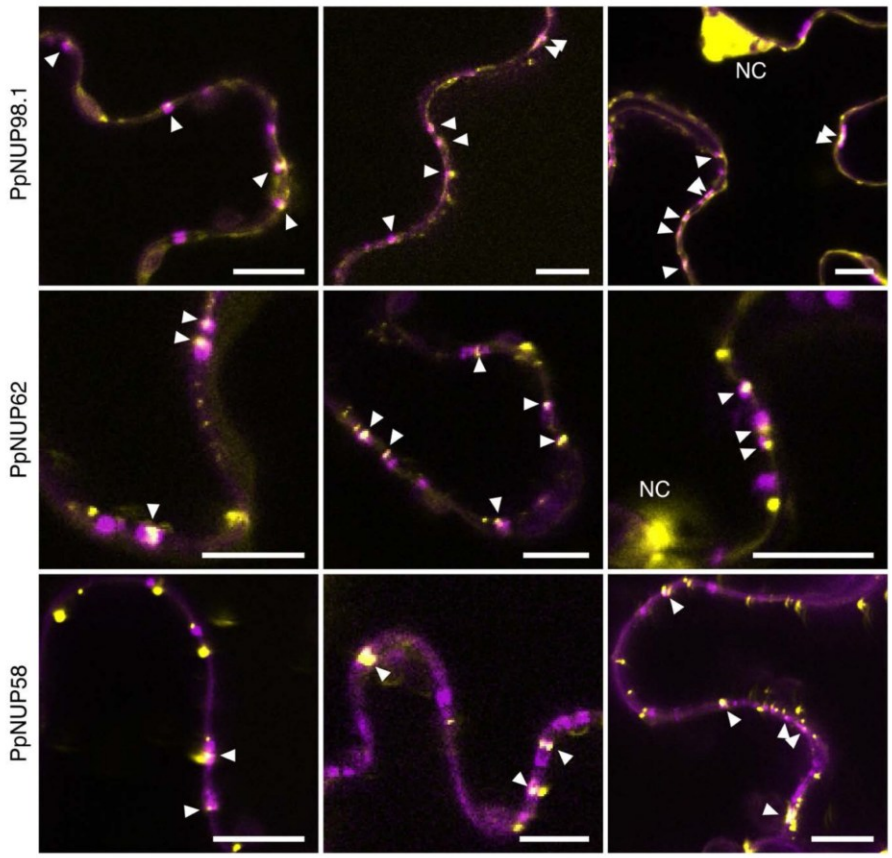


Figure 1-figure supplement 1.

Overlay of *Physcomitrium patens* FG-NUPs with the PD marker aniline blue

Localization of FG-NUPs from *P. patens* in *N. benthamiana* epidermal cells visualized by confocal microscopy. FG-NUPs were fused at their C-terminus to mVenus (yellow) and expressed transiently under the control of the inducible XVE promotor. Aniline blue (purple) was infiltrated to stain callose, which accumulates in pit fields. Arrowheads indicate overlay between NUPs and aniline blue. For each NUP, a similar localization pattern appeared in at least three independent experiments. NC = nucleus. Scale bar: 10 µm.

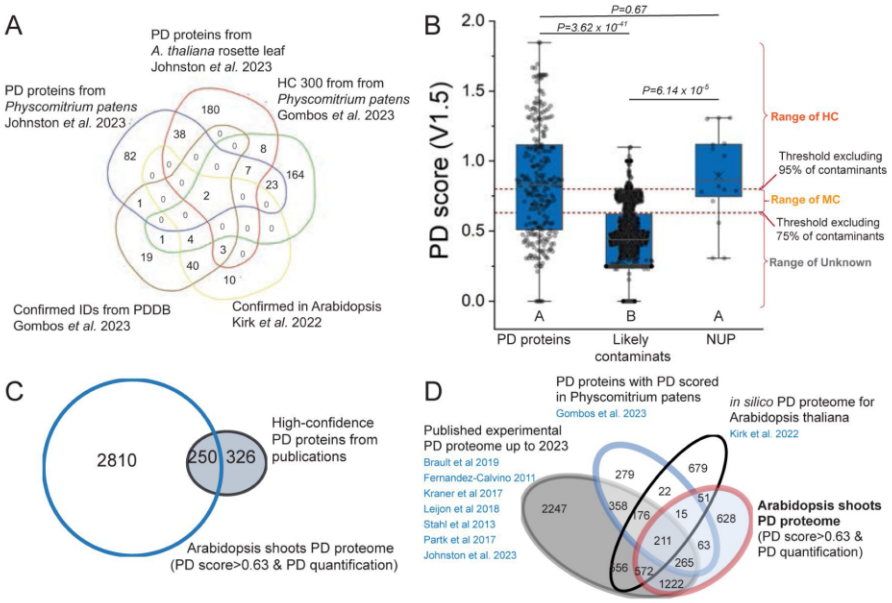


Figure 1-figure supplement 2.

Arabidopsis shoot proteome and the comparison to other PD proteomes

(**A**), Venn diagram defining high-confidence PD proteins from previous publications, e.g., confirmed Arabidopsis PD proteins, and high confidence PD proteins identified in *Physcomitrium*, and in both *Physcomitrium* and Arabidopsis leaves (Gombos et al., 2023; Johnston et al., 2023; Kirk et al., 2022). These proteins were then used as high-confidence data set to establish the PD probability threshold and were labelled as 'PD proteins' in file S3. 43% of these proteins were quantified in our Arabidopsis shoot PD proteome. (**B**), PD Scores of nuclear pore components. PD Scores (v 1.5) are shown as box plots for high-confidence PD proteins (PD proteins), typical co-purifying proteins from plastid and mitochondria identified in Arabidopsis PD preparations (likely contaminants) and proteins of the nuclear pore complex (NUP). Dotted lines indicate two thresholds based on the frequency distribution for contaminant proteins and PD proteins. The median is shown as a gray line, the mean value is denoted by a + symbol, and the whiskers cover the 95thpercentile. PD Scores above 0.83 (the upper dotted line) indicate high-confidence (HC) PD proteins; scores between 0.63 and 0.83 (between the two dotted lines) signify medium-confidence (MC) PD proteins; and scores below 0.63 are considered low confidence (LC) as their PD Scores overlapped with 75% of the contaminants. These confidence clusters were annotated in file S3. The final Arabidopsis shoot PD proteome consists of proteins with PD scores above 0.63, which are also quantifiable in the PD fraction. Capital letters represent group statistical comparisons determined by Oneway-ANOVA. The p-values of pairwise comparison using Student's t-test, are indicated on the top of the boxes. (**C**), Overlap between the Arabidopsis shoot PD proteome and other PD proteomes. Proteins with a PD score >0.63 and quantifiable in PD fraction (Arabidopsis shoot PD proteome) were compared with nine representative PD proteome studies. In the current Arabidopsis shoot PD proteome, 80% of the proteins were previously identified in published PD proteomes. Combining PD enrichment and data analysis thresholding allowed us to determine the confidence levels of PD proteins and obtain a "cleaner" PD proteome. In total, we identified 5145 proteins from PD, CW, and TC fractions, with 3347 proteins having a PD score >0.63. Among them, 3062 proteins are quantifiable in the PD fraction, constituting our Arabidopsis shoot PD proteome. Among these, 2268 proteins are categorized as high-confidence PD proteins, while 792 proteins fall into the medium-confidence category (file S3). Additionally, we discovered 20 nuclear pore proteins (NUPs), with 15 of them surpassing the threshold and being included in the final PD proteome. Among these, 11 are classified as high-confidence PD proteins, while 4 are medium-confidence PD proteins (file S3, **Figure 1-figure supplement 2B**). (**D**) Comparison of Arabidopsis shoot PD proteomes with various published PD proteomes. 80% of the proteins had been identified in previous studies.

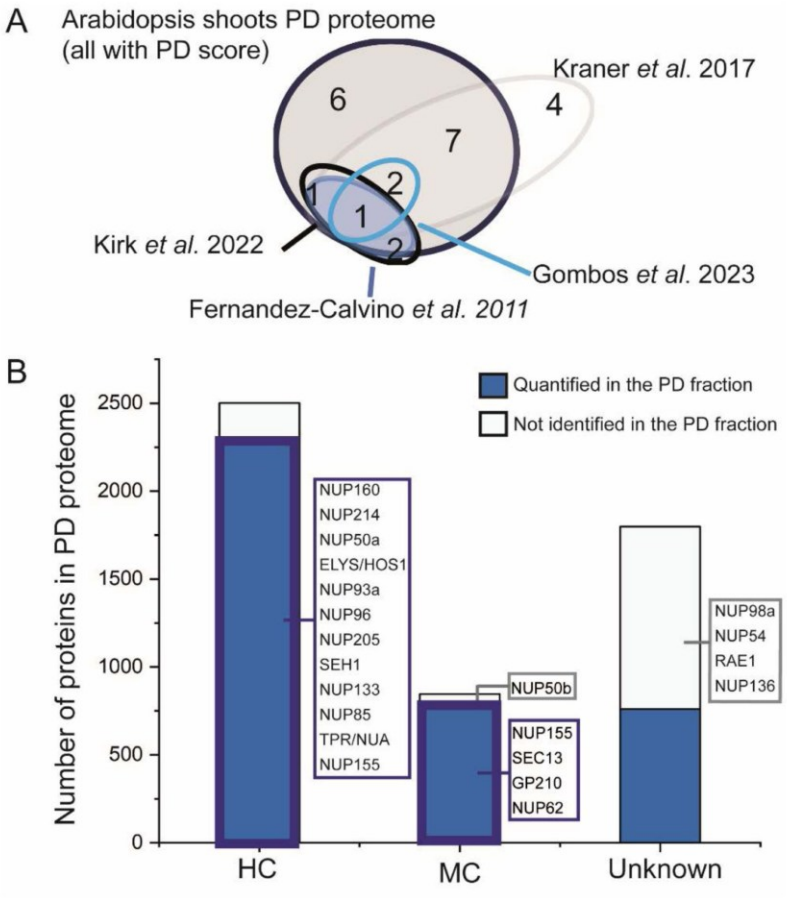


Figure 1-figure supplement 3.

NUPs are found in Arabidopsis shoot proteome and other PD proteomes. (A),

Comparison of NUPs in Arabidopsis shoot PD proteomes with published PD proteomes. Among the NUPs identified in the Arabidopsis shoot PD proteome, 73.3% (11 out of 15) were also detected in previously published PD proteomes. (**B**), Overview of identified proteins in the PD proteome. HC (PD score > 0.83), MC (0.83 > PD score > 0.63), and Unknown (PD score < 0.63). Purple-edged boxes in HC and MC mark proteins that meet Arabidopsis shoot PD proteome criteria (PD score > 0.63, quantifiable in PD fraction). Blue-edged boxes denote 16 NUPs within the Arabidopsis shoot PD proteome; Gray-edged boxes represent NUPs found also in other proteomes.

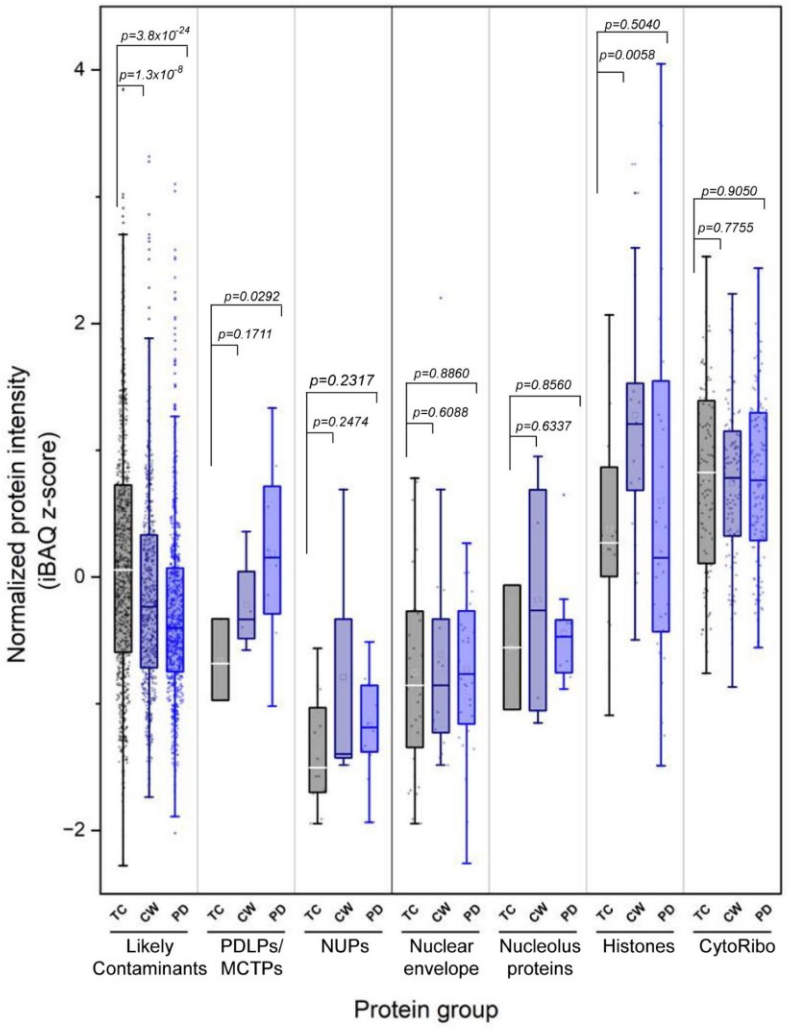


Figure 1-figure supplement 4.

Normalized protein intensities of different protein groups in total extract (TC), cell wall fraction (CW) and PD enrichment (PD)

The group of likely contaminants contains plastidic and mitochondrial proteins. *Bona fide* PD proteins are PDLPs and MCTPs. Protein categorization was based on Mapman (Usadel et al., 2005). A Student's t-test was used for statistical analysis.

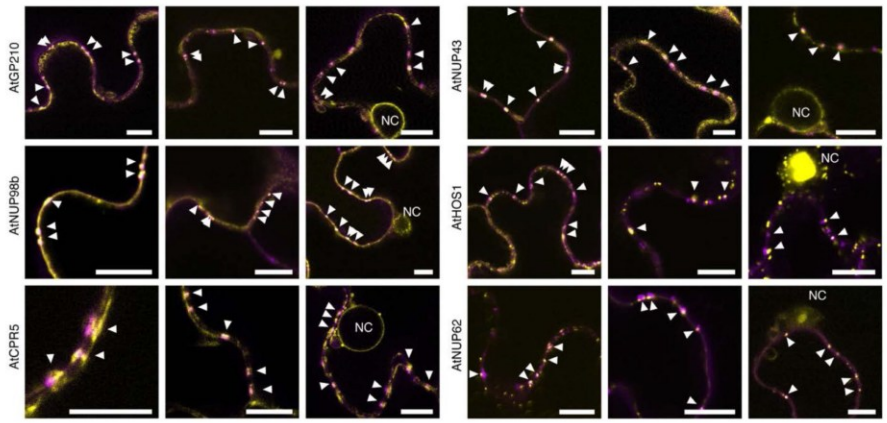


Figure 2-figure supplement 1.

Arabidopsis NUP-FP localization overlays with a PD marker

Localization of Arabidopsis NUPs in *N. benthamiana* epidermal cells visualized by confocal microscopy. NUPs were fused at their C-terminus to mVenus or mCitrine (yellow) and expressed transiently under the control of the inducible XVE promotor. Aniline blue (purple) was infiltrated to stain callose that accumulates in pit fields. Arrowheads indicate overlay between NUPs and aniline blue. NUPs shown here were found to have a significant increased PD index values compared to negative controls in **Figure 2**. For each NUP, the localization pattern was reproducible in at least in three independent experiments. NC, nuclei. Note that for comparison, we here show the same images for NUP98B and NUP62 from **Figure 2A** again. Scale bar: 10 µm.

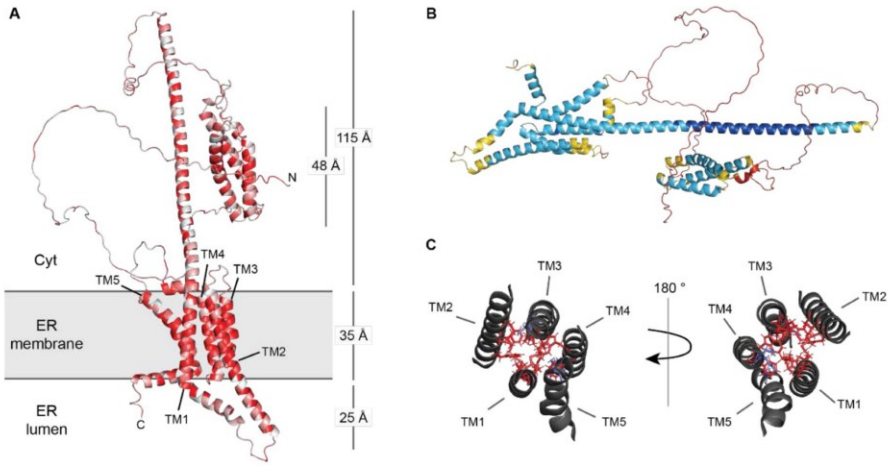


Figure 4-figure supplement 1.

Predicted structure of monomeric CPR5 and model for integration into ER-derived membranes

Topological studies using the split-GFP system (**Figure 4A,B**, **Figure 4-figure supplement 3**) are consistent with a localization of the CPR5 C-terminus in the ER lumen, while its N-terminus extends into the cytoplasm. (**A**), CPR5 is composed of a N-terminal, disordered region (residues 1-106), a soluble domain formed by 3 α-helices (107-192), linked by a second disordered region (193-265) to an approx. 115 Å long, central α-helix (266-342). Hydrophobic residues (red) of the central helix (TM1) and 4 shorter helices (TM2-TM5) form a transmembrane domain spanning approx. 35 Å, consistent with the expected thickness for ER-derived membranes. C-terminus and helical extensions of TM1 and TM2 reach into the ER lumen. (**B**), Structure colored by per-residue prediction confidence (pLDDT; dark blue: 90-100, light blue: 50-70, yellow: 50-70, red: < 50). Low confidence values (red) may indicate regions that are either intrinsically disordered or assume a structure when interacting with other proteins and therefore could partake in formation of complexes with NUPs. (**C**), View of transmembrane helical bundle from ER lumen (left) and cytoplasm (right). Amino acid side chains spanning between transmembrane helices are colored by hydrophobicity (blue: hydrophilic, red: hydrophobic). The CPR5 transmembrane domain is not predicted to form a solvent-accessible pore.

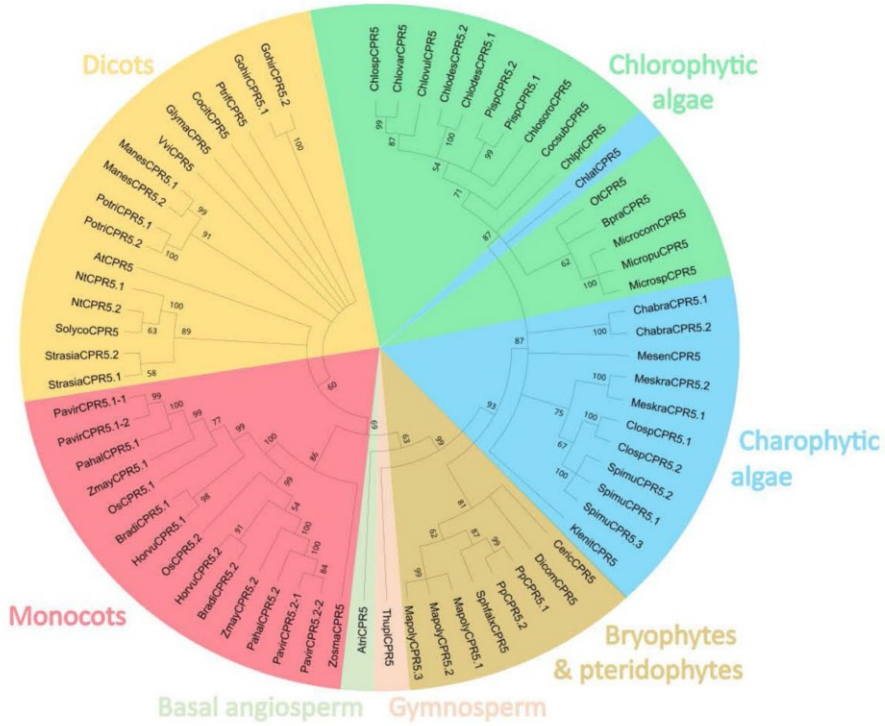


Figure 4-figure supplement 2

Phylogenetic analysis of CPR5 sequences

The accession numbers and the abbreviations corresponding to the mature protein sequences used for this analysis are given in **table S7**. The analysis was performed as described in the "Materials and Methods" section.

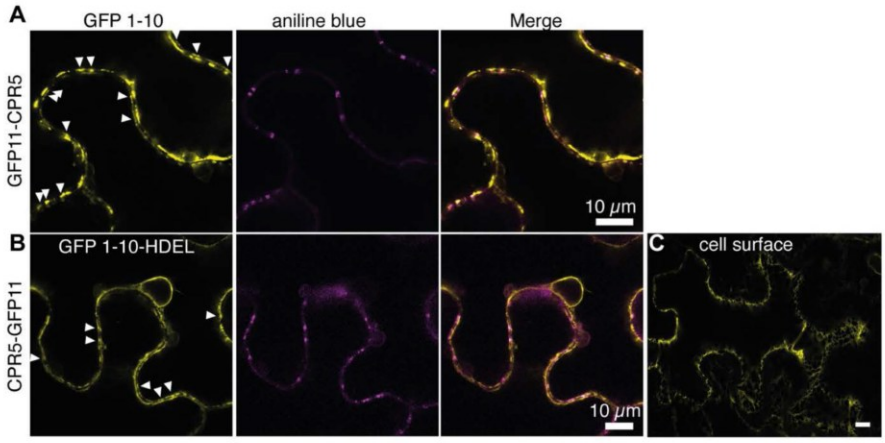


Figure 4-figure supplement 3.

The C-terminus of CPR5 faces ER lumen

(A), Transient co-expression of GFP11-CPR5 and cytosolic GFP1-10 in *N. benthamiana* leaves, same cell as shown in **Figure 4**. *Left*, GFP channel. Reconstitution can be observed also at PD (arrowheads). *Middle*, aniline blue. *Right,* merge. (**B**), *N. benthamiana* epidermal cells transiently expressing CPR5-GFP11 and ER luminal GFP1-10-HDEL, same cell as shown in **Figure 4**. *Left*, GFP channel. Reconstitution can be observed also at PD (arrowheads); *middle*, aniline blue*; right,* merge. (**C**), Surface view of the same cell as in B, showing reconstitution in the ER.

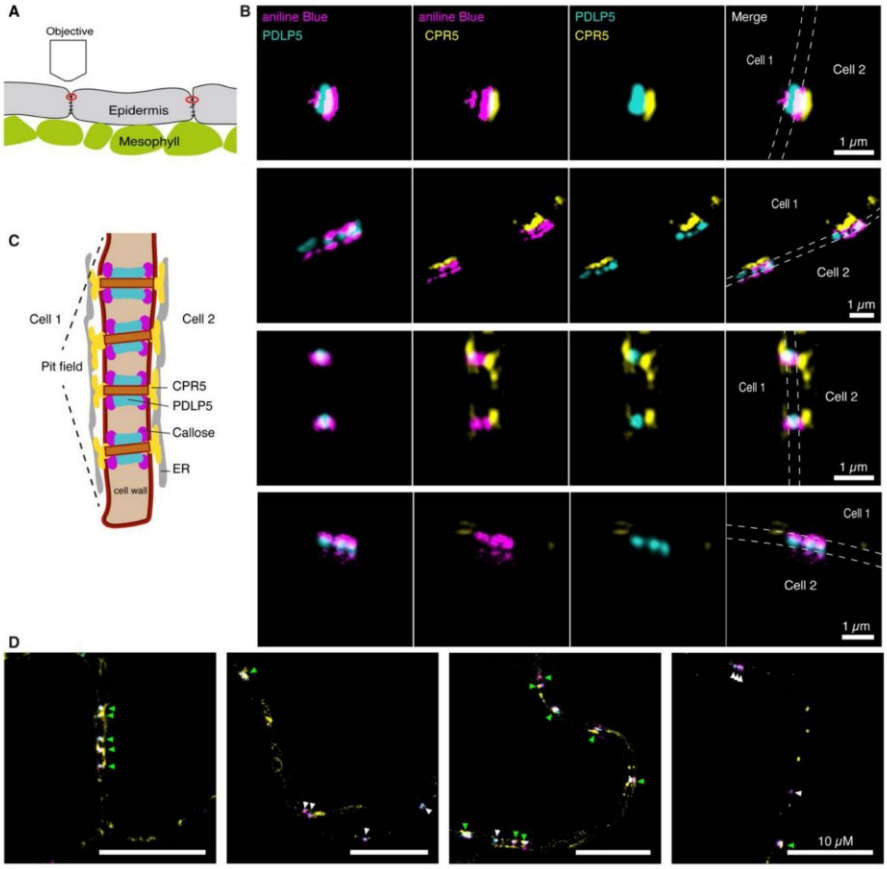


Figure 4-figure supplement 4

CPR5-mCitrine localizes at the orifices of PD

(**A),** Cartoon showing analyzed PD: only PD most proximal to the cover glass and objective were analyzed to reduce effects caused by scattering of light due to cell wall. (**B),** SIM in *N. benthamiana* leaves co-infiltrated with XVE:PDLP5-mScarlet3 and XVE:CPR5-mCitrine. Prior to the imaging, leaves were infiltrated with aniline blue. PDLP5-mScarlet3 in turquoise, CPR5-mCitrine in yellow, and aniline blue in magenta. Comparable results were obtained in four independent experiments. Dashed lines indicate approximation of cell wall boundaries. (**C),** Cartoon of pit field and localization of PDLP5 and CPR5. Fluorescence reporting on CPR5 in (B) extends laterally 200-1000 nm in the epidermal cell wall. Previously, the lateral extension of individual PD pores in the cell wall was estimated to 100 nm for basal trichome cell walls and 187 nm for epidermal cell walls (Faulkner et al., 2008; Fitzgibbon et al., 2010). The resolution achieved with SIM was not high enough to resolve single PD or determine whether pit fields consist of several simple PD (as shown in C) or a few complex (H-shaped/twinned) PD. (**D**), SIM in *N. benthamiana* leaves co-infiltrated with XVE:PDLP5-mScarlet3 and XVE:CPR5-mCitrine. Green arrowheads indicate overlay between CPR5-mCitrine, PDLP5-mScarlet3 and aniline blue; white arrowheads indicate overlay between PDLP5-mScarlet3 and aniline blue, without CPR5-mCitrine. PDLP5-mScarlet3 in turquoise, CPR5-mCitrine in yellow, and aniline blue in magenta.

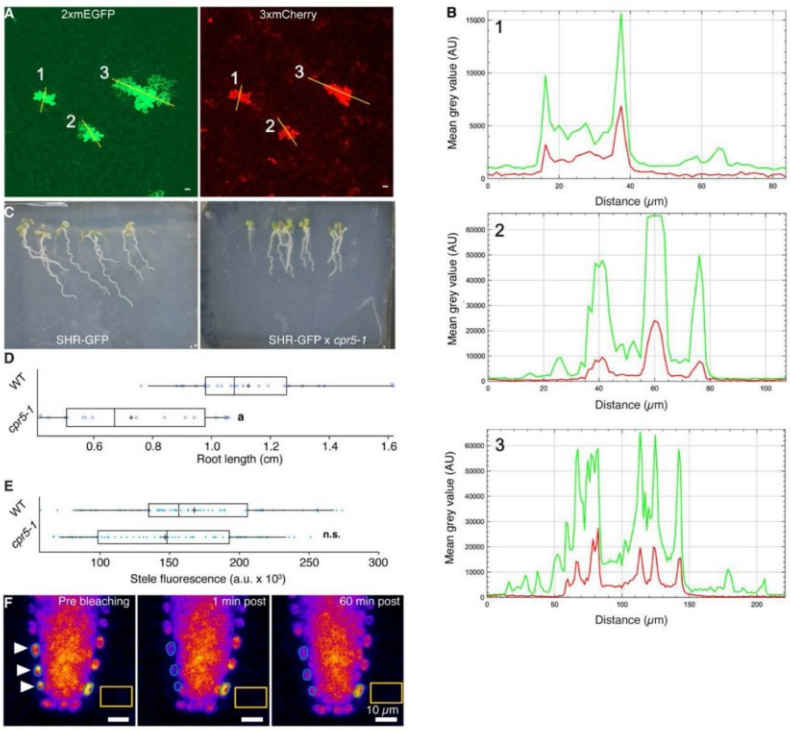


Figure 5-figure supplement 1.

Intercellular transport assays in *cpr5-1* mutants

(A), Example of three different clusters (1, 2, and 3) of fluorescent cells after bombardment in a WT Arabidopsis leaf. Each cluster reports a successful bombardment event. Left, GFP channel, right, mCherry channel. 24 h prior to the experiment, leaves were co-bombarded with gold particles coated with p35S:mEGFP-mEGFP (2xmEGFP). DNA plasmids and gold particles coated with p35S:mCherry-mCherry-mCherry (3xmCherry). **(B),** Profile plots across the different clusters, 1, 2, and 3 as shown in A. Yellow lines in A indicate the position for the profile. The bombarded cell marked with 3xmCherry overlays with the brightest cell in the GFP channel. **(C),** Six-day old seedlings with *shr*/pSHR:SHR-GFP in WT Col-0 background *(left)* and *shr*/pSHR:SHR-GFP in the *cpr5-1* background (*right*) grown on ½ MS agar. **(D),** Quantification of the root length of 6-day old WT and *cpr5-1* mutant background seedlings. $n_{(WT)}$ = 23 roots, four independent experiments, $n_{(cpr5\text{-}1)}$ = 16 roots, three independent experiments. **a** Significantly decreased root length in *cpr5-1* mutant, based on Student's *t*-test with $p = 0.00002$. **(E),** Quantification of SHR-GFP stele baseline fluorescence in *cpr5-1* mutant and WT background. $n_{(WT)}$ = 62 stele ROIs, $n_{(cpr5\text{-}1)}$ = 62 stele ROIs, with 3-4 ROIs analyzed per root. **n.s.,** no significant difference in fluorescence intensity based on Mann-Whitney U test with $p = 0.074$. **(F)**, SHR–GFP fluorescence recovery after photobleaching (FRAP) in homozygous *shr*/pSHR:SHR-GFP root endodermal cells (arrow heads). Note that for comparison, we here show the same sum projections as in **Figure 5F** (*top*). Blue circles show the position of ROIs for FRAP. Green circle shows the position of ROI for control nucleus used for normalization (see Methods). Yellow square shows the position for mean background fluorescence used for correction (see Methods).

Gene	max #FG in 200 aa window	Predicted function
Pp3c26_7720	28	NUP96
Pp3c3_17910	28	NUP 98.1
Pp3c3_28570	25	NUP 98.2
Pp3c26_7680	25	NUP 98.3
Pp3c8_3950	21	NUP 98.4
Pp3c15_14630	19	NUP62
Pp3c14_14130	17	NUP54.1
Pp3c17_4470	16	inter-alpha-trypsin inhibitor heavy chain-related
Pp3c24_6760	14	NUP58
Pp3c13_12950	14	NUP214
Pp3c10_15930	13	NUP54.2
Pp3c10_15937	13	NUP54.3
Pp3c7_12210	12	zinc finger (CCCH-type) family protein
Pp3c24_6760	11	NUP58
Pp3c13_24530	10	Epidermal growth factor receptor substrate 15-like 1

table S1.

Genome-wide search for potential phase-separating proteins with FG repeats

The 15 genes with the highest number of FG motifs within a 200-amino acid window in the *Physcomitrium* genome. For the list summarizing the genome-wide search for FG containing genes, see file S1. For Arabidopsis NUPs see file S2.

NUP	AGI	Localization at NPC	Tested for localization
NDC1	AT1G73240	membrane anchor	NA
Gp210	AT5G40480	membrane anchor	index = 1.77, *** = $2x10^{-9}$; # = $3x10^{-6}$**
CPR5	AT5G64930	membrane anchor	index = 1.48, *** = $7x10^{-8}$; # = 0.0001**
PNET1	AT1G07970	membrane anchor	NA
NUP155	AT1G14850	inner ring	index = 1.34, *** = 0.002**; # = 1.0
NUP93a	AT2G41620	inner ring	index = 1.38, *** = 0.001**; # = 1.0
NUP35/MPPN	AT3G16310	inner ring	index = 1.36, *** = 0.0002**; # = 0.549
NUP93b	AT3G57350	inner ring	index = 1.19, * = 0.43; # = 1.0
NUP188	AT4G38760	inner ring	NA
NUP205	AT5G51200	inner ring	NA
NUP160	AT1G33410	outer ring	NA
Seh1	AT1G64350	outer ring	NA
NUP96	AT1G80680	outer ring	NA
NUP133	AT2G05120	outer ring	NA
Sec13	AT2G30050	outer ring	NA
Elys/HOS1	AT2G39810	outer ring	index = 1.52, *** = $3x10^{-7}$; # = 0.001**
NUP107	AT3G14120	outer ring	NA
NUP43	AT4G30840	outer ring	index = 1.72, *** = $3x10^{-6}$; # = 0.006**
NUP75/85/SBB1	AT4G32910	outer ring	NA
NUP98a	AT1G10390	core FG-NUP	index = 1.38, *** = 0.006**; # = 1.0
NUP54	AT1G24310	core FG-NUP	NA
NUP98b	AT1G59660	core FG-NUP	index = 1.55, *** = 0.0001;** # = 0.276
NUP62	AT2G45000	core FG-NUP	index = 1.34, *** = 0.0001;** # = 0.357
NUP58	AT4G37130	core FG-NUP	index = 1.37, *** = 0.001;** # = 1.0
CG1	AT1G75340	cytoplasmic FG-NUP	NA
GLE1	AT1G13120	cytoplasmic NUP	NA
NUP214	AT1G55540	cytoplasmic FG-NUP	index = 1.29, *** = 0.041;** # = 1.0
Rae1	AT1G80670	cytoplasmic NUP	index = 1.22, * = 0.301; # = 1.0
Aladin	AT3G56900	cytoplasmic NUP	NA
MOS7/NUP88	AT5G05680	cytoplasmic NUP	NA
NUP50a	AT1G52380	basket FG-NUP	NA
NUA/TPR/ATTPR	AT1G79280	basket	NA
NUP1/NUP136	AT3G10650	basket FG-NUP	NA
NUP50b	AT3G15970	basket FG-NUP	index = 1.06, * = 1.0; # = 1.0
NUP82	AT5G20200	basket	index = 1.24, * = 0.1; # = 1.0

table S2.

List of known Arabidopsis NUPs and summary of localization results

p-values calculated from Bonferroni-corrected pairwise comparison between the tested NUP with propidium iodide marked by *; *p*-values calculated from Bonferroni-corrected pairwise comparison between the tested NUP and free mScarlet3 marked by #. Index is short for PD index (see also **Figure 2** and **3**). NA: not assessed. FG-NUPs in red.

table S4.

NPC components identified in published cell wall/PD proteomes

NUP	Reference
CPR5	(Kraner et al., 2017)
NUP93a	(Kirk et al., 2022)
NUP155	(Bayer et al., 2006; Fernandez-Calvino et al., 2011; Kraner et al., 2017)
SEC13	(Bayer et al., 2006; Gombos et al., 2023; Kraner et al., 2017)
NUP205	(Kirk et al., 2022)
NUA	(Gombos et al., 2023)
NUP50a *	(Gombos et al., 2023; Kraner et al., 2017; Li et al., 2024)
GP210	(Kraner et al., 2017)
NUP35	(Kraner et al., 2017)
HOS1	(Kraner et al., 2017)
NUP43	(Kraner et al., 2017)
NUP62	(Kraner et al., 2017)
NUP214	(Kraner et al., 2017)
NUP82	(Kraner et al., 2017)
NDC1 *	(Li et al., 2024)

* identified by TURBO-ID using PD proteins

table S5.

Nuclear localization and observation of puncta in the cell periphery, consistent with PD localization by other laboratories

NUP	Transient expression	Stable transformation/ promoter	Reference
CPR5	*p35S:YFP-CPR5*	*p35S:GFP-CPR5/cpr5-1*	(Gu et al., 2016)
CPR5*	*p35S:CFP-CPR5*		(Peng et al., 2022)
NUP98a	*p35S:GFP-Dra2-GFP*	*p35S:NtDra2-GFP*	(Gallemí et al., 2016)
NUP155	*p35S:Nup155-cYFP+p35S:nYFP-CPR5*		(Gu et al., 2016)
HOS1	*p35S:HOS1-GFP*		(Lee et al., 2012)
NUP62	*p35S:Nup62-nYFP+p35S:FLC-cYFP*		(Chen et al., 2023)

* split-FP analysis indicated interaction of CPR5 with PRL1 and FIP1

Organism/ location	# TM	Yeast	Mammalian	Chlamydomonas	Arabidopsis	*P. patens*	Ref.
NPC lumenal ring	1	POM152	GP210	n.p.	GP210	*Pp3c27_1470V3.1*	(Collins et al., 2023; Tamura et al., 2010)
NPC	1	POM121	POM121	n.p.	n.p.	n.p.	
NPC	6	NDC1	NDC1	*Cre03.g197550.t1.2*	NDC1	*Pp3c23_16320V3.1*	(Collins et al., 2023; Mansfeld et al., 2006)
NPC	3	POM33	TMEM33	*Cre02.g099650.t1.2*	*At3g02420*	*Pp3c7_9290V3.1*	this work
Ciliary gate	3	NPHP	TMEM218	*CEP290*	n.p.	n.p.	(Blasius et al., 2019; Craige et al., 2010; Epting et al., 2022; Li et al., 2016; Tang et al., 2020)
NPC	2	POM34	TMEM209	n.p.	PNET1 (*At1g07970*)	*Pp3c12_22070V3.1*	[48]
NPC green lineage	5	n.p.	n.p.	n.p.	CPR5	*Pp3c21_530V3.1* *Pp3c22_5670V3.1*	(Arra et al., 2024; Gu et al., 2016)

n.p. not present based on database searches

table S6.

Membrane/microtubule anchor proteins in NPC and ciliary gates across kingdoms

Protein name	Accession number	Species	Phylogeny	
ChabraCPR5.1	GBG69762.1	*Chara braunii*	Charophyta	Charophyceae
ChabraCPR5.2	GBG89669.1	*Chara braunii*	Charophyta	Charophyceae
ChlatCPR5	jgi|Chlat1|5100|Chrsp33S05109	*Chlorokybus atmophyticus*	Charophyta	Chlorokybophy-ceae
ClospCPR5.1	GJP55885.1	*Closterium*	Charophyta	Zygnemo-phyceae
ClospCPR5.2	GJP75531.1	*Closterium*	Charophyta	Zygnemo-phyceae
KlenitCPR5	GAQ84352.1	*Klebsormidium nitens*	Charophyta	Klebsormidio-phyceae
MesenCPR5	jgi|Mesen1|2959|ME000176S02004	*Mesotaenium endlicherianum SAG 12.97*	Charophyta	Zygnemo-phyceae
MeskraCPR5.1	jgi|Meskra657_3|1148962|CE1148961_11182	*Mesotaenium kramstae Lemmermann NIES-657 v3.0*	Charophyta	Zygnemo-phyceae
MeskraCPR5.2	jgi|Meskra657_3|1148923|CE1148922_14999	*Mesotaenium kramstae Lemmermann NIES-657 v3.0*	Charophyta	Zygnemo-phyceae
SpimuCPR5.1	jgi|Spimu1|7829|SM000018S03736	*Spirogloea muscicola CCAC 0214*	Charophyta	Spiroglo-eophycidae
SpimuCPR5.2	jgi|Spimu1|5703|SM000152S01566	*Spirogloea muscicola CCAC 0215*	Charophyta	Spiroglo-eophycidae
SpimuCPR5.3	jgi|Spimu1|9349|SM000020S05962	*Spirogloea muscicola CCAC 0216*	Charophyta	Spiroglo-eophycidae
BpraCPR5	BPRRCC1105_03G01860	*Bathycoccus prasinos*	Chlorophyta	Mamiello-phyceae
ChlodesCPR5.1	KAH7624053.1	*Chlorella desiccata (nom. nud.)*	Chlorophyta	Trebouxio-phyceae
ChlodesCPR5.2	KAG7670930.1	*Chlorella desiccata (nom. nud.)*	Chlorophyta	Trebouxio-phyceae
ChlosoroCPR5	PRW44950.1	*Chlorella sorokiniana*	Chlorophyta	Trebouxio-phyceae
ChlospCPR5	CNC64A_008G01100	*Chlorella sp NC64A*	Chlorophyta	Trebouxio-phyceae
ChlovarCPR5	XP_005848448.1	*Chlorella variabilis*	Chlorophyta	Trebouxio-phyceae
ChlovulCPR5	KAI3426217.1	*Chlorella vulgaris*	Chlorophyta	Trebouxio-phyceae
ChlpriCPR5	QDZ25445.1	*Chloropicon primus*	Chlorophyta	Chloropico-phyceae
CocsubCPR5	CV00G07110	*Coccomyxa sub-ellipsoidea C-169*	Chlorophyta	Trebouxio-phyceae
MicrocomCPR5	XP_002502434.1	*Micromonas commoda*	Chlorophyta	Mamiello-phyceae
MicropuCPR5	EuGene.0500010166|58433	*Micromonas pusilla strain CCMP1545*	Chlorophyta	Mamiello-phyceae
MicrospCPR5	M.spRCC299 v3.0|58433	*Micromonas sp or commoda RCC299 v3.0*	Chlorophyta	Mamiello-phyceae
OtCPR5	OT_02G03660	*Ostreococcus tauri*	Chlorophyta	Mamiello-phyceae
PispCPR5.1	KAI8111799.1	*Picochlorum*	Chlorophyta	Trebouxio-

table S7.

Accession numbers of CPR5 homologs used for the phylogenetic analysis shown in figure S6

		sp. BPE23		phyceae
PispCPR5.2	KAI8109780.1	*Picochlorum sp. BPE23*	Chlorophyta	Trebouxio-phyceae
MapolyCPR5.1	Mapoly0107s0002.1.p	*Marchantia polymorpha_320_v3.1*	Seedless non-tracheophyte	Marchantiopsida
MapolyCPR5.2	Mapoly0483s0001.1.p	*Marchantia polymorpha_320_v3.1*	Seedless non-tracheophyte	Marchantiopsida
MapolyCPR5.3	Mapoly0002s0001.1.p	*Marchantia polymorpha_320_v3.1*	Seedless non-tracheophyte	Marchantiopsida
PpCPR5.1	Pp3c21_530V3.1.p	*Physcomitrium patens_318_v3.3*	Seedless non-tracheophyte	Bryopsida
PpCPR5.2	Pp3c22_5670V3.1.p	*Physcomitrium patens_318_v3.3*	Seedless non-tracheophyte	Bryophyta
SphfalxCPR5	Sphfalx02G141400.1.p	*Sphagnum fallax v1.1*	Seedless non-tracheophyte	Bryophyta
DicomCPR5	Dicom.14G001200.1.p	*Diphasiastrum complanatum v3.1*	Seedless tracheophyte	Lycopodiopsida
CericCPR5	Ceric.38G046900.1.p	*Ceratopteris richardii v2.1*	Seedless tracheophyte	Polypodiopsida
AtriCPR5	ATR_00156G00170	*Amborella trichopoda*	Spermatophyta	Basal angiosperm
AtCPR5	AT5G64930	*Arabidopsis thaliana*	Spermatophyta	Dicot
BradiCPR5.1	Bradi3g57717.1.p	*Brachypodium distachyon v3.1*	Spermatophyta	Monocot
BradiCPR5.2	Bradi2g58840.1.p	*Brachypodium distachyon v3.1*	Spermatophyta	Monocot
CocitCPR5	Cocit.H3845.1.p	*Corymbia citriodora v2.1*	Spermatophyta	Dicot
GlymaCPR5	Glyma.06G145800.1.p	*Glycine max Wm82.a4.v1*	Spermatophyta	Dicot
GohirCPR5.1	Gohir.D03G045400.2.p	*Gossypium hirsutum v3.1*	Spermatophyta	Dicot
GohirCPR5.2	Gohir.A02G134000.1.p	*Gossypium hirsutum v3.1*	Spermatophyta	Dicot
HorvuCPR5.1	HORVU.MOREX.r3.6HG0618780.1	*Hordeum vulgare Morex V3*	Spermatophyta	Monocot
HorvuCPR5.2	HORVU.MOREX.r3.3HG0309890.1	*Hordeum vulgare Morex V3*	Spermatophyta	Monocot
ManesCPR5.1	Manes.13G077600.1.p	*Manihot esculenta v8.1*	Spermatophyta	Dicot
ManesCPR5.2	Manes.12G141400.1.p	*Manihot esculenta v8.1*	Spermatophyta	Dicot
NtCPR5.1	mRNA_71958	*Nicotiana tabacum K326*	Spermatophyta	Dicot
NtCPR5.2	mRNA_118909	*Nicotiana tabacum K326*	Spermatophyta	Dicot
OsCPR5.1	LOC_Os02g53070.1	*Oryza sativa_323_v7.0*	Spermatophyta	Monocot
OsCPR5.2	LOC_Os01g68970.1	*Oryza sativa_323_v7.0*	Spermatophyta	Monocot
PahalCPR5.2	Pahal.5G042600.1.p	*Panicum hallii v3.1*	Spermatophyta	Monocot
PahalCPR5.1	Pahal.1G413600.1.p	*Panicum hallii v3.2*	Spermatophyta	Monocot
PavirCPR5.1-1	Pavir.1KG111437.1.p	*Panicum virgatum v5.1*	Spermatophyta	Monocot
PavirCPR5.1-2	Pavir.1NG487400.1.p	*Panicum virgatum v5.1*	Spermatophyta	Monocot

table S7. (continued)

PavirCPR5.2-1	Pavir.5NG012660.1.p	*Panicum virgatum v5.1*	Spermatophyta	Monocot
PavirCPR5.2-2	Pavir.5KG720000.1.p	*Panicum virgatum v5.1*	Spermatophyta	Monocot
PtrifCPR5	Ptrif.0007s2410.1.p	*Poncirus trifoliata v1.3.1*	Spermatophyta	Dicot
PotriCPR5.1	Potri.005G083600.1.p	*Populus trichocarpa v4.1*	Spermatophyta	Dicot
PotriCPR5.2	Potri.007G082100.1.p	*Populus trichocarpa v4.1*	Spermatophyta	Dicot
SolycoCPR5	Solyc04g054170.4.1	*Solanum lycopersicum ITAG4.0*	Spermatophyta	Dicot
StrasiaCPR5.1	GER47577.1	*Striga_asiatica_ 008636005.1_SGA_v2.0*	Spermatophyta	Dicot
StrasiaCPR5.2	GER47578.1	*Striga_asiatica_ 008636005.1_SGA_v2.0*	Spermatophyta	Dicot
ThuplCPR5	Thupl.29379795s0007.1.p	*Thuja plicata v3.1*	Spermatophyta	Gymnosperm
VviCPR5	VIT_207s0031g01470.1	*Vitis vinifera v2.1*	Spermatophyta	Dicot
ZmayCPR5.1	Zm00001d052145_P001	*Zea mays RefGen_V4*	Spermatophyta	Monocot
ZmayCPR5.2	Zm00001d012040_P001	*Zea mays RefGen_V4*	Spermatophyta	Monocot
ZosmaCPR5	Zosma03g20130.1	*Zostera marina v3.1*	Spermatophyta	Monocot

table S7. (continued)

Primer	Sequence (5′-3′)	Description
NUP98a_Fw	TACAAAAAAGCAGGCTTCATGTTTGGCTCATCTAATCCTTTTGG	For localization
NUP98a_Rv	CAAGAAAGCTGGGTCAACTCCATCTTCTTCATCTTCGT	
NUP155_Fw	TACAAAAAAGCAGGCTTCAAGATGTCACAAGACGATGAG	
NUP155_Rv	CAAGAAAGCTGGGTCGAAGGAGAATGGACTTAAGAGAGACT	
NUP160_Fw	TACAAAAAAGCAGGCTTCATGGAGGAGAATCGTCGG	
NUP160_Rv	CAAGAAAGCTGGGTCACCGGTTGCAGAGGATACAG	
NUP50a_Fw	TACAAAAAAGCAGGCTTCATGGGTGACTCGGAAAACGT	
NUP50a_Rv	CAAGAAAGCTGGGTCAGTATCTGTAGCTGTTGGAGAGT	
NUP214_Fw	TACAAAAAAGCAGGCTTCAAGATGAGCAGAGTTGAGATTGAAG	
NUP214_Rv	CAAGAAAGCTGGGTCTTTTCTCATCTGTGTGAAGAGTTCC	
Rae1_Fw	TACAAAAAAGCAGGCTTCATGGCAACTTTTGGTGCGC	
Rae1_Rv	CAAGAAAGCTGGGTCTTTTCTGCCGGTTGCTCCAA	
Sec13_Fw	TACAAAAAAGCAGGCTTCAACATGCCAGGTCAGAAGATTGA	
Sec13_Rv	CAAGAAAGCTGGGTCAGGCTCAACAGCAGTAACTTGTTCC	
Elys/HOS1_Fw	TACAAAAAAGCAGGCTTCATGGATACGAGAGAAATCAACGGT	
Elys/HOS1_Rv	CAAGAAAGCTGGGTCTCTTGCTGCGAATCTACGTCT	
NUP93a_Fw	TACAAAAAAGCAGGCTTCATGGCGAACGACCAAGAGAT	
NUP93a_Rv	CAAGAAAGCTGGGTCAAAGCTTCGAGCCACCTTCTCG	
NUP62_Fw	TACAAAAAAGCAGGCTTCATGTCGGGGTTTCCATTTGGT	
NUP62_Rv	CAAGAAAGCTGGGTCAGACATCCAGTGCTTTGG	
NUP136_Fw	TACAAAAAAGCAGGCTTCCTAATGGCGAGCGCGGCAC	
NUP136_Rv	CAAGAAAGCTGGGTCTTTCTTCCTGGTGGATTTCTTTGC	
NUP107_Fw	TACAAAAAAGCAGGCTTCATGGATATGGATATGGACACTTCCC	
NUP107_Rv	CAAGAAAGCTGGGTCAGGTGATGAAAGTTCCTCTTGA	
NUP50b_Fw	TACAAAAAAGCAGGCTTCATGGGGGACTCCGATAATGC	
NUP50b_Rv	CAAGAAAGCTGGGTCCCTAGCATCTTCAGCACTCGGTGAG	
NUP35_Fw	TACAAAAAAGCAGGCTTCAAAATGAGTGCTGCAGCACACAGG	
NUP35_Rv	CAAGAAAGCTGGGTCAACACCGAACATCAAGTCAAAGA	
NUP93b_Fw	TACAAAAAAGCAGGCTTCATGGCGAACGACCAGGAG	
NUP93b_Rv	CAAGAAAGCTGGGTCAAAGCTTCGAGCTATCTTCTCG	
NUP43_Fw	TACAAAAAAGCAGGCTTCATGGAGATGATGCAGGATTCGT	
NUP43_Rv	CAAGAAAGCTGGGTCAGGCCTTGAGAAAACTGCTA	
NUP85_Fw	TACAAAAAAGCAGGCTTCAAAATGCCGGGTATGTCTTCGGA	
NUP85_Rv	CAAGAAAGCTGGGTCACATTCTTCGAGAAAAGCACGT	
NUP58_Fw	TACAAAAAAGCAGGCTTCATGTCGTTTTTTCCCCCAC	
NUP58_Rv	CAAGAAAGCTGGGTCTGTACGGCGTGTAGTTCGAGATTTT	
NUP82_Fw	TACAAAAAAGCAGGCTTCGAGTTCATGGCCACTCAAGGAGAAGC	
NUP82_Rv	CAAGAAAGCTGGGTCTGTCTTACAGCAGACACCGTCACTT	
Gp210_Fw	TACAAAAAAGCAGGCTTCATGGTTCCCGTCTCGTTCTG	
Gp210_Rv	CAAGAAAGCTGGGTCCATAGTGTTTTGAGGATTAAACC	
NUP205_Fw	TACAAAAAAGCAGGCTTCATGGTGTCGCCGAAAGATTT	
NUP205_Rv	CAAGAAAGCTGGGTCTACACACTTTTGGATGGCCA	
CPR5_Fw	TACAAAAAAGCAGGCTTCTTTAAGGCTATGGAAGCCCTCCTCC	
CPR5_Rv	CAAGAAAGCTGGGTCCTCGTCAGCATAGTCAGACCCACCA	
GGBmScarlet3F	AAAGGTCTCAAACAATGGACAGTACCGAAGCT	
GGBmScarlet3R	AAAGGTCTCAAGCCGGATCCCCCGGAGC	
PpNUP98.1_Fw	TGTACAAAAAAGCAGGCTTAATGTTTGGATCCAGCAGCCC	
PpNUP98.1_Rv	TGTACAAGAAAGCTGGGTAATCAAAATCCAGACCATATCCACTG	
2_Fw	AAAAAAGCAGGCTTAATGTCGGGCTTCACAGGATT	
PpNup62_Rv	AAGAAAGCTGGGTAGGCTCCACGCAAACGAGATC	
PpNup58_Fw	AAAAAAGCAGGCTTAATGGCGGGGATGTTCCAAAC	
PpNup58_Rv	AAGAAAGCTGGGTACTTTCGACGTGTGCCAC	
PpNup35.1_Fw	TACAAAAAAGCAGGCTTCATGAGTACCCCAGGCGCG	
PpNup35.1_Rv	CAAGAAAGCTGGGTCCATACCAAATACAAAATCCACAAATT	

table S8.

Primers used in this study

PDLP5_SIM_Fw	TTTGGTCTCAGGCTCTATGATCAAGACAAAGACGACG	**For SIM**
PDLP5_SIM_Rv	TTTGGTCTCACTGATTTACACCATTTCTCATCTGCA	
CPR5_SIM_Fw	TTTGGTCTCAGGCTCTATGGAAGCCCTCCTCCTC	
CPR5_SIM_Fw	TTTGGTCTCACTGAAGCATAGTCAGACCCACC	
GGDmScarlet3F	AAAGGTCTCATCAGGTATGGACAGTACCGAAGCT	
GGDmScarlet3R	AAAGGTCTCAGCAGGGATCCCCCGGAGC	
CPR5_Topol_Rv	GGGGACCACTTTGTACAAGAAAGCTGGGTATCAAGCATAGTCAGACCCACC	**For CPR5 topology**
mEGFP_Fw	GGGGACAAGTTTGTACAAAAAAGCAGGCTTCACCATGGTGAGCAAGGGCGAGG	**For microparticle bombardment**
mEGFP_Rv	GGGGACCACTTTGTACAAGAAAGCTGGGTGTTACTTGTACAGCTCGTCCATGCC	
2xmEGFP_Fw	GGGGACAAGTTTGTACAAAAAAGCAGGCTTCACCATGGTTTCTAAGGGTGAGG	
2xmEGFP_Rv	GGGGACCACTTTGTACAAGAAAGCTGGGTGTTACTTGTACAGCTCGTCCATGCC	
NUP62_F	GCTTTTTCTATTGAGGTTCAAACTTGTAAGC	**For transgenic line expressing NUP62-GFP**
NUP62_R	CCGGTCAAGAGAAATATAATAATCTCTG	
NUP62_U1	AGACATCCAGTGCTTTGGAGCC	
NUP62_D1	TGATAAGAATTACAAAAACCACATAATCTC	
NUP62GFP_HiFiF	AAGCACTGGATGTCTGGTGGAGGCGGTTCAGGCGGAGGTGG	
NUP62GFP_HiFiR	TTGTAATTCTTATCACTTGTACAGCTCGTCCATGCCGTG	

table S8. (continued)

Acknowledgements

We would like to dedicate this manuscript to the 'champion of plasmodesmata', William J. (Bill) Lucas (UC Davis). We thank Madlen Somsich (HHU) for project coordination and management. This work has received funding from the European Research Council (ERC) and the Marie Skłodowska-Curie Actions under the European Union's Horizon 2020 research and innovation program (Grant agreements 'SymPore' No. 951292 to WBF and "PDgate" No. 101023981 to MM, respectively). ARE was supported in part by funds from the Interdisciplinary Graduate and Research Academy (iGRAD) Düsseldorf (Deutsche Forschungsgemeinschaft (DFG, German Research Foundation), DFG, project ID 391465903/GRK 2466). Research was also supported by the Deutsche Forschungsgemeinschaft (DFG, German Research Foundation) under Germanýs Excellence Strategy – EXC-2048/1 – project ID 390686111, and the Alexander von Humboldt Professorship, to WBF.

Additional information

Contributions

WBF conceived of the study. J.E. performed the bioinformatic analyses; L.X., S.G. and W.S. performed proteomics and data analysis; M.D. analyzed the structure and generated **Figure 2-figure supplement 1**; S.H. helped to establish and advised on SIM. T.M.S, M.P., M.M., J.O.E., N.P., M.N., G.V.D, C.G. and A.D. performed imaging and/or transport studies; R.S. advised on imaging and data analyses; M.M. and A.R-E. performed split GFP studies, T.M.S, M.M., M.P., J.O.E., B.S., and W.B.F. analyzed the data; T.M.S., M.M., M.P., J.O.E., G.V.D, R.S. and W.B.F. wrote the manuscript.

Funding

Alexander von Humboldt Foundation (AvH Professorship to WBF)

European Research Council

https://doi.org/10.3030/951292

Marie Skłodowska-Curie Action

European Union

https://doi.org/10.3030/101023981

Deutsche Forschungsgemeinschaft (391465903/GRK 2466)

Deutsche Forschungsgemeinschaft (EXC-2048/1 – project ID 390686111)

References

Alazem M, Nuzzi SN, Burch-Smith TM (2025) **Viral Movement Proteins and Plasmodesmata: turning gatekeepers into gateways** *J Exp Bot eraf* **184** https://doi.org/10.1093/jxb/eraf184 | Google Scholar

Apelt L, Knockenhauer KE, Leksa NC, Benlasfer N, Schwartz TU, Stelzl U (2016) **Systematic protein– protein interaction analysis reveals intersubcomplex contacts in the Nuclear Pore Complex** *Mol Cell Proteomics MCP* **15**:2594–2606 https://doi.org/10.1074/mcp.M115.054627 | Google Scholar

Arra Y, Auguy F, Stiebner M, Chéron S, Wudick MM, Miras M, Schepler-Luu V, Köhler S, Cunnac S, Frommer WB, Albar L (2024) **Rice Yellow Mottle Virus resistance by genome editing of the Oryza sativa L. ssp. japonica nucleoporin gene OsCPR5.1 but not OsCPR5.2** *Plant Biotechnol J* **22**:1299–1311 https://doi.org/10.1111/pbi.14266 | Google Scholar

Ascencio-Ibanez JT, Sozzani R, Lee TJ, Chu TM, Wolfinger RD, Cella R, Hanley-Bowdoin L (2008) **Global analysis of Arabidopsis gene expression uncovers a complex array of changes impacting pathogen response and cell cycle during geminivirus infection** *Plant Physiol* **148**:436–54 https://doi.org/10.1104/pp.108.121038 | Google Scholar

Bayer EM, Bottrill AR, Walshaw J, Vigouroux M, Naldrett MJ, Thomas CL, Maule AJ (2006) **Arabidopsis cell wall proteome defined using multidimensional protein identification technology** *Proteomics* **6**:301–311 https://doi.org/10.1002/pmic.200500046 | Google Scholar

Blasius TL, Takao D, Verhey KJ (2019) **NPHP proteins are binding partners of nucleoporins at the base of the primary cilium** *PLOS One* **14**:e0222924 https://doi.org/10.1371/journal.pone.0222924 | Google Scholar

Bleckmann A, Weidtkamp-Peters S, Seidel CA, Simon R (2010) **Stem cell signaling in Arabidopsis requires CRN to localize CLV2 to the plasma membrane** *Plant Physiol* **152**:166–76 https://doi.org/10.1104/pp.109.149930 | Google Scholar

Bowling SA, Clarke JD, Liu Y, Klessig DF, Dong X (1997) **The cpr5 mutant of Arabidopsis expresses both NPR1-dependent and NPR1-independent resistance** *Plant Cell* **9**:1573–84 Google Scholar

Bowling SA, Guo A, Cao H, Gordon AS, Klessig DF, Dong X (1994) **A mutation in Arabidopsis that leads to constitutive expression of systemic acquired resistance** *Plant Cell* **6**:1845–5187 Google Scholar

Brault ML, Petit JD, Immel F, Nicolas WJ, Glavier M, Brocard L, Gaston A, Fouché M, Hawkins TJ, Crowet J-M, Grison MS, Germain V, Rocher M, Kraner M, Alva V, Claverol S, Paterlini A, Helariutta Y, Deleu M, Lins L, Tilsner J, Bayer EM (2019) **Multiple C2 domains and transmembrane region proteins (MCTPs) tether membranes at plasmodesmata** *EMBO Rep* **20**:e47182 https://doi.org/10.15252/embr.201847182 | Google Scholar

Campbell R, Cowan G, Wurzinger B, Ducreux LJM, Dessoly J, Guo W, Zhang R, Morris JA, Hedley P, Wahl V, Taylor MA, Hancock RD (2025) **GERMIN3 regulates tuber initiation and axillary**

bud activation by facilitating plasmodesmatal gating *Plant J* **122**:e70186 https://doi.org/10.1111/tpj.70186 | Google Scholar

Chen C-C, Fu S-F, Lee Y-I, Lin C-Y, Lin W-C, Huang H-J (2012) **Transcriptome analysis of age-related gain of callus-forming Capacity in Arabidopsis hypocotyls** *Plant Cell Physiol* **53**:1457–1469 https://doi.org/10.1093/pcp/pcs090 | Google Scholar

Chen G, Xu D, Liu Q, Yue Z, Dai B, Pan S, Chen Y, Feng X, Hu H (2023) **Regulation of FLC nuclear import by coordinated action of the NUP62-subcomplex and importin β SAD2** *J Integr Plant Biol* **65**:2086–2106 https://doi.org/10.1111/jipb.13540 | Google Scholar

Chopra K, Bawaria S, Chauhan R (2019) **Evolutionary divergence of the nuclear pore complex from fungi to metazoans** *Protein Sci* **28**:571–586 https://doi.org/10.1002/pro.3558 | Google Scholar

Collins PP, Broad RC, Yogeeswaran K, Varsani A, Poole AM, Collings DA (2023) **Characterisation of the trans-membrane nucleoporins GP210 and NDC1 in Arabidopsis thaliana** *Plant Sci* **332**:111719 https://doi.org/10.1016/j.plantsci.2023.111719 | Google Scholar

Craige B, Tsao C-C, Diener DR, Hou Y, Lechtreck K-F, Rosenbaum JL, Witman GB (2010) **CEP290 tethers flagellar transition zone microtubules to the membrane and regulates flagellar protein content** *J Cell Biol* **190**:927–940 https://doi.org/10.1083/jcb.201006105 | Google Scholar

Crawford KM, Zambryski PC (2001) **Non-targeted and targeted protein movement through plasmodesmata in leaves in different developmental and physiological states** *Plant Physiol* **125**:1802–1812 Google Scholar

Crawford KM, Zambryski PC (2000) **Subcellular localization determines the availability of non-targeted proteins to plasmodesmatal transport** *Curr Biol* **10**:1032–1040 https://doi.org/10.1016/S0960-9822(00)00657-6 | Google Scholar

Cui H, Levesque MP, Vernoux T, Jung JW, Paquette AJ, Gallagher KL, Wang JY, Blilou I, Scheres B, Benfey PN (2007) **An evolutionarily conserved mechanism delimiting SHR movement defines a single layer of endodermis in plants** *Science* **316**:421–5 https://doi.org/10.1126/science.1139531 | Google Scholar

del Viso F, Huang F, Myers J, Chalfant M, Zhang Y, Reza N, Bewersdorf J, Lusk CP, Khokha MK (2016) **Congenital heart disease genetics uncovers context-dependent organization and function of nucleoporins at cilia** *Dev Cell* **38**:478–492 https://doi.org/10.1016/j.devcel.2016.08.002 | Google Scholar

Deutsch EW, Bandeira N, Sharma V, Perez-Riverol Y, Carver JJ, Kundu DJ, García-Seisdedos D, Jarnuczak AF, Hewapathirana S, Pullman BS, Wertz J, Sun Z, Kawano S, Okuda S, Watanabe Y, Hermjakob H, MacLean B, MacCoss MJ, Zhu Y, Ishihama Y, Vizcaíno JA (2020) **The ProteomeXchange consortium in 2020: enabling "big data" approaches in proteomics** *Nucleic Acids Res* **48**:D1145–D1152 https://doi.org/10.1093/nar/gkz984 | Google Scholar

Dickmanns M, Pöge M, Xu P, Gombos S, Miras M, Plitzko JM, Simon R, Schulze WX, Frommer WB, Baumeister W (2025) **In situ architecture of plasmodesmata suggests mechanisms controlling intercellular exchange** *bioRxiv* Google Scholar

Dyachok J, Yoo C-M, Palanichelvam K, Blancaflor EB (2010) **Sample preparation for fluorescence imaging of the cytoskeleton in fixed and living plant roots** In: Gavin RH,

editors. *Cytoskeleton Methods and Protocols, Methods in Molecular Biology*Totowa, NJ: Humana Press pp. 157–169 https://doi.org/10.1007/978-1-60761-376-3_8 | Google Scholar

Ejike JO, Davis GV, Restrepo-Escobar A, Dalal A, Nakamura M, Frommer WB, Schladt TM (2025) **The role of phase separation for RNA and protein transport through the nuclear pore complex** *J Exp Bot eraf* **271** https://doi.org/10.1093/jxb/eraf271 | Google Scholar

Epting D, Decker E, Ott E, Eisenberger T, Bader I, Bachmann N, Bergmann C (2022) **The ciliary transition zone protein TMEM218 synergistically interacts with the NPHP module and its reduced dosage leads to a wide range of syndromic ciliopathies** *Hum Mol Genet* **31**:2295–2306 https://doi.org/10.1093/hmg/ddac027 | Google Scholar

Faulkner C, Akman OE, Bell K, Jeffree C, Oparka K (2008) **Peeking into pit fields: a multiple twinning model of secondary plasmodesmata formation in tobacco** *Plant Cell* **20**:1504–1518 https://doi.org/10.1105/tpc.107.056903 | Google Scholar

Faulkner C, Bayer EM (2017) **Isolation of plasmodesmata** *Methods Mol Biol* **1511**:187–198 https://doi.org/10.1007/978-1-4939-6533-5_15 | Google Scholar

Faulkner C, Petutschnig E, Benitez-Alfonso Y, Beck M, Robatzek S, Lipka V, Maule AJ (2013) **LYM2-dependent chitin perception limits molecular flux via plasmodesmata** *Proc Natl Acad Sci* **110**:9166–9170 https://doi.org/10.1073/pnas.1203458110 | Google Scholar

Fernandez-Calvino L, Faulkner C, Walshaw J, Saalbach G, Bayer EM, Benitez-Alfonso Y, Maule AJ (2011) **Arabidopsis plasmodesmal proteome** *PloS One* **6**:e18880 https://doi.org/10.1371/journal.pone.0018880 | Google Scholar

Fitzgibbon J, Bell K, King E, Oparka K (2010) **Super-resolution imaging of plasmodesmata using three-dimensional structured illumination microscopy** *Plant Physiol* **153**:1453–63 https://doi.org/10.1104/pp.110.157941 | Google Scholar

Frey S, Rees R, Schünemann J, Ng SC, Fünfgeld K, Huyton T, Görlich D (2018) **Surface properties determining passage rates of proteins through nuclear pores** *Cell* **174**:202–217 https://doi.org/10.1016/j.cell.2018.05.045 | Google Scholar

Gadella TWJ, van Weeren L, Stouthamer J, Hink MA, Wolters AHG, Giepmans BNG, Aumonier S, Dupuy J, Royant A. (2023) **mScarlet3: a brilliant and fast-maturing red fluorescent protein** *Nat Methods* **20**:541–545 https://doi.org/10.1038/s41592-023-01809-y | Google Scholar

Gallemí M, Galstyan A, Paulišić S, Then C, Ferrández-Ayela A, Lorenzo-Orts L, Roig-Villanova I, Wang X, Micol JL, Ponce MR, Devlin PF, Martínez-García JF (2016) **DRACULA2 is a dynamic nucleoporin with a role in regulating the shade avoidance syndrome in Arabidopsis** *Development* **143**:1623–1631 https://doi.org/10.1242/dev.130211 | Google Scholar

Giordano F, Saheki Y, Idevall-Hagren O, Colombo SF, Pirruccello M, Milosevic I, Gracheva EO, Bagriantsev SN, Borgese N, De Camilli P. (2013) **PI(4,5)P2-dependent and Ca2+-regulated ER-PM interactions mediated by the extended synaptotagmins** *Cell* **153**:1494–1509 https://doi.org/10.1016/j.cell.2013.05.026 | Google Scholar

Gombos S, Miras M, Howe V, Xi L, Pottier M, Kazemein Jasemi NS, Schladt M, Ejike JO, Neumann U, Hänsch S, Kuttig F, Zhang Z, Dickmanns M, Xu P, Stefan T, Baumeister W, Frommer WB, Simon R, Schulze WX (2023) **A high-confidence Physcomitrium patens plasmodesmata proteome by iterative scoring and validation reveals diversification of cell wall proteins during evolution** *New Phytol* **238**:637–653 https://doi.org/10.1111/nph.18730 | Google Scholar

Grison MS, Kirk P, Brault ML, Wu XN, Schulze WX, Benitez-Alfonso Y, Immel F, Bayer EM (2019) **Plasma membrane-associated receptor-like kinases relocalize to plasmodesmata in response to osmotic stress** *Plant Physiol* **181**:142–160 https://doi.org/10.1104/pp.19.00473 | Google Scholar

Gu Y, Zebell SG, Liang Z, Wang S, Kang B-H, Dong X (2016) **Nuclear pore permeabilization is a convergent signaling event in effector-triggered immunity** *Cell* **166**:1526–1538 https://doi.org/10.1016/j.cell.2016.07.042 | Google Scholar

He M, Wang J, Herold S, Xi L, Schulze WX (2022) **A rapid and universal workflow for label-free-quantitation-based proteomic and phosphoproteomic studies in cereals** *Curr Protoc* **2**:e425 https://doi.org/10.1002/cpz1.425 | Google Scholar

Hodel AE, Hodel MR, Griffis ER, Hennig KA, Ratner GA, Xu S, Powers MA (2002) **The three-dimensional structure of the autoproteolytic, nuclear pore-targeting domain of the human nucleoporin Nup98** *Mol Cell* **10**:347–358 https://doi.org/10.1016/S1097-2765(02)00589-0 | Google Scholar

Hoogenboom BW, Hough LE, Lemke EA, Lim RYH, Onck PR, Zilman A (2021) **Physics of the nuclear pore complex: Theory, modeling and experiment** *Phys Rep* **921**:1–53 https://doi.org/10.1016/j.physrep.2021.03.003 | Google Scholar

Howell AH, Christensen AH, James V, Vasina VV, Jensen KH, Foley J, Evans JE, Stone HA, Peters WS, Knoblauch M (2024) **Electric charge controls plasmodesma conductivity** *bioRxiv* https://doi.org/10.1101/2024.04.02.587779 | Google Scholar

Huang C, Mutterer J, Heinlein M (2022) **In vivo aniline blue staining and semiautomated quantification of callose deposition at plasmodesmata In: Benitez-Alfonso Y, Heinlein M, editors. Plasmodesmata: Methods and Protocols, Methods in Molecular Biology. New York** *NY: Springer US* :151–165 https://doi.org/10.1007/978-1-0716-2132-5_9 | Google Scholar

Hughes CS, Moggridge S, Müller T, Sorensen PH, Morin GB, Krijgsveld J (2019) **Single-pot, solid-phase-enhanced sample preparation for proteomics experiments** *Nat Protoc* **14**:68–85 https://doi.org/10.1038/s41596-018-0082-x | Google Scholar

Johnson CA, Malicki JJ (2019) **The nuclear arsenal of cilia** *Dev Cell* **49**:161–170 https://doi.org/10.1016/j.devcel.2019.03.009 | Google Scholar

Johnston MG, Breakspear A, Samwald S, Zhang D, Papp D, Faulkner C, de Keijzer J. (2023) **Comparative phyloproteomics identifies conserved plasmodesmal proteins** *J Exp Bot* **74**:1821–1835 https://doi.org/10.1093/jxb/erad022 | Google Scholar

Jones DT, Taylor WR, Thornton JM (1992) **The rapid generation of mutation data matrices from protein sequences** *Bioinformatics* **8**:275–282 https://doi.org/10.1093/bioinformatics/8.3.275 | Google Scholar

Jumper J, Evans R, Pritzel A, Green T, Figurnov M, Ronneberger O, Tunyasuvunakool K, Bates R, Žídek A, Potapenko A, Bridgland A, Meyer C, Kohl SAA, Ballard AJ, Cowie A, Romera-Paredes B, Nikolov S, Jain R, Adler J, Back T, Petersen S, Reiman D, Clancy E, Zielinski M, Steinegger M, Pacholska M, Berghammer T, Bodenstein S, Silver D, Vinyals O, Senior AW, Kavukcuoglu K, Kohli P, Hassabis D. (2021) **Highly accurate protein structure prediction with AlphaFold** *Nature* **596**:583–589 https://doi.org/10.1038/s41586-021-03819-2 | Google Scholar

Kehlenbach RH, Neumann P, Ficner R, Dickmanns A (2023) **Interaction of nucleoporins with nuclear transport receptors: a structural perspective** *Biol Chem* **404**:791–805 https://doi.org/10.1515/hsz-2023-0155 | Google Scholar

Kessel RG (1992) **Annulate lamellae: a last frontier in cellular organelles** In: Jeon KW, Friedlander M, editors. *Int. Rev. Cytol.* Academic Press pp. 43–120 https://doi.org/10.1016/S0074-7696(08)61858-6 | Google Scholar

Kirk P, Amsbury S, German L, Gaudioso-Pedraza R, Benitez-Alfonso Y (2022) **A comparative meta-proteomic pipeline for the identification of plasmodesmata proteins and regulatory conditions in diverse plant species** *BMC Biol* **20**:128 https://doi.org/10.1186/s12915-022-01331-1 | Google Scholar

Kohler A, Schwindling S, Conrath U (2002) **Benzothiadiazole-induced priming for potentiated responses to pathogen infection, wounding, and infiltration of water into leaves requires the NPR1/NIM1 gene in Arabidopsis** *Plant Physiol* **128**:1046–1056 https://doi.org/10.1104/pp.010744 | Google Scholar

Koizumi K, Hayashi T, Wu S, Gallagher KL (2012) **The SHORT-ROOT protein acts as a mobile, dose-dependent signal in patterning the ground tissue** *Proc Natl Acad Sci U S A* **109**:13010–13015 https://doi.org/10.1073/pnas.1205579109 | Google Scholar

Kragler F, Monzer J, Shash K, Xoconostle-Cázares B, Lucas WJ (1998) **Cell-to-cell transport of proteins: Requirement for unfolding and characterization of binding to a putative plasmodesmal receptor** *Plant J* **15**:367–381 https://doi.org/10.1046/j.1365-313X.1998.00219.x | Google Scholar

Kraner ME, Müller C, Sonnewald U (2017) **Comparative proteomic profiling of the choline transporter-like1 (CHER1) mutant provides insights into plasmodesmata composition of fully developed Arabidopsis thaliana leaves** *Plant J Cell Mol Biol* **92**:696–709 https://doi.org/10.1111/tpj.13702 | Google Scholar

Lampropoulos A, Sutikovic Z, Wenzl C, Maegele I, Lohmann JU, Forner J (2013) **GreenGate - a novel, versatile, and efficient cloning system for plant transgenesis** *PLOS One* **8**:e83043 https://doi.org/10.1371/journal.pone.0083043 | Google Scholar

Lee H, Xiong L, Gong Z, Ishitani M, Stevenson B, Zhu J-K (2001) **The Arabidopsis HOS1 gene negatively regulates cold signal transduction and encodes a RING finger protein that displays cold-regulated nucleo–cytoplasmic partitioning** *Genes Dev* **15**:912–924 https://doi.org/10.1101/gad.866801 | Google Scholar

Lee JH, Kim JJ, Kim SH, Cho HJ, Kim J, Ahn JH (2012) **The E3 ubiquitin ligase HOS1 regulates low ambient temperature-responsive flowering in Arabidopsis thaliana** *Plant Cell Physiol* **53**:1802–1814 https://doi.org/10.1093/pcp/pcs123 | Google Scholar

Lee J-Y, Wang X, Cui W, Sager R, Modla S, Czymmek K, Zybaliov B, van Wijk K, Zhang C, Lu H, Lakshmanan V. (2011) **A plasmodesmata-localized protein mediates crosstalk between cell-to-cell communication and innate immunity in Arabidopsis** *Plant Cell* **23**:3353–3373 https://doi.org/10.1105/tpc.111.087742 | Google Scholar

Lee JY, Yoo BC, Lucas WJ (2000) **Parallels between nuclear-pore and plasmodesmal trafficking of information molecules** *Planta* **210**:177–187 Google Scholar

Lee J-Y, Yoo B-C, Rojas MR, Gomez-Ospina N, Staehelin LA, Lucas WJ (2003) **Selective trafficking of non-cell-autonomous proteins mediated by NtNCAPP1** *Science* **299**:392–396 https://doi.org/10.1126/science.1077813 | Google Scholar

Li C, Jensen VL, Park K, Kennedy J, Garcia-Gonzalo FR, Romani M, Mori RD, Bruel A-L, Gaillard D, Doray B, Lopez E, Rivière J-B, Faivre L, Thauvin-Robinet C, Reiter JF, Blacque OE, Valente EM, Leroux MR (2016) **MKS5 and CEP290 dependent assembly pathway of the ciliary transition zone** *PLOS Biol* **14**:e1002416 https://doi.org/10.1371/journal.pbio.1002416 | Google Scholar

Li Z, Liu S-L, Montes-Serey C, Walley JW, Aung K (2024) **PLASMODESMATA-LOCATED PROTEIN 6 regulates plasmodesmal function in Arabidopsis vasculature** *Plant Cell* **36**:3543–3561 https://doi.org/10.1093/plcell/koae166 | Google Scholar

Lin DH, Hoelz A (2019) **The structure of the nuclear pore complex (an update)** *Annu Rev Biochem* **88**:725–783 https://doi.org/10.1146/annurev-biochem-062917-011901 | Google Scholar

Lu H, Ge P, Ma Y, Lin F, Jing D, Zhou T, Cui F (2025) **Loss-of-function of two PD-associated proteins confers resistance to rice stripe virus** *Mol Plant Pathol* **26**:e70121 https://doi.org/10.1111/mpp.70121 | Google Scholar

Ma M, Li M, Zhou R, Yu J-B, Wu Y, Zhang X, Wang J, Zhou J-M, Liang X (2023) **CPR5 positively regulates pattern-triggered immunity via a mediator protein** *J Integr Plant Biol* **65**:1613–1619 https://doi.org/10.1111/jipb.13472 | Google Scholar

Makarov AA, Padilla-Mejia NE, Field MC (2021) **Evolution and diversification of the nuclear pore complex** *Biochem Soc Trans* **49**:1601–1619 https://doi.org/10.1042/BST20200570 | Google Scholar

Mansfeld J, Güttinger S, Hawryluk-Gara LA, Panté N, Mall M, Galy V, Haselmann U, Mühlhäusser P, Wozniak RW, Mattaj IW, Kutay U, Antonin W (2006) **The conserved transmembrane nucleoporin NDC1 is required for nuclear pore complex assembly in vertebrate cells** *Mol Cell* **22**:93–103 https://doi.org/10.1016/j.molcel.2006.02.015 | Google Scholar

Miyashima S, Koi S, Hashimoto T, Nakajima K (2011) **Non-cell-autonomous microRNA165 acts in a dose-dependent manner to regulate multiple differentiation status in the Arabidopsis root** *Development* **138**:2303–2313 https://doi.org/10.1242/dev.060491 | Google Scholar

Mosalaganti S, Obarska-Kosinska A, Siggel M, Taniguchi R, Turoňová B, Zimmerli CE, Buczak K, Schmidt FH, Margiotta E, Mackmull M-T, Hagen WJH, Hummer G, Kosinski J, Beck M (2022) **AI-based structure prediction empowers integrative structural analysis of human nuclear pores** *Science* **376**:eabm9506 https://doi.org/10.1126/science.abm9506 | Google Scholar

Nakajima K, Sena G, Nawy T, Benfey PN (2001) **Intercellular movement of the putative transcription factor SHR in root patterning** *Nature* **413**:307–311 https://doi.org/10.1038/35095061 | Google Scholar

Narsai R, Law SR, Carrie C, Xu L, Whelan J (2011) **In-depth temporal transcriptome profiling reveals a crucial developmental switch with roles for RNA processing and organelle metabolism that are essential for germination in Arabidopsis** *Plant Physiol* **157**:1342–1362 https://doi.org/10.1104/pp.111.183129 | Google Scholar

Ng SC, Biswas A, Huyton T, Schünemann J, Reber S, Görlich D (2023) **Barrier properties of NUP98 FG phases ruled by FG motif identity and inter-FG spacer length** *Nat Commun* **14**:747–747 https://doi.org/10.1038/s41467-023-36331-4 | Google Scholar

Ng SC, Güttler T, Görlich D (2021) **Recapitulation of selective nuclear import and export with a perfectly repeated 12mer GLFG peptide** *Nat Commun* **12**:4047 https://doi.org/10.1038/s41467-021-24292-5 | Google Scholar

Nicolas WJ, Grison MS, Trépout S, Gaston A, Fouché M, Cordelières FP, Oparka KJ, Tilsner J, Brocard L, Bayer EM (2017) **Architecture and permeability of post-cytokinesis plasmodesmata lacking cytoplasmic sleeves** *Nat Plants* **3**:17082 https://doi.org/10.1038/nplants.2017.82 | Google Scholar

Okuma E, Nozawa R, Murata Y, Miura K (2014) **Accumulation of endogenous salicylic acid confers drought tolerance to Arabidopsis** *Plant Signal Behav* **9**:e28085 https://doi.org/10.4161/psb.28085 | Google Scholar

Otero S, Helariutta Y, Benitez-Alfonso Y (2016) **Symplastic communication in organ formation and tissue patterning** *Curr Opin Plant Biol* **29**:21–28 https://doi.org/10.1016/j.pbi.2015.10.007 | Google Scholar

Paultre DSG, Gustin M-P, Molnar A, Oparka KJ (2016) **Lost in transit: long-distance trafficking and phloem unloading of protein signals in Arabidopsis homografts** *Plant Cell* **28**:2016–2025 https://doi.org/10.1105/tpc.16.00249 | Google Scholar

Pendle A, Benitez-Alfonso Y (2015) **Immunofluorescence detection of callose deposition around plasmodesmata sites** *Methods Mol Biol Clifton NJ* **1217**:95–104 https://doi.org/10.1007/978-1-4939-1523-1_6 | Google Scholar

Peng S, Guo D, Guo Y, Zhao H, Mei J, Han Y, Guan R, Wang T, Song T, Sun K, Liu Y, Mao T, Chang H, Xue J, Cai Y, Chen D, Wang S (2022) **CONSTITUTIVE EXPRESSER of PATHOGENESIS-RELATED GENES 5 is an RNA-binding protein controlling plant immunity via an RNA processing complex** *Plant Cell* **34**:1724–1744 https://doi.org/10.1093/plcell/koac037 | Google Scholar

Penzo A, Palancade B (2023) **Puzzling out nuclear pore complex assembly** *FEBS Lett* **597**:2705–2727 https://doi.org/10.1002/1873-3468.14713 | Google Scholar

Pletan M, Wang E, Gohmann L, Tsai B (2025) **An ER-associated structure sequesters misassembled FG-rich nucleoporins to help maintain nuclear pore complex function** *J Cell Sci* **138**:jcs263659 https://doi.org/10.1242/jcs.263659 | Google Scholar

Pöge M, Dickmanns M, Xu P, Li M, Schiøtz OH, Kaiser CO, Ma J, Bieber A, Capitanio C, Brenner J, Riggi M, Klumpe S, Miras M, Jasemi NSK, Schulze WX, Simon R, Frommer WB, Plitzko JM, Baumeister W (2025) **Making plant tissue accessible for cryo-electron tomography** *eLife* **14** https://doi.org/10.7554/eLife.106455.1 | Google Scholar

Qu F, Morris TJ (2002) **Efficient infection of Nicotiana benthamiana by tomato bushy stunt virus Is facilitated by the coat protein and maintained by p19 through suppression of gene silencing** *Mol Plant-Microbe Interactions®* **15**:193–202 https://doi.org/10.1094/MPMI.2002.15.3.193 | Google Scholar

Rappsilber J, Ishihama Y, Mann M (2003) **Stop and go extraction tips for matrix-assisted laser desorption/ionization, nanoelectrospray, and LC/MS sample pretreatment in proteomics** *Anal Chem* **75**:663–670 https://doi.org/10.1021/ac026117i | Google Scholar

Ross-Elliott TJ, Jensen KH, Haaning KS, Wager BM, Knoblauch J, Howell AH, Mullendore DL, Monteith AG, Paultre D, Yan D, Otero S, Bourdon M, Sager R, Lee J-Y, Helariutta Y, Knoblauch M, Oparka KJ (2017) **Phloem unloading in Arabidopsis roots is convective and regulated by the phloem-pole pericycle** *eLife* **6**:e24125 https://doi.org/10.7554/eLife.24125 | Google Scholar

Sakulkoo W, Osés-Ruiz M, Oliveira Garcia E, Soanes DM, Littlejohn GR, Hacker C, Correia A, Valent B, Talbot NJ (2018) **A single fungal MAP kinase controls plant cell-to-cell invasion by the rice blast fungus** *Science* **359**:1399–1403 https://doi.org/10.1126/science.aaq0892 | Google Scholar

Scheer U, Franke WW (1972) **Annulate lamellae in plant cells: Formation during microsporogenesis and pollen development in Canna generalis Bailey** *Planta* **107**:145–159 https://doi.org/10.1007/BF00387720 | Google Scholar

Schindelin J, Arganda-Carreras I, Frise E, Kaynig V, Longair M, Pietzsch T, Preibisch S, Rueden C, Saalfeld S, Schmid B, Tinevez JY, White DJ, Hartenstein V, Eliceiri K, Tomancak P, Cardona A. (2012) **Fiji: an open-source platform for biological-image analysis** *Nat Methods* **9**:676–82 https://doi.org/10.1038/nmeth.2019 | Google Scholar

Shimada TL, Shimada T, Hara-Nishimura I (2010) **A rapid and non-destructive screenable marker, FAST, for identifying transformed seeds of Arabidopsis thaliana** *Plant J* **61**:519–528 https://doi.org/10.1111/j.1365-313X.2009.04060.x | Google Scholar

Shimozono S, Miyawaki A (2008) **Engineering FRET constructs using CFP and YFPMethods in Cell Biology** In: *Fluorescent Proteins* Academic Press pp. 381–393 https://doi.org/10.1016/S0091-679X(08)85016-9 | Google Scholar

Song L i, Zhou X-Y, Li L i, Xue L-J, Yang X i, Xue H-W. (2009) **Genome-wide analysis revealed the complex regulatory network of brassinosteroid effects in photomorphogenesis** *Mol Plant* **2**:755–772 https://doi.org/10.1093/mp/ssp039 | Google Scholar

Takao D, Wang L, Boss A, Verhey KJ (2017) **Protein interaction analysis provides a map of the spatial and temporal organization of the ciliary gating zone** *Curr Biol* **27**:2296–2306 https://doi.org/10.1016/j.cub.2017.06.044 | Google Scholar

Tamura K, Fukao Y, Iwamoto M, Haraguchi T, Hara-Nishimura I (2010) **Identification and characterization of nuclear pore complex components in Arabidopsis thaliana** *Plant Cell* **22**:4084–4097 https://doi.org/10.1105/tpc.110.079947 | Google Scholar

Tamura K, Stecher G, Kumar S (2021) **MEGA11: Molecular Evolutionary Genetics Analysis Version 11** *Mol Biol Evol* **38**:3022–3027 https://doi.org/10.1093/molbev/msab120 | Google Scholar

Tang Y, Huang A, Gu Y (2020) **Global profiling of plant nuclear membrane proteome in Arabidopsis** *Nat Plants* **6**:838–847 https://doi.org/10.1038/s41477-020-0700-9 | Google Scholar

Tee EE, Faulkner C (2024) **Plasmodesmata and intercellular molecular traffic control** *New Phytol* **243**:32–47 https://doi.org/10.1111/nph.19666 | Google Scholar

Tee EE, Samwald S, Faulkner C (2022) **Quantification of cell-to-cell connectivity using particle bombardment** *Methods Mol Biol Clifton NJ* **2457**:263–272 https://doi.org/10.1007/978-1-0716-2132-5_17 | Google Scholar

Terry LJ, Wente SR (2009) **Flexible gates: dynamic topologies and functions for FG nucleoporins in nucleocytoplasmic transport** *Eukaryot Cell* **8**:1814–1827 https://doi.org/10.1128/EC.00225-09 | Google Scholar

Thomas CL, Bayer EM, Ritzenthaler C, Fernandez-Calvino L, Maule AJ (2008) **Specific targeting of a plasmodesmal protein affecting cell-to-cell communication** *PLoS Biol* **6**:e7 https://doi.org/10.1371/journal.pbio.0060007 | Google Scholar

Usadel B, Nagel A, Thimm O, Redestig H, Blaesing OE, Palacios-Rojas N, Selbig J, Hannemann J, Piques MC, Steinhauser D, Scheible W-R, Gibon Y, Morcuende R, Weicht D, Meyer S, Stitt M (2005) **Extension of the visualization tool MapMan to allow statistical analysis of arrays, display of corresponding genes, and comparison with known responses** *Plant Physiol* **138**:1195–1204 https://doi.org/10.1104/pp.105.060459 | Google Scholar

Wang F, Wang L, Qiao L, Chen J, Pappa MB, Pei H, Zhang T, Chang C, Dong C-H (2017) **Arabidopsis CPR5 regulates ethylene signaling via molecular association with the ETR1 receptor** *J Integr Plant Biol* **59**:810–824 https://doi.org/10.1111/jipb.12570 | Google Scholar

Wang S, Gu Y, Zebell SG, Anderson LK, Wang W, Mohan R, Dong X (2014) **A noncanonical role for the CKI-RB-E2F cell-cycle signaling pathway in plant effector-triggered immunity** *Cell Host Microbe* **16**:787–794 https://doi.org/10.1016/j.chom.2014.10.005 | Google Scholar

Winter CM, Szekely P, Popov V, Belcher H, Carter R, Jones M, Fraser SE, Truong TV, Benfey PN (2024) **SHR and SCR coordinate root patterning and growth early in the cell cycle** *Nature* :1–6 https://doi.org/10.1038/s41586-023-06971-z | Google Scholar

Xiao L, Jiang S, Huang P, Chen F, Wang X, Cheng Z, Miao Y, Liu L, Searle I, Liu C, Wu X-X, Fu Y-F, Chen Q, Zhang X-M (2020) **Two Nucleoporin98 homologous genes jointly participate in the regulation of starch degradation to repress senescence in Arabidopsis** *BMC Plant Biol* **20**:292 https://doi.org/10.1186/s12870-020-02494-1 | Google Scholar

Xie W, Nielsen ME, Pedersen C, Thordal-Christensen H (2017) **A split-GFP gateway cloning system for topology analyses of membrane proteins in plants** *PLOS One* **12**:e0170118 https://doi.org/10.1371/journal.pone.0170118 | Google Scholar

Yu M, Heidari M, Mikhaleva S, Tan PS, Mingu S, Ruan H, Reinkemeier CD, Obarska-Kosinska A, Siggel M, Beck M, Hummer G, Lemke EA (2023) **Visualizing the disordered nuclear transport machinery in situ** *Nature* **617**:162–169 https://doi.org/10.1038/s41586-023-05990-0 | Google Scholar

Zavaliev R, Epel BL (2015) **Imaging callose at plasmodesmata using aniline blue: quantitative confocal microscopy** *Methods Mol Biol Clifton NJ* **1217**:105–119 https://doi.org/10.1007/978-1-4939-1523-1_7 | Google Scholar

Zhang C, An N, Jia P, Zhang W, Liang J, Zhang X, Zhou H, Ma W, Han M, Xing L, Ren X (2020) **Genomic identification and expression analysis of nuclear pore proteins in Malus domestica** *Sci Rep* **10**:17426 https://doi.org/10.1038/s41598-020-74171-0 | Google Scholar

Zimmerli CE, Allegretti M, Rantos V, Goetz SK, Obarska-Kosinska A, Zagoriy I, Halavatyi A, Hummer G, Mahamid J, Kosinski J, Beck M (2021) **Nuclear pores dilate and constrict in cellulo**

Science **374**:eabd9776. https://doi.org/10.1126/science.abd9776 | Google Scholar

Author information

T Moritz Schladt*
Heinrich Heine University Düsseldorf, Faculty of Mathematics and Natural Sciences, Institute for Molecular Physiology, Düsseldorf, Germany
ORCID iD: 0000-0002-9160-4664

For correspondence: schladti@hhu.de
*Equal contribution

Manuel Miras*†
Heinrich Heine University Düsseldorf, Faculty of Mathematics and Natural Sciences, Institute for Molecular Physiology, Düsseldorf, Germany
ORCID iD: 0000-0002-3636-0265

*Equal contribution
†New address: Department of Stress Biology and Plant Pathology, CEBAS-CSIC, Murcia, Spain

Jona Obinna Ejike*
Heinrich Heine University Düsseldorf, Faculty of Mathematics and Natural Sciences, Institute for Molecular Physiology, Düsseldorf, Germany, Cluster of Excellence on Plant Sciences, Heinrich Heine University Düsseldorf, Düsseldorf, Germany
ORCID iD: 0000-0002-4601-8551

*Equal contribution

Mathieu Pottier*‡
Heinrich Heine University Düsseldorf, Faculty of Mathematics and Natural Sciences, Institute for Molecular Physiology, Düsseldorf, Germany
ORCID iD: 0000-0003-1551-4699

*Equal contribution
‡New address: Université de Lorraine, INRAE, IAM, Nancy, France

Lin Xi
Department of Plant Systems Biology, University of Hohenheim, Stuttgart, Germany
ORCID iD: 0000-0002-6811-9505

Andrea Restrepo-Escobar
Heinrich Heine University Düsseldorf, Faculty of Mathematics and Natural Sciences, Institute for Molecular Physiology, Düsseldorf, Germany
ORCID iD: 0000-0003-2870-394X

Masayoshi Nakamura
Institute for Transformative Biomolecules (WPI-ITbM), Nagoya University, Nagoya, Japan, New address: Department of Biochemistry and Molecular Biology, Saitama University, Saitama, Japan
ORCID iD: 0000-0002-7107-4942

Niklas Pütz
Heinrich Heine University Düsseldorf, Faculty of Mathematics and Natural Sciences, Institute for Molecular Physiology, Düsseldorf, Germany
ORCID iD: 0009-0006-1153-5918

Sebastian Hänsch
Cluster of Excellence on Plant Sciences, Heinrich Heine University Düsseldorf, Düsseldorf, Germany, Center for Advanced Imaging; Heinrich Heine University Düsseldorf, Düsseldorf, Germany
ORCID iD: 0000-0002-7762-2516

Chen Gao
Heinrich Heine University Düsseldorf, Faculty of Mathematics and Natural Sciences, Institute for Molecular Physiology, Düsseldorf, Germany
ORCID iD: 0000-0003-4750-3900

Julia Engelhorn
Heinrich Heine University Düsseldorf, Faculty of Mathematics and Natural Sciences, Institute for Molecular Physiology, Düsseldorf, Germany, Cluster of Excellence on Plant Sciences, Heinrich Heine University Düsseldorf, Düsseldorf, Germany
ORCID iD: 0000-0002-6680-3012

Marcel Dickmanns
Heinrich Heine University Düsseldorf, Faculty of Mathematics and Natural Sciences, Institute for Molecular Physiology, Düsseldorf, Germany, Department of Molecular Structural Biology, Max Planck Institute of Biochemistry, Martinsried, Germany
ORCID iD: 0000-0003-4001-707X

Gwendolyn V Davis
Heinrich Heine University Düsseldorf, Faculty of Mathematics and Natural Sciences, Institute for Molecular Physiology, Düsseldorf, Germany
ORCID iD: 0000-0003-4704-4863

Ahan Dalal
Heinrich Heine University Düsseldorf, Faculty of Mathematics and Natural Sciences, Institute for Molecular Physiology, Düsseldorf, Germany, Cluster of Excellence on Plant Sciences, Heinrich Heine University Düsseldorf, Düsseldorf, Germany
ORCID iD: 0000-0003-1876-1484

Sven Gombos
Department of Plant Systems Biology, University of Hohenheim, Stuttgart, Germany
ORCID iD: 0000-0003-4177-526X

Ronja Lange
Heinrich Heine University Düsseldorf, Faculty of Mathematics and Natural Sciences, Institute for Molecular Physiology, Düsseldorf, Germany
ORCID iD: 0009-0009-2475-2438

Rüdiger Simon
Cluster of Excellence on Plant Sciences, Heinrich Heine University Düsseldorf, Düsseldorf, Germany, Department of Molecular Structural Biology, Max Planck Institute of Biochemistry, Martinsried, Germany
ORCID iD: 0000-0002-1317-7716

Waltraud X Schulze
Department of Plant Systems Biology, University of Hohenheim, Stuttgart, Germany
ORCID iD: 0000-0001-9957-7245

Wolf B Frommer
Heinrich Heine University Düsseldorf, Faculty of Mathematics and Natural Sciences, Institute for Molecular Physiology, Düsseldorf, Germany, Cluster of Excellence on Plant Sciences, Heinrich Heine University Düsseldorf, Düsseldorf, Germany, Institute for Transformative Biomolecules (WPI-ITbM), Nagoya University, Nagoya, Japan
ORCID iD: 0000-0001-6465-0115

For correspondence: frommew@hhu.de

Editors

Reviewing Editor
Heather McFarlane
University of Toronto, Toronto, Canada

Senior Editor
Jürgen Kleine-Vehn
University of Freiburg, Freiburg, Germany

Reviewer #1 (Public review):

Summary:

Plasmodesmata are channels that allow cell-cell communication in plants; based on the functional similarities between facilitated transport within plasmodesmata and into the nucleus, the authors speculate that nuclear pore complex proteins might be involved in plasmodesmata function. In this manuscript, they localize nuclear pore complex proteins to plasmodesmata using proteomics and heterologous overexpression. They also document a possible plasmodesmata transport defect in a mutant affecting one nuclear pore complex protein.

Strengths:

The main strength of this manuscript is the interesting and novel hypothesis. This work could open exciting new directions in our understanding of plasmodesmata function and cell-cell communication in plants. They also localized many NUPs (12/35 Arabidopsis NUPs).

Weaknesses:

The main weakness of this manuscript is that the data are incomplete. While the authors appropriately and frequently acknowledge caveats to their data, two controls are essential to interpret the results that fluorescently-tagged NUPs localize to the plasmodesmata: (1) assessment of the expression level of these fluorescently-tagged NUPs to determine whether the plasmodesmata localization might be an overexpression artefact; (2) assessment of the function of the fluorescently-tagged NUPs, either by molecular complementation of a knockout mutant phenotype or by biochemical methods to test whether the fluorescently-tagged NUP incorporates into nuclear pore complexes. Conducting these experiments for even one fluorescently-tagged NUP would substantially strengthen this manuscript.

https://doi.org/10.7554/eLife.108676.1.sa2

Reviewer #2 (Public review):

Summary:

The authors aim to address whether nuclear pore complex components localize and function at PD in plant cells to mediate cell-to-cell communication.

Strengths:

(1) Novelty and Significance:
The core hypothesis, drawing parallels between PD and NPC transport, is highly original and addresses a critical gap in understanding plant intercellular communication. The idea that phase-separated domains formed by FG-NUPs could act as diffusion barriers at PD offers a plausible and sophisticated explanation for their complex transport properties, including size exclusion and facilitated translocation. This could fundamentally change how we view PD function.

(2) Comprehensive Evidence:
The study employs a rigorous and diverse set of experimental approaches, including a comprehensive bioinformatic analysis of both moss and Arabidopsis NUPs in available PD proteomic datasets, extensive imaging analysis of Nup localization in vivo, and functional transport assays using a loss-of-function nup mutant (cpr5). The transport assay is particularly important to provide functional evidence linking CPR5 to PD-mediated transport. The finding that callose levels were not significantly different in cpr5 mutants under these conditions is helpful and supports a distinct, callose-independent mechanism of transport regulation.

(3) Objectivity:
The authors are forthright in discussing the limitations and potential artifacts of their own data, clearly distinguishing between observations and definitive conclusions.

Weaknesses:

While the claims are generally justified as hypotheses or consistent observations, the authors themselves extensively detail the caveats, which are worth reiterating for clarity:

(1) Potential Overexpression Artifacts in Localization:
Although efforts were made to control expression levels, the authors acknowledge that transient overexpression could still lead to NUP accumulation at PD, either as a physiologically relevant accumulation under excess conditions or due to mis-targeting, or even as storage depots. The resolution of confocal microscopy also does not allow for a definitive conclusion on the nature of the location.

(2) Proteomics Purity:
The authors note that the presence of NUPs in PD fractions/proteomics cannot definitively rule out contamination, as PD cannot currently be purified to absolute homogeneity and is often contaminated with other organelles, including the nucleus.

(3) CPR5 Mutant Interpretation:
While cpr5 mutants exhibited reduced macromolecular transport, the authors state that they cannot exclude that the reduced transport is due to secondary effects in the cpr5 mutants, which show rather severe phenotypic defects. This is an important distinction, as CPR5 has known roles in defense responses and hormone signaling that could indirectly influence PD integrity, independent of callose deposition. The lack of effect on small molecule transport is a good control, but the broader pleiotropic effects of cpr5 mutants remain a consideration.

(4) Conceptual Distinction between NPC and PD:
The authors correctly point out that while similarities exist, the physical assembly of NUPs at PD must differ from that at the NPC due to the presence of the desmotubule and smaller cytoplasmic sleeve width at PD. Moreover, nucleocytoplasmic transport depends on karyopherin proteins that interact with the NPC central channel to complete the transport. Yet the role of karyopherins in this case is not clear. Therefore, the proposed "PD pore complex" may bear some NPC features, but not be identical.

https://doi.org/10.7554/eLife.108676.1.sa1

Reviewer #3 (Public review):

Summary:

This manuscript presents a step towards testing the hypothesis that plasmodesmata have homology to nuclear pores. The similarities between the two structures have long been noted as both structures allow the transport of proteins and nucleic acids, and both structures are composed of curved membranes. The manuscript has identified nuclear pore proteins (NUPs) in plasmodesmal protein fractions and uses live imaging in a non-endogenous system and functional assays of a mutant to propose that this might be a bona fide association.

The conclusions the authors seek to draw are that: NUPs are present in plasmodesmal protein fractions; NUPs localise at plasmodesmata; NUPs might form a pore-gating complex at plasmodesmata, regulating non-specific (2xGFP) and specific (SHR) transport through plasmodesmata

The authors then use these conclusions to propose the possibility that phase separation mediates transport through plasmodesmata. If there is phase separation at plasmodesmata or a nuclear pore-like complex, it would revolutionise the community. However, this data is insufficient to act as a cornerstone for such a discovery.

Strengths:

The strength of the manuscript lies in the boldness and novelty of the idea.

Weaknesses:

The weaknesses lie in the lack of informative controls. The authors' own assessments of their data suggest they agree with this - in their abstract alone, they point out that the transport defects they observe might be off-target effects, and suggest there is a requirement in the future to determine whether the NUPs are bona fide PD components.

Across the proteomic and live imaging experiments, the conclusions could be stronger if they compared the NUP localisation and accumulation with ER proteins - the question of whether NUPs behave like other ER proteins is not addressed. As NUPs reside in the nuclear envelope, continuous with the ER, and the ER traverses plasmodesmata, a comparison between the NUPs and ER proteins would be extremely informative.

Regarding the proteomic identification of NUPs in plasmodesmal fractions, the authors place significant weight on their own metric for PD enrichment, the PD score. As I understand it, this a metric derived from addition of two factors: a two component enrichment score that is the difference between intensity of peptides of a given protein in the PD fraction and cell wall fraction, added to the difference between intensity of peptides of a given protein in the PD fraction and total cell fraction, and a feature score that is a factor that describes representation of protein domains contained in said given protein in the plasmodesmal fraction relative to the representation of that domain in proteins in the whole proteome. The features chosen for analysis are not indicated, and the feature factor, as I understand it, is a score common to all proteins with a given feature. While each of the factors carries a measure of meaning and information, I do not understand how adding them is mathematically or biologically meaningful.

https://doi.org/10.7554/eLife.108676.1.sa0

Chapter 4

Methodology – Making plant tissue accessible for cryo-electron tomography

Making plant tissue accessible for cryo-electron tomography

Status: Peer-reviewed preprint. Revision in preparation.

DOI: https://doi.org/10.7554/eLife.106455.1

4.1 Summary

Background and research question

Cryo-electron tomography (cryo-ET) enables three-dimensional visualization of the molecular interior of cells. Technical challenges in sample preparation have limited its application to a small set of predominantly unicellular organisms. Vitrification, an essential requirement for preserving samples in a near-native state and recording high quality data, is difficult to achieve for thick samples. Recent methodological advances are beginning to extend cryo-ET from single cells to tissues, yet, due to their high water content and large cell size, plants have proven exceptionally challenging specimens. Because the resolution range of cryo-ET is uniquely suited to investigate the structure and composition of intact plasmodesmata, this study aimed to develop and evaluate cryo-ET workflows allowing vitrification and imaging of various plant tissues.

Experimental approach

Plunge-freezing, at the time the established cryo-ET sample preparation method, was initially tested but found to be unsuitable for vitrifying even relatively thin plant tissues such as the branched protonema filaments of *Physcomitrium patens* (15-50 µm in diameter). To improve vitrification, two strategies were evaluated: the use of cryoprotectants and high-pressure freezing. A range of cryoprotectants was tested, however, either failed to improve vitrification or caused substantial cell damage through plasmolysis at sufficiently high concentrations. High-pressure freezing workflows were therefore developed and assessed for their ability to achieve vitrification and preserve the molecular organization within cells. Following high-pressure freezing, samples are embedded in vitrified buffer within metal sample carriers of approximately 500 µm thickness, which poses additional challenges for localizing subcellular targets and generating electron-transparent sections (final section thickness ~150-250 nm). To

address these challenges, advanced workflows for thin-sectioning by cryo-focused ion beam (cryo-FIB) milling, and subcellular target localization by FIB-integrated cryo-fluorescence microscopy were implemented and adapted to plant samples.

Key findings

Plunge-freezing in the presence of cryoprotectants was insufficient to vitrify and preserve the tested plant tissues. Vitrification could only be achieved by high-pressure freezing, requiring subsequent sample processing by advanced cryo-FIB milling and cryo-fluorescence-based targeting approaches. Workflows for vitrification, subcellular targeting by integrated cryo-fluorescence microscopy, sample thinning by advanced cryo-FIB milling, and cryo-ET of plant tissue samples were established. As a proof of principle, the native spatial distribution of rubisco within chloroplasts of *Physcomitrium patens* was resolved, and sub-nanometer resolution reconstructions were obtained. Applicability of the workflows to tissues from additional plant species, including *Arabidopsis thaliana* and *Limonium bicolor*, was demonstrated.

Contributions to this chapter

I contributed to this chapter by establishing and maintaining plant culturing at the Department of Molecular Structural Biology, performing initial plunge-freezing and cryo-protectant screening experiments, and later sample vitrification by high-pressure freezing. I contributed to implementing and testing of the described FIB-milling workflows (with MP, PX, ML, OS, COJK, JM, JB, SK), cryo-fluorescence microscopy (with MP, PX, AB, CC), data analysis (with MP, PX), structure modeling of *P. patens* rubisco, and manuscript editing (with MP, COJK, SK, JMP, WB).

4.2 Results

Plant Biology

Making plant tissue accessible for cryo-electron tomography

Reviewed Preprint
v1 • May 12, 2025
Not revised

Matthias Pöge, Marcel Dickmanns, Peng Xu, Meijing Li, Oda H Schiøtz, Christoph OJ Kaiser, Jianfei Ma, Anna Bieber, Cristina Capitanio, Johann Brenner, Margot Riggi, Sven Klumpe, Manuel Miras, Neda S Kazemein Jasemi, Waltraud X Schulze, Rüdiger Simon, Wolf B Frommer, Jürgen M Plitzko, Wolfgang Baumeister

Emeritus Group Molecular Structural Biology, Max Planck Institute of Biochemistry, Martinsried, Germany • Heinrich Heine University Düsseldorf, Faculty of Mathematics and Natural Sciences, Institute of Molecular Physiology, Düsseldorf, Germany • Shenzhen Medical Academy of Research and Translation, Shenzhen, China • Research Group CryoEM Technology, Max Planck Institute of Biochemistry, Martinsried, Germany • State Key Laboratory of Medicinal Chemical Biology and College of Life Sciences, Nankai University, Tianjin, China • Research Department Molecular Machines and Signaling, Max Planck Institute of Biochemistry, Martinsried, Germany • Department of Cell and Virus Structure, Max Planck Institute of Biochemistry, Martinsried, Germany • Department of Stress Biology and Plant Pathology, CEBAS-CSIC, Murcia, Spain • Heinrich Heine University Düsseldorf, Faculty of Mathematics and Natural Sciences, Department of Developmental Genetics, Düsseldorf, Germany • Division of Molecular Embryology, German Cancer Research Center (DKFZ), Heidelberg, Germany • Department of Plant Systems Biology, University of Hohenheim, Stuttgart, Germany • Cluster of Excellence on Plant Sciences (CEPLAS), Heinrich Heine University, Düsseldorf, Germany • Institute of Transformative Bio-Molecules, Nagoya University, Nagoya, Japan

https://en.wikipedia.org/wiki/Open_access
Copyright information

eLife Assessment

Thick multicellular plant samples provide unique challenges when it comes to cryo-preservation, which has resulted in limited successful examples for structural studies using in situ cryo-electron tomography. To address this deficiency, this **important** study describes procedures for high-pressure-freezing, focused ion-beam milling, and cryo-electron tomography imaging of certain plant types. The results described in the paper provide **solid** evidence for the usefulness of the methods described, although some reservations remain about the applicability of the methods to a wider range of plant cell types.

https://doi.org/10.7554/eLife.106455.1.sa3

Abstract

Cryo-Electron Tomography (cryo-ET) allows to visualize the molecular architecture of pristinely preserved cells and tissues. The workflow of sample preparation for cryo-ET is rather complex; it involves vitrification by rapid freezing followed by cryo-Focused Ion Beam (FIB) milling rendering the volumes of interest thin enough for cryo-ET data acquisition. The established protocols for single cells grown on or deposited on EM-grids are not suitable for multicellular plant tissues. Plunge-freezing does not yield vitrified samples in most cases and

must be replaced by high-pressure freezing. This, in turn, necessitates extensive modifications of the subsequent FIB milling procedures. In this communication we describe procedures for sample screening, targeted FIB milling guided by cryo-fluorescence microscopy and a novel lamella trimming step that allows to obtain homogenously thin lamellae suitable for cryo-ET. We have tested all the steps along the workflow with a variety of plant tissues including the moss *Physcomitrium patens* and tissues of *Arabidopsis thaliana* and *Limonium bicolor*. We could demonstrate that the workflow optimized for plant tissues allows to attain subnanometer resolution in cases where subtomogram averaging is applicable.

Main text

New imaging modalities in conjunction with advances in sample preparation can pave the way for unprecedented insights into the structural organization of cells and tissues. Cryo-Electron Tomography (cryo-ET), i.e. the application of tomographic principles of image acquisition and reconstruction to biological materials in a frozen-hydrated state, allows to visualize the molecular architecture of unperturbed cellular environments[1]. It combines the power of high-resolution three-dimensional (3D) imaging with close-to-life structural preservation and provides faithful representations of the physiological state of cells[2].

Instead of disrupting cells, fractioning their molecular inventory, and studying its components in isolation, cryo-ET allows to visualize them *in situ* embedded in their functional environments. Thereby, the network of interactions underlying cellular physiology is preserved and can be revealed[3]. Moreover, many supramolecular assemblies cannot be isolated without compromising their structural integrity. Advances in technology and methodology have established structural biology in cells or *in situ* as a viable alternative[4]. Today, cryo-ET is widely deployed and increasingly popular at the interface of molecular biology and cell biology – with exception of the plant sciences, where technical issues have hampered its use.

The critical part of the process is the vitrification of plant tissues by rapid freezing. Typically, plant cells are larger (diameter 10 – 100 µm) than yeast, algae or mammalian cells and they often contain solute depleted vacuoles occupying up to 90 % of their cellular volume[5]. Plunge-freezing[6], the most convenient way to achieve vitrification, works reliably only for cells smaller than 10 µm. While cryoprotectants[7] may be used to increase vitrification depth, for larger cells and tissues, High-Pressure Freezing[8] (HPF) must be applied and still not always guarantees full vitrification. Moreover, it is challenging to make HPF compatible with the subsequent step of the cryo-ET workflow: thinning the sample to make it suitable for electron tomography data acquisition. This is achieved by Focused Ion-Beam (FIB) milling, where material is ablated from the ice-embedded sample until thin sheets (lamellae) with thicknesses of 100 - 300 nm are obtained[9]. To ensure that features of interest are included in the lamella, FIB milling is often guided by cryo-Fluorescence Light Microscopy (FLM), pinpointing the spatial location of structures of interest[10,11]. Recently, progress has been made in the preparation lamellae from HPF samples for cryo-ET[12–20]. These new procedures, however, have not yet been put into practice for plant tissue.

Therefore, almost all structural studies of plant systems have opted for an alternative route, namely HPF followed by freeze substitution. In this process, high-pressure frozen samples are dehydrated, metal-impregnated and embedded in a resin allowing sectioning and imaging at room temperature[21]. While this approach generally preserves cellular ultrastructure better than chemical fixation followed by metal staining and resin embedding[22], it is impossible to ascertain that vitrification has been adequately achieved in the first instance. To visualize and interpret structures at the molecular level, the only suitable method is cryo-ET, with samples unadulterated by dehydration and chemical modifications.

In this study, we describe workflows suitable for the preparation of plant tissues for cryo-ET. First, we applied them to protonemata and phyllids of the moss *Physcomitrium patens*[23] forming one-dimensional chains and two-dimensional sheets, respectively, of cylindrical cells with diameters of 15-30 µm. We employed FIB-milling guided by FLM, specifically targeting cell junctions, to show that features small compared to the size of whole cells can be addressed. Later we adapted the methods to several other species including more challenging tissues to demonstrate the potential of the workflows, which we believe are not limited to plants but widely applicable also to other, multicellular systems.

Results

Plunge-freezing does not vitrify *Physcomitrium patens* tissues

First, we applied the standard plunge-freezing and FIB milling workflow to *P. patens* protonemata and phyllids. As the cells were exposed on the surface of grids, the identification of cell junctions was possible using secondary electron images derived with the Scanning Electron Microscope (SEM) and FIB, without the need for fluorescence targeting by correlation to FLM data (**Extended Data Fig. 1**). Overviews of lamellae recorded in a Transmission Electron Microscope (TEM), however, revealed that the cells were not vitreous (**Fig. 1a**, N = 15). The formation of large ice crystals during plunge-freezing resulted in distortion of the cellular architecture and the generation of severe TEM imaging artefacts.

We also performed plunge-freezing with glycerol, sucrose and proline additives serving as cryoprotectants (**Table 1**). These, however, did either not prevent crystalline ice formation or induce plasmolysis (data not shown). In some cases, the tissue was even severely dehydrated (**Extended Data Fig. 1f**). Thus, we concluded that it is challenging to vitrify *P. patens* tissues by plunge-freezing. While the success of plunge-freezing is sample dependent, we anticipate similar vitrification problems for vascular plants and mosses with cells of similar or larger size.

The "Waffle" Method utilized for *P. patens*

Next, we tested the "Waffle" Method[18] to vitrify protonemata. The tissue was placed on the back of an EM-grid, i.e. on the reverse side of a continuous support film and squeezed into the buffer-filled wells formed by the EM-grid bars and support film prior to HPF. While this approach damages cells on top of grid bars, the cells within grid squares remain intact. Hence, using EM-grids with large squares (50-100 mesh) maximizes the area of intact, vitreous tissue.

In contrast to plunge-frozen samples, the cells on "waffle" grids are embedded in a layer of vitreous buffer and not exposed at the sample surface (**Extended Data Fig. 3a**). Therefore, we screened "waffle" grids in a cryo-FLM recording the green cellular autofluorescence to identify single layers of intact protonemata tissue with cell junctions in the center of grid squares (**Fig. 2a,b**). Furthermore, squares with multiple cell layers were ignored as only a single layer of protonemata fits into the 25 µm high well of the used grids without mechanical damage caused by compression (**Extended Data Fig. 3b-c**).

Subsequently, we loaded the samples into a FIB/SEM instrument equipped with an integrated Fluorescence Light Microscope (int-FLM) for lamella preparation. While lamella milling of plunge frozen samples can be done by ablating material with the FIB from a shallow angle, milling "waffle" grids requires additional steps. First, the target area must be located laterally, i.e. parallel to the sample surface. Then holes, referred to as trenches, are milled around the target area with the FIB axis perpendicular to the sample surface (trench milling orientation, **Extended Data Fig. 2**). Afterwards, the axial position of the target area is determined followed by thinning the sample from a shallow angle to obtain a lamella (lamella milling orientation, **Extended Data Fig. 2**).

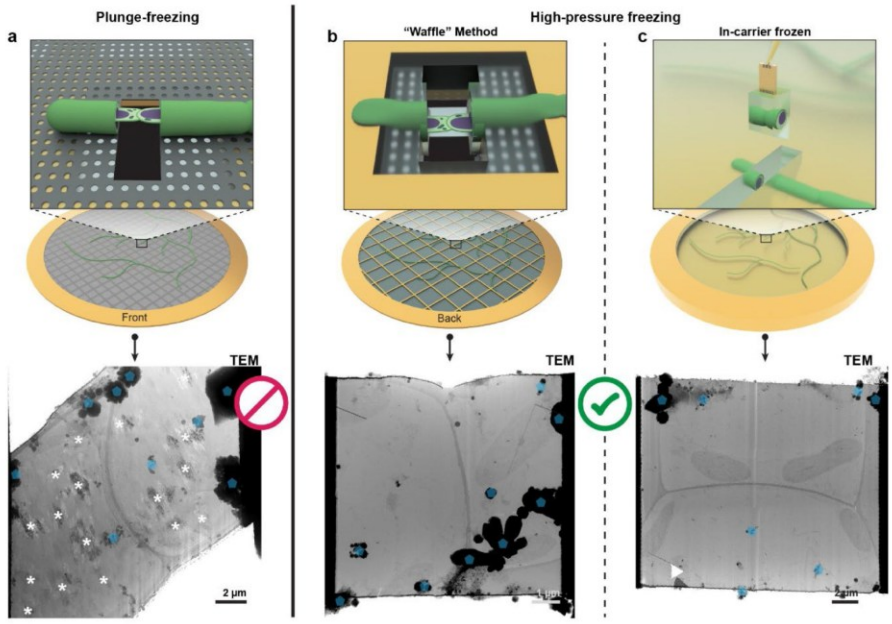


Fig. 1

Plunge-freezing versus High-Pressure Freezing (HPF) for the moss *Physcomitrium patens*.

The top and bottom row show schemes of the samples and corresponding examples of TEM overview images, respectively. **a,** Plunge-freezing. Patterns introduced by crystalline ice are indicated by asterisks (*). **b**,**c**, High-pressure freezing. Samples prepared by the "Waffle" Method or in-carrier HPF in (**b**) and (**c**), respectively. TEM overviews of lamellae from HPF samples show no indication of crystalline ice. In (a)-(c), ice crystals contaminating the lamella surface which were introduced during transfers between microscopes are marked by blue transparent pentagons.

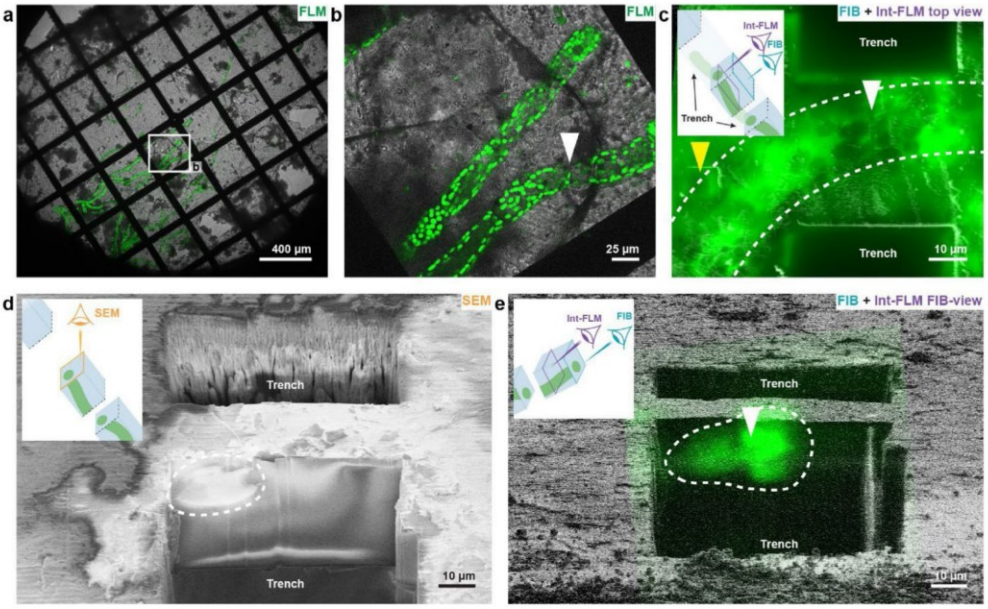


Fig. 2

Sample screening and targeted lamella preparation

a,b, Sample screening using a cryo-fluorescence light microscope (FLM). An overview of a "waffle" grid is shown in (**a**). The white rectangle indicates the position of the grid squares in (**b**) containing a target area. Displayed in (**a**) and (**b**) are the transmitted light channel (gray) and the cellular autofluorescence (green). **c**, Lateral targeting. Overlay of a FIB image (gray) and cellular autofluorescence (green) recorded with the integrated Fluorescence Light Microscope (int-FLM). Both images (**Extended Data Fig. 3g**) were acquired with the stage in trench milling orientation resulting in sample top views. **d,e**, axial targeting. **d**, SEM image of the block-face exposed through trench milling. **e**, Overlay of FIB (gray) and int-FLM FIB-view image (green) of the cellular autofluorescence. Both images were recorded with the stage in lamella milling orientation. Cell junctions and locations of cells are marked with white arrowheads and dashed lines, respectively, in (**b**-**e**).

Correlating the FLM images with FIB images is difficult due to the near-featureless surface of "waffle" grids. For lateral targeting, a marker hole was milled in trench milling orientation (**Fig. 2c**) into a grid square containing a target area identified previously in the FLM. Marker and target area were then localized in sample top views recorded with the int-FLM (**Extended Data Fig. 2d**) and the measured distance between them was used to guide trench milling (**Extended Data Fig. 2e**). To ensure that the cell junction is contained within the final lamella with a thickness of only a few hundred nanometers, it must also be targeted in the axial dimension, i.e. within the thickness of the sample. For plunge frozen samples, 3D-correlative light microscopy and FIB milling allows axial targeting by using cryo-FLM z-stacks[10]. This approach, however, is difficult to apply to thick samples, because of poor axial resolution, depth dependent aberrations and difficulties in registration between 3D-stacks and FIB images of HPF samples. We applied two different imaging modalities for axial targeting. First, cellular components like cell walls, membranes or organelles can be visualized by SEM block-face imaging[24], if they are exposed at the FIB milled surface after trench milling (**Fig. 2d**, **Extended Data Fig. 2c**). Second, when the target area is buried beyond the surface, the int-FLM can be used in the "FIB-view" mode (Capitanio *et al.*, will soon be described in a manuscript). Here, int-FLM images are not acquired as top views but with the stage in lamella milling orientation (**Extended Data Fig. 2b**) from the same shallow angle at which the lamella is thinned to its final thickness (**Fig. 2e**).

Next, the lamella was further thinned in several successive steps (**Extended Data Fig. 4**). At a thickness of 6 µm a notch similar to reference[18] but larger was milled to allow for movements of more than 1 µm to prevent lamella bending in the type of samples studied here (**Extended Data Fig. 4b**). Afterwards, the lamella was thinned to its final thickness of 100-300 nm (**Extended Data Fig. 4c**) and imaged in a TEM. Lamella overviews reveal the subcellular organization in *P. Patens* protonemata unperturbed by crystalline ice (**Fig. 1b**, **Fig. 3d**).

Optimization of Serial Lift-Out for lamella quality

The cell junctions we targeted in this work have a diameter of 15-25 µm. The process of "waffle" milling results in a single lamella of a few hundred nanometers in thickness. Thus, about 98% of the targeted volume is lost. Additionally, as targeting and trench milling are time-consuming processes, the yield of a single lamella per site renders the technique low throughput. An alternative to "waffle" milling is Serial Lift-Out[19]. Here, the entire target area is extracted by lift-out (Supplementary Movie 1 and 2) and cut into several sections that are attached to a receiver grid. Those sections are then fine milled, resulting in multiple lamellae sampling the target area, increasing the throughput and the contextual information obtained[19].

We explored both attachment methods proposed in the original paper: single-sided and double-sided attachment. For the single sided attachment, redeposition milling was used to attach only one side of a section to a pin (**Extended Data Fig. 6**, Supplementary Movie 3). In our hands, this was the simplest attachment method as it required less precise maneuvering of the lift-out system, but the resulting lamellae often bent during fine milling (**Extended Data Fig. 6f**), especially when thinned below 200 nm as described previously[19]. Lamella loss during the transfer between microscopes was also more frequent (Supplementary Figure 6). Furthermore, lamellae were unstable during data acquisition, often resulting in poor data quality.

For the double-sided attachment, the width of the lift-out block was adjusted to fit precisely between two grid bars of a 400×100 mesh grid. Attachment of the section on both sides (**Extended Data Fig. 7**, Supplementary Movie 4) prevents bending during fine milling and results in lamellae which are stable during microscope transfers and data acquisition. This approach, however, requires more precision with the micromanipulator system and user experience.

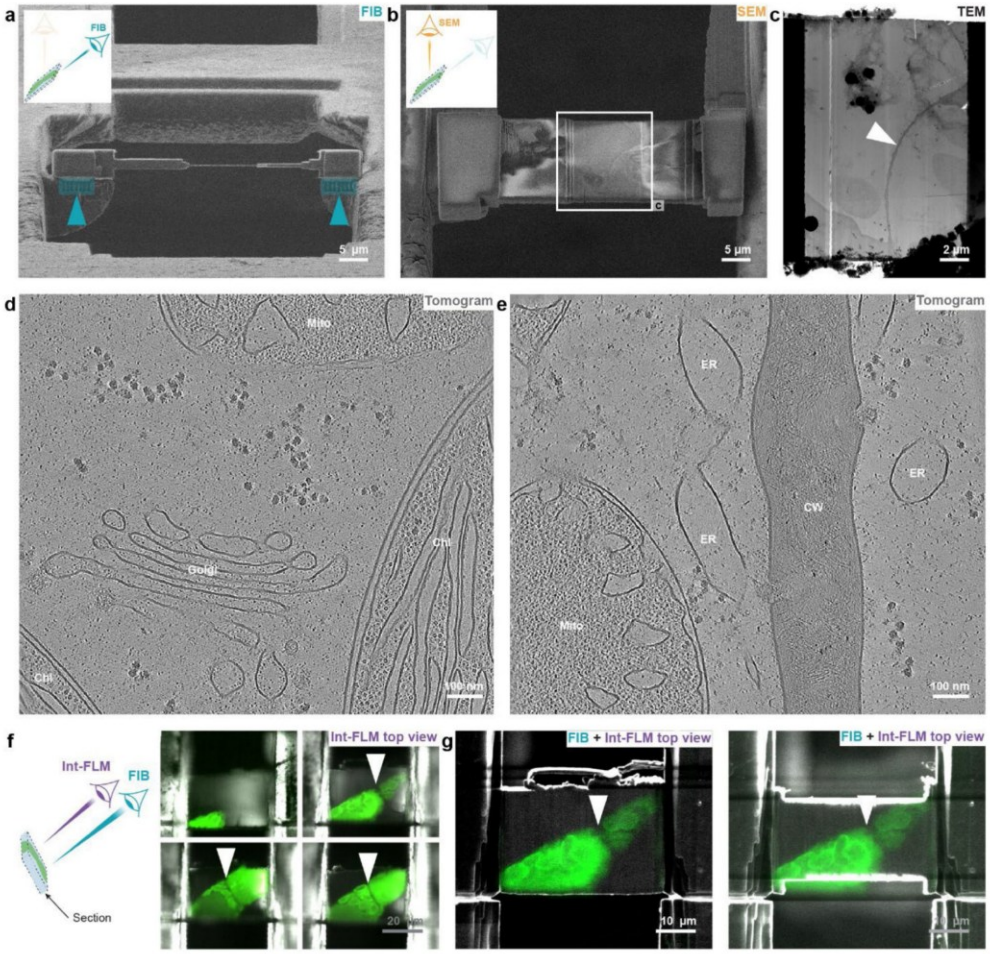


Fig. 3

Serial Lift-Out with double sided attachment from below and section trimming.

a-c, Double-sided attached lamellae with the attachment from below. FIB and SEM images are shown in (**a**) and (**b**), respectively. The attachment sites are marked in blue. The white rectangle in (**b**) marks the field of view in (**c**). **c**, TEM overview image of the lamella. **d**,**e**, Single slices of denoised tomograms. Chl indicates Chloroplasts, Mito Mitochondria, ER the cortical Endoplasmatic Reticulum and CW the cell wall. **f**, Four int-FLM top views of successive Serial Lift-Out sections (reflected light in gray and cellular autofluorescence in green). The junction between cells (white arrowhead), is only contained in three of them. **g**, Overlay of FIB (gray) and int-FLM top view images (green) of the top right section in (**f**) before and after section trimming in the left and right panel, respectively.

In the context of the present study, we adapted the double-sided attachment method to focus on lamella quality rather than quantity. To this end, we milled plateaus into grid bars onto which the lift-out block could then be placed. The sections were then attached to the plateaus from below (**Fig. 3a**, **Extended Data Fig. 8**, Supplementary Movie 5). While milling the plateaus increases the expenditure of time (15-25 min per section), it leads to robust attachment and is easier to learn for lift-out beginners because it requires less precision concerning the dimensions of the lift-out block. The reduced precision requirement also allows Serial Lift-Out to be performed on FIB systems with stage instabilities or with imperfections in the FIB optics. For all three attachment methods, we obtained vitreous lamellae (**Fig. 1b**, **Fig. 3c**) and recorded tomograms revealing the subcellular organization of *P. patens* with an unprecedented level of detail (**Fig. 3**, Supplementary Movie 6).

Generating homogeneously thin lamellae is challenging, especially if they are larger than 10-20 µm along the milling direction. To improve lamella quality, we included an additional step to the Serial Lift-Out workflow, namely section trimming. After the attachment, int-FLM top views were acquired for all sections to check which of them contained the target area (**Fig. 3f**). This also allowed to identify regions of the sections with no features of interest which were removed by FIB milling in trench milling orientation (**Fig. 3g**), minimizing the depth of the lamella in the thinning direction. During the lift-out process, the front of the lift-out block becomes damaged and uneven due to repeated ion exposures. At least 2 µm of the section front were also removed to create a new, smooth front. This trimming step makes fine milling faster because less material must be ablated and allows to generate homogeneously thin lamellae as the smooth front prevents curtaining[25].

Lift-out in different stage orientations

On “waffle” grids of *P. patens*, the axis of the cylindrical protonemata cells is always roughly parallel to the grid surface. Thus, on-grid “waffle” milling and lift-out with the stage in the lamella milling orientation (**Extended Data Fig. 5** left panel, Supplementary Movie 1) will inevitably yield sections roughly parallel to this axis (longitudinal sections). Performing lift-out in the trench milling orientation on cells with the protonemal axis oriented roughly parallel to the lift-out direction, cross-sections can be obtained (**Extended Data Fig. 5** right panel, Supplementary Movie 2), analogous to *Caenorhabditis elegans* L1 larval cross-sections in reference[19]. Thus, it is possible to address samples which can only be frozen in distinct orientations from different directions, which is crucial to study subcellular structures with defined orientation within cells.

In-carrier high-pressure freezing

During “waffle” freezing, *P. patens* protonemata can be damaged for two reasons. First, the filaments are larger than the squares of the EM-grids used and cells running across grid bars will be squeezed. Second, often multiple cell layers were pressed into the 25 µm high well formed by the grid bars which is not high enough to accommodate them without compression. To avoid this mechanical damage, we high-pressure froze protonemata directly in HPF carriers with a 2 mm wide and 100 µm deep cavity.

While the procedure of in-carrier high-pressure freezing is fast, it comes with additional challenges. First, samples cannot be screened easily in a FLM because carriers do not fit into the commercial shuttle. Thus, montage overviews were recorded with the int-FLM (**Extended Data Fig. 9a**). In our systems, this takes longer and yields poorer quality images due to widefield imaging and the low numerical aperture of the objective. Nevertheless, the obtained montage overviews were sufficient to identify target areas. Trench milling aided by int-FLMs was then performed as described in the previous section (**Extended Data Fig. 9b**).

Second, lamellae must be prepared by lift-out methodologies as trench milling through the carrier is impractical. Additionally, the lift-out block must be detached from the bulk also from below and not only on all four sides as for "waffle" grids. This requires milling an undercut after trench milling in lamella milling orientation (**Extended Data Fig. 9c**, Supplementary Movie 7 and 8).

Third, in-carrier HPF samples are thicker than typical "waffle" grids. Thus, the axial targeting via SEM block-face imaging or FIB-view imaging with the int-FLM is crucial to ensure that the undercut is milled below the target area and that it is extracted completely (**Extended Data Fig. 9c**). Apart from these technical complications, lift-out and sectioning was then performed as for "waffle" samples, with the added benefit that in-carrier HPF potentially allows to vitrify thicker samples.

Subtomogram averaging of rubisco

In order to test if structural details are preserved throughout the presented workflows, we subjected rubisco[26], an abundant enzyme in chloroplasts, to subtomogram averaging[27]. We acquired a small dataset composed of 10 tomograms on *P. patens* chloroplasts, picked rubisco positions by template matching and computationally aligned and classified subtomograms. **Fig. 4a** shows an example of a chloroplast tomogram (Supplementary Movie 9), and **Fig. 4b** the corresponding 3D rendered image of segmented chloroplast membranes with an intermediate, low-resolution rubisco average pasted at the determined particle positions (see supplementary material). We docked a model of an octamer of large rubisco subunits predicted by AlphaFold 3[28] into the final average of about 6000 subtomograms (**Fig. 4c**). The α-helices of the predicted model fit well into the experimental density (**Fig. 4d**) indicating that we attained an average with subnanometer resolution (Supplementary Figure 4, $FSC_{@0.143}$ = 0.79 nm, $FSC_{@0.5}$ = 0.95 nm).

Based on the determined positions of rubisco complexes within tomograms, we calculated the local rubisco density which has a peak at 16 nm in contrast to a simulated random distribution (**Fig. 4e**). This indicates that rubisco is not randomly distributed within *P. patens* chloroplasts similar to previous findings in the pyrenoid of the green alga *Chlamydomonas reinhardtii*[29]. These results demonstrate that subnanometer structural details are preserved throughout the presented workflows and that it is now possible to perform *in situ* structural biology studies in multicellular plants.

The high-pressure freezing workflow applied to other tissues and plants

To demonstrate the application of the HPF methods presented to other tissues and plant species, we further used it on phyllids, the leaf-like structures formed by *P. patens*. Small pieces of phyllids were dissected and frozen with the "Waffle" Method. The samples were screened to avoid investigating areas which have been damaged during dissection or freezing (**Extended Data Fig 10a-c**). We were able to obtain vitreous lamellae and tomographic data from this tissue (Fig. 6a,b, Supplementary Movie 10).

Next, we adapted the "waffle" workflow for *Arabidopsis thaliana* embryos. While the embryos easily fit into grid squares, they are with about 50 µm thicker than the 25 µm high bars of EM-grids used here (**Extended Data Fig. 10d,e**). To avoid mechanical damage, an additional spacer ring was added onto the grid before "waffle" freezing, which increased the thickness of the "waffle" sample to around 75 µm and prevented squeezing of the embryos in the process (**Extended Data Fig. 10d,e**). *A. thaliana* embryos were successfully vitrified, and tomographic data acquired (**Figure 5c-d**, Supplementary Movie 11).

As a last study subject, we high-pressure froze the first true leaves of *Limonium bicolor* (**Extended Data Fig. 10f**) in the 300 µm deep cavity of HPF carriers. We targeted the blue autofluorescent salt glands (**Extended Data Fig. 10g-h**) again aided by the int-FLM and performed Serial Lift-

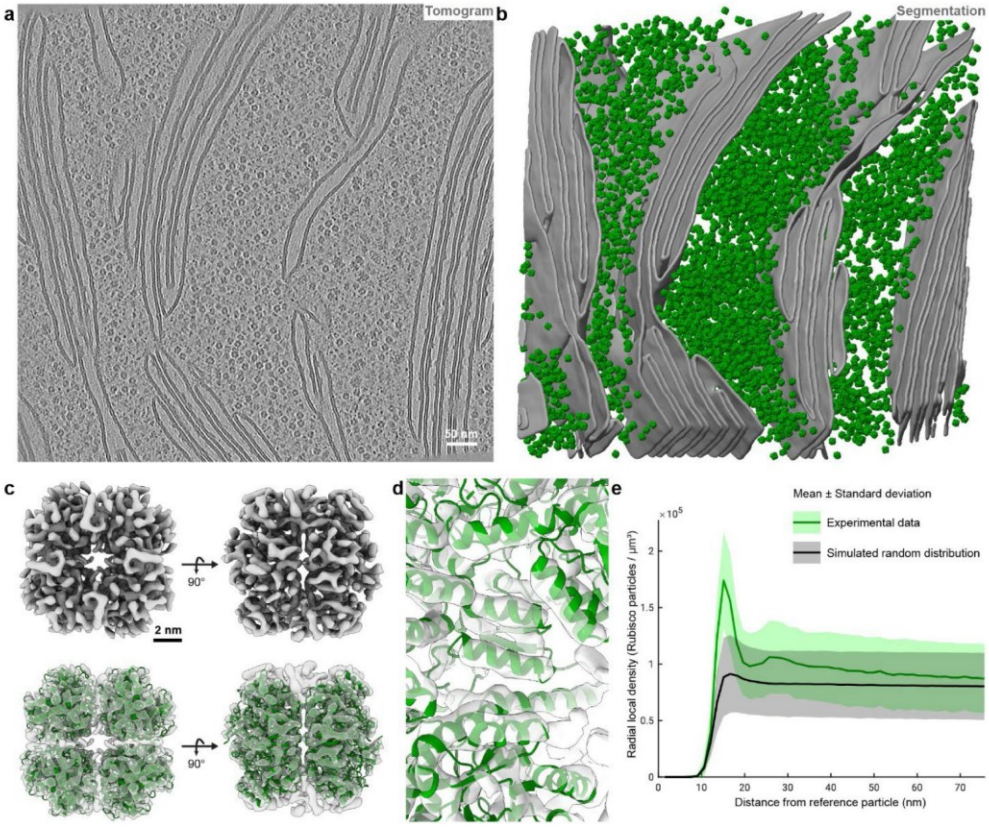


Figure 4

Subtomogram averaging of rubisco.

a, Slice of a denoised tomogram recorded on a chloroplast (Supplementary Movie 9). **b**, Three-dimensional rendered representation with segmented chloroplast membranes (gray) and the rubisco subtomogram average (green) pasted at the positions determined after template matching and subtomogram classification. **c**, Rubisco subtomogram average in isosurface representation (top row) and an octameric model of large rubisco subunits predicted by AlphaFold 3 docked into the average (bottom row). **d**, Close-up view of the average shown in (**c**) revealing that predicted α-helices fit well into the experimental density map. **e**, The local density of rubisco particles as a function of the distance from the reference particle. Green line and area are the average of experimental density ± one standard deviation, respectively, obtained from 10 tomograms. Black line and gray area are the mean ± one standard deviation obtained for a simulated random particle distribution.

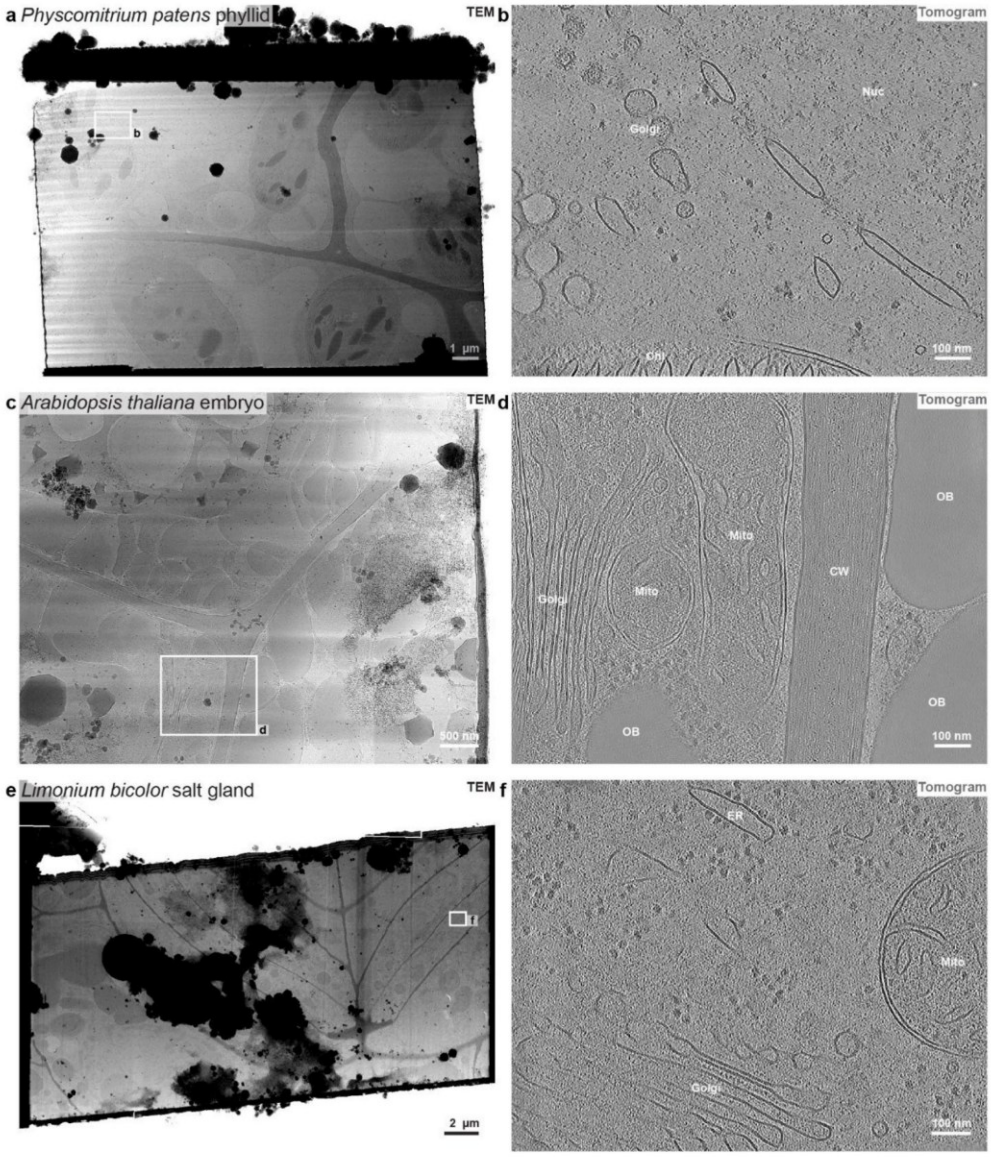


Fig. 5

The cryo-ET workflow applied to other tissues and species.

a,**b**, *Physcomitrium patens* phyllid sample. **a**, TEM overview image of a single-sided attached lamella. **b**, a single slice of a tomogram recorded on the nuclear envelope (Supplementary Movie 10). **c**,**d**, *Arabidopsis thaliana* embryo sample. **c**, Low magnification TEM image of a lamella. **d**, Single tomographic slice of the cell wall between cells (Supplementary Movie 11). **e**,**f** Salt gland of *Limonium bicolor*. **e**, TEM overview image of a double-sided attached lamella. **f**, Single slice of a tomogram. Chl indicates Chloroplasts, Mito Mitochondria, OB oil bodies, Nuc the nucleus, CW the cell wall and ER the Endoplasmatic reticulum. All tomographic slices are from computationally denoised tomograms (Supplementary Movie 12).

Out. A TEM overview of a salt gland section and a tomographic slice are depicted in **Fig. 5e** and **f**, respectively, revealing its cellular architecture in a near-native state (Supplementary Movie 12). These results illustrate that the presented HPF methods are broadly applicable.

Discussion

Compared to the "standard" cryo-ET workflow, comprising plunge-freezing, on-grid lamella milling and data acquisition, working with high-pressure frozen samples is technologically more demanding and has a lower throughput and success rate. Hence, if a sample can be vitrified by plunge-freezing, it still is the method of first choice. We must assume, however, that most plant tissues are too thick to be vitrified by plunge-freezing and must instead be high-pressure frozen.

Depending on the size of the sample, there are several high-pressure freezing variants. For the "Waffle" Method without spacer ring, the thickness of the EM-grid defines the maximum thickness of the sample. While standard EM-grids have a thickness of 20-25 µm, thicknesses between 8-100 µm are commercially available. Additionally, the shape (e.g. square, hexagon, hole and slot) and the size of the mesh can be chosen to match the shape of the tissue. For samples exceeding 100 µm thickness, spacer rings can be added, as exemplified here on *A. thaliana* embryos. The advantage of "waffle" grids is that they allow on-grid lamella preparation and no undercut is required when performing lift-out. Samples with diameters of up to 2 mm and a maximum thickness of 200-300 µm can potentially be high-pressure frozen in HPF carriers without risking squeezing damage by grid bars. In this case, on-carrier lamella preparation is currently technologically impractical and lift-out methodologies are required.

Vitrification is fundamental for preserving the sample in a near-native state and has a strong impact on the cryo-ET data quality and subsequently subtomogram averaging. We obtained data from clearly vitrified, thus apparently structurally intact samples in many cases. The success rate, however, was very sample-dependent. All our *A. thaliana* embryo and *L. bicolor* samples were vitreous (N = 4 and N = 1, respectively), perhaps due to the cells, which are densely packed with cellular components and the absence of large vacuoles. For *P. Patens*, the success rate was 47% (N = 45, Supplementary Figure 6a). Occasionally, even cells from within the same grid square differed in their vitrification state. We applied similar methods to the trichomes of *Nicotiana benthamiana* and observed large ice crystals in all of them (N = 10). This illustrates that obtaining consistent vitrification results with high-pressure freezing can still be a major challenge for some samples. Moreover, certain samples require harvesting or dissection before being manually mounted in HPF carriers, which inevitably damages or stresses the cells and may result in artifacts. Hence, the preparation of samples for HPF should be as sift as possible while minimizing the perturbation of the system under investigation. It would therefore be beneficial to develop new protocols or even methods, that are largely user independent or completely automated, highly reproducible and capable of even vitrifying larger and thicker tissues[30,31].

Additionally, HPF samples demand a targeted approach, since the cells are not exposed on the sample surface but submerged in a layer of vitreous buffer. The localization of target areas requires fluorescent markers or autofluorescence. For lateral targeting in the x-y-plane of the sample, grids were screened in a stand-alone cryo-FLM to identify suitable grid squares. Next, int-FLMs proved practical to guide trench milling. To ensure that the target area is contained within the final lamella or lift-out block, its axial position (location within sample thickness) must be determined. SEM block-face imaging after trench milling is one option. It is only applicable, however, if sufficiently contrast-rich features, like membranes, in the vicinity of the target area are exposed at the block-face. The second option is FIB-view imaging which can be applied if a fluorescently labelled or autofluorescent target is discernible in int-FLM images.

On-grid “waffle” milling has the lowest methodological entry barrier and does not require lift-out. It is faster for screening several locations per grid and assessing the sample quality than Serial Lift-Out. At the same time, it exhibits a lower throughput by obtaining only a single lamella per targeted area. Additionally, fine milling for our “waffle” samples must be done at relatively high stage tilts (20°) to fully access the target area and it is often difficult to remove all material below lamellae. Both factors restrict the angular range for tomographic data acquisition and, in turn, compromises data quality. For large target areas, like in our case the junction between cells, Serial Lift-Out is the preferred method. While it requires some training and a lift-out system, after sectioning, fine milling is faster and more straightforward than for “waffle” milling and can be performed at shallow angles. The full ±60° tilt range for cryo-ET, can therefore be accessed.

For plant samples, single-sided attachment is the fastest lift-out approach requiring least user precision. But smaller lamella dimensions, potential bending and instabilities during data collection must be considered. In comparison, double-sided attachment yields lamellae that are easier to thin homogeneously without bending and produce higher quality data. For the double-sided attachment, we tested two methods. The side-attachment (i), as described originally in reference[19] needs little modifications of the receiver grid and consequently requires less expenditure of time. Yet, fitting the lift-out block precisely between the grid bars allows only for an error of a few hundred nanometers. Hence, it requires most user expertise, a mechanically very stable stage and lift-out system as well as well-aligned ion optics. The attachment from below (ii) is more time-consuming due to the additional generation of plateaus but adjusting the size of the lift-out block and placing it on the plateaus tolerates manipulation errors of a few micrometers. Therefore, the attachment from below is likely easier to adopt for lift-out novices.

The additional trimming step introduced here focuses on obtaining highest lamella quality over quantity. First, int-FLM top views of Serial Lift-Out sections confirm that the target area is captured within followed by removal of regions that do not contain material of interest in trench milling orientation. This minimizes the lamella size in the fine milling direction and centers the target between smooth fronts which is important to obtain homogeneously thin lamellae during the subsequent fine milling in lamella milling orientation.

To further increase the throughput and reduce the experience defined entry barrier, automation is important. Since we explored multiple samples which all behaved differently, all milling steps were performed manually. The whole lamella preparation workflow, however, is per-se very repetitive and time-consuming. Several software tools already exist[15,32–34] which can be used for on-grid “waffle” milling and fine milling of lift-out sections. Yet, robust automated protocols for targeted trench milling, lift-out and sectioning must still be developed.

In summary, we applied various HPF and lamella preparation methods to different plant species and tissues. We discuss their advantages and disadvantages and provide detailed descriptions of the procedures that worked best for plant tissues. We demonstrate that subnanometer structural details are preserved in the process and that meaningful spatial information can be retrieved using rubisco as a model case. Hence, the presented toolbox allows for the first time to do *in situ* structural biology in plant tissues and can likely be adapted to other multicellular systems.

Methods

Plunge-frozen and high-pressure frozen samples were prepared with a Vitrobot Mark 4 (Thermo Fisher Scientific, Waltham, Massachusetts, USA) and a Leica EM-ICE (Leica Microsystems, Wetzlar, Germany), respectively. Three gallium cryo-focused ion beam (FIB) devices were used: (i) a Scios (Thermo Fisher Scientific, Waltham, MA, U.S.A) equipped with an integrated fluorescence microscope (int-FLM: Meteor (Delmic, Delft, Netherlands), MPLFLN 50x objective (Olympos), NA = 0.8, working distcance = 1 mm), (ii) an Aquilos 1 (Thermo Fisher Scientific) with an int-FLM

(Meteor (Delmic), LMPLFLN 50x objective (Olympos), NA = 0.5, working distance = 10.6 mm) and an Aquilos 2 (Thermo Fisher Scientific). All FIBs were additionally equipped with a needle micromanipulator (EasyLift, Thermo Fisher Scientific) for lift-out experiments. The procedures described in the following (including stage orientation and milling pattern orientation) are only correct for the standard FIB/SEM geometry employing a shuttle with a pre-tilt of 45° (**Extended Data Fig. 2a**) and scan rotation for FIB and SEM of 180°.

Physcomitrium patens culture/growth

Physcomitrium patens (Hedw.) Gransden ecotype was cultivated on solid BCDAT medium overlayed with cellophane sheets at 25°C and 18h white light/6h dark cycle as described in[35]. Protonemata were harvested after 2 weeks. For plunge-freezing, the tissue was blended in liquid BCDAT medium, allowed to regenerate for 2 – 4 h and then used for cryo-sample preparations. Gametophores were harvested after 4 weeks. For cryo-fixation, individual phyllids or the gametophore tip containing multiple phyllids were cut off, transferred to liquid BCDAT medium and immediately applied to EM-grids or HPF carriers.

Plunge-freezing and FIB milling of *P. patens* tissues

BCDAT suspended tissues were applied to glow-discharged EM-grids (Quantifoil Cu 200 mesh, holy carbon film R2/1) and transferred to a Vitrobot Mark IV (Thermo Fisher Scientific), temperature set to 25°C and humidity control switched of. Blotting was performed with a Teflon sheet from support film side and a filter paper from the reverse side for 10 s with a blot force 10, before plunging into a liquid ethane-propane mixture[36].

Additionally, different cryoprotectants were tested. Either by culturing *P. patens* on solid BCDAT medium containing cryoprotectants, by incubating *P. patens* after blending in liquid BCDAT medium containing cryoprotectants, by adding 3 µL BCDAT containing cryoprotectants to the EM-grid right before plunging or by combinations of these methods. The different methods with the tested concentrations are listed in **Table 1**. The use of cryoprotectants either did not prevent the formation of crystalline ice or induced plasmolysis (data not shown) and sometimes even dehydrated the tissue (**Extended data Fig. 1f**).

Grids were clipped into cartridges with cutouts (Thermo Fisher Scientific) and loaded into the FIB/SEM instrument. A layer of metal organic platinum was applied for 40 s using the gas injection system (GIS) with the stage in the deposition position (here, stage tilt = 25°, stage rotation = 0°, stage z = 12.5 mm, the GIS deposition position may be different for other instruments). Lamellae were milled with the stage in lamella milling orientation (stage tilt = 15°, stage rotation = 0°, **Extended Data Fig. 2c**). This was done in several steps reducing the thickness to 6 µm, 3 µm and 1.5 µm at currents of 1 nA, 0.5 nA and 0.3 nA, respectively. Fine milling was performed at 50 pA, aiming for a final lamella thickness of 200-250 nm. Finally, the lamella was polished at 30 pA at a stage tilt of 14° and 16° only from the bottom and the top, respectively (**Extended Data Fig. 1a-d**).

The “waffle” workflow for *Physcomitrium patens* protonemata

Grids were high-pressure frozen and milled using an adapted workflow of the “Waffle” Method[18], similar to the procedure described in[19]. The FIB milling and imaging step described in the following were performed in two main stage orientations. The lamella milling orientation (stage tilt = 15-20°, stage rotation = 0) and trench milling orientation (stage tilt = 7°, stage rotation = 180°). A scheme of the stage orientations is depicted in **Extended Data Fig. 2**. More details about the workflow can be found in the step-by-step protocol (Pöge *et al.*, will soon be published as a protocol).

Table 1

Plunge-freezing of *P. patens* with cryoprotectants

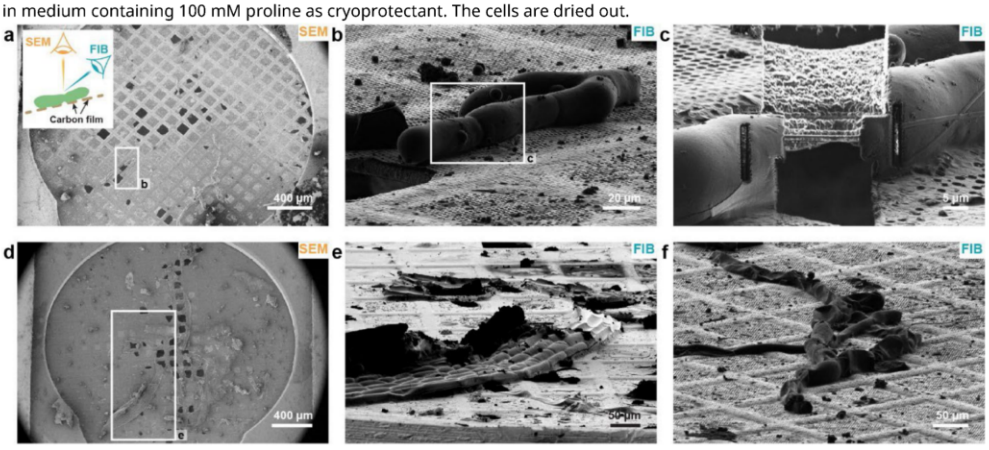
List of the tested plunge-freezing methods with the employed concentrations of cryoprotectants.

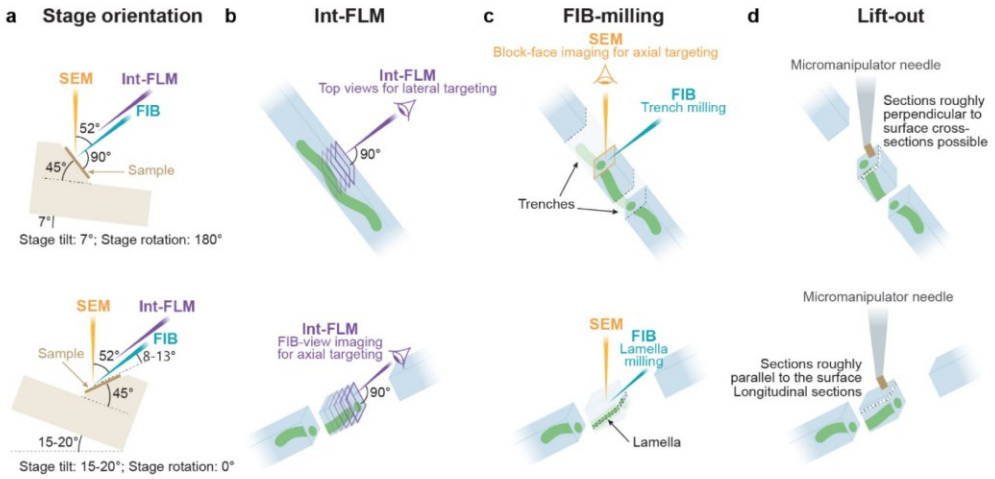
	Culture on Solid BCDAT medium with		Incubation in liquid BCDAT medium with			Before plunging, add 3 µL BCDAT with	
	Cryoprotectant	Concentration	Cryoprot.	Conc. (w/V)	Inc. time	Cryoprotectant	Concentration
Method 1						Sucrose	10 %, 15 %, 20 % (w/V)
Method 2	Proline	50 mM, 75 mM, 100 mM				Proline	50 mM, 75 mM, 100 mM
Method 3	Proline	50 mM, 75 mM, 100 mM	Sucrose	10 %, 20 %	2 h		
Method 4						Glycerol	10 % (w/V)

Extended Data Fig. 1

Plunge-frozen *P. Patens* tissues and the use of cryoprotectants

a-c, Plunge frozen protonemata. **a**, SEM overview image of a grid. **b**,**c**, FIB image before and after lamella milling, respectively. **d**,**e**, SEM and FIB images of plunge frozen phyllids, respectively. **f**, Protonemata grown on medium and plunged in medium containing 100 mM proline as cryoprotectant. The cells are dried out.





Extended Data Fig. 2

The different stage orientations used during lamella preparation

Top and bottom row show the trench milling and lamella milling orientation, respectively, for the geometry in FIB/SEM instruments produced by Thermo Fisher Scientific using a shuttle with 45° pre-tilt. **a**, The shuttle with respect to stage tilt, stage rotation and the relative location of the FIB and SEM beams. **b**, Use of the integrated fluorescence light microscope (int-FLM). In trench milling orientation (top panel), the int-FLM records sample top views for lateral targeting and in lamella milling orientation (bottom panel) it can be used in FIB-view mode for axial targeting. **c**, FIB milling. In trench milling orientation (top panel), the ion beam is normal to the sample surface and used to mill trenches above and below the target area. In Lamella milling orientation (bottom panel), the FIB is used to thin the lamella to a thickness of about 100-300 nm from a shallow angle. **d**, Lift-out. In trench milling orientation (top panel), the lift-out results in sectioning planes roughly normal to the sample surface and cross-sections of protonemata can be obtained. In lamella milling orientation (bottom panel), sectioning planes are roughly parallel to the sample surface resulting in longitudinal sections of protonemata.

High-pressure freezing of “waffle” grids

As described in[19], before the experiment, 6mm Type B carriers (300 µm cavity on one side and flat on the other, Leica Microsystems, Wetzlar, Germany) were incubated overnight in a 1:1 mixture of 4 M NaOH and commercial bleach, rinsed 3x with water, 1x with Acetone and dried. Next, the carriers were dipped into a cetyl palmitate solution (0.5-1% (m/v) in diethyl ether), excess of liquid was removed with a filter paper and the carriers were dried on a filter paper with the flat side facing up. Commercially available Copper 50, 75 or 100 mesh grids with continuous support film (Carbon coated Formvar, Graticules Optics Ltd, Tonbridge, UK) were used to support the sample. As freezing buffer, a 1:1 mixture of growth medium and 40% (m/v) Ficoll 400 (Roth, Karlsruhe, Germany) was prepared. A 2 µL droplet was applied to the flat side of a carrier, a grid with the support film facing down placed on it and the excess of buffer removed with a small piece of Whatman No 1 filter paper (Whatman, Maidstone, UK) until the grid was lying flat on the carrier with a thin layer of buffer between them. 3 µL buffer were added onto the grid and distributed with the pipet tip until the whole grid surface was covered. Air bubbles were removed with tweezers. Next, a small patch of *P. Patens* protonemata was picked from a plate and placed in the center of the grid. A second carrier was placed on top, flat side down, and the whole sandwich tightly squeezed together for 10 s followed by immediate high-pressure freezing. The resulting “waffle” grids were separated from the carriers, clipped into cartridges with cutouts (Thermo Fisher Scientific) and stored until use in liquid nitrogen (LN_2).

Cryo-fluorescence light microscopy

“Waffle” grids have a near featureless surface in SEM and FIB images (**Extended Data Fig. 3a**). Fluorescence microscopy is therefore vital for targeted lamella preparation. For initial screening, clipped grids were loaded into a confocal laser scanning microscope equipped with cryo-stage (Leica TFS SP8, Leica Microsystems, 50x Air objective: Leica Objective No. 506520, NA 0.9, two hybrid detectors and one photomultiplier tube). We always detected the reflected light (excitation wavelength: 488 nm; emission filter: 480-496 nm), the green autofluorescence of the tissue (excitation wavelength: 488 nm; emission filter: 500-750 nm) and the transmitted light. Dependent on the sample thickness, we adjusted the laser power to have enough signal while not overexposing the detectors. Initially, a grid map was acquired (**Extended Data Fig. 3b**) with a spiral scan (512×512 pixel per tile image, pin hole size = 600 µm, pixel size = 580 nm). Promising grid squares containing cell junctions were subsequently imaged by acquiring z-stacks encompassing the whole sample thickness (2048 x 2048 pixel per image, pin hole size = 125 µm, pixel size = 140 nm, z step size = 1 µm, 25-50 steps). Images were recorded using the LAS X software (Leica Microsystems, Wetzlar, Germany). The FLM images displayed in the figures are exclusively single slices of z-stacks and no maximum intensity projections. Squares with several layers of protonemata were ignored because the ~25 µm high wells of the used grids can only accommodate a single cell layer risking squeezing damaged during freezing (**Extended Data Fig. 3d**). Here we used a confocal laser scanning microscope, but a standard widefield system equipped with a cryo-stage could also be used for this screening step.

Lateral targeting and trench milling

Grids were loaded into a FIB/SEM instrument with integrated fluorescence light microscope (int-FLM). A protective layer of metal-organic platinum was applied for 45 s using the GIS with the stage in trench milling orientation (stage tilt = 7°, stage rotation = 180°, **Extended Data Fig. 2**). With the stage in trench milling orientation the coincidence point of FIB and SEM was found on a grid square which contained a target area and a marker pattern (cross-section, xyz: 8 x 8 x 0.5 µm) was milled at a safe distance from the target area. For lateral targeting, sample top views (**Extended Data Fig. 2b** top panel) were recorded with the int-FLM using a reflected light channel (excitation wavelength = 485 nm, no emission filter) to focus on the surface and to find the marker and a green-fluorescence channel (excitation wavelength = 485 nm, emission wavelength =

525 nm). The junctions between *P. patens* cells could be detected based on the green cellular autofluorescence without additional labelling. Z-stacks were acquired (pixel size = 168 nm, 20-25 z-slices, z-step = 1 µm). The distance as well as the location of the target area with respect to the marker was determined (**Extended Data Fig. 3f**) using the Odemis software (Delmic). Dependent on the sample thickness, the laser power was adjusted to have enough signal to detect the target area but kept at the bare minimum to not melt the sample.

Based on the measured distance of the target area from the marker, the position of trench milling patterns were defined. The drift suppression function of the instrument was activated during all trench milling steps. First, two cross-sections with an xy-size of 40×30 µm were milled above and below the target area with a distance of 40 µm at an ion current of 7 nA (step I in **Extended Data Fig. 3e**). Next, the trenches were elongated at 15 nA to a height of 50 µm and 80-120 µm (step II in **Extended Data Fig. 3e**), on bottom and top, respectively. The target area containing block was further thinned in two steps to an xy-size of 35×30 µm and 30×20 µm at 5 nA and 3 nA, respectively (step III and IV in **Extended Data Fig. 3e**). Top views were acquired with FIB and int-FLM after each milling step to adjust the positioning of the patterns, assuring that the targeted area was centered after trench milling (**Extended Data Fig. 3g-h**). Then the block-face on top was polished at 1 nA.

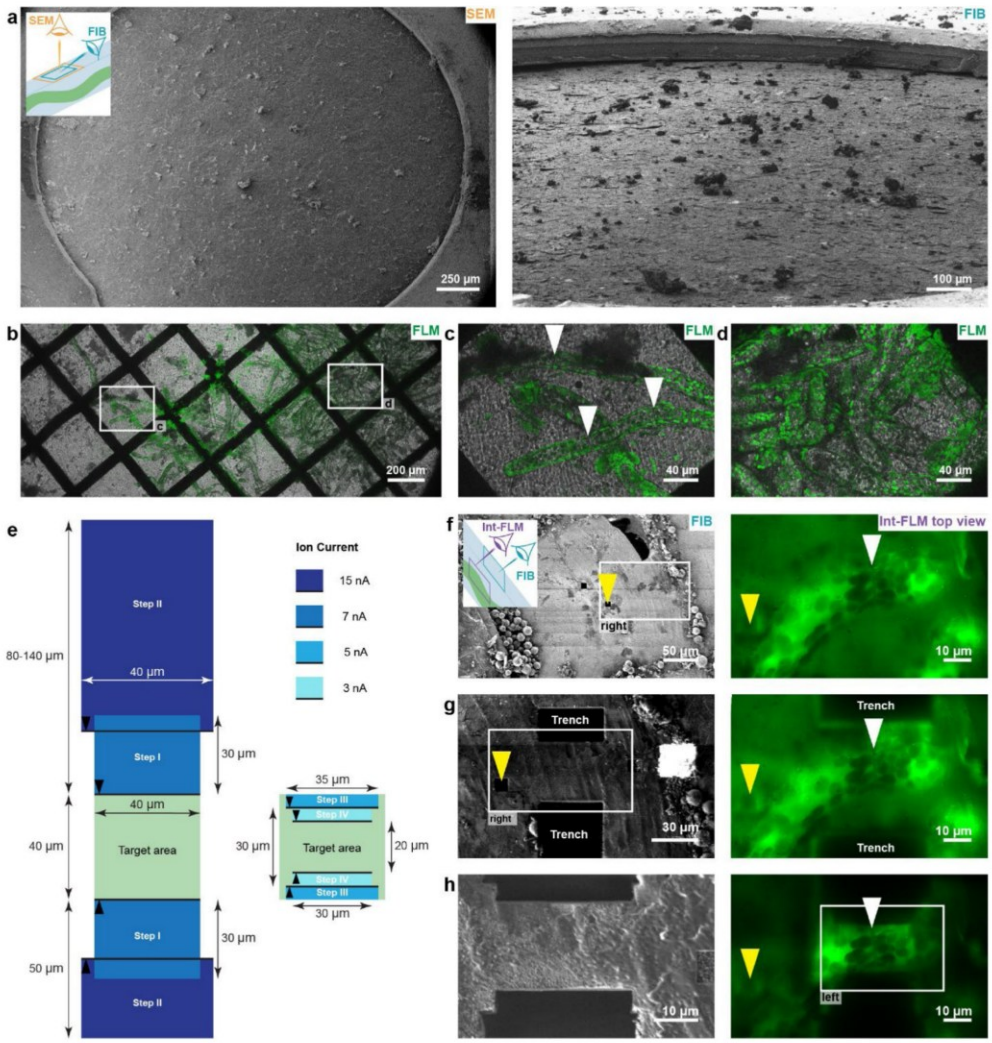
Axial targeting

The images of the int-FLM allow to reliably localize the target area laterally, i.e. in parallel to the sample surface. Due to the limited numerical aperture of the objective, the wide-field epifluorescence optical setup of the int-FLM and depth dependent aberrations, the axial resolution is limited. The axial localization of the target area within the thickness of the sample is crucial to place the patterns for lamella fine milling. Two methods were used for the axial targeting: (i) SEM block-face imaging and (ii) FIB-view imaging with the int-FLM.

After trench milling, with the stage still in trench milling orientation, the SEM images the side surface of the block (**Extended Data Fig. 2c**, top panel). Cellular structures, like membranes, exposed at the FIB milled front of the block, can be visualized with by SEM imaging, even for non-metal stained, vitrified samples[37]. Before the image was recorded, the auto-stigmator function was run on a nearby spherical contamination. The whole block-face was then centered in the SEM field-of-view, the SEM focused on the edge between grid surface and block-face and the auto brightness-contrast function run on the block-face itself. SEM images were acquired with a dwell time of 50 ns, 100 line integrations at U = 3 kV, I = 13 pA with an image size of 3072 x 2048 pixel (**Figure 2d**). If inherent material contrast is sufficiently strong, the approximate distance of the target area from the sample surface can then be measured in the SEM image using the FIB/SEM user interface.

For FIB-view imaging, the int-FLM was used to image the side of the block after trench milling in lamella milling orientation (**Extended Data Fig. 2b**, bottom panel) at the angle at which the lamella will be milled. For optimal imaging, the lamella front has to be normal to the optical path of the int-FLM (Capitanio *et al.*, will soon be described in a manuscript). This allows to avoid major depth-dependent refractive-index-mismatch-induced aberrations[38]. Normal incidence is achieved by changing the stage tilt angle during trench milling steps III-IV (**Extended Data Fig. 3e**). The required stage tilt depends on the stage tilt required for FIB-view imaging which, in turn, is dependent on the stage tilt for lamella fine milling. For waffle milling, FIB-view images were recorded at a stage tilt of 20° in lamella milling orientation, requiring trench milling steps III-IV at - 6° stage tilt. The required stage tilt for trench milling steps III-IV ($\alpha_{\text{Trench milling}}$) as a function of the stage tilt for FIB-view imaging ($\alpha_{\text{FIB-view}}$) can be calculated according to this equation:

$$\alpha_{\text{Trench milling}} = -\alpha_{\text{FIB-view}} + 14°$$



Extended Data Fig. 3

Targeted trench milling aided by the int-FLM

a, SEM and FIB images of a "waffle" grid. **b**-**d**, FLM images of a "waffle" grid (transmitted light in gray and cellular autofluorescence in green). Grid overview in (**b**). The squares mark the field of views in (**c**) and (**d**) which are grid squares containing single and multiple cell layers, respectively. The cells in (**d**) were likely damaged during HPF. **e**, Scheme summarizing all trench milling steps. All trench milling steps are performed in trench milling orientation (**Extended Data Fig. 2**). The milling direction is always towards the target area (indicated by black arrowheads) using regular cross-sections. **f**-**h** FIB (gray) and int-FLM top view images of cellular autofluorescence (green) for successive trench milling steps in the left and right panel, respectively. Int-FLM top views were recorded between trench milling steps to assure the target area was properly centered. First, a marker pattern was milled (yellow arrowhead) and identified in int-FLM images. From there the distance to the target area was measured (white arrowhead) in (**f**). This information was used to place the patterns for milling step I in (**e**). The results are shown in (**g**). After trench milling the target area is centered within the block between trenches (**h**). In (f)-(g) white rectangles indicate the field of view in the second image.

This equation is only valid for the standard geometry used in FIB/SEM instruments employing a shuttle with a pre-tilt of 45°. Care must be taken that the difference between trench milling and FIB-view imaging is not only the stage tilt but also the stage rotation. Trench milling is performed with a stage rotation of 180° and FIB-view imaging with a stage rotation of 0° (**Extended Data Fig. 2**).

First, the lamella front and the target area were identified in the reflected light channel (excitation wavelength = 485 nm, no emission filter) and the green-fluorescence channel (excitation wavelength = 485 nm, emission wavelength = 525 nm), respectively and z-stack recorded (pixel size = 168 nm, 20 z-slices, z-step = 1 µm) using the Odemis software (Delmic). To target the junction between cells, it was sufficient to roughly measure its distance from the sample surface in the Odemis software. For smaller targets, the lamella front can be protected by a layer of metal organic platinum using the GIS and reference marker milled as described (Capitanio *et al.*, will soon be described in a manuscript)

Fine milling of "waffle" lamellae

The surfaces of the block after trench milling were coated with a thick layer of metal organic platinum using the GIS in trench milling orientation and in lamella milling orientation for 15 s and 3 times 20 s, respectively. Fine milling was performed at a stage tilt of 20° in lamella milling orientation (**Extended Data Fig. 2c**). First, all material below the target area was removed at an ion current of 3 nA. Next, regular cross-sections were used to thin the lamella to an xy-size of 30×10 µm with a beam current of 3 nA and then down to 30×6 µm with 1 nA (**Extended Data Fig. 4a**). At this point, a notch similar to[18], but larger, was introduced at current of 0.5 nA (**Extended Data Fig. 4b**). Subsequently, the width of the milling patters was reduced in x to 18-20 µm and the lamella thinned at 0.5 nA to 3 µm, 0.3 nA to 1.5 µm and 0.1 nA to 0.8 µm using regular cross-section patterns (**Extended Data Fig. 4c**). Fine milling was performed with rectangle patterns milled in parallel, aiming for a lamella thickness of 250 nm at 50 pA. Finally, the stage was tilted to 19° and 20.5-21°, removing material only on bottom and top, respectively, at 30 pA.

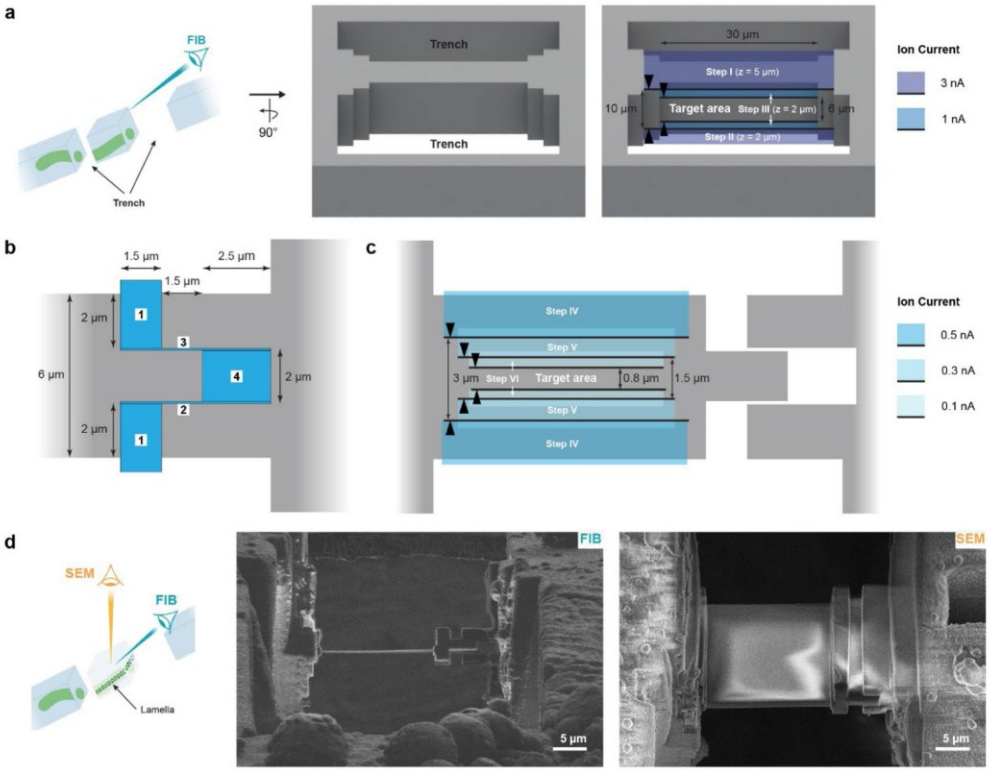
Serial Lift-Out

The EasyLift system (Thermo Fisher Scientific) installed on a Scios and an Aquilos 2 was used for the lift-out experiments. Prior to the lift-out, a copper adapter was attached to the needle of the EasyLift system as described in[19].

Lift-out

The first step of the lift-out experiment was targeted trench milling, as described for "waffle" milling in the previous sections. The width of the block between the trenches depends on the size of the target area. The trenches, however, should be roughly 10 µm wider than the desired width of the final lift-out block as it must be detached from the bulk sample on both sides.

We use redeposition milling to attach a copper adapter to the needle of the micromanipulator, the lift-out block to the copper adapter and the sections to the receiver grid. The pattern used for redeposition milling is an array of regular cross-section with lateral dimensions of 0.5 x 2.5 µm at a distance of 0.25 µm with the multi-pass option set to one. The cross-section patterns are placed along the whole interface of the surfaces that are being attached, on the copper face and the 2.5 µm long dimension is always perpendicular to the attached surface. The milling direction is always away from the interface and the z-dimension of all cross-sections set to 4 µm. On FIB/SEM instruments with imperfect ion beam optics alignment, it can be beneficial to make increase the



Extended Data Fig. 4

Fine milling of “waffle” lamellae

a-**c**, Scheme of the milling patterns used for “waffle” lamella preparation. The block after trench milling and rotating the stage into the lamella milling orientation is shown in (**a**). First the lamella is thinned to a thickness of 6 µm. Then a broad notch is milled (**b**) and the lamella further thinned down (**c**). All thinning steps in (**a**) and (**c**) were milled with regular cross-section with milling direction towards the target area indicated by black arrowheads. Fine milling was then performed with rectangle patterns milled in parallel. **d**, FIB and SEM image of a “waffle” lamella.

size of the cross-sections and the distance between them by 40 – 60 % in all directions. A more detailed description of the milling patterns and the whole workflow can be found in the step-by-step protocol (Pöge *et al.*, will soon be published as a protocol).

We used two distinct lift-out orientations: (i) from the trench milling orientation, the lift-out direction is roughly in the plane of the sample surface or (ii) from the lamella milling orientation where it is roughly perpendicular to the sample surface (**Extended Data Fig. 2d**). For (i) the copper adapter was positioned in the center of the block-face directly after trench milling (**Extended Data Fig. 5b**). Afterwards, the lift-out was performed as described in[19]. For (ii), after trench milling the stage was moved to the lamella milling orientation and a thick layer of metal organic platinum applied by opening the GIS for 3×20 s. Next, all material above and below the target area was removed at 3 nA and the top of the block polished at 1 nA. Then, the copper adapter was positioned in the center on top of the lift-out block and redeposition milling was used to attach it to the lift-out block (**Extended Data Fig. 5a**). Only then was the lift-out block detached from the bulk sample on both sides and subsequently extracted.

Lift-out from different stage orientations can help imaging cells with preferred orientation on the grid from different directions. Lift-out in trench milling orientation results in cross-sections of protonemata if the axis of the filament runs parallel to the lift-out direction (**Extended Data Fig. 5c,e**). In contrast lift-out in lamella milling orientation results in longitudinal sections of protonemata (**Extended Data Fig. 5d,f**).

Lift-in using single-sided attachment

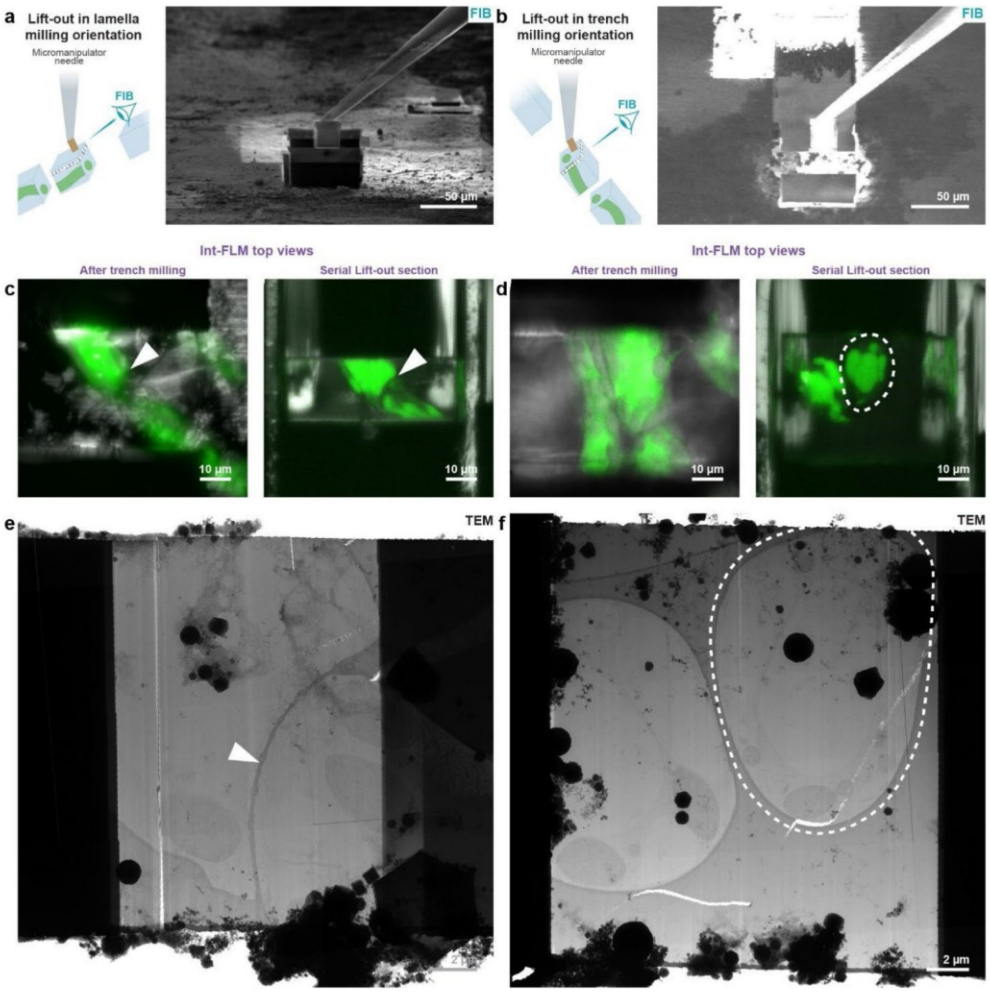
For the single-sided lift-in attachment, copper 4-pin half-moon grids (Pelco FIB-Lift-Out-Grids, Plano GmbH, Wetzlar, Germany) were used as receiver grids. After loading, the grid was rotated into trench milling orientation and marker lines milled on either side at the tip of each pin. After rotating back to lamella milling orientation, the needle, with the lift-out block attached, was reinserted and the lower front edge of the lift-out block was aligned to the marker line (**Extended Data Fig. 6a**). Redeposition milling at 1 nA was used to attach the bottom part of the lift-out block to the pin (**Extended Data Fig. 6b**). The needle was then moved 200 nm up in z to apply some strain. A horizontal line pattern was milled to section the lowest 3-4 µm of the lift-out block and a vertical line pattern above the attachment patterns at the interface between lift-out block and pin used to fully detach the remaining lift-out block. This process of attachment and sectioning was repeated until the lift-out block was sliced up. More details about the exact milling patterns can be found in the step-by-step protocol (Pöge *et al.*, will soon be published as a protocol).

Section trimming

For each section, top views images were recorded with the int-FLM in trench milling orientation to identify sections containing the target area (**Extended Data Fig. 6c**). Next, the GIS was used for 20 s in trench milling orientation. The section was subsequently trimmed down at 3 nA to primarily contain the target area (**Extended Data Fig. 6d**), and the front edge on top was polished at 1 nA. To protect the new lamella front, the GIS was used for 15 s and 3×20 s in trench milling and lamella milling orientation, respectively. This trimming step minimizes the size of the lamella and generates a smooth, coated lamella front, which makes the subsequent fine milling faster and easier.

Fine milling of lamellae with single-sided atatchment

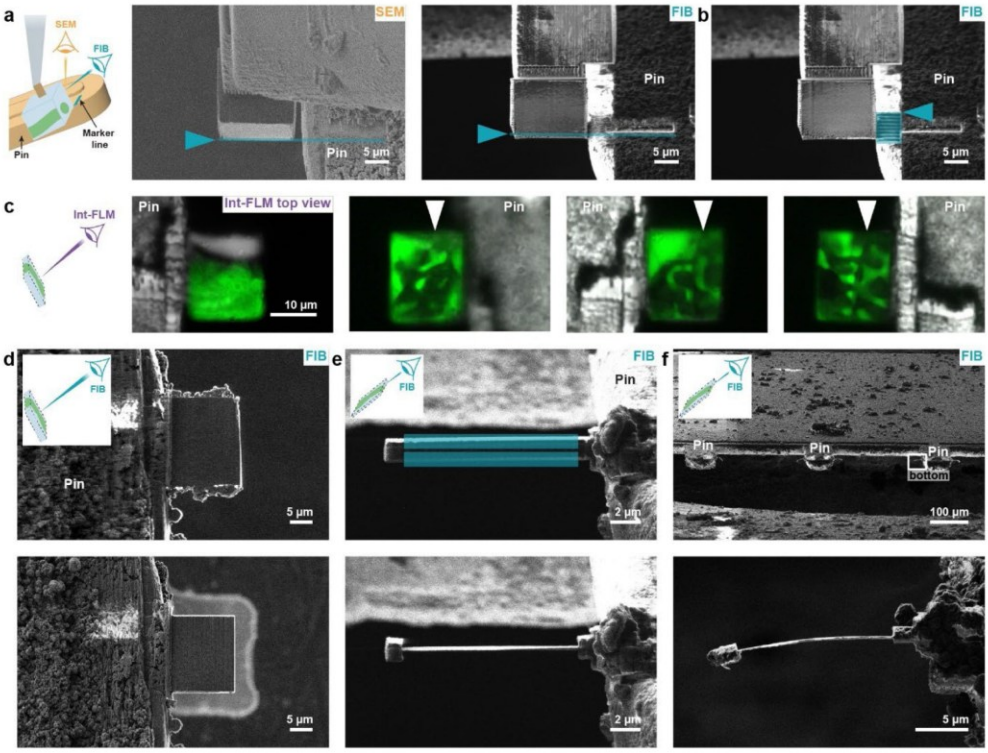
The sections were thinned in lamella milling orientation (stage tilt = 15°) at 1 nA to 2.5 µm and at 0.3 nA to 1.5 µm using regular cross-section patterns. Opposite of the attachment site, a 1.5×1.5 µm block was left which prevents folding[39] of the lamella (**Extended Data Fig. 6e**). Fine milling was done at 50 pA using rectangle patterns milled in parallelset at a distance of 250 nm from one



Extended Data Fig. 5

Lift-out in different stage orientations

The left panel shows data for the lift-out with the stage in lamella milling orientation, the right panel for the lift-out in trench milling orientation. **a**,**b**, FIB images with the needle attached to the lift-out block. **c**,**d**, Int-FLM top views. The left image and the right image were recorded after trench milling and after sectioning, respectively (reflected light in gray and cellular autofluorescence in green). **e**,**f**, TEM overviews of the final lamellae obtained from the sections in (**c**) and (**d**). The outlines of protonemata cross-sections are marked by dashed lines and cell junctions by white arrowheads.



Extended Data Fig. 6

Serial Lift-Out with single-sided attachment

a, Alignment of the lift-out block to the marker line (blue line and arrowhead) in FIB and SEM. **b**, Attachment of the lower part of the lift-out block on one side. The patterns for redeposition milling are indicated in blue. **c**, Int-FLM top views of single-sided attached Serial Lift-Out sections acquired in trench milling orientation (reflected light in gray, cellular autofluorescence in green). The junction between cells is only contained the three right-most sections, marked by white arrowheads. **d**, Section trimming in trench milling orientation. A section before and after trimming is shown in the top and bottom panel, respectively. **e**, Single-sided attached lamella before and after fine milling in the top and bottom panel, respectively. The milling patterns are indicated in blue. A 1.5×1.5 µm block is left opposite of the attachment site. **f**, Single-sided attached lamellae often bend during or after fine milling.

another, followed by tilting to 14° and 15.5°-16° while milling only on bottom and top, respectively, at 30 pA. Lamellae with single-sided attachment had the tendency to bend (**Extended Data Fig. 6f**) making fine milling difficult. Additionally, they often broke during transfers into the TEM and displayed sample movement during data acquisition. By reducing the width of the lamella from the attachment site and increasing its depth along the attachment site, this could be reduced but not completely prevented, especially for lamellae thinner than 200 nm. Thus, we strongly recommend using the double-sided attachment procedure as described below.

Lift-in using double-sided attachment from the sides

For the double-sided attachment, as described in[19], the lift-out block must fit precisely between two neighboring 400 mesh bars of a 400×100 mesh grid (~40 µm). As such, the trench milling patterns were adjusted so that the final lift-out block had a width of 42-45 µm. When mounting the 400×100 mesh grid into the shuttle, it is crucial that the 100 mesh bars are aligned horizontally. Marker lines were milled in trench milling orientation in the middle of 400 mesh bars (**Extended Data Fig. 7a**). Lift-in was performed in lamella milling orientation (stage tilt = 15°). After precise vertical alignment of the 400 mesh bars by rotating the stage, the width of the lift-out block was adjusted to fit precisely between them by FIB milling using cross-sections at 1 nA. The lower front edge of the lift-out block was then aligned to the marker lines of the grid bars in the FIB and SEM channels (**Extended Data Fig. 7b**).

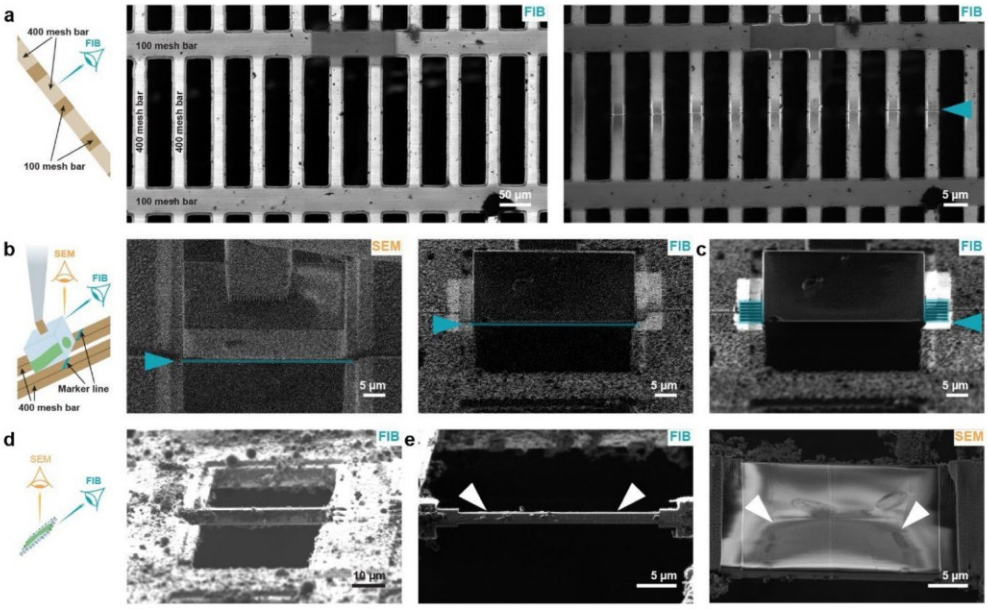
Redeposition milling at 1 nA was used to attach the lower part of the lift-out block to the grid bars on both sides (**Extended Data Fig. 7c**). Then, the needle was moved up in z by 200 nm. A horizontal line pattern was milled to detach the lower 4 µm of the lift-out block and two vertical line patterns were milled on both sides above the attachment patterns at the interface between lift-out block and grid bars to fully detach the remaining lift-out-block. This process of attachment and sectioning was repeated until the whole lift-out block was sliced up. More details about the exact milling patterns can be found in the step-by-step protocol (Pöge *et al.*, will soon be published as a protocol).

Similar to single sided attachment, after sectioning, top views were recorded for each lamella precursor with the int-FLM in trench milling orientation. Regions that did not contain the target area were removed at 3 nA and the front edge on top was polished at 1 nA (**Figure 4**). To protect the new lamella front, the GIS was used for 15 s and 3×20 s in trench milling in lamella milling orientation, respectively.

Fine milling was performed in lamella milling orientation (stage tilt = 15°) in several steps. First, the top of the section was removed at 1 nA. Subsequently, the lateral location of the target area was determined based on either the int-FLM top views recorded prior to section trimming or an SEM block-face image (**Extended Data Fig. 7e**). Using this information, the milling patterns were centered around the target area to reduce the width of the lamella to a minimum. Afterwards, sections were thinned at 1 nA to 2.5 µm, 0.3 nA to 1.5 µm and 0.1 nA to 0.8 µm using regular cross-section patterns. Fine milling was done at 50 pA using rectangle patterns with a distance of 250 nm milled in parallel, followed by tilting to 14° and 15.5°-16° while milling only on bottom and top, respectively, at 30 pA.

Lift-in using double-sided attachment from below

The idea of the attachment from below is to mill two plateaus into neighboring grid bars, both at the same height and parallel to the bottom of the lift-out block. Thus, the lift-out block can be placed on the plateaus instead of being placed between grid bars. Before the lift-out experiment, a 400×100 mesh grid was loaded into the FIB at room temperature and modified. In trench milling orientation, with an ion current of 64 nA, 8×90 µm wide (xy-size) rectangular cavities were milled into the neighboring 400 mesh bars with the lower end of the patterns in the middle of rectangle (**Extended Data Fig. 8a**). The modified grids can be stored until further use.



Extended Data Fig. 7

Serial Lift-Out with double-sided attachment from the sides

a, Milling of marker lines for the alignment of the lift-out block. Grid bars before and after marker line milling in the left and right panel, respectively. Marker lines are indicated by a blue arrowhead. **b**, Alignment of the lift-out block to the marker lines. SEM and FIB images are shown in the left and right panel, respectively. The bottom front edge of the lift-out block is indicated by a blue line and the marker line by a blue arrowhead. **c**, Attachment of the lift-out block on both sides. Patterns for redeposition milling are indicated in blue. **d**, FIB image of a lift-out section. **e**, FIB and SEM image of the section in the left and right panel, respectively, after the top layer was removed. The SEM image reveals the location of the cell junction as target area (white arrowheads) which was, subsequently, used to minimize the width of the milling patterns for lamella fine milling.

For the lift-out experiment, a modified 400×100 mesh grid was loaded with the 100 mesh bars aligned horizontally in lamella milling orientation (stage tilt 15°). Before the first Serial Lift-Out sections could be attached, the actual plateaus were milled in the back of the cavities (**Extended Data Fig. 8b**). First, regular cross-section patterns were milled, preparing the rough plateaus, followed by two rectangle patterns milled in parallel on either side to assure that the plateaus have the same height. The width of the resulting attachment site is between 50-55 µm. The lift-out block must be 1-2 µm slimmer to fit in the gap but must still overlap several micrometers with the plateaus on both sides. This was achieved by adjusting the width of lift-out block during trench milling.

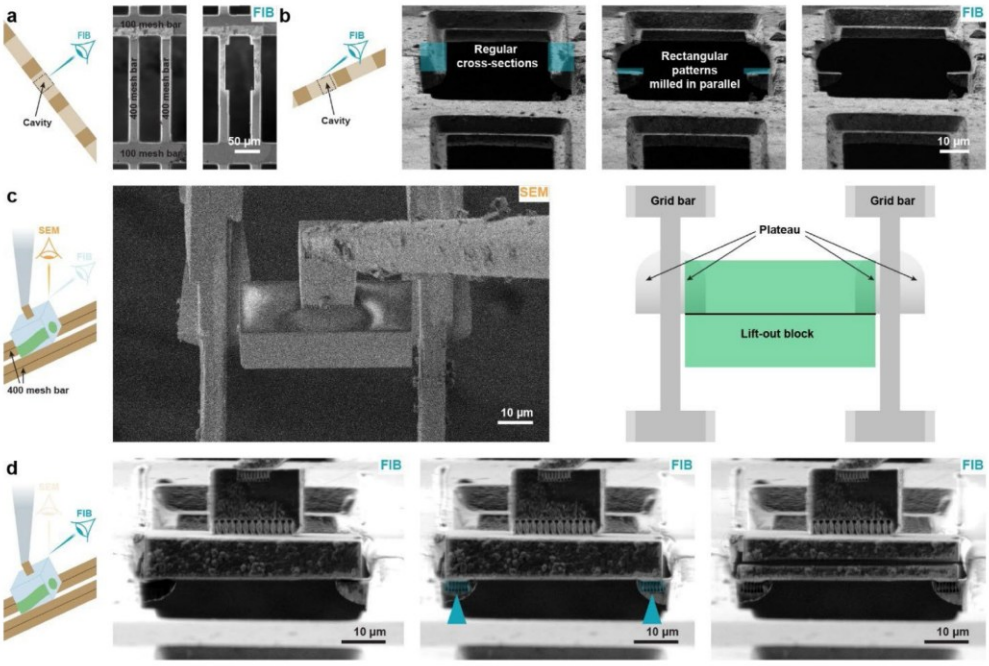
After the lift-out, the bottom of the lift-out block was polished resulting in a surface parallel to the plateaus. Next, the center of the lift-out block was aligned to the front edge of the plateaus (**Extended Data Fig. 8c**). Redeposition milling was used to attach the lower part of the lift-out block on both sides to the plateaus (**Extended Data Fig. 8d**). After the attachment, the needle was moved up in z by 200 nm and a line pattern was used to detach the lowest 3 µm of the lift-out block. This process of attachment and sectioning was repeated until the whole lift-out block was sliced up. Afterwards, top views were recorded with the int-FLM for each section followed by trimming and fine milling as described in the previous section.

In-carrier high-pressure freezing for *P. patens*

Commercially available 3mm Type A and Type B carriers (Leica Microsystems, Wetzlar, Germany) were used for in-carrier HPF. Type A has a 100 µm deep well on one side and a 200 µm well on the other. Type B has only a single 300 µm deep well and is flat on the other side. Carriers were incubated overnight in a 1:1 mixture of 4 M NaOH and commercial bleach, rinsed 3x with water, 1x with Acetone and dried. Subsequently, the type only B carriers were coated by dipping them into cetyl palmitate solution (0.5 (m/v) in diethyl ether), removing excess of liquid with filter paper and drying carriers with the flat side facing up on filter paper. As freezing buffer, a 1:1 mixture of growth medium and 40% Ficoll 400 was used. The 100 µm well of the type A carrier was filled with 2 µL freezing buffer and the droplet spread over the entire well with the pipet tip. A small patch of *P. patens* tissue was placed in the droplet, air bubbles were removed with tweezers and the excess of buffer removed with filter paper until the meniscus of the droplet almost vanished. The type B carrier was placed on top with the flat side down, the sandwich squeezed together and immediately high-pressure frozen. Afterwards, the sample containing type A carriers were recovered and stored until further use.

In-carrier HPF samples were not screened in our FLM as they don not fit into the commercial shuttle. Hence, they were screened using the int-FLM. After loading the samples into the FIB, the sample surface was protected by a layer of metal organic platinum for 45 s by using the GIS with the stage in trench milling orientation. Afterwards, marker patterns were milled (xy-dimensions: 6 x 16 µm and 8 x 8 µm at a distance of ~10 µm with z-dimension = 0.5 µm) and top view images were recorded with the int-FLM, covering area of 1000 µm x 1000 µm around the marker pattern (**Extended Data Fig. 9a**). Targeted trench milling was performed as described for “waffle” grids (**Extended Data Fig. 9b**) with the exception that target areas were also selected based on their proximity to the sample surface, which could be roughly estimated based on where the fluorescence was localized within the acquired int-FLM z-stacks.

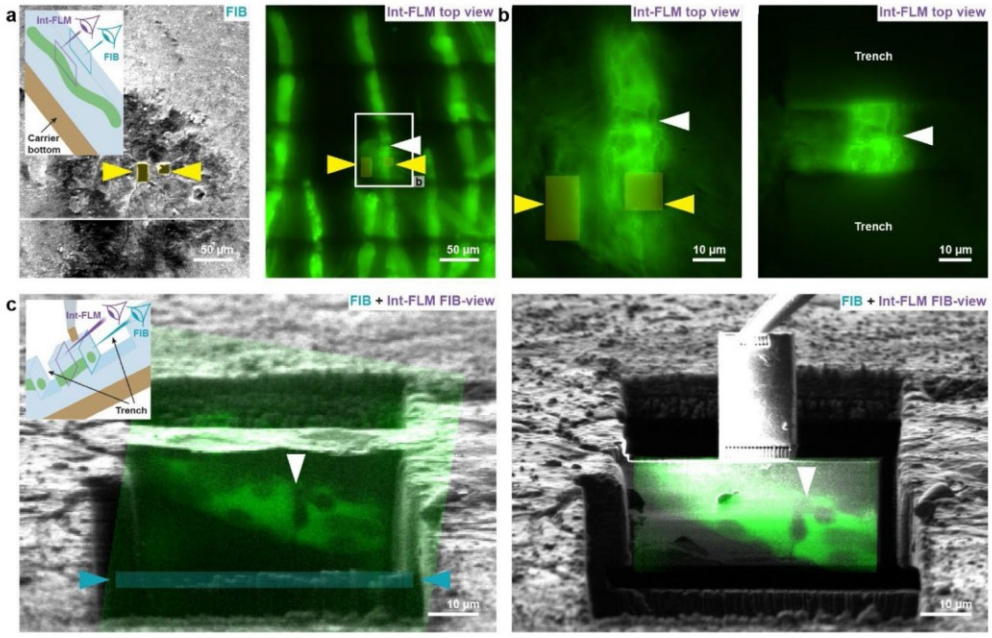
To fully detach the lift-out block from an in-carrier HPF sample, an additional undercut is necessary. First, the axial location of the target area was determined either by FIB-view imaging with the int-FLM (**Extended Data Fig. 9c**) or SEM block-face imaging (**Fig. 2d**). With the stage in lamella milling orientation, the front of the lift-out block protected by metal organic platinum and the undercut milled below the target area at 3 nA. Afterwards, the lift-out was performed as described in the previous section either from the trench milling or the lamella milling orientation.



Extended Data Fig. 8

Serial Lift-Out with double-sided attachment from below

a, Preparation of 8×90 µm cavities in trench milling orientation. **b**, Preparation of the plateaus in lamella milling orientation. Left panel: FIB image of cavities before milling. Middle panel: after milling regular cross-section patterns (xyz: 9 x 8 x 20 µm) generating the rough shape of the plateaus. Due to stage drift, they can have different heights. Right panel: After rectangle patterns were milled in parallel (xyz: 9 x 1 x 20 µm) to even out height differences. This allows the attachment of the bottom of the lift-out block to both plateaus from below. Milling patterns are indicated by blue rectangles. **c**, Alignment of the lift-out block with respect to the plateaus in the SEM. The center of the block should be roughly on top of the front edge of the plateaus (sketch in right panel). Precision of the placement, however, is not imperative. **d**, the lift-out block placed on the plateaus, after attachment from below and after sectioning in the left, middle and right panel, respectively. Patterns for redeposition milling are depicted in blue.



Extended Data Fig. 9

Preparation of in-carrier frozen HPF samples for lift-out

a, Screening of in-carrier frozen HPF sample using the int-FLM. FIB and a montage of int-FLM top view images in left and right panel, respectively. The field-of-view in (**b**) is marked by a white rectangle. **b**, Int-FLM images before and after trench milling in the left and right panel, respectively. In (**a**) and (**b**), marker patterns are labelled with yellow arrowheads and yellow rectangles. **c**, Milling of the undercut, aided by the int-FLM for in-carrier frozen samples. Overlay of FIB images (gray) and int-FLM FIB-view image of cellular autofluorescence (green) before and after milling the undercut in the left and right panel, respectively. Both images were recorded in lamella milling orientation. The undercut is marked by a blue rectangle. In (**a**)-(**c**) cell junctions are labelled by white arrowheads.

Lamella sputter coating after fine milling

Lamellae were sputter coated after fine milling. The sputtering systems on the used Aquilos 1 and Aquilos 2 introduce 5-15 nm sized spheroidal platinum particles onto the lamella surfaces. The sputtering conditions were set to U = 1 kV, p = 0.1-0.2 mbar, I = 10-15 mA, t = 2-4 s. These particles aid frame and tilt-series alignment during TEM data processing. The fiducial based tilt-series alignment resulted in higher quality tomograms than patch tracking approaches.

"Waffle" workflow for *P. patens* phyllids

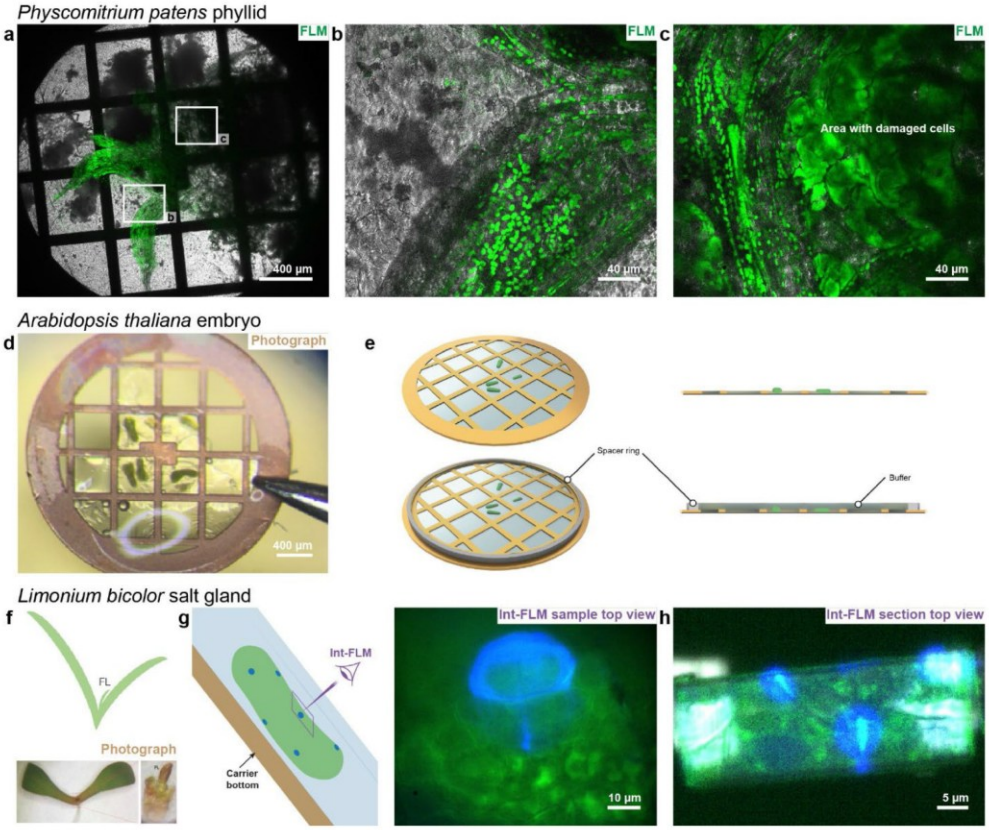
The "waffle" grids of *P. patens* phyllids were prepared similar to protonemata. A cleaned and cetyl palmitate coated 6 mm type B carrier was placed with the flat side facing up on filter paper and a 3 µL droplet of freezing buffer placed on it. Next, a 50 mesh EM-grid with continuous support film (Carbon coated Formvar, Graticules Optics Ltd, Tonbridge, UK) was placed on the droplet with the support side facing down and excess of buffer removed until the grid was resting flat on the carrier. A 3 µL droplet of freezing buffer was added on top of the grid and distributed to fill all wells formed by support film and grid bars and air bubbles removed with sharp tweezers. A small piece of phyllid was cut from the gametophore with fine surgical tools and placed in the center of the grid. A second coated 6 mm type B carrier was placed with the flat side facing down on top, the sandwich squeezed together and excess of buffer removed with a filter paper. Next the sandwich was mounted for HPF and squeezed tightly for 10 s right before freezing. Areas of tissue that were damaged in the process could be identified in the FLM (**Extended Data Fig. 10a-c**). In areas with largely intact cells, individual chloroplasts can be resolved (**Extended Data Fig. 10b**), whereas for damaged cells, the green autofluorescence signal is diffusely distributed throughout the whole cell (**Extended Data Fig. 10c**). Lamellae were otherwise prepared by "waffle" milling or lift-out as described in the previous sections.

The "waffle" workflow for extracted *Arabidopsis thaliana* embryos

A. thaliana ecotype Columbia (Col_0) was grown 5-7 weeks in soil at 22.5° with a photoperiod of 16/8 h (day/night). The isolation of embryos was performed on the preparation table of the Leica EM-ICE high-pressure freezer using its integrated binocular microscope. As freezing buffer, 20% Ficoll 400 (w/v) dissolved in PBS was used. The first eight siliques were cut with fine scissors and placed on a glass slide in a drop of freezing buffer. Next, embryos were hand dissected with sharp tweezers as described in reference[40] and collected. A 50 mesh EM-grid with continuous support film (Carbon coated Formvar, Graticules Optics Ltd, Tonbridge, UK) was placed with the support facing down in a 3 µm droplet of freezing buffer on the flat side of a cetyl palmitate coated 6 mm Type B HPF carrier. The excess of buffer was blotted away with filter paper until the support film was flat on the carrier. Several embryos were picked up with tweezers and placed in the wells formed by grid bars and support film (**Extended Data Fig. 10d**). A spacer ring (Provider) with a height of 50 µm was added onto the grid and filled with a 2 µL drop of freezing buffer. Air bubbles were removed with tweezers. Afterwards, the sandwich was closed with a second 6 mm type B carrier flat side facing down, the sample high-pressure frozen, the grid recovered and stored in a grid box in LN_2.

Targeting the salt gland of in-carrier frozen *Limonium bicolor*

The culture conditions *L. bicolor* Kuntze, fluorescence microscopy detection of salt glands and HPF procedures are similar to those described previously[41] with minor modifications. Namely, *L. bicolor* seeds were stored in a refrigerator at 4 C before use. The seeds were then surface disinfected in 70% (v/v) ethanol for 5 min and subsequently in 6% (w/v) sodium hypochlorite (freshly prepared) for 20 min and then thoroughly washed with deionized water. Fully filled seeds were selected and planted in MS culture medium plates. These plates were incubated in a plant tissue culture room at a temperature of 26/22°C (day/night), a photoperiod of 16/8 h (day/night) and



Extended Data Fig. 10

HPF workflows applied to other tissues and species

a-**c**, *Physcomitrium patens* phyllids. **a**, FLM overview of a phyllid "waffle" grid. **b**, Grid square containing seemingly intact tissue. **c**, Grid square containing damaged tissue. **d**,**e** *Arabidospsi thaliana* embryos. **d**, Image of embryos placed in the squares of a 50 mesh grid. **e**, Schematic of a "waffle" grid with and without a spacer ring. Embryos fit into grid squares but are thicker than the grid bars and would therefore be damaged during freezing (top panel). The addition of a spacer ring, as described in[18], prevents squeezing damage and can allow high-pressure freezing of thicker samples. **f**-**h**, Salt gland of *Limonium bicolor*. **f**, Dissection of the first true leaf (FL). The top panel shows a scheme of the FL location in 2 weeks old plants. The bottom panel are photographs of a whole two weeks old plant before and the dissected FL in the left and right panel, respectively. **g**, int-FLM top view image of the salt gland of in-carrier frozen FL. **h**, int-FLM image top view image of a Serial Lift-Out section containing a fraction of the salt gland. In (**g**) and (**h**) autofluorescence of the salt gland is shown in blue, the cellular autofluorescence in green and the reflected light in gray.

a light intensity of 600 µmol·m-2·s-1. After 2 weeks, the first true leaf (FL, **Extended Data Fig. 10f**) of the whole plant was dissected with an thin knife, placed in the 300 µm deep cavity of a 3 mm Type B HPF carrier filled with with 20% (w/v) Ficoll 400. Afterwards, the cavity was closed off with a second Type B carrier, flat side facing down, the specimen was high-pressure frozen and the sample containing carrier recovered. Fluorescence targeting of the salt gland was performed using the int-FLM recording green autofluorescene (excitation wavelength = 485 nm, emission wavelength = 525 nm), blue autofluorescence (excitation wavelength = 385 nm, emission wavelength = 432 nm) as well as the reflected light (excitation wavelength = 385 nm, no emission filter, **Extended Data Fig. 10g**). Serial Lift-Out with the attachment from below was then performed as described in the previous sections (**Extended Data Fig. 10h**).

TEM Imaging

One part of the TEM data was collected on a Titan Krios G2 (Thermo Fisher Scientific) with BioQuantum energy filter (Gatan, Pleasanton, California, USA) and K2 summit camera (Gatan). Automated data acquisition was performed in SerialEM[42,43] (version 4.1). Lamella montages were recorded at 8700x magnification (pixel size = 2.6 nm). Tomograms were acquired at 42000x, 53000x or 64000x magnification (pixel sizes of 3.52 Å, 2.62 Å and 1.98 Å, respectively), at target defoci of −4 µm to −6 µm, using a dose symmetric tilt scheme between ±50°to ±60° with an angular increment of 2° or 3°, taking the pretilt of the lamellae into account. The exposure time was kept constant for all tilt images resulting in total doses per tilt-series of 80-125 $e^-/Å^2$. Typically, 10 frames were recorded per tilt image and saved in TIF-file format.

The other part of the data was recorded on a Titan Krios G4 equipped with a Selectris X energy filter and a Falcon 4i camera (Thermo Fisher Scientific). Lamella montages were recorded at a magnification of 8700x (pixel size = 2.8 nm). Tomograms were recorded at 42000x or 64000x (pixel sizes of 2.93 Å and 1.89 Å, respectively) with defoci between −3 µm and −6 µm. Data was acquired using the Tomography 5 software package version 5.12.0 (Thermo Fisher Scientific) and stored in EER file format.

Data preprocessing

Tilt-series were processed using the TOMOMAN[44] (version 0.6.9) pipeline. Movie frames were motion corrected in MotionCor2[45] (version 1.4.7). EER frames were grouped to obtain between 8 and 20 frames per movie. Bad tilt images, i.e. improperly tracked images or blurry images due to lamella instabilities, were removed after manual inspection and dose-weighting was performed according to[46] using the corresponding TOMOMAN scripts. If tilt-series contained at least 5 platinum fiducials introduced by sputtering evenly distributed over the field-of-view, IMOD[47] (version 4.11.25) fiducial tracking was employed for tilt-series alignment. Otherwise, AreTomo[48] version 1.3.3 was used for tilt-series alignment. Afterwards, 4x binned tomograms were reconstructed with the weighted back projection algorithm implemented in IMOD.

For denoising, tilt series containing only the information of odd or even frames were obtained during motion correction. The odd and even tilt-series were preprocessed to generate 4x binned odd and even tomograms using the same alignment files as for the full tilt-series. Denoising was performed in cryo-CARE[49]. First, 800-1000 training volumes with a box size 72^3 voxel were cropped from the odd and even tomograms. A network was trained for each tomogram over 150 epochs with 75 steps and a Unet depth of 3. The network was then used to denoise the 4x binned tomograms. All TEM data, including tomograms and lamella overviews, were visualized with IMOD[50] (version 4.11.25). Only slices of denoised tomograms are shown in this work.

Subtomogram averaging of rubisco

The detailed workflow for subtomogram averaging and spatial analysis for rubisco is described in the Supplementary Information. In brief, a subset of 10 tomograms were recorded on *P. patens* protonemata chloroplasts with defoci between −2.5 and −5 µm. Tilt-series were aligned and reconstructed in IMOD and imported into WARP[51] (version 1.0.9). Membranes were segmented using MemBrain-seg[52] and the chloroplast volumes were manually annotated in Amira (Amira 3D 2021.2, Thermo Fisher Scientific) to create a mask for score maps as output of template matching. A first template was created by picking 500 rubisco complexes manually (50 complexes per tomogram) and aligning them in RELION[53] (version 3.0.5) rubisco was picked by template matching in StopGap[54] (version 0.7.0). After several rounds of subtomogram alignment and classification in RELION and tilt-series alignment in *M*[55] (version 1.0.9) the final density map was calculated using 6,180 particles and applying C4 symmetry (**Fig. 4c**). An octamer of large rubisco subunits (monomer UniProt accession P34915) was predicted in AlphaFold3[28] and docked into the final subtomogram average using the "fit" function in ChimeraX[56] (version 1.6.1) without further refinement of the model (**Fig. 4c-d**). The spatial analysis of rubisco particles was performed based on 55,000 particles after a first round of classification in RELION similar to[57]. The 3D rendered image of chloroplast membranes and rubisco positions was displayed in ChimeraX using the ArtiaX plug-in[58].

Acknowledgements

We thank Dustin Morado, Tillman Schäfer, Daniel Bollschweiler, Dominik Hrebik and Hui Guo for support with the TEMs, the lab of Ben Engel for many fruitful discussions, Iuliia Iermak for help with 3D rendering and Florian Beck for invaluable input on data processing. The *Limonium bicolor* Kuntze (Plumbaginaceae)[59,60] seeds were kindly provided by Fang Yuan and Bao-Shan Wang from Shandong Normal University. This work received funding from the European Research Council (ERC Grant agreements 'SymPore' no. 951292).

Additional files

Supplementary information

References

1. Lučič V., Rigort A., Baumeister W (2013) **Cryo-electron tomography: the challenge of doing structural biology in situ** *J. Cell Biol* **202**:407–419

2. Beck M., Baumeister W (2016) **Cryo-Electron Tomography: Can it Reveal the Molecular Sociology of Cells in Atomic Detail?** *Trends Cell Biol* **26**:825–837

3. Plitzko J. M., Schuler B., Selenko P (2017) **Structural Biology outside the box—inside the cell** *Curr. Opin. Struct. Biol* **46**:110–121

4. Asano S., Engel B. D., Baumeister W (2016) **In Situ Cryo-Electron Tomography: A Post-Reductionist Approach to Structural Biology** *J. Mol. Biol* **428**:332–343

5. Raven J. A. (1987) **The role of Vacuoles** *New Phytol* **106**:357–422

6. Dobro M. J., Melanson L. A., Jensen G. J., McDowall A. W. (2010) **Chapter Three - Plunge Freezing for Electron Cryomicroscopy** In: Jensen G. J. B. T.-M., editors. *Cryo-EM Part A Sample Preparation and Data Collection* Academic Press pp. 63–82

7. Bäuerlein F. J. B., et al. (2017) **In Situ Architecture and Cellular Interactions of PolyQ Inclusions** *Cell* **171**:179–187

8. Dubochet J (1995) **High-pressure freezing for cryoelectron microscopy** *Trends Cell Biol* **5**:366–368

9. Rigort A., et al. (2012) **Focused ion beam micromachining of eukaryotic cells for cryoelectron tomography** *Proc. Natl. Acad. Sci* **109**:4449–4454

10. Arnold J., et al. (2016) **Site-Specific Cryo-focused Ion Beam Sample Preparation Guided by 3D Correlative Microscopy** *Biophys. J* **110**:860–869

11. Bieber A., et al. (2022) **In situ structural analysis reveals membrane shape transitions during autophagosome formation** *Proc. Natl. Acad. Sci* **119**:e2209823119

12. Mahamid J., et al. (2015) **A focused ion beam milling and lift-out approach for site-specific preparation of frozen-hydrated lamellas from multicellular organisms** *J. Struct. Biol* **192**:262–269

13. Harapin J., et al. (2015) **Structural analysis of multicellular organisms with cryo-electron tomography** *Nat. Methods* **12**:634–636

14. Schaffer M., et al. (2019) **A cryo-FIB lift-out technique enables molecular-resolution cryo-ET within native Caenorhabditis elegans tissue** *Nat. Methods* **16**:757–762

15. Klumpe S., et al. (2021) **A modular platform for automated cryo-FIB workflows** *eLife* **10**:e70506

16. Kuba J., et al. (2021) **Advanced cryo-tomography workflow developments – correlative microscopy, milling automation and cryo-lift-out** *J. Microsc* **281**:112–124

17. Klumpe S., et al. (2022) **Recent Advances in Gas Injection System-Free Cryo-FIB Lift-Out Transfer for Cryo-Electron Tomography of Multicellular Organisms and Tissues** *Micros. Today* **30**:42–47

18. Kelley K., et al. (2022) **Waffle Method: A general and flexible approach for improving throughput in FIB-milling** *Nat. Commun* **13**:1857

19. Schiøtz O. H., et al. (2023) **Serial Lift-Out: sampling the molecular anatomy of whole organisms** *Nat. Methods* https://doi.org/10.1038/s41592-023-02113-5

20. Nguyen H. T. D., et al. (2024) **Serialized on-grid lift-in sectioning for tomography (SOLIST) enables a biopsy at the nanoscale** *Nat. Methods* **21**:1693–1701

21. Hippe-Sanwald S (1993) **Impact of freeze substitution on biological electron microscopy** *Microsc. Res. Tech* **24**:400–422

22. Gilkey J. C., Staehelin L. A (1986) **Advances in ultrarapid freezing for the preservation of cellular ultrastructure** *J. Electron Microsc. Tech* **3**:177–210

23. Rensing S. A., Goffinet B., Meyberg R., Wu S. Z., Bezanilla M (2020) **The moss physcomitrium (Physcomitrella) patens: A model organism for non-seed plants** *Plant Cell* **32**:1361–1376

24. Schertel A., et al. (2013) **Cryo FIB-SEM: Volume imaging of cellular ultrastructure in native frozen specimens** *J. Struct. Biol* **184**:355–360

25. Schaffer M., et al. (2017) **Optimized cryo-focused ion beam sample preparation aimed at in situ structural studies of membrane proteins** *J. Struct. Biol* **197**:73–82

26. Nawaz M. A., Kasote D. M., Ullah N., Usman K., Alsafran M (2024) **RuBisCO: a sustainable protein ingredient for plant-based foods** *Front. Sustain. Food Syst* **8**

27. Briggs J. A. G (2013) **Structural biology in situ—the potential of subtomogram averaging** *Curr. Opin. Struct. Biol* **23**:261–267

28. Abramson J., et al. (2024) **Accurate structure prediction of biomolecular interactions with AlphaFold 3** *Nature* **630**:493–500

29. Freeman Rosenzweig E. S., et al. (2017) **The Eukaryotic CO2-Concentrating Organelle Is Liquid-like and Exhibits Dynamic Reorganization** *Cell* **171**:148–162

30. Fuest M., et al. (2019) **In situ Microfluidic Cryofixation for Cryo Focused Ion Beam Milling and Cryo Electron Tomography** *Sci. Rep* **9**

31. Gemin O., et al. (2024) **EasyGrid: A versatile platform for automated cryo-EM sample preparation and quality control** *bioRxiv* https://doi.org/10.1101/2024.01.18.576170

32. Zachs T., et al. (2020) **Fully automated, sequential focused ion beam milling for cryo-electron tomography** *eLife* **9**:e52286

33. Buckley G., et al. (2020) **Automated cryo-lamella preparation for high-throughput in-situ structural biology** *J. Struct. Biol* **210**

34. Cleeve P., et al. (2023) **OpenFIBSEM: A universal API for FIBSEM control** *J. Struct. Biol* **215**

35. Cove D. J., et al. (2009) **Culturing the moss Physcomitrella patens** *Cold Spring Harb. Protoc* **4**:1–6

36. Tivol W. F., Briegel A., Jensen G. J (2008) **An Improved Cryogen for Plunge Freezing** *Microsc. Microanal* **14**:375–379

37. Vidavsky N., et al. (2016) **Cryo-FIB-SEM serial milling and block face imaging: Large volume structural analysis of biological tissues preserved close to their native state** *J. Struct. Biol* **196**:487–495

38. Diel E. E., Lichtman J. W., Richardson D. S (2020) **Tutorial: avoiding and correcting sample-induced spherical aberration artifacts in 3D fluorescence microscopy** *Nat. Protoc* **15**:2773–2784

39. Ji D., et al. (2019) **Freestanding crystalline oxide perovskites down to the monolayer limit** *Nature* **570**:87–90

40. Xiang D., et al. (2011) **Genome-Wide Analysis Reveals Gene Expression and Metabolic Network Dynamics during Embryo Development in Arabidopsis** *Plant Physiol* **156**:346–356

41. Feng Z.-T., et al. (2015) **K+ accumulation in the cytoplasm and nucleus of the salt gland cells of Limonium bicolor accompanies increased rates of salt secretion under NaCl treatment using NanoSIMS** *Plant Sci* **238**:286–296

42. Mastronarde D. N (2003) **SerialEM: A Program for Automated Tilt Series Acquisition on Tecnai Microscopes Using Prediction of Specimen Position** *Microsc. Microanal* **9**:1182–1183

43. Mastronarde D. N (2005) **Automated electron microscope tomography using robust prediction of specimen movements** *J. Struct. Biol* **152**:36–51

44. Khavnekar S., Erdmann P., Wan W (2023) **TOMOMAN: Streamlining Cryo-electron Tomography and Subtomogram Averaging Workflows Using TOMOgram MANager** *Microsc. Microanal* **29**:1020

45. Zheng S. Q., et al. (2017) **MotionCor2: anisotropic correction of beam-induced motion for improved cryo-electron microscopy** *Nat. Methods* **14**:331–332

46. Grant T., Grigorieff N (2015) **Measuring the optimal exposure for single particle cryo-EM using a 2.6 Å reconstruction of rotavirus VP6** *eLife* **4**:e06980–e06980

47. Mastronarde D. N., Held S. R (2017) **Automated tilt series alignment and tomographic reconstruction in IMOD** *J. Struct. Biol* **197**:102–113

48. Zheng S., et al. (2022) **AreTomo: An integrated software package for automated marker-free, motion-corrected cryo-electron tomographic alignment and reconstruction** *J. Struct. Biol. X* **6**:100068

49. Buchholz T., Jordan M., Pigino G., Jug F (2019) **Cryo-CARE: Content-Aware Image Restoration for Cryo-Transmission Electron Microscopy Data** In: *2019 IEEE 16th International Symposium on Biomedical Imaging (ISBI 2019)* pp. 502–506 https://doi.org/10.1109/ISBI.2019.8759519

50. Kremer J. R., Mastronarde D. N., McIntosh J. R (1996) **Computer Visualization of Three-Dimensional Image Data Using IMOD** *J. Struct. Biol* **116**:71–76

51. Tegunov D., Cramer P (2019) **Real-time cryo-electron microscopy data preprocessing with Warp** *Nat. Methods* **16**:1146–1152

52. Lamm L., et al. (2024) **MemBrain v2: an end-to-end tool for the analysis of membranes in cryo-electron tomography** *bioRxiv* https://doi.org/10.1101/2024.01.05.574336

53. Zivanov J., et al. (2022) **A Bayesian approach to single-particle electron cryo-tomography in RELION-4.0** *eLife* **11**:e83724

54. Wan W., Khavnekar S., Wagner J (2024) **STOPGAP: an open-source package for template matching, subtomogram alignment and classification** *Acta Crystallogr. Sect. D* **80**:336–349

55. Tegunov D., Xue L., Dienemann C., Cramer P., Mahamid J (2021) **Multi-particle cryo-EM refinement with M visualizes ribosome-antibiotic complex at 3.5 Å in cells** *Nat. Methods* **18**:186–193

56. Pettersen E. F., et al. (2021) **UCSF ChimeraX: Structure visualization for researchers, educators, and developers** *Protein Sci* **30**:70–82

57. Martinez-Sanchez A., Baumeister W., Lučić V (2022) **Statistical spatial analysis for cryo-electron tomography** *Comput. Methods Programs Biomed* **218**

58. Ermel U. H., Arghittu S. M., Frangakis A. S (2022) **ArtiaX: An electron tomography toolbox for the interactive handling of sub-tomograms in UCSF ChimeraX** *Protein Sci* **31**:e4472

59. Yuan F., et al. (2015) **Comparative transcriptome analysis of developmental stages of the imonium bicolor leaf generates insights into salt gland differentiation** *Plant. Cell Environ* **38**:1637–1657

60. Yuan F., et al. (2022) **The genome of the recretohalophyte Limonium bicolor provides insights into salt gland development and salinity adaptation during terrestrial evolution** *Mol. Plant* **15**:1024–1044

Author information

Matthias Pöge
Emeritus Group Molecular Structural Biology, Max Planck Institute of Biochemistry, Martinsried, Germany
ORCID iD: 0000-0003-2331-4638

For correspondence: bcube.poege@gmail.com

Marcel Dickmanns
Emeritus Group Molecular Structural Biology, Max Planck Institute of Biochemistry, Martinsried, Germany, Heinrich Heine University Düsseldorf, Faculty of Mathematics and Natural Sciences, Institute of Molecular Physiology, Düsseldorf, Germany
ORCID iD: 0000-0003-4001-707X

Peng Xu
Emeritus Group Molecular Structural Biology, Max Planck Institute of Biochemistry, Martinsried, Germany

Meijing Li
Emeritus Group Molecular Structural Biology, Max Planck Institute of Biochemistry, Martinsried, Germany, Shenzhen Medical Academy of Research and Translation, Shenzhen, China

Oda H Schiøtz
Research Group CryoEM Technology, Max Planck Institute of Biochemistry, Martinsried, Germany
ORCID iD: 0009-0008-3301-8270

Christoph OJ Kaiser
Research Group CryoEM Technology, Max Planck Institute of Biochemistry, Martinsried, Germany
ORCID iD: 0000-0002-8481-6845

Jianfei Ma
Emeritus Group Molecular Structural Biology, Max Planck Institute of Biochemistry, Martinsried, Germany, State Key Laboratory of Medicinal Chemical Biology and College of Life Sciences, Nankai University, Tianjin, China

Anna Bieber
Emeritus Group Molecular Structural Biology, Max Planck Institute of Biochemistry, Martinsried, Germany, Research Department Molecular Machines and Signaling, Max Planck Institute of Biochemistry, Martinsried, Germany
ORCID iD: 0000-0001-5014-6620

Cristina Capitanio
Emeritus Group Molecular Structural Biology, Max Planck Institute of Biochemistry, Martinsried, Germany, Research Department Molecular Machines and Signaling, Max Planck Institute of Biochemistry, Martinsried, Germany
ORCID iD: 0000-0002-5297-9156

Johann Brenner
Research Group CryoEM Technology, Max Planck Institute of Biochemistry, Martinsried, Germany
ORCID iD: 0000-0003-1306-3564

Margot Riggi
Department of Cell and Virus Structure, Max Planck Institute of Biochemistry, Martinsried, Germany
ORCID iD: 0000-0002-8930-5331

Sven Klumpe
Research Group CryoEM Technology, Max Planck Institute of Biochemistry, Martinsried, Germany
ORCID iD: 0000-0002-8350-6503

Manuel Miras
Heinrich Heine University Düsseldorf, Faculty of Mathematics and Natural Sciences, Institute of Molecular Physiology, Düsseldorf, Germany, Department of Stress Biology and Plant Pathology, CEBAS-CSIC, Murcia, Spain
ORCID iD: 0000-0002-3636-0265

Neda S Kazemein Jasemi
Heinrich Heine University Düsseldorf, Faculty of Mathematics and Natural Sciences, Department of Developmental Genetics, Düsseldorf, Germany, Division of Molecular Embryology, German Cancer Research Center (DKFZ), Heidelberg, Germany
ORCID iD: 0000-0002-7842-6998

Waltraud X Schulze
Department of Plant Systems Biology, University of Hohenheim, Stuttgart, Germany
ORCID iD: 0000-0001-9957-7245

Rüdiger Simon
Heinrich Heine University Düsseldorf, Faculty of Mathematics and Natural Sciences, Department of Developmental Genetics, Düsseldorf, Germany
ORCID iD: 0000-0002-1317-7716

Wolf B Frommer
Heinrich Heine University Düsseldorf, Faculty of Mathematics and Natural Sciences, Institute of Molecular Physiology, Düsseldorf, Germany, Cluster of Excellence on Plant Sciences (CEPLAS), Heinrich Heine University, Düsseldorf, Germany, Institute of Transformative Bio-Molecules, Nagoya University, Nagoya, Japan
ORCID iD: 0000-0001-6465-0115

Jürgen M Plitzko
Research Group CryoEM Technology, Max Planck Institute of Biochemistry, Martinsried, Germany
ORCID iD: 0000-0002-6402-8315

Wolfgang Baumeister
Emeritus Group Molecular Structural Biology, Max Planck Institute of Biochemistry, Martinsried, Germany
ORCID iD: 0000-0001-8154-8809

Editors

Reviewing Editor
Sjors Scheres
MRC Laboratory of Molecular Biology, Cambridge, United Kingdom

Senior Editor
Volker Dötsch
Goethe University Frankfurt, Frankfurt am Main, Germany

Reviewer #1 (Public review):

Summary:

This in situ cryo-ET workflow of selected plant structures provides several detailed strategies using plunge-freezing and the HPF waffle method and lift-out for notoriously difficult samples (compared to cell culture, yeast, and algae, which are far more prevalent in the literature).

Strengths:

A very difficult challenge whereby the authors demonstrate successful vitrification of selected plants/structures using waffle and lift-out approaches for cryoET. Because there are relatively few examples of multi-cellular plant cryo-ET in the literature, it is important for the scientific community to be motivated and have demonstrated strategies that it is achievable. This manuscript has a number of very helpful graphics and videos to help guide researchers who would be interested in undertaking that would help shorten the learning curve of admittedly tedious and complex workflows. This is a slow and tedious process, but you have to start somewhere, and I applaud the authors for sharing their experiences with others, and I expect will help other early adopters to come up to speed sooner.

Weaknesses:

While important, the specific specimen and cell-types selected that were successful (perhaps other plant specimen and tissues tried were unsuccessful and thus not reported) in this approach did not demonstrate success to broadly applicable to other much more prevalent and interesting and intensive areas plant biology and plant structures (some mentioned in more detail below).

This manuscript is essentially a protocol paper and in its paragraph form, and even with great graphics, will definitely be difficult to follow and reproduce for a non-expert. Also considering the use of 3 different FIB-SEM platforms and 2 different cryo-FLM platforms, I wonder if a master graphic of the full workflow(s) could be prepared as a supplementary document that walks through the major steps and points to the individual figures at the critical steps to make it more accessible to the broader readership.

Multiple times in the manuscript, important workflow details seemed to point to and be dependent on two "unpublished" manuscripts:

(1) Line 583, 755, 790, 847-848, (Poge et al., will soon be published as a protocol).

(2) Lines 140, 695, 716 (Capitanio et al., will soon be described in a manuscript).

It is not clear if/when these would be publicly available. It may be important to wait until these papers can be included in published form.

https://doi.org/10.7554/eLife.106455.1.sa2

Reviewer #2 (Public review):

Summary:

Poge et al. present a workflow for studying plant tissue by combining high-pressure freezing, cryo-fluorescence microscopy, FIB milling, and cryo-electron tomography (cryo-ET). They tested various plant tissues, including Physcomitrium patens, Arabidopsis thaliana, and Limonium bicolor. The authors successfully produce thin lamellae suitable for cryo-ET studies. Using sub-tomogram averaging, they determined the Rubisco structure at subnanometer resolution, demonstrating the potential of this workflow for plant tissue studies.

Strengths:

This manuscript is likely the first to systematically apply FIB milling and cryo-ET to plant tissue samples. It provides a detailed methodological description, which is not only valuable for plant tissue studies but also adaptable to a broader range of biological tissue samples. The study compares the plunge freezing method with a high-pressure freezing method, demonstrating that high-pressure freezing can vitrify thick tissues while preserving their native state. Additionally, the authors explore two methods for plant tissue sample preparation, the "waffle" method and in-carrier high-pressure freezing combined with the "lift-out" approach. The "waffle" method is suitable for samples less than 25um, while the in-carrier high-pressure freezing method can process samples up to 100um.

Weaknesses:

The described workflow is very complicated and requires special expertise. The success rate of this workflow is not very high, particularly for high-pressure freezing and life-out technology. Further improvements are needed for automation and increasing throughput.

https://doi.org/10.7554/eLife.106455.1.sa1

Reviewer #3 (Public review):

Summary:

The authors aimed to improve cryo-TEM workflows for plant cells. The authors present details on high-pressure-freezing protocols to vitrify, ion-mill, and image certain plant cell types.

Strengths:

Clear step-by-step outline on how to preserve and image cryo samples derived from plants.

Weaknesses:

A general current weakness of cryo-TEM is the problem of vitrifying cells that are embedded in tissues. The vast majority of cells in the plant body are currently not accessible to this technology. This is not a weakness of this specific manuscript but a general problem.

The manuscript is well organized and well written, and the discussion covers practically all questions I had while reading the results section. I only have a few comments, all of which I consider minor.

https://doi.org/10.7554/eLife.106455.1.sa0

Chapter 5

Application – Imaging native plasmodesmata in 3D

In situ architecture of plasmodesmata in *Physcomitrium patens* resolved by cryo-ET

Status: In review.

Preprint DOI: https://doi.org/10.1101/2025.07.24.666190

5.1 Summary

Background and research question

Plasmodesmata have been imaged using traditional electron microscopy since the 1950s, revealing their overall pore architecture and the presence of plasma membrane, desmotubules, and unidentified protein components. Proteomics and in vivo localization by fluorescence microscopy have implicated numerous proteins as putative plasmodesmal components. However, a proper model of molecular organization within plasmodesmal pores is still lacking. Using cryo-electron tomography, this study aimed to resolve their overall architecture in detail, potentially allowing to identify individual proteins and their spatial organization within the pore.

Experimental approach

Physcomitrium patens was selected as a model system because a high density of plasmodesmata at cell-cell interfaces had been observed before (Chapter 2). Samples from the two dominant tissues, filamentous protonemata and leafy gametophores, were vitrified by high-pressure freezing and sectioned by cryo-focused ion beam (cryo-FIB) milling using the workflows developed in Chapters 4. In addition to wild-type tissue, conditions previously associated with increased or decreased cell-to-cell movement through plasmodesmata were imaged, attempting to resolve open and closed conformations. Pore characteristics were measured, quantified and compared between tissues and conditions. Subtomogram averaging was applied to resolve repetitive protein assemblies identified within plasmodesmata. Proteomic analysis and proteome-scale structure prediction was employed to identify the proteins forming the resolved assemblies, followed by bioinformatical analysis of their structure and sequence properties. All findings and resulting hypotheses were incorporated into an updated structure-function model of plasmodesmata.

Key findings

Across all examined cell-cell interfaces of *P. patens*, exclusively unbranched plasmodesmata were observed. Treatment with the stress hormone abscisic acid, associated with plasmodesmal closure, induced deposition of the cell wall polymer callose and constriction of plasmodesmal neck regions. It further revealed a previously undescribed mode of gating, where pronounced deposition of cell wall material led to fully sealed apertures with plasmodesmal membranes and cytosolic sleeves becoming severed from their cellular counterparts. In contrast, overexpression of a callose-degrading GHL17 enzyme characterized in Chapter 2 resulted in shorter and wider plasmodesmata, consistent with increased permeability. Subtomogram averaging resolved the structure of protein assemblies, constitutively coating desmotubule membranes in all imaged plasmodesmata. Multiple C2 domain and Transmembrane Proteins (MCTPs) are identified as the assemblies' components. MCTPs contain reticulon homology domains, likely responsible for desmotubule membrane tubulation, as well as extended intrinsically disordered linker domains with electrostatic sticker-spacer architecture that occupy the cytosolic route at plasmodesmata. Based on previous considerations of permeability barriers in the nuclear pore involving multivalent interactions between mobile cargo and stationary disordered protein networks, disordered regions of MCTPs are proposed to contribute to selective permeability at plasmodesmata.

Contributions to this Chapter

I contributed by conceiving experiments (with RS, WXS, WBF, WB), sample preparation and vitrification, sample thinning by FIB milling (with MP, PX), cryo-ET data analysis (with MP, PX), proteomics data analysis (with SG, WXS), and protein structure prediction. I analyzed MCTP conservation, sequence properties and domain organization, modeled the in situ structure of the MCTP assembly, prepared all figures except Supplementary Fig. 4 and wrote the manuscript with editing by MP, PX, RS, WXS, WBF, and WB.

5.2 Introduction

In situ architecture of plasmodesmata in *Physcomitrium patens* resolved by cryo-ET

Authors: Marcel Dickmanns[1,2]*, Matthias Pöge[1]†, Peng Xu[1], Sven Gombos[3], Zoe K. Barr[4], Manuel Miras[2]‡, Jürgen M. Plitzko[5], Rüdiger Simon[4,6], Waltraud X. Schulze[3], Wolf B. Frommer[2,6,7]*, Wolfgang Baumeister[1]*

Affiliations:

[1]Department of Molecular Structural Biology, Max Planck Institute of Biochemistry, Martinsried 82152, Germany.

[2]Heinrich Heine University Düsseldorf, Faculty of Mathematics and Natural Sciences, Institute of Molecular Physiology, Düsseldorf 40225, Germany.

[3]Department of Plant Systems Biology, University of Hohenheim, Stuttgart 70593, Germany.

[4]Heinrich Heine University Düsseldorf, Faculty of Mathematics and Natural Sciences, Institute of Developmental Genetics, Düsseldorf 40225, Germany.

[5]Research Group CryoEM Technology, Max Planck Institute of Biochemistry, Martinsried 82152, Germany.

[6]Cluster of Excellence on Plant Sciences (CEPLAS), Heinrich Heine University, Düsseldorf 40225, Germany.

[7]Institute of Transformative Bio-Molecules, Nagoya University, Chikusa, Nagoya 464-8601, Japan.

*Corresponding authors. Email: dickmanns@biochem.mpg.de (MD); frommew@hhu.de (WBF); baumeist@biochem.mpg.de (WB)

†Present address: Electron Microscopy Facility, Max Planck Institute of Molecular Cell Biology and Genetics, Dresden 01307, Germany.

‡Present address: Department of Stress Biology and Plant Pathology, CEBAS-CSIC, Murcia 30100, Spain

Abstract

Plasmodesmata are nanoscopic channels that traverse plant cell walls, enabling direct intercellular exchange through membrane and cytosolic continuity. Although numerous plasmodesmal components have been identified, their molecular organization remains poorly defined. Here, we used cryo-electron tomography to resolve the in situ architecture of plasmodesmata in *Physcomitrium patens* across tissues and physiological states. We show how callose-related cell wall remodeling shapes pore architecture to modulate permeability, including a previously undescribed fully sealed state, and identify helical protein assemblies formed by Multiple C2 domain and Transmembrane Proteins (MCTPs). These MCTP assemblies scaffold a central endoplasmic reticulum tubule and tether it to the plasma membrane, while their disordered linker regions with polyampholyte charge patterning populate the cytosolic sleeve. These findings define core architectural features of plasmodesmata and provide a structural framework for understanding how membrane, protein, and cell wall components coordinate intercellular connectivity in plants.

Main text

Multicellular organisms rely on intercellular communication to coordinate growth, development, and responses to environmental cues[1]. In plants, communication is complicated by the presence of a several hundred nanometers thick cell wall. Direct molecular exchange across this barrier is facilitated by plasmodesmata (PD), nanoscopic intercellular channels with complex architecture and composition. PD traverse the cell wall and establish continuity between the cytosol, plasma membrane, and endoplasmic reticulum (ER) of adjacent cells[2]. In animal tissues, direct cytoplasmic exchange largely occurs via transient protein channels which cluster at gap junctions. Cytoplasmic bridges containing shared membranes, however, are rare and typically restricted to the germline such as in the ring canals of insect germ cell cysts[1,3]. In contrast, PD are ubiquitous across both germline and somatic plant tissues, forming an almost organism-wide continuum of cells. This continuity necessitates control of PD permeability to maintain cellular homeostasis and tissue identity[4,5]. Although PD are central to plant physiology and development, their molecular architecture and mechanisms governing permeability control remain incompletely understood. Proteomics-based approaches have identified hundreds of putative PD-associated proteins[6–13], but an integrated molecular model is still lacking. Genetic dissection of individual components remains challenging, as loss-of-function mutants often exhibit severe systemic phenotypes or lethality[9,14,15]. In some cases, conditional expression systems or partial knockdowns have enabled functional studies, but genetic redundancy among PD-associated proteins further complicates analysis[16–18]. Fluorescence microscopy allows tracking of candidate protein localization and dynamics but lacks the spatial precision to resolve protein organization at PD and is prone to mislocalization artifacts from overexpression and fluorescent labeling.

Hitherto, insight into PD ultrastructure has relied on electron microscopy[19,20] and electron tomography[21,22] of dehydrated, heavy-metal-stained and resin-embedded samples. These approaches revealed some features of PD architecture and formation, yet the required treatments denature biomolecules and compromise molecular interpretation[23]. Recent advances in sample preparation and preservation have made cryo-electron tomography (cryo-ET) applicable to plant tissues[24]. In cryo-ET, three-dimensional imaging of pristinely preserved samples at macromolecular resolution allows the visualization of membrane interfaces and reveals the organization of protein complexes in their native cellular context. In this study, we used cryo-ET to resolve the architecture of PD in *Physcomitrium patens* and describe mechanisms controlling the permeability of plant cell-cell interfaces.

5.3 Results

In situ architecture of plasmodesmata

While PD in land plants share a common evolutionary origin[25], their architecture varies across species and tissues. In vascular plants, like *Arabidopsis thaliana*, PD have diverse morphologies, including funnel-shaped and highly branched forms, reflecting tissue-specific adaptations[26–29]. PD in non-vascular plants like the moss *Physcomitrium patens* remain less studied[20,30]. To investigate their PD architecture, we recorded tomograms of cell-cell junctions in the two dominant tissues of *P. patens*, protonemata (n = 22 PD) and gametophores (n = 21 PD). Unlike the morphological diversity observed in vascular plants, we exclusively found unbranched PD in *P. patens*, exhibiting canonical features (Fig. 1). Each channel consists of a cell wall cavity lined by the plasma membrane and traversed by a central tubular extension of the endoplasmic reticulum (ER), with a cytosol-filled intermembrane space, the cytosolic sleeve, between ER and plasma membrane (Fig. 1; Supplementary Video 1 and 2). In wild type, PD length correlates linearly with cell wall thickness, with thicker cell walls in gametophores necessitating longer PD (Supplementary Fig. 1). The neck regions directly adjacent to the apertures at each end of the plasmodesmal channel consistently represent the narrowest segments, assumed to impose structural constraints on molecular passage. The central, ER-derived desmotubule, varies in diameter. In protonemata, desmotubules appeared wider at neck regions (24.1 ± 2.2 nm) and narrower at the center of PD (10.5 ± 1.5 nm), while they remained uniformly wide (24.5 ± 3.1 nm) in gametophores. Desmotubules connect seamlessly to the cortical ER of adjacent cells, regardless of cortical ER morphology, which can appear tubular (67%, top cells in Fig. 1, n = 61) with diameters substantially wider than the desmotubule inside PD or as sheets (33%, bottom cells in Fig. 1, n = 30) extending in parallel to the cell wall and cellular plasma membrane. Within the cytosolic sleeve, additional electron-dense material was observed. In protonemata, these likely proteinaceous features are most prominent at the neck regions, coinciding with wider desmotubule segments, but can also be detected along central desmotubule segments, where they are distributed

sparsely. In gametophores, where desmotubules remain uniformly wide, these features are densely distributed along the entire length of PD. At narrow neck regions in both tissues, electron-dense material is most concentrated, obscuring desmotubules and the surrounding cytosolic sleeves.

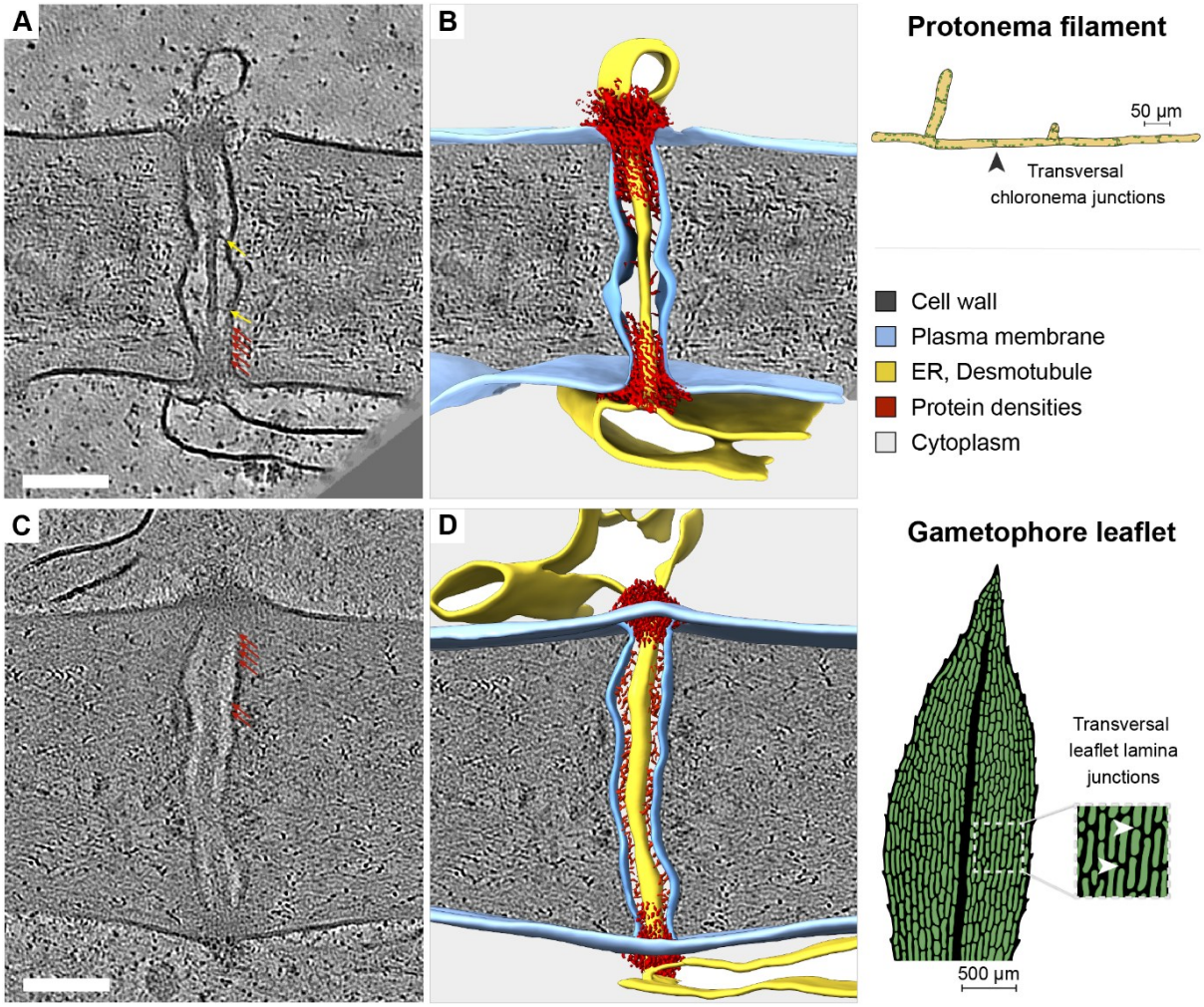


Fig. 1 | In situ architecture of plasmodesmata in *P. patens* revealed by cryo-ET. (**A**) 2D slices of a cryo-electron tomogram; cross-section of a cell wall between two cells within a protonema filament connected by a plasmodesma. Tethers connect wider desmotubule segments (red arrows) or narrower, central segments (yellow arrows) to the plasma membrane. (**B**) 3D-rendered segmentation of tomographic volume in A. (**C**) Slice through a plasmodesma connecting two gametophore leaflet lamina cells across their transversal cell wall interface. (**D**) Segmentation of the tomographic volume in C. Scale bars: 100 nm.

Impact of callose deposition and degradation on plasmodesmata architecture

To balance intercellular exchange and cellular homeostasis, plants dynamically regulate PD permeability. A key mechanism involves callose, a β-1,3-glucan cell wall polymer, which is deposited around neck regions by callose synthases and degraded by β-1,3-glucanases[17,31–33]. Synthesis and degradation either narrow or widen PD apertures, modulating permeability in response to developmental and environmental cues[34]. Under conditions such as water scarcity, pathogen infection or during winter dormancy, plants induce callose synthesis via the stress-response hormone abscisic acid (ABA)[35–38]. Unlike cellulose, which forms a dense fibrillar meshwork in the bulk cell wall, callose-

rich deposits are structurally more amorphous[39]. Cryo-ET of ABA-treated protonemata revealed large, granulated deposits of cell wall material around PD neck regions (Fig. 2a,b). While neck regions generally became constricted after ABA treatment, 45% of PD apertures (15 of n = 33, from 20 PD) exhibited a more severe phenotype, where deposition led to complete abscission of cellular plasma membranes, ER, and cytosolic sleeves (Supplementary Video 3, Supplementary Fig. 2). The cortical ER remained tethered to the plasma membrane near the former connection site to the desmotubule. These drastic changes in PD architecture provide a structural explanation for the ABA-induced reduction in intercellular trafficking reported in *P. patens*[40]. In contrast, we previously found that overexpression of the callose-degrading β-1,3-glucanase PpGHL17_1 increases permeability of cell-cell interfaces[11]. To determine whether and how increased permeability correlates with changes in PD architecture, we performed cryo-ET on a glucanase-overexpressing line, hereafter referred to as GHL17 (Fig. 2c,d; Supplementary Video 4; n = 38 PD). We found PD in protonemata of GHL17 to be shorter and wider, not only around neck regions but along the entire channel (Fig. 2e-h; Supplementary Fig. 1).

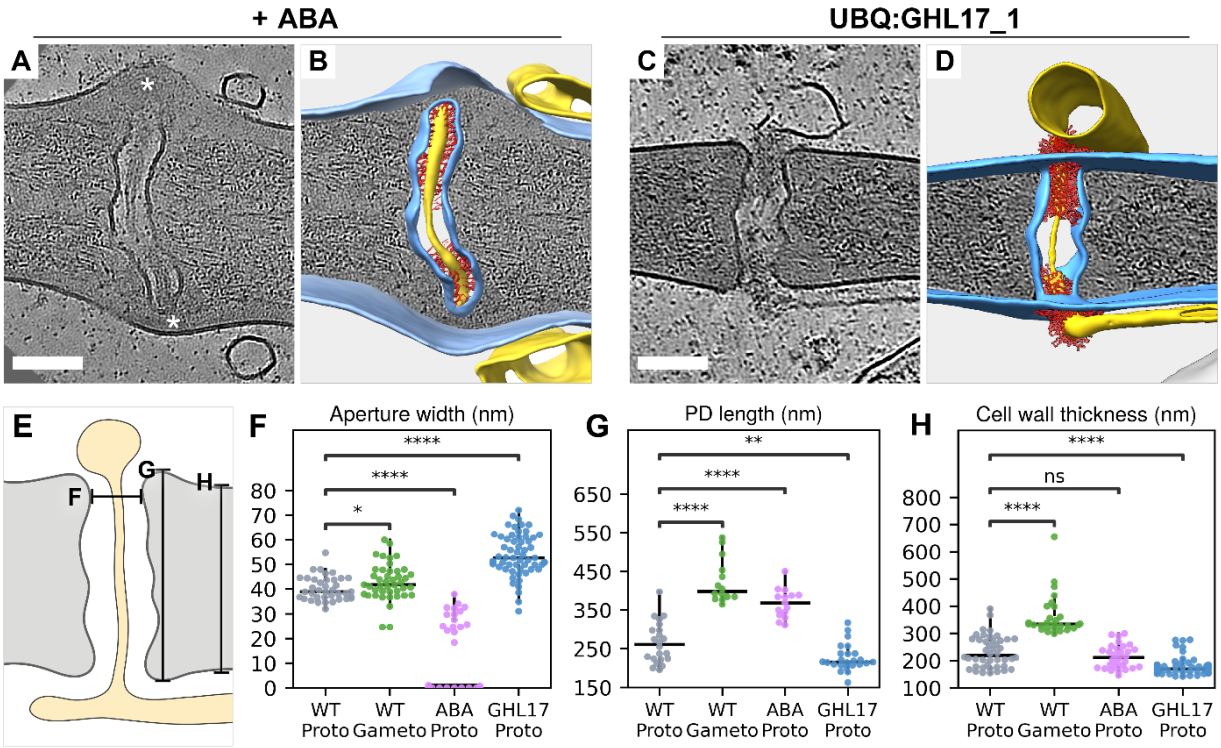


Fig. 2 | Deposition and degradation of the cell wall polymer callose gates plasmodesmata. (**A**) Incubating protonemata in 50 µM abscisic acid (ABA) for 17 h alters PD morphology. Asterisks mark putative callose deposits, disconnecting PD from cellular membranes and cytosol. (**B**) Segmentation of tomographic volume in A. (**C**) Overexpression of the callose-degrading enzyme GHL17 results in shorter and wider PD. (**D**) Segmentation of tomographic volume in C. (**E-H**) Effects of callose levels on PD architecture. (E) Schematic indicating measurement positions. (**F**) Aperture diameter at neck regions, representing the narrowest positions within PD. (**G**) PD length. (**H**) Bulk cell wall thickness. Mann-Whitney-Wilcoxon test (*P = 0.0252; ****P ≤ 0.0001; ns, not significant). Scale bars: 100 nm.

In accordance with PD conductance models predicting lower resistance and thus increased molecular flow in wider and shorter PD[28,41], these architectural changes explain the enhanced cell-cell permeability phenotype in GHL17. Callose quantification by aniline blue staining indicated lower callose levels at GHL17 cell-cell interfaces compared with WT, and elevated levels in ABA-treated WT tissue (Supplementary Fig. 3). Cell wall material with granulated texture seen at PD necks in tomograms was weakly pronounced in WT and GHL17 and expanded upon ABA-treatment, supporting the interpretation that granulated textures correspond to callose-rich deposits.

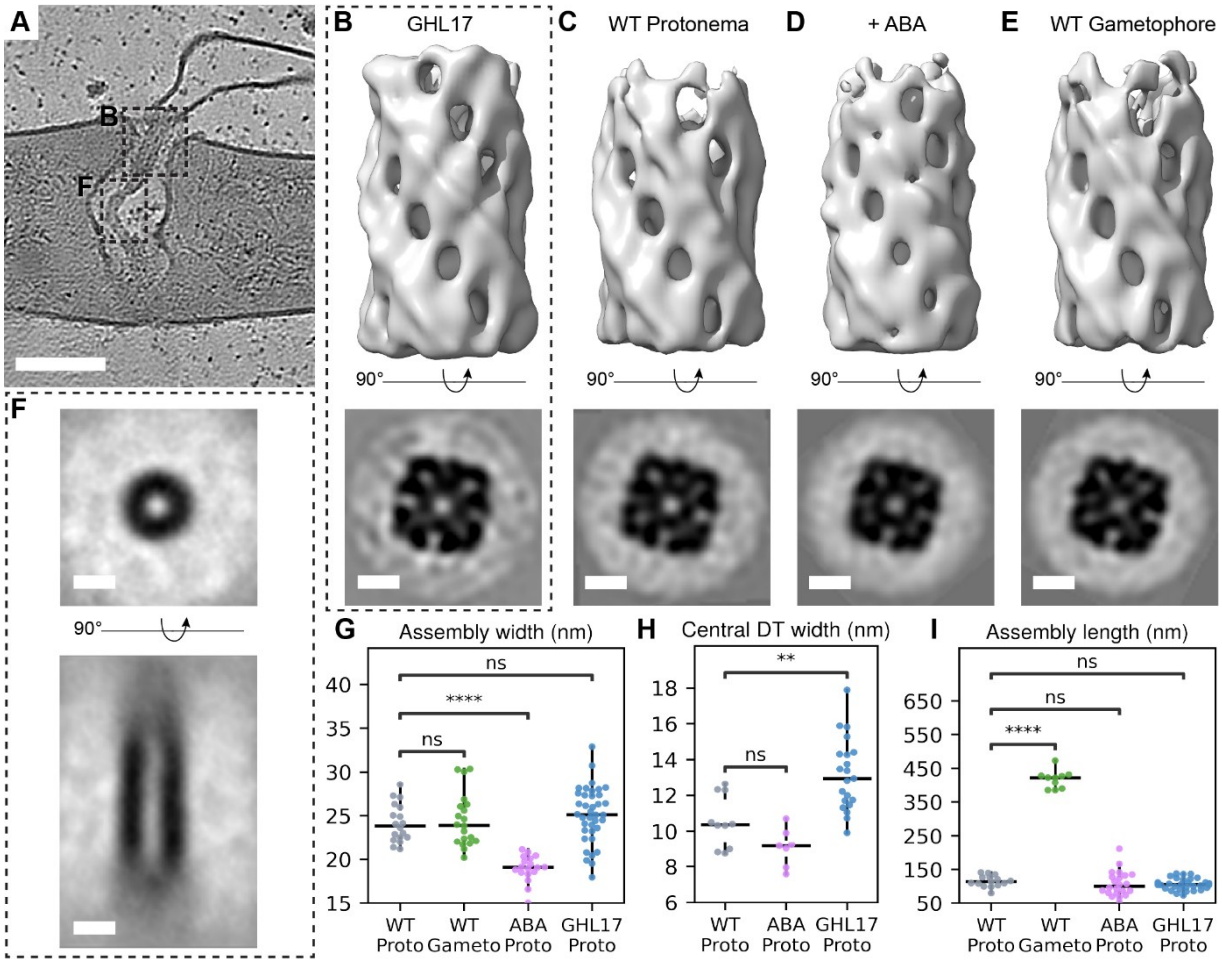


Fig. 3 | Helical desmotubule-coating assemblies are core architectural features of plasmodesmata. (**A**) Tomographic slice through a plasmodesma in GHL17 protonema. Dotted rectangles exemplify regions where subtomograms for averaging along the desmotubule were extracted. (**B-E**) Resolved desmotubule-coating assemblies in (**B**) GHL17 protonemata, (**C**) WT protonemata, (**D**) ABA-treated WT protonemata and (**E**) WT gametophores. Top panel: Side view of 3D-rendered assemblies. Bottom panel: 2D cross-sections through assemblies. (**F**) Transverse (top) and longitudinal (bottom) cross-sections of the averaged central desmotubule segment in protonemata, where assemblies are absent. (G-I). In situ measures of assemblies. (**G**) Assembly width. (**H**) Diameter of central desmotubule segment in protonemata. (**I**) Assembly length. Mann-Whitney-Wilcoxon test (**P = 0.0019; ****P ≤ 0.0001; ns, not significant). Scale bars: (**A**) 100 nm; (**B-F**) 10 nm.

Helical protein assemblies coat desmotubules at PD neck regions

Benefiting from wider PD in GHL17 protonemata, we identified periodic densities decorating all desmotubules at neck regions, while central segments lacked such features (Fig. 3a). These coatings cover approximately the first third of the desmotubule on both sides of PD in protonemata. In GHL17, the electron-dense material that had partially obscured desmotubules at neck regions of WT PD now appeared to extend from the desmotubule coatings towards the plasma membrane. Prompted by the periodic appearance of the coatings, we performed subtomogram averaging along the desmotubule (Supplementary Fig. 4). At neck regions, we resolved assemblies of structurally repetitive units winding around the desmotubule and anchored to the membrane, forming a helical lattice composed of four intertwined wraps (Fig. 3b). The electron-dense material extending from the surface of the assemblies towards the plasma membrane escaped structure determination by averaging, consistent with a flexible arrangement. Similar helical assemblies were recovered by averaging desmotubules in WT protonemata (Fig. 3c), ABA-treated protonemata (Fig. 3d), and gametophores (Fig. 3e), indicating that they are defining architectural features of PD in *P. patens*, consistently present across different cell types and physiological conditions. Averaging of central desmotubule segments confirmed that these ordered coatings are restricted to PD neck regions in protonemata (Fig. 3f). Notably, we measured slightly reduced diameters of desmotubule coats under ABA treatment (Fig. 3g), whereas GHL17 overexpression was associated with a significantly wider central, coat-free desmotubule region (Fig. 3h). Besides differences in desmotubule diameter, assembly lengths varied across tissues and conditions, but also between individual PD (Fig. 3i). In gametophores, the entire desmotubule is coated, whereas in protonemata, assemblies are confined to the neck regions. The variability in length and overall periodic structure suggests a modular organization assembled from recurring protein units.

MCTPs constitute the desmotubule coat

To elucidate the molecular composition of desmotubule-coating assemblies, we derived a list of candidate proteins from a proteome of PD-enriched cell wall fractions (data S1). Proteins predicted to localize to the ER and those with potential scaffolding functions were included, while excluding those assigned to the secretory pathway. We predicted structures of the remaining 43 candidate proteins and generated synthetic density maps for comparison with experimental maps of the assembly and subsequently performed rigid body fitting. Among all tested candidates, exclusively Multiple C2 domain and Transmembrane Proteins (MCTPs) matched the experimental data (Fig. 4; Supplementary Fig. 5; Supplementary Video 5). MCTPs co-localize with PD markers in land plants and have been identified in proteomes of PD fractions across species[6–13]. In *P. patens*, the MCTP family includes six homologs (PpMCTPs; Supplementary Table 1; Supplementary Fig. 6) with conserved domain topology, three of which are highly enriched in PD fractions (PpMCTP1, 2, and 5). PpMCTP1 and

PpMCTP5 have previously been localized to PD in vivo[11,12]. We now also tested localization of *Pp*MCTP2 and *Pp*MCTP4 by transient expression in *N. benthamiana*. Both homologs appear ER localized with accumulation at cell-cell interfaces where they co-localized with the plasmodesmal callose marker aniline blue (Supplementary Fig. 7). In flowering plants, the MCTP family is increasingly well characterized with multiple homologs localizing to PD where they are implicated in membrane tethering[10,22,42,43]. At the C-terminus MCTPs contain a reticulon homology domain (RHD)[22,44]. RHDs are widely conserved across eukaryotes and function in ER shaping[45,46], including in ER-containing cytoplasmic bridges in the insect germline[47]. Consistent with our structural data, genetic and biochemical studies have indicated that plant MCTPs can form higher-order assemblies in vivo[22,48] with support from recent modeling studies suggesting that their reticulon homology domains may mediate intermolecular interactions[49]. Through structure prediction and assessment of multiple oligomeric configurations, we identified dimers as the most likely arrangement of *Pp*MCTPs, with interfaces formed by two central α-helices per monomer and their membrane-embedded RHDs (Supplementary Fig. 6 and 8). Given the high sequence conservation among *Pp*MCTPs (77% global identity, 94% at the dimer interface), heterodimerization appears likely. Predicted homo- and heterodimers are nearly identical in overall structure, differing primarily in the length of a glycine-rich linker connecting the N-terminal C2A domain to C2B (the C2A-B linker domain), which ranges from 80 to 150 residues across family members (Supplementary Fig. 6 and Table 1). In total, *Pp*MCTPs contain four C2 domains. C2B, C2C, and C2D are positioned around the central dimer interface, while C2A is flexibly tethered via the extended C2A-B linker domain (Fig. 4a). To determine how MCTPs organize within the desmotubule-coating assembly, we excluded the positionally flexible C2A and its linker and fitted the N-terminally truncated dimers into the density map obtained by subtomogram averaging. These truncated dimer units fully account for the resolved helical assemblies coating desmotubules in situ (Fig. 4b; Supplementary Fig. 5), affirming MCTPs as their fundamental building blocks.

Although side chain interactions remain unresolved at this resolution, we identified potential contact sites of individual dimer units at the domain-level. In the resolved assembly, C2B domains interlace with C2B domains of adjacent dimers in the neighboring helical wrap (Fig. 4c), while C2C and C2D domains contact adjacent dimers within the same wrap (Fig. 4d). The ability of C2 domains to mediate protein-protein interactions has been reported for other C2-containing proteins[50,51]. Deletion of C2C in *Arabidopsis thaliana* MCTP4 (*At*MCTP4) disrupts PD association[22], supporting its role in stabilizing MCTP assemblies at PD. MCTPs have recently been described to prevent ER membrane abscission at the developing cell plate during cytokinesis, thereby facilitating PD formation through incomplete cell division[22]. The densely packed assemblies resolved here may provide the structural basis for this function, stabilizing the desmotubule and shielding it against membrane severing (Fig. 4e). Supporting this, we observed that under ABA-induced callose deposition, MCTP assemblies remain intact and are internalized into the cell wall along with desmotubules, plasma membrane

tethers and cytosolic sleeves (Fig. 2a,b). Severing occurs cytoplasm-proximal to the assembly, retaining it as well as the central desmotubule and plasma membrane in position within the sealed pore.

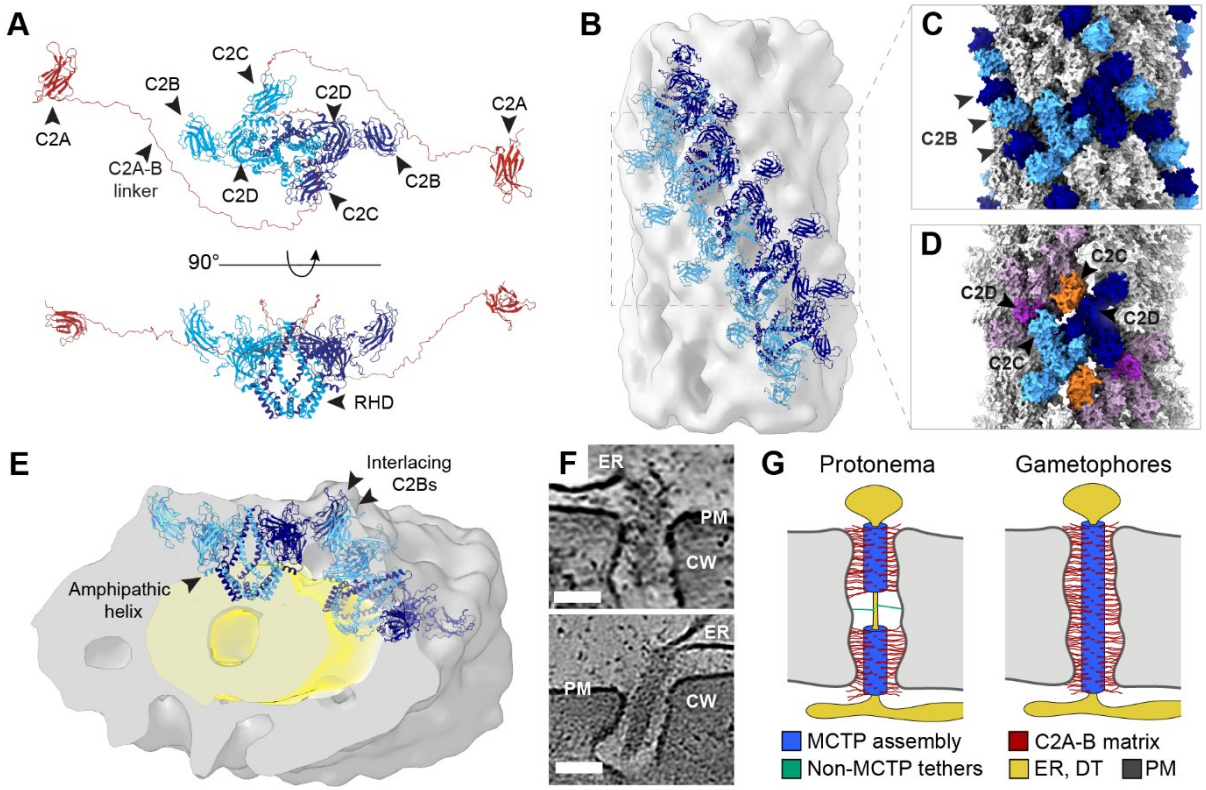


Fig. 4 | Arrangement of *Pp*MCTPs in the desmotubule-coating assembly. (**A**) Structure prediction of full-length, dimeric *Pp*MCTP2. N-terminal C2A domains connect through flexible linkers (red) to the dimerizing core (monomers in light and dark blue). Four central α-helices form the dimer interface. Reticulon homology domains (RHDs) anchor the dimer to the ER-derived desmotubule membrane. C2B, C2C and C2D domains are accessible for protein-protein interactions. (**B**) Subtomogram average of the desmotubule-coating assembly with docked models of dimeric PpMCTP (blue), tiled along one of four helical wraps. Flexible linkers and C2As are not resolved in average. (**C**) Surface rendering of the assembly. C2B domains of dimers from adjacent helical wraps interlace (light and dark blue). (**D**) Dimers within the same helical wrap contact via C2C and C2D domains. (**E**) Angled cross-section of the assembly (grey) with two docked dimers (blue) and desmotubule membrane region (yellow). (**F**) Magnified views of *Pp*MCTP assemblies in situ. Scale bars: 50 nm. (**G**) Schematic of desmotubule organization in protonemata and gametophore tissues. MCTP assemblies (blue) coat desmotubules (DT), with C2A domains and C2A-B linkers (red) extending towards the plasma membrane (PM). In protonemata, central desmotubule regions are not coated by MCTP assemblies, with occasional tethers extending to the plasma membrane (green). In gametophores, desmotubules are fully coated by MCTP assemblies.

Extended C2A domains enable desmotubule-plasma membrane tethering

In mature, post-cytokinetic cells, MCTPs contribute to permeability control through a callose-independent mechanism[16]. Higher-order mutants of *At*MCTPs exhibit increased intercellular transport, and molecular dynamics simulations suggest that the C2B, C2C, and C2D domains of *At*MCTP4 can interact with PIP4 lipids in the plasma membrane. This lipid-mediated tethering has been proposed to modulate cytosolic sleeve diameter

and thereby influence permeability independently of callose turnover[16]. While we cannot exclude membrane binding of these domains, we did not observe direct contacts between the plasma membrane and the surface of the resolved fraction of *Pp*MCTP assemblies, containing C2B, C2C, and C2D domains (Fig. 4c,f). However, with theoretical lengths of 30 - 50 nm, fully extended C2A-B linkers are sufficiently long to bridge the cytosolic sleeve, allowing C2A binding at the plasma membrane. We therefore measured the distance between the assembly surface and the plasma membrane in GHL17 plasmodesmata and found a maximum tether span of 26.4 nm (19.8 ± 4.2 nm, n = 72, Supplementary Fig. 1f). While C2A domains and their linkers are too small and flexible to be resolved by subtomogram averaging, we observed electron-dense material in individual tomograms extending from the assembly surface toward the plasma membrane, coinciding with plausible trajectories of extended C2A-B linker domains (Fig. 4f). These densities terminate at membrane-proximal positions, consistent with C2A-mediated lipid binding, supporting a model in which C2A domains serve as the primary tethers linking desmotubule coats to the plasma membrane in *P. patens*.

C2A-B linkers populating cytosolic sleeves

Despite high overall conservation across the MCTP family, C2A-B linker domains are the most variable sequence regions, hinting at potential functional diversification. We initially noticed these linkers for their high glycine content at the sequence level. In subsequent structure predictions, they consistently scored below 50 in pLDDT, an established predictor of intrinsic disorder[52]. Our in situ data indicate that C2A-B linkers populate cytosolic sleeves and are particularly concentrated at the narrow neck regions, prompting us to examine their potential role. Sequence analysis revealed that they are polyampholytes - that is, they contain a balanced distribution of oppositely charged residues interspersed with flexibility-promoting amino acids (Supplementary Fig. 6). Also referred to as sticker-spacer architectures, such motifs have been implicated in multivalent protein-protein interactions and phase-separated states[53]. Consistent with these properties, sequence-based prediction algorithms classify all *P. patens* C2A-B linkers as disordered and assign a high intrinsic propensity for liquid-liquid phase separation (LLPS propensity > 93%; Supplementary Fig. 9). While some MCTPs in flowering plants lack C2A domains, the majority of Arabidopsis homologs retain all four C2 domains (*At*MCTP2,6,7,8,9,10,14,15,16) and harbor C2A-B linkers with polyampholyte characteristics and comparable disorder and LLPS predictions (Supplementary Fig. 9), indicating potential functional relevance across land plants.

5.4 Discussion

In this work, we report native architectures of plasmodesmata across tissues and physiological states in *P. patens* using cryo-ET. We recover similar overall pore dimensions as described in classical TEM and freeze-substitution studies, while also uncovering previously unrecognized features. Specifically, we resolve how abscisic acid signaling reduces intercellular permeability by inducing plasmodesmal closure coinciding with increased callose levels. While callose-mediated constriction of plasmodesmal apertures is a well-established regulatory mechanism, our data reveal an additional outcome: local remodeling of the cell wall downstream of ABA can function as an apoplasmic gate, capable of fully sealing channels and abolishing both cytosolic and membrane continuity between cells. In flowering plants, sustained ABA signaling underlies several physiological arrest states, including bud dormancy[54], floral meristem arrest[38,55], and seed dormancy[56], all associated with reduced symplasmic connectivity. In *P. patens*, week-long ABA exposure similarly induces a symplasmically isolated 'brood-cell' state[57]. The pore architectures captured here after 17 h of ABA exposure may represent an early phase of brood-cell transition, characterized by plasmodesmal closure but preceding other developmental hallmarks of brood-cells such as thickening of bulk cell walls, or reflect a distinct PD-regulatory program. Consistent with this interpretation, we observed cell wall thickening specifically at plasmodesmata neck regions following ABA treatment, without corresponding changes in the bulk cell wall. PD-localized cell wall bulging has also been reported following callose synthase induction in Arabidopsis, although whether it can result in complete channel sealing remained unresolved[58]. Notably, short-term ABA-induced inhibition of cell to cell movement is reversible within 24 h of hormone removal in *P. patens*[40], raising the question if and how membrane continuity is re-established when callose plugs are degraded.

Across all imaged conditions, desmotubules were coated by modular helical protein assemblies with tethers connecting to the plasma membrane. Although desmotubule-associated particles and tethers have been described previously[19–21], their molecular identity remained unresolved. By combining subtomogram averaging with proteome-scale structure prediction, we identify MCTPs as the building blocks of desmotubule coats and their disordered C2A-B linker regions as likely candidates for the observed tethers. In mature gametophores, where MCTP assemblies and tethers span the full plasmodesmal length, reduced intercellular transport has been reported[30], whereas loss of MCTPs in Arabidopsis roots increases cell-to-cell conductivity[16], illustrating that MCTP levels correlate with PD permeability. C2A-B linkers exhibit polyampholyte charge patterning, high predicted disorder, and sequence-based propensity for multivalent interactions, raising the possibility that they contribute to permeability control within the cytosolic sleeve. Models invoking phase-separated protein networks as molecular basis for selective permeability, analogous to FG-NUPs in the nuclear pore, have been discussed for PD[13,59,60]. The linker sequences described here are predicted to allow

condensation, but are more consistent with a mechanism based on non-specific electrostatic rather than hydrophobic interactions. Notably, plasmodesmal permeability has recently been shown to depend on solute charge in addition to size[61]. Polyampholyte linkers, by presenting a distribution of charged residues, may underlie such electrostatic selectivity. As MCTP assemblies are constitutively present, and sleeve diameter at neck regions is tuned by callose, the mechanisms could act synergistically. Low callose levels widen the sleeve and dilute the linker network, whereas high callose levels constrict the sleeve and increase local crowding (Supplementary Fig. 2).

Altogether, our data indicates that MCTP dimers form helical coats around the desmotubule, anchored via RHDs which contribute to membrane tubulation. Assemblies are stabilized by protein-protein interactions at C2B, C2C and C2D domains. C2A domains mediate tethering of the desmotubule to the plasma membrane, while polyampholyte C2A-B linkers populate cytosolic sleeves, potentially forming dynamic diffusion barriers (Fig. 4g).

References

1. Chaigne, A. & Brunet, T. Incomplete abscission and cytoplasmic bridges in the evolution of eukaryotic multicellularity. Current Biology 32, R385–R397 (2022).

2. Bayer, E. M. & Benitez-Alfonso, Y. Plasmodesmata: Channels Under Pressure. Annual Review of Plant Biology 75, 291–317 (2024).

3. Snapp, E. L., Iida, T., Frescas, D., Lippincott-Schwartz, J. & Lilly, M. A. The Fusome Mediates Intercellular Endoplasmic Reticulum Connectivity in Drosophila Ovarian Cysts. MBoC 15, 4512–4521 (2004).

4. Kitagawa, M., Wu, P., Balkunde, R., Cunniff, P. & Jackson, D. An RNA exosome subunit mediates cell-to-cell trafficking of a homeobox mRNA via plasmodesmata. Science 375, 177–182 (2022).

5. Sessions, A., Yanofsky, M. F. & Weigel, D. Cell-Cell Signaling and Movement by the Floral Transcription Factors LEAFY and APETALA1. Science 289, 779–781 (2000).

6. Fernandez-Calvino, L. et al. Arabidopsis Plasmodesmal Proteome. PLOS ONE 6, e18880 (2011).

7. Park, S.-H. et al. NbEXPA1, an α-expansin, is plasmodesmata-specific and a novel host factor for potyviral infection. The Plant Journal 92, 846–861 (2017).

8. Leijon, F., Melzer, M., Zhou, Q., Srivastava, V. & Bulone, V. Proteomic Analysis of Plasmodesmata From Populus Cell Suspension Cultures in Relation With Callose Biosynthesis. Frontiers in Plant Science 9, (2018).

9. Kraner, M. E., Müller, C. & Sonnewald, U. Comparative proteomic profiling of the choline transporter-like1 (CHER1) mutant provides insights into plasmodesmata composition of fully developed Arabidopsis thaliana leaves. The Plant Journal 92, 696–709 (2017).

10. Brault, M. L. et al. Multiple C2 domains and transmembrane region proteins (MCTPs) tether membranes at plasmodesmata. EMBO reports 20, e47182 (2019).

11. Gombos, S. et al. A high-confidence Physcomitrium patens plasmodesmata proteome by iterative scoring and validation reveals diversification of cell wall proteins during evolution. New Phytologist 238, 637–653 (2023).

12. Johnston, M. G. et al. Comparative phyloproteomics identifies conserved plasmodesmal proteins. Journal of Experimental Botany 74, 1821–1835 (2023).

13. Schladt, T. M. et al. Identification of nuclear pore proteins at plasmodesmata: potential role in intercellular transport? eLife 14, (2025).

14. Benitez-Alfonso, Y. et al. Control of Arabidopsis meristem development by thioredoxin-dependent regulation of intercellular transport. Proceedings of the National Academy of Sciences 106, 3615–3620 (2009).

15. De Storme, N. et al. GLUCAN SYNTHASE-LIKE8 and STEROL METHYLTRANSFERASE2 Are Required for Ploidy Consistency of the Sexual Reproduction System in Arabidopsis. The Plant Cell 25, 387–403 (2013).

16. Pérez-Sancho, J. et al. Plasmodesmata act as unconventional membrane contact sites regulating intercellular molecular exchange in plants. Cell 188, 958-977.e23 (2025).

17. Benitez-Alfonso, Y. et al. Symplastic Intercellular Connectivity Regulates Lateral Root Patterning. Developmental Cell 26, 136–147 (2013).

18. Ishikawa, K., Tamura, K., Fukao, Y. & Shimada, T. Structural and functional relationships between plasmodesmata and plant endoplasmic reticulum–plasma membrane contact sites consisting of three synaptotagmins. New Phytologist 226, 798–808 (2020).

19. Ding, B., Turgeon, R. & Parthasarathy, M. V. Substructure of freeze-substituted plasmodesmata. Protoplasma 169, 28–41 (1992).

20. Cook, M. E., Graham, L. E., Botha, C. E. J. & Lavin, C. A. Comparative ultrastructure of plasmodesmata of Chara and selected bryophytes: toward an elucidation of the evolutionary origin of plant plasmodesmata. American Journal of Botany 84, 1169–1178 (1997).

21. Nicolas, W. J. et al. Architecture and permeability of post-cytokinesis plasmodesmata lacking cytoplasmic sleeves. Nature Plants 3, 17082 (2017).

22. Li, Z. P. et al. Plant plasmodesmata bridges form through ER-dependent incomplete cytokinesis. Science 386, 538–545 (2024).

23. Peters, W. S., Jensen, K. H., Stone, H. A. & Knoblauch, M. Plasmodesmata and the problems with size: interpreting the confusion. Journal of Plant Physiology 257, 153341 (2021).

24. Pöge, M. et al. Making plant tissue accessible for cryo-electron tomography. eLife 14, (2025).

25. Raven, J. A. Evolution of Plasmodesmata. Annual Plant Reviews online 18, 33–52 (2018).

26. Ehlers, K. & Kollmann, R. Formation of branched plasmodesmata in regenerating Solanum nigrum-protoplasts. Planta 199, 126–138 (1996).

27. Oparka, K. J. et al. Simple, but Not Branched, Plasmodesmata Allow the Nonspecific Trafficking of Proteins in Developing Tobacco Leaves. Cell 97, 743–754 (1999).

28. Ostermeyer, G. P., Jensen, K. H., Franzen, A. R., Peters, W. S. & Knoblauch, M. Diversity of funnel plasmodesmata in angiosperms: the impact of geometry on plasmodesmal resistance. Plant J 110, 707–719 (2022).

29. Tee, E. E. & Faulkner, C. Plasmodesmata and intercellular molecular traffic control. New Phytologist 243, 32–47 (2024).

30. Wegner, L. & Ehlers, K. Plasmodesmata dynamics in bryophyte model organisms: secondary formation and developmental modifications of structure and function. Planta 260, 45 (2024).

31. Cui, W. & Lee, J.-Y. Arabidopsis callose synthases CalS1/8 regulate plasmodesmal permeability during stress. Nature Plants 2, 16034 (2016).

32. Iglesias, V. A. & Meins Jr, F. Movement of plant viruses is delayed in a β-1,3-glucanase-deficient mutant showing a reduced plasmodesmatal size exclusion limit and enhanced callose deposition. The Plant Journal 21, 157–166 (2000).

33. Fitzgibbon, J., Bell, K., King, E. & Oparka, K. Super-resolution imaging of plasmodesmata using three-dimensional structured illumination microscopy. Plant Physiol 153, 1453–1463 (2010).

34. Wu, S.-W., Kumar, R., Iswanto, A. B. B. & Kim, J.-Y. Callose balancing at plasmodesmata. Journal of Experimental Botany 69, 5325–5339 (2018).

35. Mehra, P. et al. Hydraulic flux–responsive hormone redistribution determines root branching. Science 378, 762–768 (2022).

36. Tee, E. E., Johnston, M. G., Papp, D. & Faulkner, C. A PDLP-NHL3 complex integrates plasmodesmal immune signaling cascades. Proceedings of the National Academy of Sciences 120, e2216397120 (2023).

37. Tylewicz, S. et al. Photoperiodic control of seasonal growth is mediated by ABA acting on cell-cell communication. Science 360, 212–215 (2018).

38. Murata, Y., Nagata, K. & Abe, M. Cell-to-cell translocation of florigen is inhibited by low ambient temperature through abscisic acid signaling in Arabidopsis thaliana. Proceedings of the National Academy of Sciences 122, e2507987122 (2025).

39. Abou-Saleh, R. H. et al. Interactions between callose and cellulose revealed through the analysis of biopolymer mixtures. Nat Commun 9, 4538 (2018).

40. Kitagawa, M. et al. Abscisic Acid Acts as a Regulator of Molecular Trafficking through Plasmodesmata in the Moss Physcomitrella patens. Plant and Cell Physiology 60, 738–751 (2019).

41. Deinum, E. E., Mulder, B. M. & Benitez-Alfonso, Y. From plasmodesma geometry to effective symplasmic permeability through biophysical modelling. eLife 8, e49000 (2019).

42. Liu, L. et al. FTIP1 Is an Essential Regulator Required for Florigen Transport. PLOS Biology 10, e1001313 (2012).

43. Vaddepalli, P. et al. The C2-domain protein QUIRKY and the receptor-like kinase STRUBBELIG localize to plasmodesmata and mediate tissue morphogenesis in Arabidopsis thaliana. Development 141, 4139–4148 (2014).

44. Joshi, A. S., Ragusa, J. V., Prinz, W. A. & Cohen, S. Multiple C2 domain–containing transmembrane proteins promote lipid droplet biogenesis and growth at specialized endoplasmic reticulum subdomains. Molecular Biology of the Cell 32, 1147 (2021).

45. Voeltz, G. K., Prinz, W. A., Shibata, Y., Rist, J. M. & Rapoport, T. A. A Class of Membrane Proteins Shaping the Tubular Endoplasmic Reticulum. Cell 124, 573–586 (2006).

46. Wang, N. et al. Mechanism of membrane-curvature generation by ER-tubule shaping proteins. Nat Commun 12, 568 (2021).

47. Röper, K. Rtnl1 is enriched in a specialized germline ER that associates with ribonucleoprotein granule components. Journal of Cell Science 120, 1081–1092 (2007).

48. Tran, T. M. et al. Maize Carbohydrate Partitioning Defective33 Encodes an MCTP Protein and Functions in Sucrose Export from Leaves. Molecular Plant 12, 1278–1293 (2019).

49. Sritharan, S., Versini, R., Petit, J. D., Bayer, E. E. & Taly, A. Consensus structure prediction of A. thaliana's MCTP4 structure using prediction tools and coarse grained simulations of transmembrane domain dynamics. PLOS ONE 20, e0326993 (2025).

50. Remans, K., Bürger, M., Vetter, I. R. & Wittinghofer, A. C2 Domains as Protein-Protein Interaction Modules in the Ciliary Transition Zone. Cell Reports 8, 1–9 (2014).

51. Cui, M., Gupta, S. K. & Bauer, P. Role of the plant-specific calcium-binding C2-DOMAIN ABSCISIC ACID-RELATED (CAR) protein family in environmental signaling. European Journal of Cell Biology 102, 151322 (2023).

52. Akdel, M. et al. A structural biology community assessment of AlphaFold2 applications. Nat Struct Mol Biol 29, 1056–1067 (2022).

53. Lin, Y.-H., Forman-Kay, J. D. & Chan, H. S. Sequence-Specific Polyampholyte Phase Separation in Membraneless Organelles. Phys. Rev. Lett. 117, 178101 (2016).

54. Pan, W. et al. Epigenetic silencing of callose synthase by VIL1 promotes bud-growth transition in lily bulbs. Nat. Plants 9, 1451–1467 (2023).

55. Sánchez-Gerschon, V. et al. Transcription factors HB21/40/53 trigger inflorescence arrest through abscisic acid accumulation at the end of flowering. Plant Physiol 195, 2743–2756 (2024).

56. Wang, C. et al. Disruption of BG14 results in enhanced callose deposition in developing seeds and decreases seed longevity and seed dormancy in Arabidopsis. The Plant Journal 113, 1080–1094 (2023).

57. Arif, M. A. et al. ABA-Induced Vegetative Diaspore Formation in Physcomitrella patens. Front. Plant Sci. 10, (2019).

58. Vatén, A. et al. Callose Biosynthesis Regulates Symplastic Trafficking during Root Development. Developmental Cell 21, 1144–1155 (2011).

59. Lee, J. Y., Yoo, B. C. & Lucas, W. J. Parallels between nuclear-pore and plasmodesmal trafficking of information molecules. Planta 210, 177–187 (2000).

60. Ejike, J. O. et al. The role of phase separation for RNA and protein transport through the nuclear pore complex. Journal of Experimental Botany eraf271 (2025) doi:10.1093/jxb/eraf271.

61. Howell, A. H. et al. Electric charge controls plasmodesma conductivity. 2024.04.02.587779 Preprint at https://doi.org/10.1101/2024.04.02.587779 (2024).

62. Mastronarde, D. N. Automated electron microscope tomography using robust prediction of specimen movements. Journal of Structural Biology 152, 36–51 (2005).

63. Khavnekar, S., Erdmann, P. S. & Wan, W. TOMOMAN: a software package for large-scale cryo-electron tomography data preprocessing, community data sharing and collaborative computing. J Appl Cryst 57, 2010–2016 (2024).

64. Kremer, J. R., Mastronarde, D. N. & McIntosh, J. R. Computer visualization of three-dimensional image data using IMOD. Journal of Structural Biology 116, 71–76 (1996).

65. Zheng, S. et al. AreTomo: An integrated software package for automated marker-free, motion-corrected cryo-electron tomographic alignment and reconstruction. Journal of Structural Biology: X 6, 100068 (2022).

66. Lamm, L. et al. MemBrain v2: an end-to-end tool for the analysis of membranes in cryo-electron tomography. 2024.01.05.574336 Preprint at https://doi.org/10.1101/2024.01.05.574336 (2025).

67. Tegunov, D. & Cramer, P. Real-time cryo-electron microscopy data preprocessing with Warp. Nat Methods 16, 1146–1152 (2019).

68. Tang, G. et al. EMAN2: An extensible image processing suite for electron microscopy. Journal of Structural Biology 157, 38–46 (2007).

69. Buchholz, T.-O., Jordan, M., Pigino, G. & Jug, F. Cryo-CARE: Content-Aware Image Restoration for Cryo-Transmission Electron Microscopy Data. Preprint at https://doi.org/10.48550/arXiv.1810.05420 (2018).

70. Liu, Y.-T. et al. Isotropic reconstruction for electron tomography with deep learning. Nat Commun 13, 6482 (2022).

71. Meng, E. C. et al. UCSF ChimeraX: Tools for structure building and analysis. Protein Science 32, e4792 (2023).

72. Wan, W., Khavnekar, S. & Wagner, J. STOPGAP: an open-source package for template matching, subtomogram alignment and classification. Acta Crystallogr D Struct Biol 80, 336–349 (2024).

73. Zivanov, J. et al. New tools for automated high-resolution cryo-EM structure determination in RELION-3. eLife 7, e42166 (2018).

74. Jumper, J. et al. Highly accurate protein structure prediction with AlphaFold. Nature 596, 583–589 (2021).

75. Evans, R. et al. Protein complex prediction with AlphaFold-Multimer. 2021.10.04.463034 Preprint at https://doi.org/10.1101/2021.10.04.463034 (2022).

76. Abramson, J. et al. Accurate structure prediction of biomolecular interactions with AlphaFold 3. Nature 630, 493–500 (2024).

77. Hardenberg, M., Horvath, A., Ambrus, V., Fuxreiter, M. & Vendruscolo, M. Widespread occurrence of the droplet state of proteins in the human proteome. Proceedings of the National Academy of Sciences 117, 33254–33262 (2020).

78. Erdős, G. & Dosztányi, Z. AIUPred: combining energy estimation with deep learning for the enhanced prediction of protein disorder. Nucleic Acids Research 52, W176–W181 (2024).

79. Schindelin, J. et al. Fiji: an open-source platform for biological-image analysis. Nat Methods 9, 676–682 (2012).

80. Muller, A., Fujita, T. & Coudert, Y. Callose Detection and Quantification at Plasmodesmata in Bryophytes. in Plasmodesmata: Methods and Protocols (eds Benitez-Alfonso, Y. & Heinlein, M.) 177–187 (Springer US, New York, NY, 2022). doi:10.1007/978-1-0716-2132-5_11.

81. Kong, L. et al. Cryo-EM of the dynamin polymer assembled on lipid membrane. Nature 560, 258–262 (2018).

5.5 Methods

Preparation of *Physcomitrium patens* tissues for cryo-ET

Culturing, sample preparation, cryo-fixation, and FIB milling procedures are described in detail in Pöge et al.[24]. Briefly, *P. patens* (Hedw.) Gransden ecotype was grown at 25 °C on BCDAT agar medium overlaid with cellophane, under 18 h white light / 6 h dark cycles. Small protonemata patches were detached using tweezers, submerged in freezing buffer (BCDAT liquid medium supplemented with Ficoll 400 dissolved in H2O to a final concentration of 20% [w/v]), and immediately high-pressure frozen (LEICA EM ICE, Leica Mikrosysteme GmbH, Wetzlar, Germany). Gametophores were collected after 4 weeks by manually dissecting individual phyllids with fine scissors, followed by immediate immersion in freezing buffer and high-pressure freezing. Samples were vitrified using both the ‘waffle method’ and freezing in 3 mm carriers with a 100 µm deep cavity, optimized for subsequent Serial Lift-Out FIB milling. GHL17 samples (UBQ:*Pp*GHL17_1-mVenus line, documented in Gombos et al. 2023[11]) were prepared as described for wild type.

ABA treatment of Physcomitrium patens protonemata

ABA stock solutions are prepared at 1000x concentration (50 mM), dissolved in DMSO. Two week old wild type cultures were treated by adding 7 ml of liquid BCDAT growth media containing 50 µM ABA to the agar dish. After 15 min incubation, the solution was decanted. 17 h after initial ABA exposure, cells were high-pressure frozen as described.

Cryo-ET: Data acquisition

Tilt series were collected using a Titan Krios G3i instrument at 300 kV, equipped with a Selectris X energy filter and a Falcon 4i camera (Thermo Fisher Scientific). Tilt series were recorded using the Tomography5 software package (Thermo Fisher Scientific). A dose-symmetric tilt scheme was used with an angular increment of 3°. Magnification was set to 64,000x (pixel size = 1.89 Å) and a dose rate of 3 e−/Å^2 per tilt, resulting in a total dose of 100 e−/Å^2 per tilt series. The target defocus ranged from -3.0 to -6.0 µm. A small dataset was collected on a Titan Krios G2 equipped with a Gatan post column energy filter and K2 Summit (Gatan) camera. Here, tilt series were recorded at a magnification of 42,000x (pixel size = 3.52 Å) using the SerialEM software[62].

Tomogram reconstruction and segmentation

Tilt series were processed as described in Pöge et al.[24]. Preprocessing including motion correction, removal of bad tilt images and dose filtering were performed in TOMOMAN (version 0.6.9,[63]). If tilt-series contained at least 5 platinum fiducials evenly distributed over the field-of-view, IMOD (version 4.11.25,[64]) fiducial tracking was employed for tilt-series alignment. Otherwise, AreTomo (version 1.3.3,[65]) was used for tilt-series alignment. Afterwards, 4x binned tomograms were reconstructed with the weighted back projection algorithm implemented in IMOD. Membranes were segmented with MemBrain-Seg[66]. While this software reliably traces intracellular membranes, it barely picked plasmodesmata membranes. Hence, the latest built-in model (v10) was refined following the instructions available at https://teamtomo.org/membrain-seg/Usage/Training/. Furthermore, tilt-series were imported into WARP (version 1.0.9,[67]). Membrane tethering densities within cytosolic sleeves were segmented using a convolutional neural network (CNN) trained in EMAN 2.9968. Because these features span only 1-2 pixels in width, training and segmentation were performed on bin2 tomograms which were denoised with cryo-CARE[69] and subsequently processed with IsoNet70 employing the default parameters. For each tomogram, 1000-1200 negative reference regions were selected from areas containing cell wall, cytosol, or non-PD membranes. Additionally, 30-50 positive reference areas were selected per tomogram, representing regions along the full PD channel. Positive references were manually annotated, serving as training input (training parameters: learnrate = 0.0001; iterations = 200; ncopy = 5; batch = 20; nkernel = 40,40,1; ksize = 9,7,5; poolsz = 2,1,1, box size = 128). While picking up tethers within cytosolic sleeves, the network failed to identify

individual tethers at highly dense PD aperture regions. For those regions an additional voxel density thresholding step was performed in Amira (Thermo Fisher Scientific). All tomograms displayed in this work were denoised with cryo-CARE and visualized with IMOD (version 4.11.25). Segmentations were curated in Amira and jointly rendered in ChimeraX[71].

Cryo-ET: Tomogram analysis

PD dimensions were manually annotated with the contour tool in 3dmod and the corresponding distances calculated in MATLAB (version 2022a). Data visualization and statistical analysis were performed in Python using the libraries matplotlib, numpy, csv, pandas, seaborn, scipy, and statannotations. Statistical comparisons were conducted using two-sided Mann-Whitney-Wilcoxon tests, implemented via the statannotations.Annotator class.

Cryo-ET: Subtomogram averaging of the desmotubule-coating assembly

For each desmotubule-coating assembly, a two-point contour was manually defined in 3dmod. The first point marked the beginning of the complex within the PD channel, and the second was placed at the channel opening toward the cytoplasm. In gametophore samples containing a single continuous assembly spanning the entire PD, a single long contour was defined from one channel opening to the other. Subtomograms (4× binned, voxel size = 7.6 Å, box size = 64 voxels) were extracted at 1 nm intervals along the line connecting these two points. Euler angles for θ (Theta) and ψ (Psi) were calculated such that the z-axis of each subtomogram aligned parallel to the desmotubule contour axis; ϕ (Phi) angles were randomized. Initial alignment was performed in STOPGAP (v0.7.0,[72]) with shifts only allowed perpendicular to the axis of the PD channel without ϕ angle search. The reference for the first iteration was the average of the extracted subtomograms without alignment (Supplementary Fig. 4). Subsequently, the average of the current iteration was used for the next one. All references were filtered to a resolution of 35-40 Å. For the GHL17 dataset, pseudo-symmetry expansion and a second alignment step in STOPGAP were performed. From every initial subtomogram position after the first alignment step, 11 new positions were defined by shifting 6 nm radially outward onto the desmotubule surface with an angular distance of ~33°. Euler angles were updated to align the subtomogram z-axis perpendicular to the desmotubule surface using the STOPGAP script sg_motl_shift_and_rotate.m. Subtomograms were re-extracted at these oversampled positions (4× binned, voxel size = 7.6 Å, box size = 48 voxels) and aligned with exhaustive search over all three Euler angles, allowing a maximum shift of 11 nm. Following alignment, subtomograms were distance-filtered by removing particles within 8 nm of one another, retaining only the subtomograms with the highest alignment score (fast local correlation function in STOPGAP). Subsequently, subtomograms were extracted in WARP (2× binned, voxel size = 3.8 Å, box size = 96

voxels) and subjected to 3D classification, refinement, and postprocessing in RELION (v3.0.5,[73]). Resolution of the GHL17-derived average was estimated according to the Fourier Shell Correlation (FSC0.143 ≈ 33 Å, Supplementary Fig. 4). To enable comparison of desmotubule-coating assembly across all datasets, subtomograms were extracted in WARP (voxel size = 7.6 Å, box size = 64 voxels) directly after the initial alignment in STOPGAP without symmetry expansion. These subtomograms were classified and aligned in RELION. During postprocessing, all averages were filtered to a resolution of 40 Å, enabling comparison (Fig. 3b-e).

Proteome-derived list of desmotubule-coating candidates

The Physcomitrium patens high-confidence PD proteome (HC300[11]) was filtered for plasma membrane and endoplasmic reticulum-localized proteins containing at least one transmembrane or known membrane-binding domain. In addition, proteins annotated with potential scaffolding functions, as well as those lacking functional annotation in P. patens, were included. Transporters, hydrolytic enzymes, proteins with known functions in vesicle transport, and proteins predicted to be secretory pathway-targeted were excluded. This filtering yielded 43 candidate proteins for further assessment (Supplementary Data S1).

Structure predictions of candidate proteins

Monomeric structures of all candidate proteins were predicted using AlphaFold v2.3.1[74]. While monomers could in principle fit within the experimental density, their small size allowed a wide range of orientations, often resulting in biologically implausible placements (e.g., membrane-associated domains facing the cytosolic sleeve) or complete burial within the map without accounting for key structural features. These ambiguities precluded reliable identification of monomeric fits. To address this, each protein was further evaluated individually using structural, biochemical, and localization information from the literature, with the goal of identifying higher-order oligomers from a combination of monomeric PD proteins that could recapitulate the desmotubule-coating assembly. For proteins with documented oligomeric states, dimeric and trimeric structures were predicted using AlphaFold Multimer v2.3.1[75]. Predicted complexes with high confidence (0.8*ipTM + 0.2*pTM ≥ 0.60) were subjected to rigid-body fitting into the experimental density. For models containing extended disordered regions (pLDDT < 50), truncated variants retaining only structured domains and short interdomain linkers were generated. Non-MCTP candidates failed to align meaningfully with the density, producing fits that either occupied the volume nonspecifically or conflicted with membrane topology. Adding repeating units of non-MCTP oligomers did not recover the observed organization of the coat (Supplementary Fig. 5a). In contrast, truncated PpMCTP dimers aligned closely with the experimental density, recapitulating the periodic features of the desmotubule-coating assembly

(Supplementary Fig. 5b,c). To quantify the fit, we generated a full model by tiling PpMCTP dimers using rigid-body fitting, simulated a corresponding density map from the atomic model at the resolution of the experimental average, then calculated the cross-correlation between the synthetic and experimental map (Supplementary Fig. 5d).

Assessment of MCTP structure by structure predictions

To explore the structural basis of MCTP oligomerization, we predicted monomeric, dimeric and trimeric structures for each of the six PpMCTPs using AlphaFold v2.3.1 and AlphaFold Multimer v2.3.1. Dimeric assemblies were further modeled for all pairwise combinations of PpMCTPs to evaluate the plausibility of homo- vs. heterodimerization (Supplementary Fig. 6c). Only predictions with a weighted score of 0.8*ipTM + 0.2*pTM ≥ 0.6 were considered. Resulting structure predictions were further assessed based on pLDDT and PAE scores. For trimer predictions, the flexible N-terminus was truncated to reduce compute. All AlphaFold3 predictions were performed on https://alphafoldserver.com/[76].

In silico profiling of sequence-encoded biophysical properties of full-length MCTPs

FuzDrop was used to predict propensity for droplet-formation (pDP) along full length MCTP sequences and liquid-liquid phase separation potential (pLLPS) for the C2A-B linker domains[77]. We also applied AIUPred for disorder prediction[78]. pLDDT scores from AlphaFold2-Multimer (ranging from 1-100) were normalized by dividing by 100 to match the 0-1 scale of FuzDrop and AIUPred.

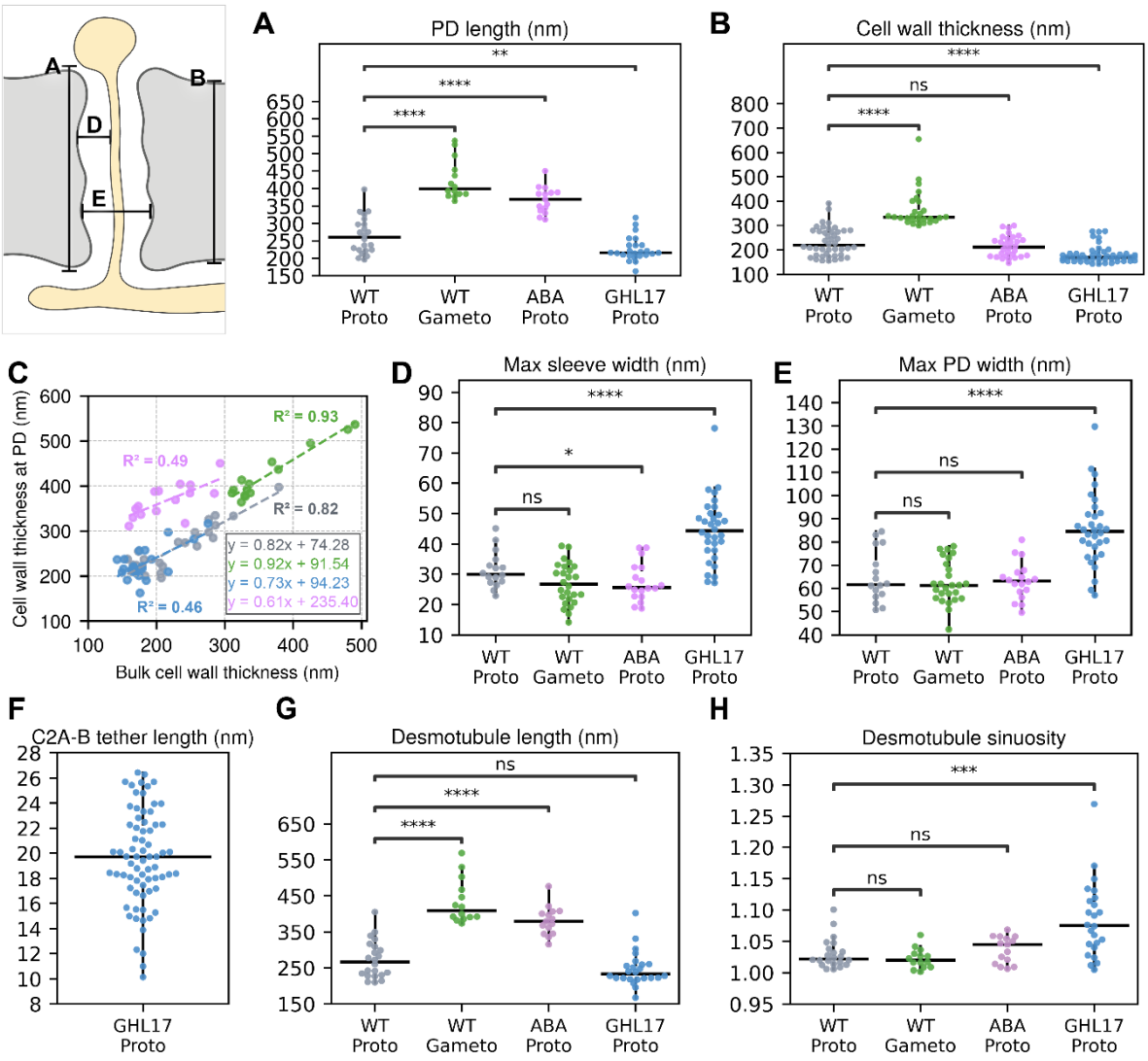
Callose quantification

Physcomitrium patens samples, grown as described above, were incubated for 1 h in 0.1% (w/v) aniline blue dissolved in 0.1 M Sorenson's Phosphate Buffer at pH 7.2. Imaging of three biological replicates per condition was performed using a Zeiss LSM 880 Airyscan with Objective C Plan-Apochromat 40x/1.2 Water DIC M27. Z-stacks were recorded at 1 µm distance steps, 1024x1024 frame size, 8 times averaging, 1.0 numerical zoom and pinhole 2.4 A.U, with excitation at 405 nm and an emission detection range of 420 – 520 nm. Quantification was performed in Fiji ImageJ2[79]. Analysis was applied according to Muller et al.[80]. Briefly, a rectangular ROI, sufficiently sized to encompass the cell-cell interface, was set and saved for repeated use across samples. Measurements of "Area" and "Integrated Density" were recorded. Net signal values were calculated from the RawIntDens values at a cell-cell interface minus the RawIntDens value of the background signal.

In vivo localization of *Pp*MCTPs

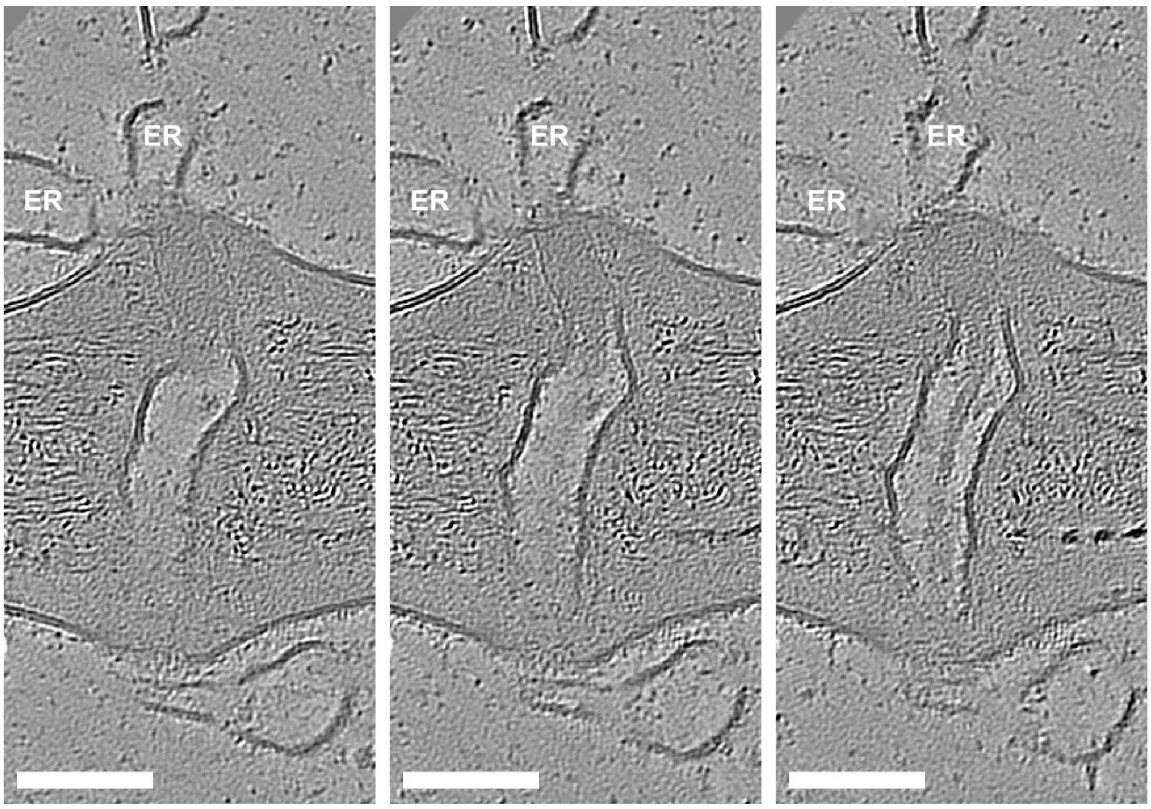
*Pp*MCTP2 and *Pp*MCTP4 were amplified by PCR, cloned into D-TOPO entry vectors and subsequently a Gateway LR reaction was performed with Gateway destination vector pVS331. The reaction with LR Clonase II (Invitrogen) was conducted as per manufacturer's instructions. Agrobacterium cultures (strain GV3101::pMP50 with p19 helper plasmid for silencing suppression) were transformed with the expression plasmids. Fresh streaks of transformed Agrobacteria were used to inoculate 4ml LB culture per plasmid, grown overnight at 28ºC with shaking. Cultures were pelleted (20800 rcf, 1min), resuspended in 1.5 ml infiltration buffer (50 µM acetosyringone, 0.01 M MgCl2, 0.01 M 2-(N-morpholino)ethanesulfonic acid (MES)) and incubated for 1 hour in the dark. The concentration was adjusted to an OD600 of 0.1 by diluting with infiltration buffer. N. benthamiana leaves were infiltrated at the abaxial epidermis with a syringe after pricking with a needle 5 days prior to imaging. Expression was induced by spraying abaxial sides of leaves with β-estradiol (20 µM β-estradiol, 0.1% (v/v) Tween®-20) 24 hours prior to imaging. 0.1% (w/v) aniline blue solution in 0.1 M Sorenson's Phosphate Buffer at pH 7.2 was infiltrated 5 minutes before leaf discs were mounted on a microscope slide. Single Z-slices were recorded using a Zeiss LSM 880 Airyscan with Objective C Plan-Apochromat 40x/1.2 Water DIC M27, focusing on the cell periphery. Cell-wide localization was recorded as Z-stacks with 1 µm z-distance steps. Aniline blue was excited at 405 nm and an emission detected at 420 – 520 nm, mVenus was excited at 514 nm and emission detected at 516 – 565 nm; scanning parameters: 524x524 frame size, 4 times averaging, 1.0 numerical zoom, and pinhole 1.0 A.U. Quantification was performed in Fiji ImageJ2[79], and PD indices were calculated as described in Gombos et al.[11]. The Fiji macro is available at https://github.com/SHaensch/2022_PD-index-quantification.

5.6 Supplementary Materials

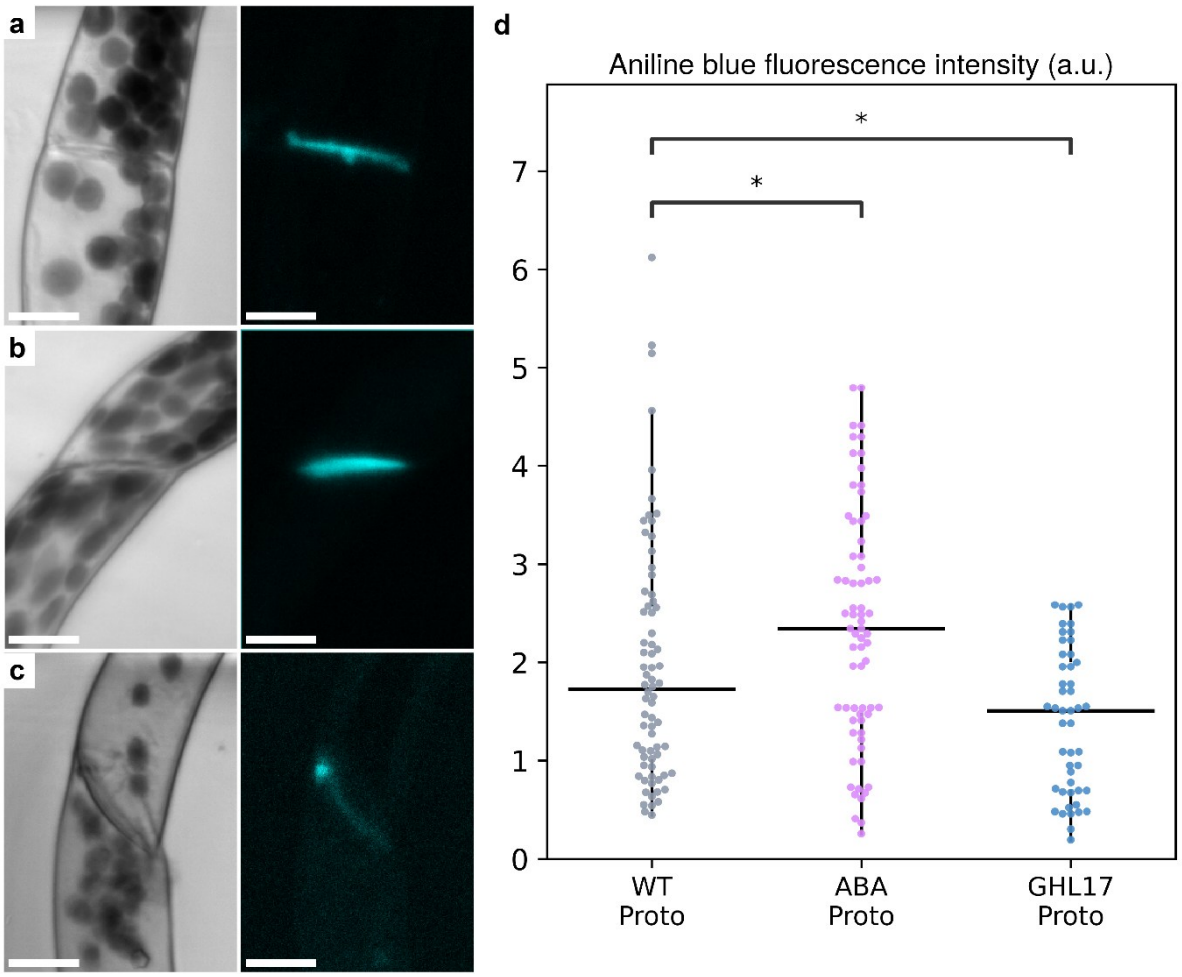


Supplementary Fig. 1 | In situ measurements of plasmodesmata and cell wall dimensions. Quantification of plasmodesmata features in wild type protonemata (WT Proto, grey), wild type gametophores (WT Gameto, green), ABA-treated wild type protonemata (ABA Proto, magenta), and UBQ:GHL17_1 protonemata (GHL17 Proto, blue). (**A**) Plasmodesmata length. For sealed plasmodesmata in ABA-treated tissue, end-to-end length including callose plugs was measured. (**B**) Bulk cell wall thickness measured in regions away from plasmodesmal channels, excluding bulged regions at plasmodesmata necks. Short-term ABA treatment (50 µM for 17h) specifically induces bulging at plasmodesmata neck regions, whereas constitutive GHL17 overexpression broadly affects cell wall thickness at and away from plasmodesmata. (**C**) Scatter plot of cell wall thickness at PD (approximating PD length) versus bulk cell wall thickness with linear regression fits per data set (dashed lines); slopes and R^2 (coefficient of determination) values indicate the degree and consistency of coupling. Lower R^2 in ABA and GHL17 data reflects increased local cell wall heterogeneity compared to WT. (**D**) Maximum width of cytoplasmic sleeve between desmotubule and plasma membrane. (**E**) Maximum width of plasmodesmal channels, measured from plasma membrane to plasma membrane. (**F**) Length of tethers originating from surfaces of desmotubule-coating assemblies and terminating at the plasma membrane. (**G**) Total length of desmotubules measured along their curvature. (**H**) Sinuosity of

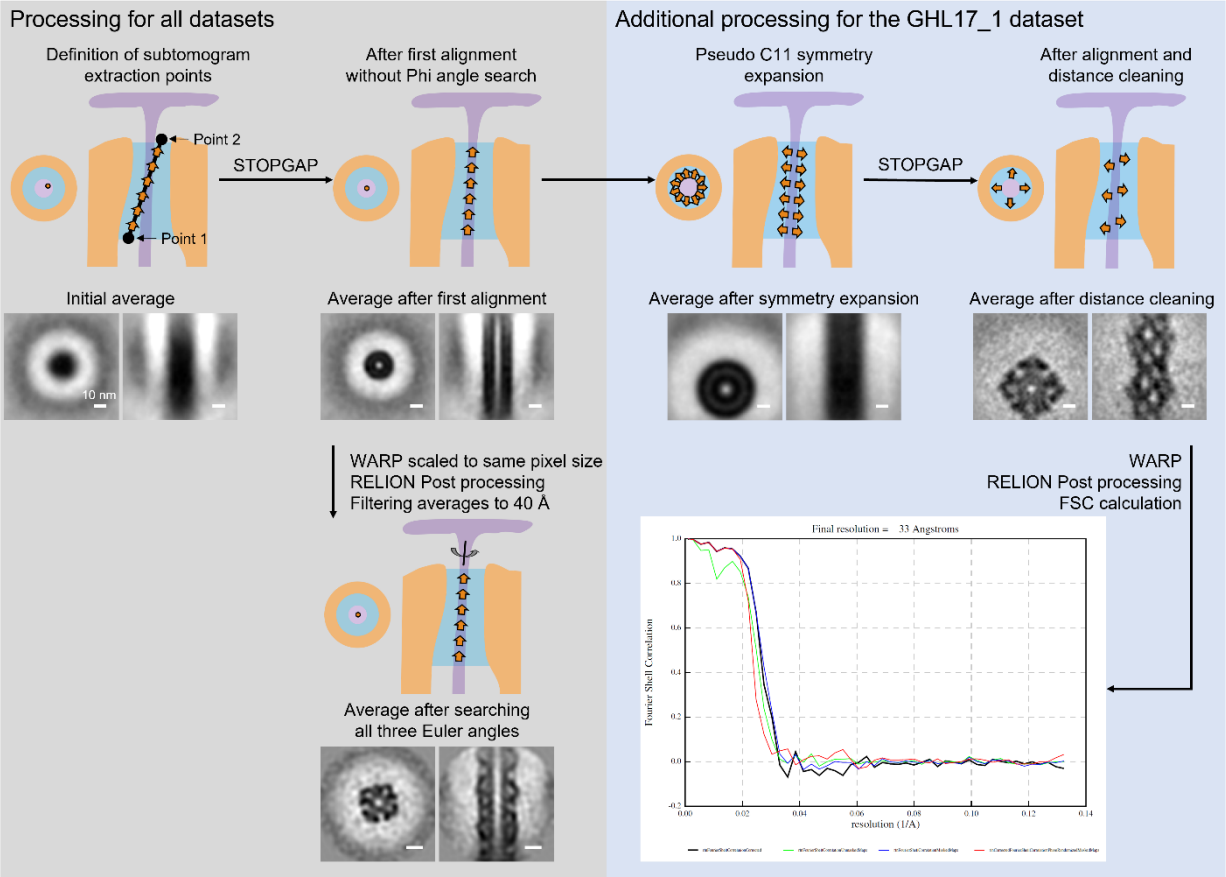
desmotubules as an indicator of curvature. Desmotubules in GHL17 plasmodesmata have lengths similar to those in wild type but are accommodated within shorter channels, resulting in increased sinuosity. Mann-Whitney-Wilcoxon test (*P = 0.04; **P = 0.008; ***P = 0.0004; ****P ≤ 0.0001; ns, not significant).



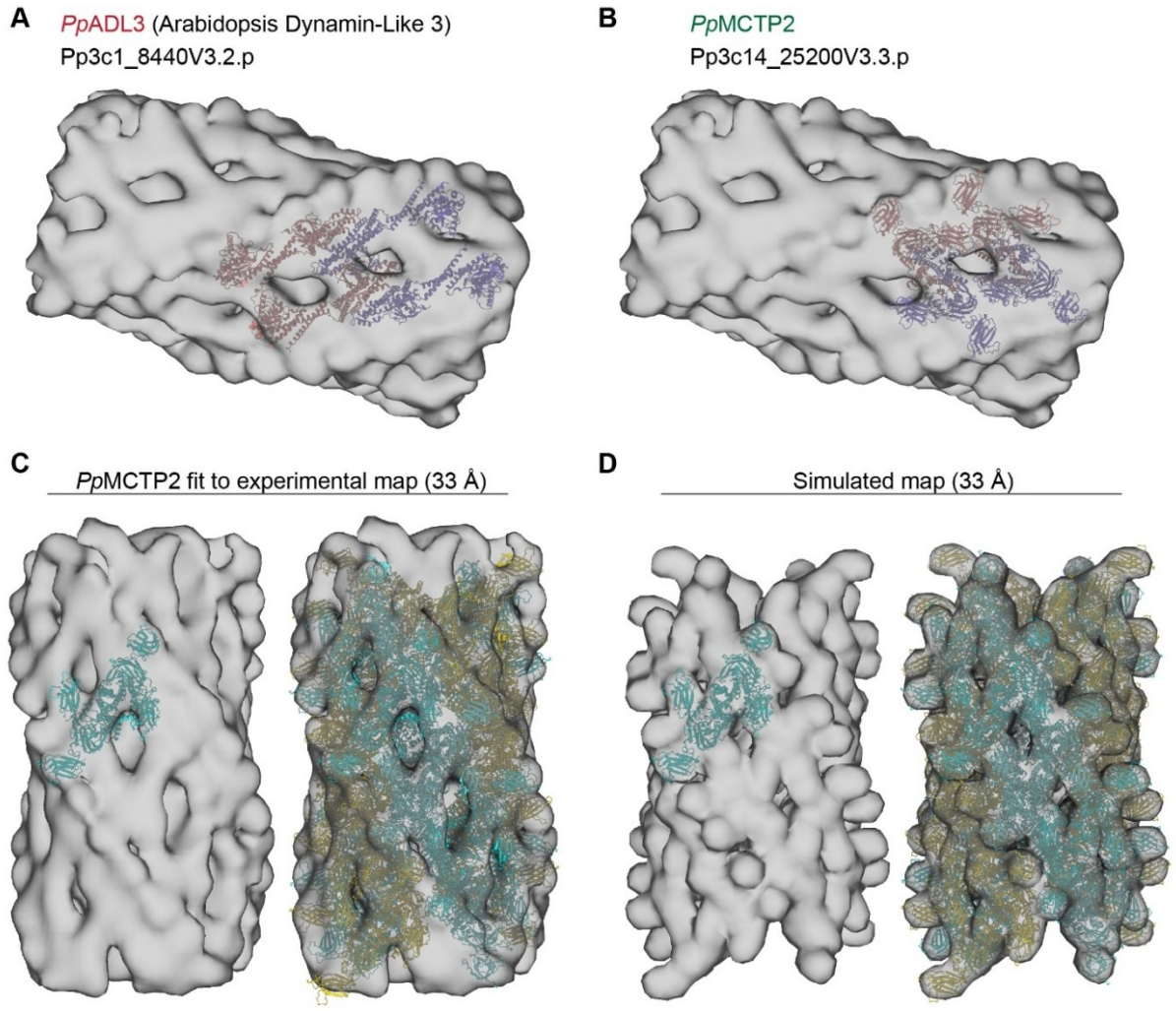
Supplementary Fig. 2 | Tomographic z-slices of a plasmodesmal aperture after ABA-treatment. Localized cell wall bulging is observed at the neck region without detectable membrane severing. Electron-dense material is accumulated within the cytosolic sleeve, obscuring parts of the desmotubule.



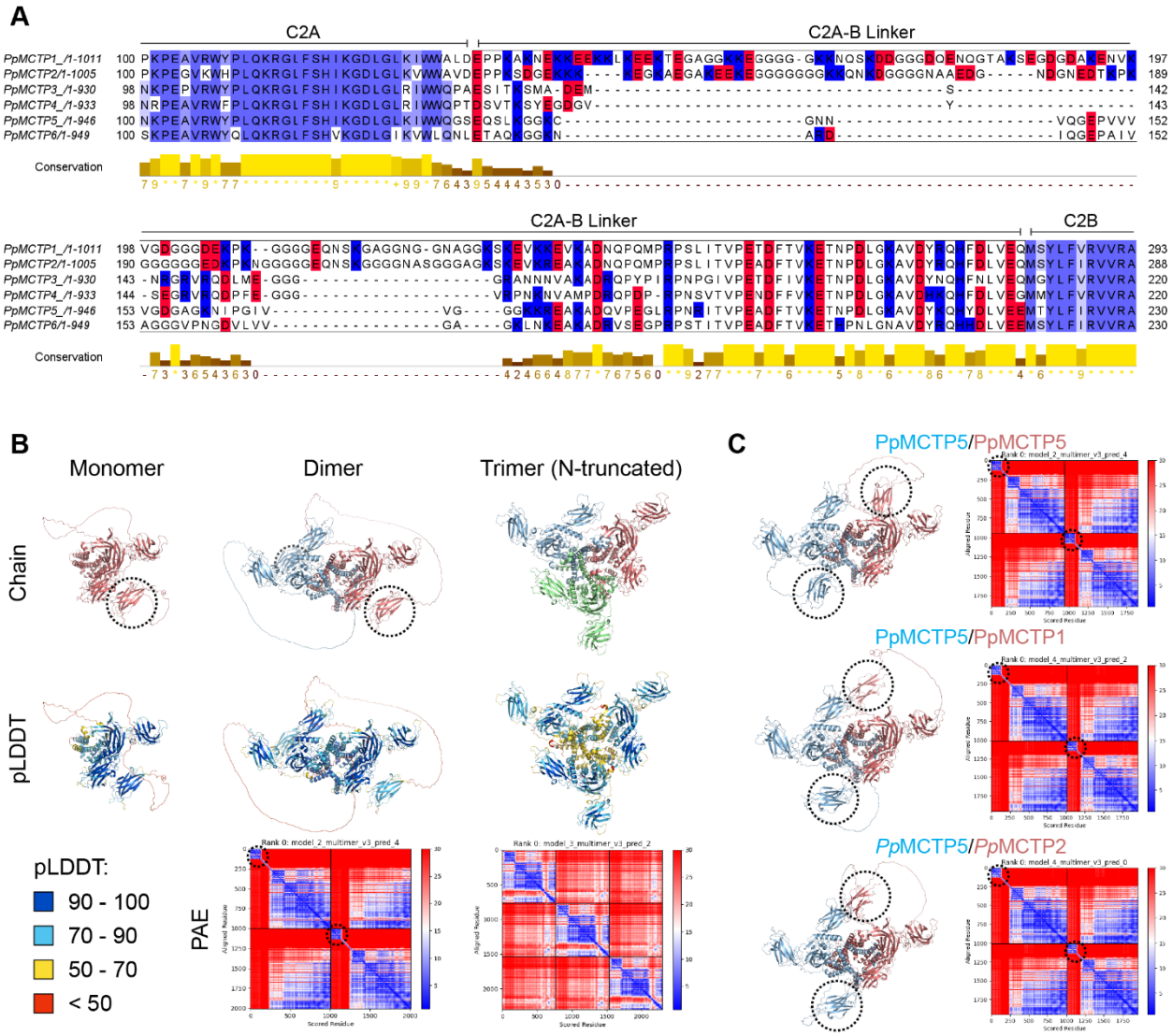
Supplementary Fig. 3 | Callose quantification by aniline blue staining in *P. patens*. a-c, Z-projections of protonemata cell-cell interfaces in transmitted light (left) and fluorescence of aniline blue (right, cyan) marking callose. **a,** Wild type protonemata. **b,** ABA-treated wild type protonemata. **c,** UBQ:GHL17_1 protonemata. **d,** Quantification of aniline blue fluorescence intensity. Mann-Whitney-Wilcoxon test (*P ≤ 0.05). Scale bars: (**a-c**) 10 µm.



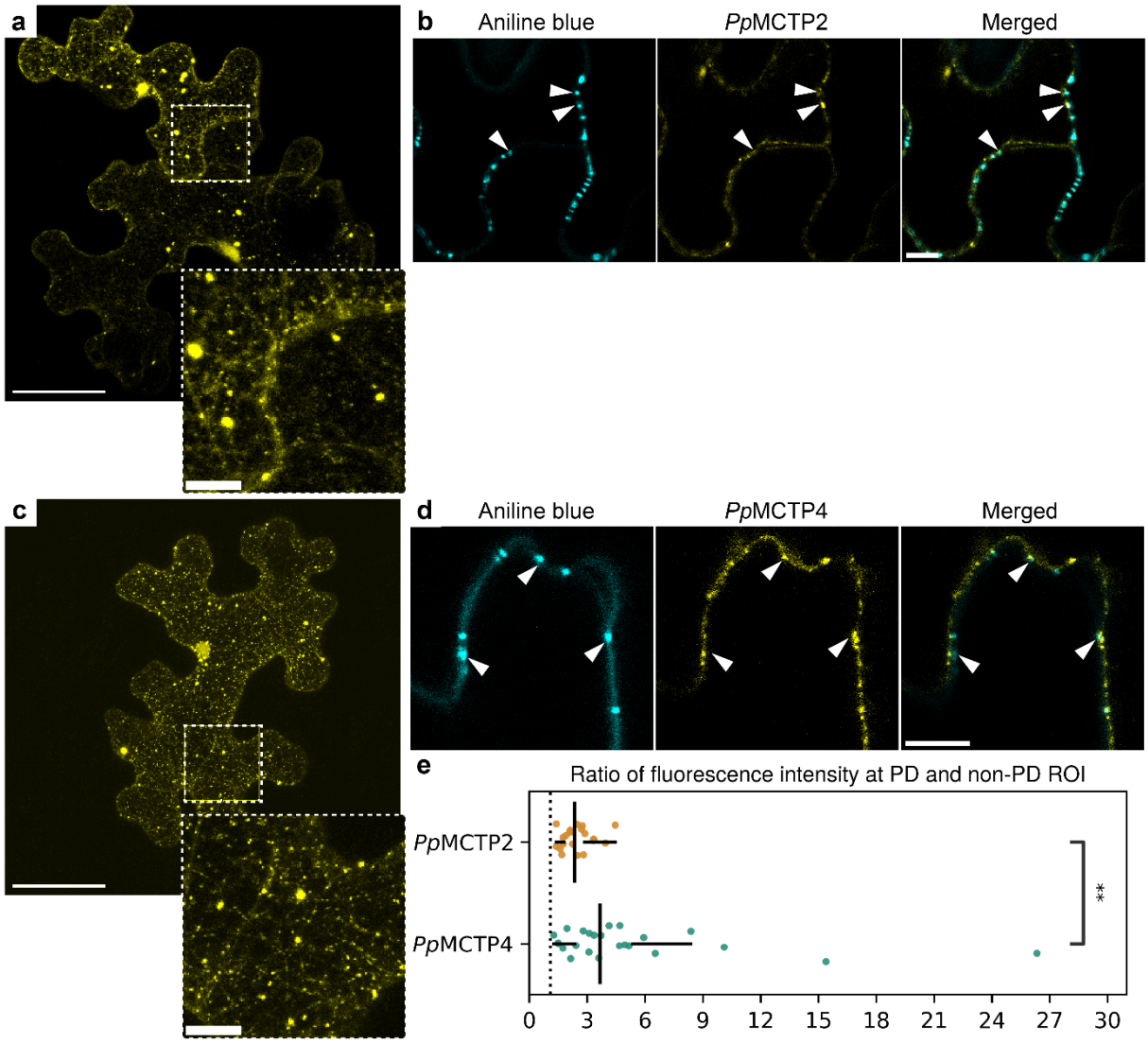
Supplementary Fig. 4 | Subtomogram averaging workflow. For each alignment step, the top panel shows a schematic representation, and the bottom panel displays an xy cross-section and an xz-plane side view through the center of the resulting subtomogram average. Subtomogram extraction points are indicated by orange arrowheads. The direction of each arrow represents the subtomogram z-axis as defined by the Euler angles θ (Theta) and ψ (Psi). Scale bars: 10 nm.



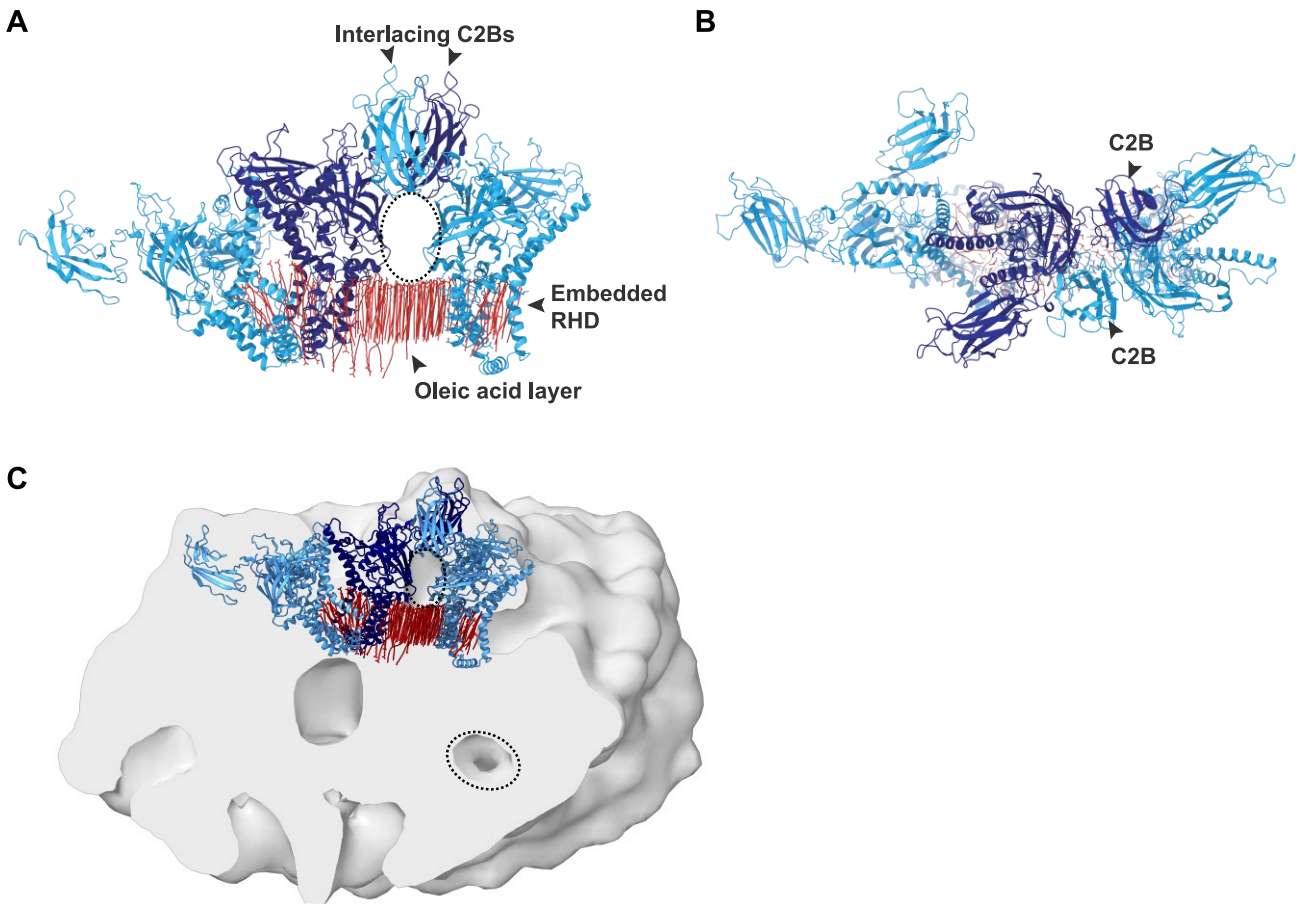
Supplementary Fig. 5 | Fitting of predicted candidate protein structures into experimental density map. To evaluate potential components of the desmotubule-associated coat, we tested candidates identified in PD-enriched proteomes. Dynamin-related proteins emerged as plausible candidates based on their property to assemble into large complexes associated with ER and their membrane tubulating function[81]. Such assemblies are formed by repeating dynamin dimers. (**A**) Two predicted PpADL3 dimers were fitted into the experimental density map of the desmotubule-coating assembly (monomers in pink and purple). Although the dimer models span the assembly lumen, the fit leaves substantial regions unaccounted for and fails to recapitulate structural features. (**B**) In contrast, PpMCTP2 dimers align closely with the experimental map, matching local geometries. (**C**) A full molecular model was generated by tiling PpMCTP2 dimeric core units along the resolved coat. Dimers colored in cyan and yellow, alternating colors between helical wraps. (**D**) From the full molecular model based on the experimental map, we generated a corresponding synthetic map. Filtered to 33 Å resolution, the synthetic map closely resembled the experimental density map. The cross-correlation coefficient between synthetic and experimental map is 0.92, indicating a good overall agreement between model and experiment.



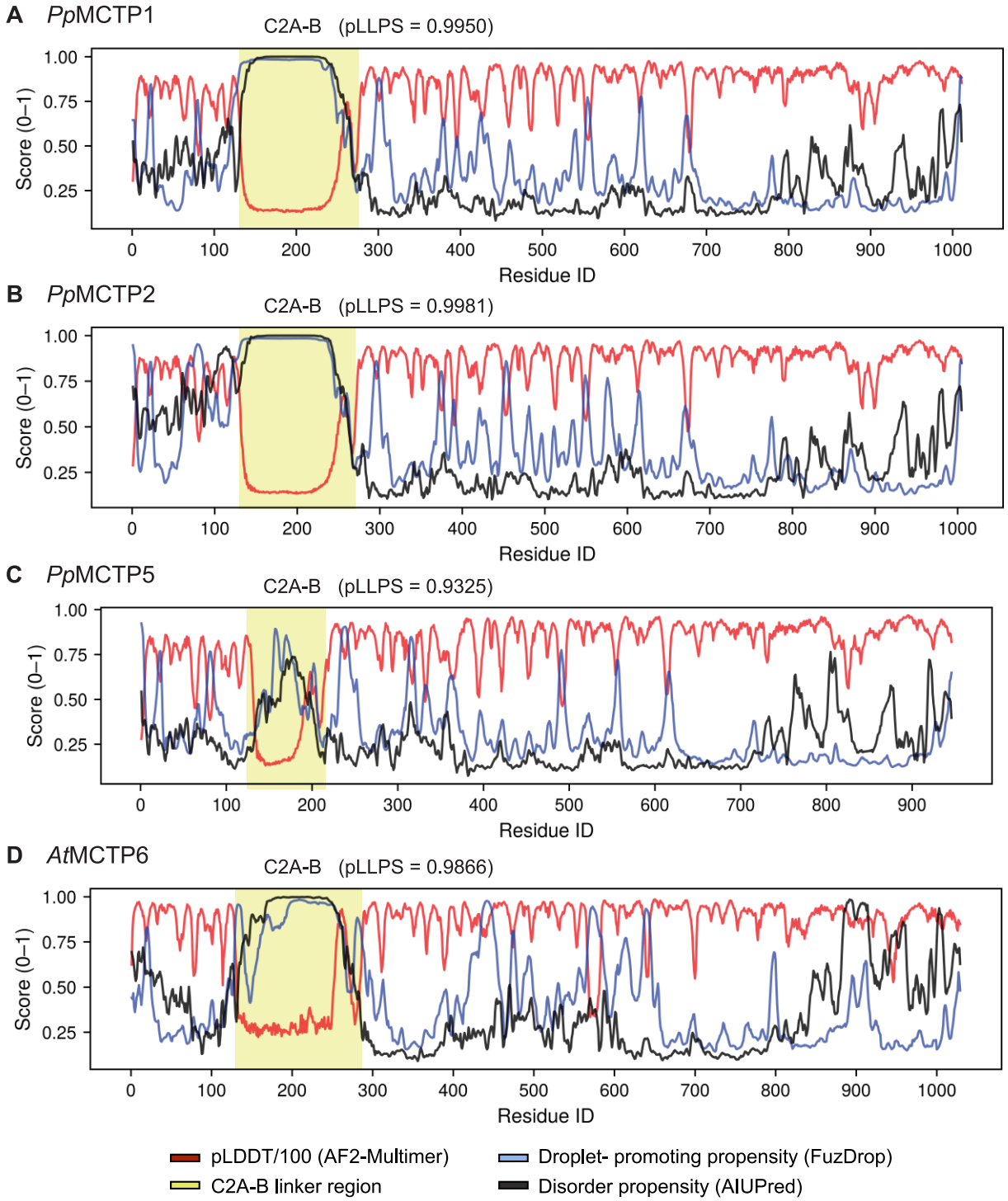
Supplementary Fig. 6 | Sequence and structural analysis of PpMCTPs. (**A**) Alignment of C2A-B linker domains. While C2 domains are highly conserved, the linker domains vary in length and residue composition. These linkers are glycine-rich and polyampholyte, with evenly distributed charges (blue: positive, red: negative). This composition suggests high solubility and flexibility, with a propensity for unspecific intra or intermolecular interactions. Identical residues in C2A and C2B are colored in blue. (**B**) AlphaFold2-predicted structures of monomeric, dimeric, and trimeric PpMCTP2 with corresponding model confidence metrics. Dotted circles mark positionally flexible C2A domains. While the predicted local distance difference test scores (pLDDT) within C2A domains itself are high, indicating well-defined local structure, the predicted aligned error (PAE) between the C2A domain and the rest of the protein exceeds 30 Å, suggesting that the domain is positionally flexible while maintaining its domain integrity. In contrast, C2A-B linker domains exhibit low pLDDT (< 50) and high PAE (> 30 Å), supporting intrinsic flexibility. Central helices and RHDs show increased pLDDT in the dimer compared to the monomer. In trimeric models, both pLDDT and PAE indicate reduced model confidence at oligomerization interfaces, supporting the dimer model as the favorable oligomeric arrangement. For trimer predictions, the flexible N-terminus was truncated to reduce compute, as it does not participate in oligomer contacts. (**C**) Structure predictions reveal no substantial differences between homo- and hetero-PpMCTP dimers. Besides the positional variability of C2A domains (dotted circles) and C2A-B linker domains, the predicted conformations are nearly identical and no apparent shift in confidence metrics is observed. Combined, sequence analysis and structure prediction suggest that both homo- and heterodimeric pairings of all six PpMCTPs are biochemically, structurally and evolutionarily plausible.



Supplementary Fig. 7 | In vivo localization of *Pp*MCTPs in *N. benthamiana*. a,c, Maximum intensity z-projections showing (**a**) *Pp*MCTP2 and (**c**) *Pp*MCTP4 localization in epidermis cells. Dashed rectangles indicate region magnified in inset. **b,d,** Dotted localization patterns of the plasmodesmal marker aniline blue (cyan) and mVenus-*Pp*MCTPs (yellow) in single z-slices focused at the cell periphery. White triangles exemplify co-localization. **e,** PD index quantification of *Pp*MCTPs. Proteins with a PD index > 1.1 (dotted line) are considered enriched at plasmodesmata[11]. Mann-Whitney-Wilcoxon test (**P = 0.0086). Scale bars: (**a,c**) 500 µm, inset 10 µm; (**b,d**) 10 µm.



Supplementary Fig. 8 | Structure prediction of trimeric *Pp*MCTP in the presence of fatty acids recapitulates the experimentally determined desmotubule coating assembly. AlphaFold3 enables structure prediction of proteins in the presence of selected ligands. When added in excess, the fatty acid ligand oleic acid approximates membrane-like chemical properties and improves prediction accuracy for membrane proteins. (**A**) Side and (**B**) top view of predicted trimeric *Pp*MCTP2 (monomers shown in alternating light and dark blue) with 140 oleic acid molecules (red) forming a layer around the reticulon homology domains (RHDs). C2B domains interlace as observed in the experimentally resolved desmotubule-coating assembly. Dotted ellipse marks unoccupied spot between membrane and interlaced C2Bs. C2A and the flexible C2A-B linker are excluded. (**C**) Angled cross-section of the experimental map with docked trimeric AlphaFold3 model. Unoccupied spots underneath interlaced C2B domain pairs align well in the model and experimental map (dotted circles).



Supplementary Fig. 9 | In silico profiling of sequence-encoded biophysical properties of full-length MCTPs. (**A**) PpMCTP1, (**B**) PpMCTP2, (**C**) PpMCTP5, and (**D**) Arabidopsis AtMCTP6. Shared y-axis shows per-residue confidence scores from AlphaFold2-Multimer predictions (pLDDT/100, red), predicted droplet-promoting propensity (pDP) from FuzDrop (blue), and predicted disorder propensity from AIUPred (black). C2A-B linker domains are indicated in yellow. Liquid-liquid phase separation potentials (pLLPS, FuzDrop) of C2A-B linker domains are stated for each homolog.

Supplementary Table 1 | *Pp*MCTP gene identifiers and protein names.

Protein name	Gene ID v6	Gene ID v3	Proteome rank (Gombos et al. 2023)	C2A-B linker length
*Pp*MCTP1	Pp6c10_5830	Pp3c10_11080	158	150 aa
*Pp*MCTP2	Pp6c14_13840	Pp3c14_25200	20	145 aa
*Pp*MCTP3	Pp6c25_4790	Pp3c27_540	319	80 aa
*Pp*MCTP4	Pp6c16_4930	Pp3c16_9250	318	80 aa
*Pp*MCTP5	Pp6c25_4800	Pp3c27_520	5	88 aa
*Pp*MCTP6	Pp6c16_4910	Pp3c16_9260	Not detected	88 aa

Gene identifiers, protein names, rank in proteome sorted by enrichment in PD fractions, and length of C2A-B linkers in amino acids. *Pp*MCTP1, 2, 3, 4, and 5 are found in the proteome with *Pp*MCTP1, 2 and 5 being most abundant.

Chapter 6

Methodology – Preparation of moss tissue for cryo-electron tomography

Preparation of Moss Tissue for Cryo-Electron Tomography by High-Pressure Freezing, Focused Ion Beam Milling and Lift-Out

Status: Manuscript in preparation.

6.1 Summary

Background and summary

The previous chapter described the development of cryo-electron tomography (cryo-ET) workflows that enable cryo-ET of plant tissue samples. The process remains technically demanding, low-throughput and requires substantial user experience. In an attempt to lower the barrier to entry, this protocol outlines the workflow step-by-step and provides practical advice. Vitrification efficiency is quantified and discussed. From a total of 45 high-pressure frozen *Physcomitrium patens* samples, 21 (47%) produced vitreous lamellae.

Contributions to this chapter

I contributed to this chapter by establishing and maintaining plant culturing at the Department of Molecular Structural Biology, sample preparation and vitrification by high-pressure freezing. I contributed to implementing and testing of the described FIB-milling workflows (with MP, PX, OS, COJK, JB, SK), cryo-fluorescence microscopy (with MP, PX, AB, CC), data analysis (with MP, PX), and manuscript editing (with MP, COJK, SK, JMP, WB).

6.2 Results

Preparation of Moss Tissue for Cryo-Electron Tomography by High-Pressure Freezing, Focused Ion Beam Milling and Lift-Out.

Matthias Pöge[1,$,*], Marcel Dickmanns[1,2], Peng Xu[1], Oda H. Schiøtz[3], Christoph O. J. Kaiser[3], Anna Bieber[1,4], Cristina Capitanio[1,4], Johann Brenner[3], Margot Riggi[5], Sven Klumpe[3], Waltraud X. Schulze[6], Rüdiger Simon[7], Wolf B. Frommer[2,9,10], Jürgen M. Plitzko[3], Wolfgang Baumeister[1]

[1] Emeritus Group Molecular Structural Biology, Max Planck Institute of Biochemistry, Martinsried, Germany

[2] Heinrich Heine University Düsseldorf, Faculty of Mathematics and Natural Sciences, Institute of Molecular Physiology, Düsseldorf, Germany

[3] Research Group CryoEM Technology, Max Planck Institute of Biochemistry, Martinsried, Germany

[4] Department Molecular Machines and Signaling, Max Planck Institute of Biochemistry, Martinsried, Germany

[5] Department of Cell and Virus Structure, Max Planck Institute of Biochemistry, Martinsried, Germany

[6] Department of Plant Systems Biology, University of Hohenheim, Stuttgart, Germany

[7] Heinrich Heine University Düsseldorf, Faculty of Mathematics and Natural Sciences, Department of Developmental Genetics, Düsseldorf, Germany

[9] Cluster of Excellence on Plant Sciences (CEPLAS), Heinrich Heine University, 40225 Düsseldorf, Germany

[10] Institute of Transformative Bio-Molecules, Nagoya University, Chikusa, Nagoya 464-8601, Japan

[$]Present address: Electron Microscopy Facility, Max Planck Institute of Molecular Cell Biology and Genetics, Dresden, Germany

*For correspondence: poege@mpi-cbg.de

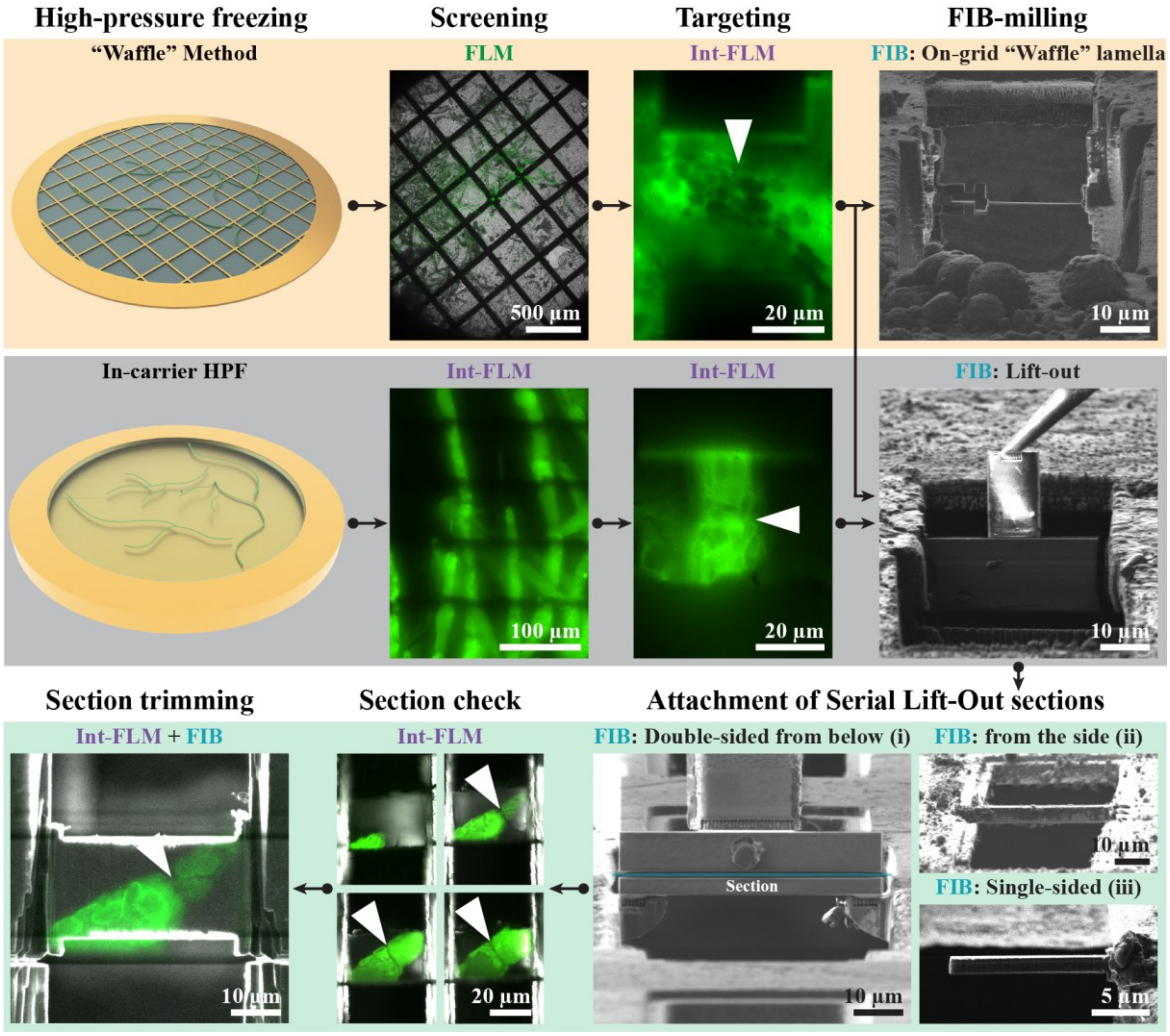
Abstract

Cryo-Electron Tomography (cryo-ET) is a powerful imaging technique that allows to visualize the molecular landscape within cells. In contrast to traditional preparations for electron microscopy deploying chemical fixation and contrasting agents, cryo-ET directly images the inherent contrast of cryo-fixed, i.e. vitrified samples, providing a faithful and near-native representation of cellular ultrastructure and its macromolecular constituents. While cryo-ET in combination with thinning by Focused Ion Beam (FIB) milling is well established for single small or thin cells that can be vitrified by plunge freezing, its application to tissues is still challenging in terms of vitrification and thinning strategies. Intact plant tissues are particularly difficult to scrutinize, due to their relatively large cell size and the presence of vacuoles which often occupy a large fraction of cells and usually do not vitrify. Here, we describe two methods for vitrification of the filamentous tissue (Protonemata) of moss (Physcomitrium patens) by two High-Pressure Freezing (HPF) approaches. We also describe in detail how to prepare thin sections (lamellae) suitable for cryo-ET data acquisition by either on-grid FIB milling or lift-out with three different attachment methods that can be applied depending on skill and experimental setup of users. For the preparation of lift-out lamellae, we introduce an additional trimming step which can help to improve lamella quality. We illustrate how subcellular structures can be targeted by aiming for cell junctions using cryo-Fluorescence Light Microscopy (FLM). The different preparation procedures can be used for samples of different sizes and other multicellular systems.

Key Features

- This protocol builds on Serial Lift-Out (Schiøtz et al. 2023) but was adapted for moss and can be applied to other species and tissues as described in (Pöge et al. 2025, Dickmanns et al. 2025).
- It requires a high-pressure freezer (i.e. Leica EM ICE), a cryo-light microscope (i.e. Leica TCS SP8) and a FIB-SEM instrument with lift-out system (i.e. Thermo Fisher Scientific Aquilos II) ideally with integrated fluorescence light microscope (i.e. Delmic METEOR).
- We describe two high-pressure freezing approaches for different specimen sizes and procedures for sample screening and targeted lamella preparation aided by cryo-fluorescence light microscopy.
- We describe on-grid lamella preparation and three lift-out approaches with a novel, more robust attachment mode.
- By applying an additional trimming step for lift-out sections, this protocol was optimized for lamella quality rather than quantity.

Graphical abstract



Overview of the protocol's workflows. First, *P. patens* protonemata cells are high-pressure frozen either by the "Waffle" Method or inside an HPF carrier. Next samples are screened in an external cryo-Fluorescence Light Microscope (FLM) or a FLM integrated (int-FLM) into a cryo-Focused Ion Beam (FIB) instrument. For "waffle" grids, on-grid lamella preparation is possible. To generate lamellae from in-carrier frozen samples, lift-out is required. For the Serial Lift-Out approach, in which the initial lift-out block is cut into several sections attached to a receiver grid, three distinct modes are described: (i) double sided attachment from below, (ii) double-sided attachment from the side and (iii) single-sided attachment. Before fine milling, sections can be assessed for the presence of the target area and trimmed to remove excessive material.

Background

Cryo-Electron Tomography (cryo-ET) is a powerful method at the interface between structural biology and cell biology which allows to visualize the molecular landscape within cells in 3D (Lučič, Rigort, and Baumeister 2013; Turk and Baumeister 2020). The first step in the workflow is cryo-fixation by vitrification, in which the sample is rapidly cooled to temperatures well below -150°C while avoiding the formation of crystalline ice, i.e. transferring water into a vitreous state (Dubochet 2007). This step is critical because it arrests the cell in a frozen-hydrated, near-native state. Cells thinner than approximately 10 µm can often be vitrified by plunge-freezing. In this process, cells are applied as a thin film onto a grid for electron microscopy and plunged into a cryogen

(Dobro et al. 2010). Cells thicker than a few hundred nanometers must then be thinned before they can be imaged in a Transmission Electron Microscope (TEM). Here, cryo-Focused Ion Beam (FIB) milling has become the method of choice in the field: a focused beam of Gallium ions is used to ablate material above and below an area of interest until only a sufficiently thin sheet of material remains that is still supported by the bulk sample on its sides (Rigort et al. 2012). These sheets are termed lamellae. To identify target areas within vitreous samples, cryo-Correlative-Light-and-Electron-Microscopy (CLEM) techniques have been developed, which correlate FIB and SEM images to images recorded in an external cryo-Fluorescence Light Microscope (FLM) (Arnold et al. 2016) or an FLM integrated (int-FLM) into the chamber of the FIB system (Yang et al. 2023). The resulting lamellae are then imaged in a cryo-TEM. In cryo-ET, a set of TEM images are recorded in the same area from a defined range of angles. This data is used to computationally yield a 3D reconstruction of the pleomorphic environment of the cell, a volume referred to as tomogram (Koning, Koster, and Sharp 2018).

Many multicellular samples, however, are too thick to be vitrified by plunge-freezing. Especially intact plant tissues are challenging due to their large size and the presence of vacuoles occupying large fractions of the cell with the tendency to not vitrify. An alternative approach to achieve vitrification is High-Pressure Freezing (HPF) (Dubochet 1995; Moor 1987). The specimen is sandwiched between metal carriers and a pressure of approximately 2000 bar is applied while the sample is cooled by a jet of liquid nitrogen. Under these conditions, samples with a thickness of up to 200-300 µm can potentially be vitrified. Working with HPF samples, however, is more challenging and time consuming than working with plunge frozen samples. Throughput as well as success rate are lower and CLEM approaches required to target biological material are tedious and time-consuming.

In this protocol, we describe in detail how we adapt the “Waffle” Method (Kelley et al. 2022) and use in-carrier high-pressure freezing for protonemata of the moss Physcomitrium Patens, which are filaments of single, cylindrical cells with diameters of 15-30 µm (Rensing et al. 2020). We lay out how to use cryo-FLM in cryo-FIB milling for targeted lamella preparation either by on-grid milling or Serial Lift-Out (Schiøtz et al. 2023) with three different attachment methods. The presented sample and lamella preparation strategies have advantages and disadvantages which are discussed in (Pöge et al. 2025) and can be deployed for other specimen beyond plant tissues. We uncovered many pitfalls and critical steps which are pointed out at the respective steps in the workflow. Thus, we anticipate that this protocol can be a valuable resource for labs getting started with cryo-ET on multicellular samples.

Procedure

This protocol describes two options for HPF of *P. patens* protonemata: (i) a modified

version of the “Waffle” Method (Kelley et al. 2022) adapted from (Schiøtz et al. 2023) and (ii) in-carrier high-pressure freezing. Furthermore, four procedures to prepare lamellae for cryo-ET are described: (i) on-grid “waffle” milling, (ii) lift-out with double sided attachment from below, (iii) lift-out with double sided attachment from the sides and (iv) lift-out with single sided attachment. The protocol is specifically aiming for junctions between *P. patens* cells. These cell junctions are small compared to the whole cell and it is convenient to employ an integrated-Fluorescence Light Microscope (int-FLM) for targeted trench milling. The targeting approach, however, can be used for any cellular structure that can be discerned in int-FLM images, e.g. by the expression of fluorescent fusion marker proteins.

I. The “waffle” workflow

A. Growing *Physcomitrium patens* protonemata

Culture *P. patens* protonemata as described in (Cove et al. 2009):

1. Autoclave the solid growth medium and cellophane sheets.
2. Melt the solid growth medium by heating it in a microwave, if it is not liquid anymore.
3. In a laminar flow bench, plate 40 mL of the still liquid solid growth medium on a sterile petri dish.
4. After the solid growth medium is solidified, add an autoclaved cellophane sheet on top and streak out air bubbles underneath with sterile, flat tweezers.
5. Harvest 2 weeks old moss tissue from a previously prepared plate (~1 g per plate), add to a 50 ml Falcon tube filled with 20 ml ddH_2O.
6. Homogenize with the tissue with the disperser rod (3x3 s pulses on lowest speed setting)
7. Spread 1 mL homogenized *P. patens* liquid culture on a freshly prepared, cellophane-overlayed plate.
8. Grow *P. patens* for 2 weeks in a growth chamber at 25°C with 18 h and 6 h light and dark cycle, respectively.

B. “Waffle” freezing adopted from (Schiøtz et al. 2023)

1. Clean 6 mm type B HPF carriers (with one 300 µm cavity and one flat side) the day before freezing.
    a. Incubate carriers overnight in a 15 mL Falcon tube with cleaning solution.
    b. Wash carriers 3x with ddH_2O and 3x with acetone.

c. Dry carriers on filter paper.

2. Coat carriers with cetyl palmitate.
   Note: Work under a fume hood.

   a. Dip clean type B carriers, one at a time, with tweezers into the cetyl palmitate solution.

   b. Remove excess of liquid by shaking it off and pushing the side of carriers against filter paper.

   c. Dry carriers on filter paper with the flat side facing up.
   Critical: There should be a slight haze on the carrier, only obvious under the binocular. If the layer is visible to the bare eye, the layer is likely too thick.

3. Prepare the Leica EM ICE high-pressure freezer and test the system.

   a. Cool down the high-pressure freezer and the sample container.

   b. Insert the sample container and wait for the system status to change to ready.

   c. Freeze two samples with only the two half cylinders and a middle plate assembled without HPF carriers.
   Note: *This allows the system parts to equilibrate and adjust to the working temperature. It will also report the freezing curves, allowing to assess the normal working state of the machine. The pressure should persist at slightly above 2,000 bar for at least 250 ms and not longer than 450 ms. If that is not the case, contact the Leica support.*

4. Place a clean and coated type B HPF carrier on a filter paper with the flat side facing up.

5. Add a 3 µL droplet of freezing buffer on the flat side of the carrier.

6. Place an EM grid with the continuous support film side facing down on the droplet.
   Critical: The sample will be added on the "back" of the grid, i.e. the grid bar side by filling it into the wells formed by the grid bars and the support film. For plunge-freezing, the sample is applied on the other side onto the film.

7. Remove excess buffer with a 0.5x2 cm piece of filter paper until the grid is lying flat on the carrier.
   Critical: Initially, there will be convex cushions of buffer formed between carrier and support film. Blot until these cushions collapse and the support film contacts the carrier surface. This can be observed using the binocular

8. Add 3 µL of buffer freezing buffer onto the grid and distribute it with the pipet tip or tweezers until the whole grid surface is covered.

9. Remove air bubbles by poking them with sharp tweezers. Alternatively, use slightly open tweezers and let the bubbles float into the liquid that is lifted between the tweezer legs by capillary force.
   Critical: Air bubbles in the sample will be compressed upon high-pressure freezing and affect local pressure buildup negatively. They also expand again when the freezing chamber is depressurized and induce cracks in the sample compromising subsequent steps.
10. Pick up a small patch of a protonemata from a plate and place it in the center of the grid.
    Critical: Try not to squeeze the tissue with tweezers. This will damage the cells. Lift the tissue with the tip of a single leg of the tweezers to avoid squeezing.
11. If new air bubbles were created during the transfer of the tissue, remove them.
12. Place a second coated type B carrier with the flat side down on top of the sample and press the sandwich lightly.
13. Remove excess buffer with filter paper around the carrier sandwich.
14. Place the sandwich in the middle plate on the lower plastic half cylinder.
15. Turn your tweezers upside down and press the sandwich thoroughly for 10 s with the reverse tweezer end.
    Note: Pressing with the reverse tweezer end avoids damage to the tweezer tips or the carrier.
16. Immediately close the sample holder lid and freeze the sample.
17. After all grids are high-pressure frozen, recover the grids by separating them from the carriers.
    a. Remove all half-cylinders.
    b. Remove middle plates and carriers that fell apart and have no grid attached to them.
    c. If the sandwich is still in the middle plate, place it over a sufficiently large cavity (e.g. grid box holder) and push with blunt tweezers.
    d. Collect all carriers with grids attached to them.
    e. Place single carriers into e.g. a grid box holder against the side wall
    f. Use sharp tweezers to press at the 3, 6, 9 and 12 o' clock positions to break the continuous ice layer on the carrier.
    g. Push the grid to the side, exerting 50% of the force in the lateral direction and 50 % in the downwards direction.

18. Mount the grids in cartridges with cutout for FIB milling.

    a. Before clipping, apply a red mark on the top of the cartridge in the 6 o'clock position opposite of the cutout and two blue markers in the 3 and 9 o'clock position.
    Note: This will help aligning the grid when loading it into microscopes.

    b. Clip the grid into the marked cartridge with the support film facing the clip ring.
    Critical: In the "Waffle" method, the sample is applied to the "back" of the grid on the opposite side of the support film. During clipping, the side with the support film must face the clip ring and the sample containing side the cartridge. This assures that the sample side is facing up when loading the grid into microscopes.

19. Pause Point: Store grids in grid boxes at liquid nitrogen temperatures until use.

C. Sample screening in a cryo-fluorescence light microscopy

1. Prepare the light microscope (e.g. Leica TCS SP8) by cooling it down, starting the lasers and letting the system equilibrate for 30-60 min with the objective roughly at the height used for data acquisition.

2. Load a clipped "waffle" grid.

3. Focus on the sample and adjust the imaging parameters on some *P. patens* cells by recording reflected light (excitation: 488 nm; emission filter: 483-493 nm or no emission filter), cellular autofluorescence (excitation: 488 nm; emission filter: 500-750 nm) and transmitted light.
    Note: The transmitted light and the autofluorescence of P. patens protonemata are sufficient to identify junctions between cells. For this target, no additional fluorescent marker is needed.
    Critical: Keep the laser power as low as possible while still being able to identify your target area. A too high laser power can devitrify your sample. The highest laser power that is safe to use depends on the system. We usually stay well below 10% laser power.
    Critical: Adjust laser power and detector gain to not overload the HyD detectors. The most adequate imaging settings are dependent on the sample thickness.

4. Record a grid map (Figure 1A, Spiral scan, Tile image size = 512 x 512, pin hole size = 600 µm, pixel size = 580 nm).
    Note: The pinhole can be fully open for this step, to collect as much fluorescence signal as possible, also from layers above and below the focal plane.

5. Identify the location of grid squares containing target areas, in our case single layers of undamaged *P. patens* protonemata with cell junctions at a distance of

at least 50 µm from grid bars (Figure 1B).
Note: The distance to the grid bars is necessary to allow for on-grid lamella preparation. Furthermore, if those cells are partially on top of grid bars they likely were damaged during high-pressure freezing and should be avoided.
*Critical: Avoid grid squares with multiple cell layers. P. patens protonemata have a diameter of 15-25 µm while the grid bars of typical EM grids are about 25 µm high. Multiple cell layers do not fit into the wells formed by the grid bars. Hence, multiple cell layers were likely squeezed and damaged by mechanical stress during high-pressure freezing (*Figure 1*C).*
Critical: For on-grid lamella preparation, target areas should be located within ~800 µm from the center of the grid to assure that they are within the range of the TEM stage for cryo-ET data acquisition.

6. Optional: acquire z-stacks of target area containing grid squares (Figure 1B, z-step size ≤ 1 µm encompassing the whole sample thickness, Image size 2048 x 2048 pixel, Pin hole size = 125 µm, pixel size = 140 nm,).

7. Pause Point: Unload the grid and store it in grid boxes at liquid nitrogen temperatures until use.

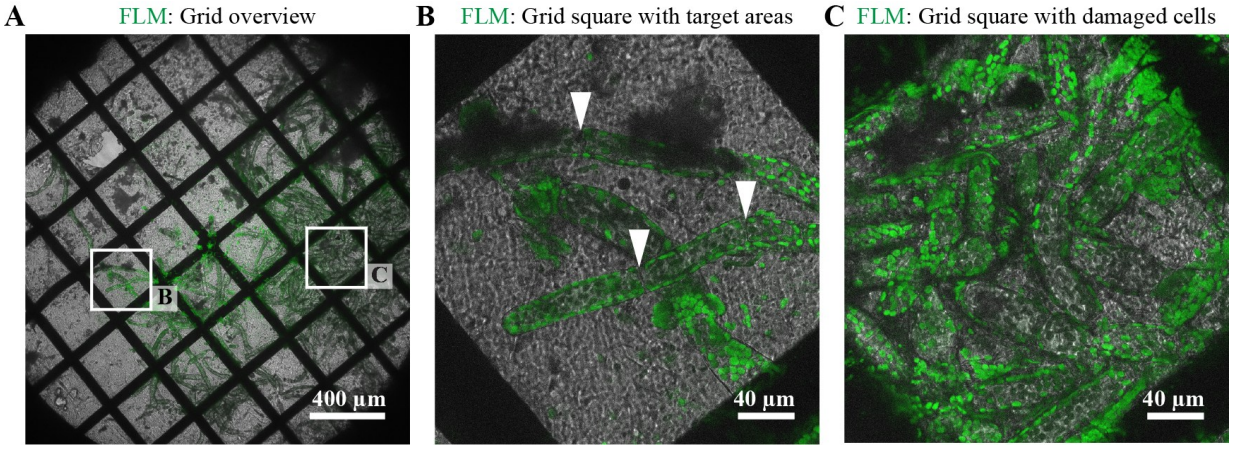


Figure 1. Sample screening in a cryo-Fluorescence Light Microscopy (FLM). Shown are the transmitted light (gray) and cellular autofluorescence (green) images of *P. patens* cells. **A**. Overview of a *P. patens* protonemata "waffle" grid (75 mesh). **B**. Grid square containing apparently intact protonemata with cell junctions (white arrowheads) in the center of the square. **C**. Grid square packed with multiple layers of protonemata. This tissue likely was mechanically damaged during HPF due to compression of the cells.

D. Trench milling in a dual Focused Ion Beam and Scanning Electron Microscope (FIB/SEM) with lateral targeting guided by an integrated-Fluorescence Light Microscope (int-FLM)

Note: Lateral targeting and trench milling are performed in trench milling orientation (stage tilt = 7°, relative rotation = 180°, Figure 2). In this stage orientation the optical axis of FIB and int-FLM are normal to the sample surface. Hence, FIB and int-FLM record sample top views.

*Critical: The stage orientation angles and milling patterns described are only correct for the standard Thermo- Fisher Scientific FIB/SEM geometry (*Figure 2*), a shuttle with a 45° pretilt and the FIB/SEM scan rotation set to 180°.*

Critical: Activate the drift suppression function of the FIB/SEM instrument during all trench milling steps. Activate at lowest SEM magnification and drag the green targeting cross to the region that is to be milled.

1. Load a grid containing promising squares into a FIB/SEM instrument equipped with int-FLM.
2. Move the stage into the lamella milling orientation (stage tilt = 20°, relative rotation = 0°, Figure 2).
3. Find the coincidence point of FIB and SEM roughly in the center of the grid and take a FIB and SEM image.
   Note: FIB imaging setting: U = 30 kV, I = 1.5-10 pA, SEM imaging settings: U = 3 kV, I = 13 pA. Use the Everhart-Thornley Detector (ETD) for detection.
4. Clear ice contamination with the FIB.
   Critical: Do this before sputtering or applying a layer of metal organic platinum with the Gas Injection System (GIS) as this will fix the contamination to the grid surface.
   Note: A fine paint brush cooled to LN2 temperature can be used before loading the grid into the FIB/SEM system to remove vast amounts of frost on the front and/or back side of the grid.
   a. Set to the lowest FIB magnification at an ion current (I) of 1 nA (dwell time = 50 ns, no line integration).
   b. Activate the selected area window (hotkey F7) and adjust its size to about 100x100 µm.
   c. Start scanning and rapidly move the selected area window over you grid from left to right and front to back while placing it on contaminated areas. You should see the contamination “hop” away (Figure 3).

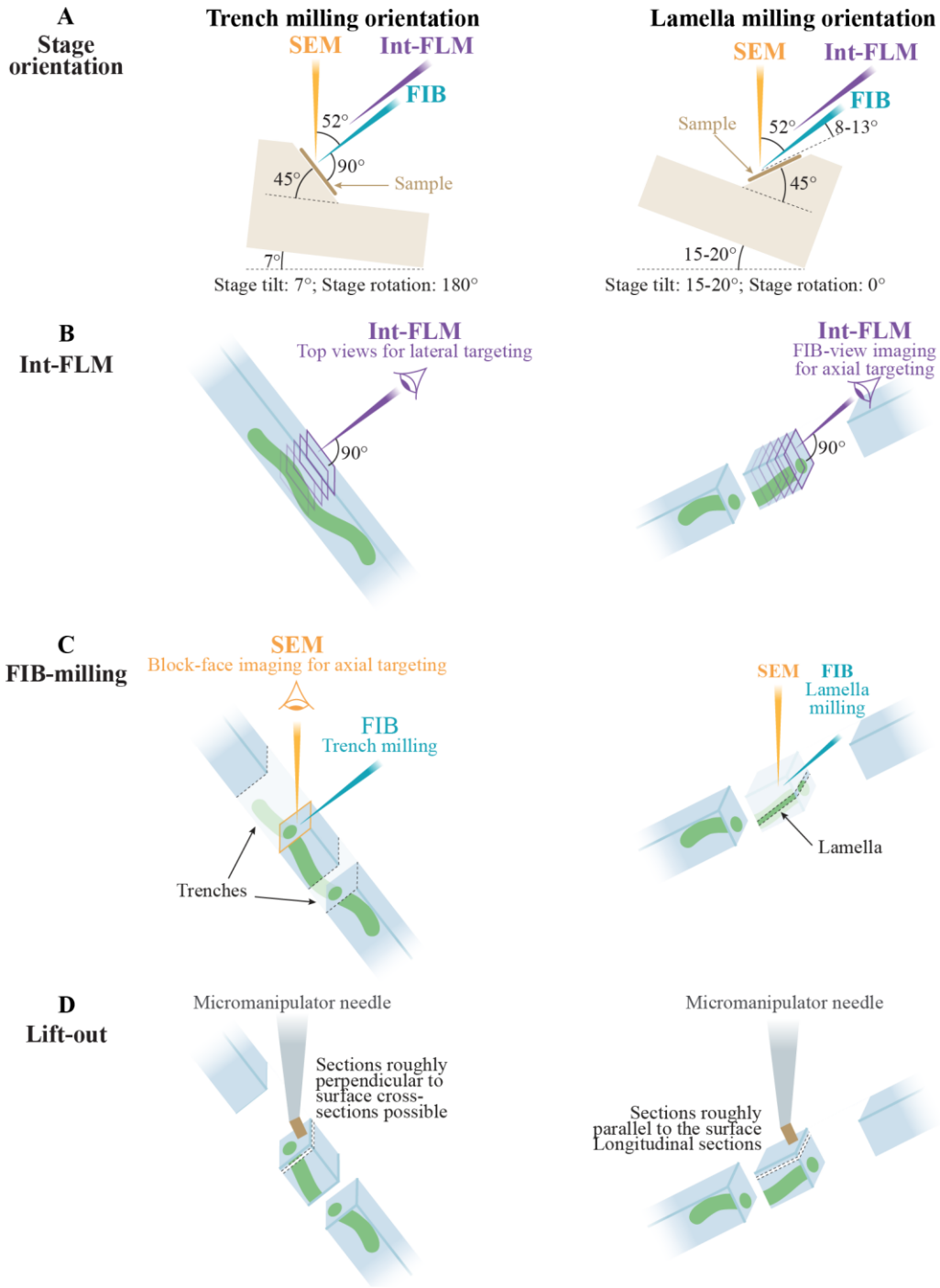


Figure 2. Scheme of the different stage orientations and their impact on imaging and lift-out steps. The left and right column illustrate the trench milling and lamella milling orientation, respectively, that mainly differ in respect to a stage rotation of 180°. The angles apply for the geometry in FIB/SEM instruments produced by Thermo Fisher Scientific using a shuttle with 45° pretilt. **A**, The shuttle with respect to stage tilt, stage rotation and the relative angles of the FIB, SEM and int-FLM optical axes. **B**, Imaging planes of the int-FLM in respect to the sample in both stage orientations. In trench milling orientation (left), the int-FLM imaging plane corresponds to the grid plane and is used for lateral targeting recording sample top views. In lamella milling orientation (right) the int-FLM images a plane close to the transverse section of the grid plane and may be used for axial targeting ("FIB-view" mode). **C**, Imaging planes of the SEM and FIB modes. In trench milling orientation (left), the ion beam is normal to the sample surface and used to mill trenches to the side of the target area. In Lamella milling orientation (right), the ion beam is used to obtain thin lamellae from a shallow angle. **D**, The orientation of the lift-out system in relation to the sample. In trench milling orientation (left), lift-out results in sectioning planes transverse to the sample surface and can yield cross-sections of protonemata. In lamella milling orientation (right), lift-out will yield sectioning planes at shallow angles towards the sample surface, resulting in longitudinal sections of protonemata.

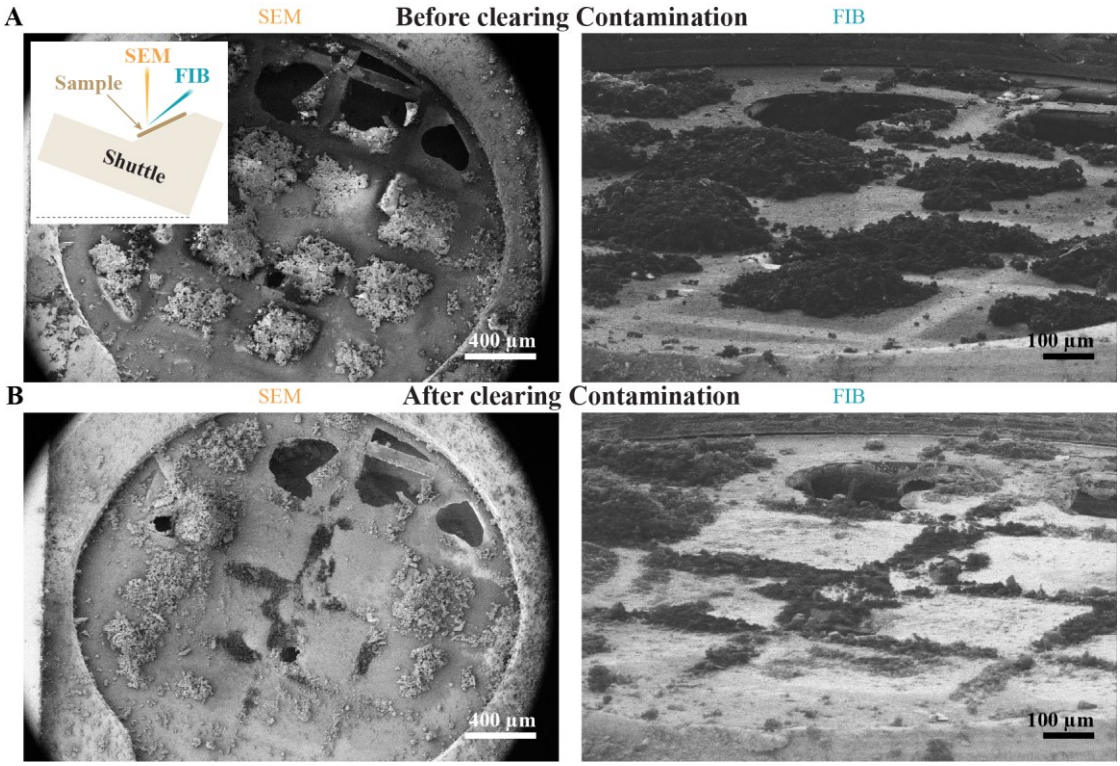


Figure 3. Clearing of contamination using the FIB. A. A heavily contaminated "waffle" grid. The inset illustrates the location of the sample in the 45° pretilt shuttle with respect to the imaging direction of FIB and SEM. **B**. After scanning at 1 nA with the selected area window over the grid surface, most of the ice is removed from the grid squares.

5. Optionally: Sputter coat the grid (p = 0.1 mbar, U = 1 kV, I = 10-30 mA, t = 15-30 s).
   Note: The resulting Platinum layer mitigates charging for thicker samples resulting in higher quality of FIB and SEM images and more precise trench milling without drift suppression activated.

6. Rotate the stage to trench milling orientation (tilt = 7°, relative rotation = 180°, Figure 2).

7. Apply a layer of metal-organic platinum with the Gas Injection System (GIS) by moving the stage in trench milling orientation to the GIS working distance, inserting the GIS needle and opening the GIS valve for 40 s (layer thickness ~ 200 nm on our systems).
   Note: The GIS working distance and the thickness of the deposited layer of metal organic platinum may vary between different FIB/SEM instruments. A calibration curve for your own instrument can be generated to estimate the thickness of the deposited layer depending on valve opening times (see also General Notes point 6).

8. *Find the coincidence point on a grid square containing a target area as identified in the FLM before.*

Note: the nearly featureless surface of "waffle" grids makes the correlation of external FLM and FIB images difficult. Thus, the int-FLM is convenient for targeted FIB milling. Yet, you should be able to estimate roughly where your target area is located within the grid square.

9. Mill a marker at a distance of 10-40 µm from your target area (cross-section, I = 3 nA, z = 0.5 µm).
   Note: An asymmetric marker can be beneficial, if FIB and int-FLM images are rotated with respect to one another. For example, an 8x8 µm square with 6x16 µm rectangle aligned with their lower edges at a distance of 8 µm (Figure 4A).

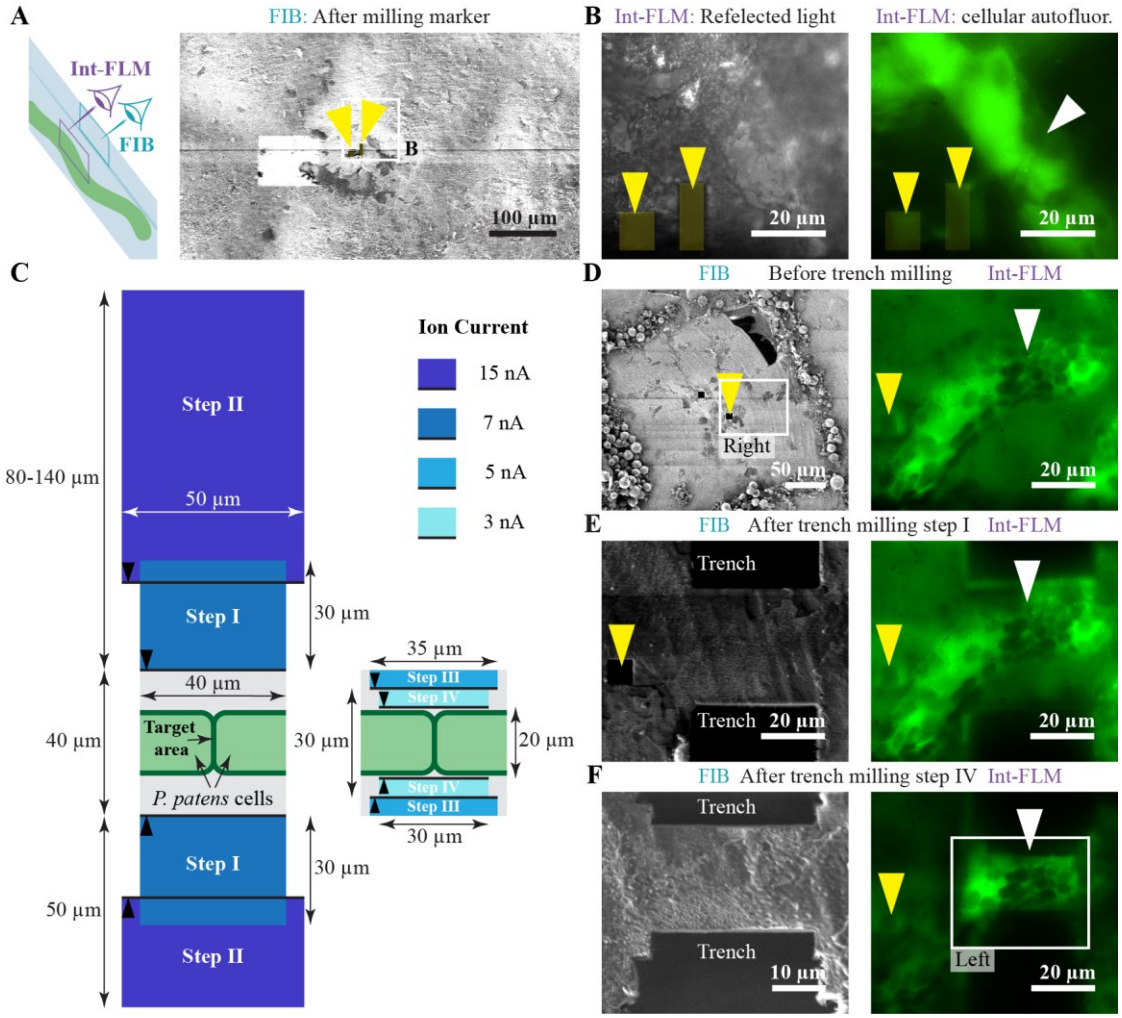


Figure 4. Lateral targeting and trench milling guided by the integrated Fluorescence Light Microscope (int-FLM). **A.** Sample top view image recorded with the FIB. The asymmetric marker pattern is marked by yellow arrowheads. The scheme on the left illustrates the location of the sample with respect to the imaging direction of FIB and int-FLM. **B.** Top views recorded with the int-FLM. The left panel shows the reflected light channel with marker holes, the right panel the cellular autofluorescence revealing a cell junction. **C.** Scheme of the trench milling patterns (only valid for FIB scan rotation of 180°). Black arrowheads indicate the milling direction. **D-F.** FIB and int-FLM (cellular autofluorescence) top view images of successive trench milling steps. Recording int-FLM images after each trench milling step is necessary to precisely center the target area. Marker holes and target areas are indicated by yellow and white arrow heads, respectively. The FIB milling patterns are provided in the section Supplementary information.

10. Use the int-FLM to record sample top views.

    a. With the stage in trench milling orientation, focus the int-FLM on the sample surface and locate the marker pattern (Figure 4B).
    Note: This is easiest accomplished using reflected light (excitation: 470 nm ± 10 nm; no emission filter)

    b. Use the int-FLM to identify the target area nearby. For *P. patens* cell junctions, use cellular autofluorescence (excitation: 470 nm ± 10 nm; emission filter: 515 nm ± 15 nm, Figure 4B).
    Critical: Keep the laser power as low as possible while still being able to identify your target area. A too high laser power may devitrify your sample.

    c. Determine the location of the target area with respect to the marker pattern. Measure the exact distance in the Odemis software.
    Note: If marker and target area are not within the same field-of-view in the int-FLM, consider milling another marker closer to the target area.

    d. Optional: Record z-stacks of the target area using the int-FLM (pixel size = 168 nm, 20-25 z-slices, z-step = 1 µm) to estimate the location of the target area within the thickness of the sample.
    Note: For on-grid lamella preparation, we prefer target areas close to the top sample surface. It is substantially harder to prepare lamellae near the bottom surface, especially for thick samples.
    Note: If both FLM and int-FLM imaging are employed for targeting, the used excitation wavelengths and emission filters should ideally be the same for both imaging modalities. This assures most reliable targeting. That is not the case here. Therefore, the fluorescence signals of FLM and int-FLM images (e.g. Figure 2 compared to Figure 4) appear different.

11. Use the relative location of the target area with respect to the marker pattern to define patterns for trench milling in the FIB user interface.

12. Mill trenches (holes) above and below the target area in trench milling orientation (Figure 4C).
    Critical: use regular cross-sections (Material: Si, Multipass: 4x) as they ablate material faster and generate smoother surfaces than rectangle patterns. The milling direction is always towards the target area.
    Critical: Activate the drift suppression for every trench milling step. Before you change the ion current, deactivate the drift suppression, change the ion current and activate drift suppression again.
    Critical: If FIB-view imaging with the int-FLM is used for axial targeting (see next section), trench milling steps c-e must be performed at a different stage tilt depending on the desired stage tilt for FIB-view imaging. For example, FIB-view imaging at a stage tilt of 20° requires trench milling steps c-e at -6°.

a. FIB mill two horizontally aligned cross-sections with xyz-dimensions of 40x30x3 µm and a distance of 40 µm above and below the target area at 7 nA.

b. Vertically expand the trenches to 50 µm and 80-120 µm (z-dimension = 2.5 µm) below and above the target area, respectively, at 15 nA away from the target area.
Critical: The top trench should be as long as possible before it reaches a grid bar to be able to remove all the material below the lamella during thinning.

c. Reduce the size target area between the trenches in two steps to 35x30 µm (xy- dimension) at 5 nA (cross-section z = 2.5 µm).
Critical: If you want to use FIB-view imaging for targeting within the thickness of the sample (axial targeting), trench milling steps c-e must be performed at a different stage tilt ($\alpha_{Trench\ milling}$) dependent on the stage tilt you want to use for FIB (see next section).

$$\alpha_{Trench\ milling} = -\alpha_{FIB\text{-}view} + 14°$$

This is only correct for the standard Thermo Fisher Scientific FIB/SEM geometry and a shuttle with a pretilt of 45°.
Critical: In our hands, initial targeting is often imperfect. Record int-FLM images after each trench milling step and adjust the position of the patterns for the next step to improve positioning. This ensures that the target area is centered after trench milling (Figure 4D-F).

d. Reduce the size of the block between trenches 30x20 µm (xy- dimension) at 3 nA (cross-section z = 2.5 µm).

e. Polish the top front at 1 nA with a 1.5x30x3.5 µm cross-section (xyz-dimension). This face will be exposed to the ion beam during lamella milling and should be as smooth as possible (Figure 5A,B).

A. Axial targeting

Note: Top views recorded with the int-FLM reliably localize the target area in the xy-plane of the grid. Due to the used widefield imaging system with low numerical aperture air objectives, however, the z-resolution is limited. Locating the target area in z (axial) is crucial to place the patterns for lamella milling and to assure that the target area is contained in the final lamella. Two methods can be employed axial targeting.

1. Record a long exposure SEM block face image after trench milling (Figure 5),
Note: Do the SEM block face imaging with the stage in trench milling orientation (Figure 2). The top front of the target area containing block is now exposed to the SEM. During fine milling, in lamella milling orientation. This front will be exposed to the FIB.
Critical: For lamella fine milling, the top front must be protected by a thick layer

of metal-organic platinum. The image of the block face must be recorded before this layer is applied.
Critical: SEM block-face images can only be used for the rough axial targeting and only if cellular features are exposed at the top block face. Additionally, these features must generate sufficient contrast in SEM images. This is the case for e.g. membrane structures and lipid bodies.

a. If not yet done so, set the SEM acceleration voltage and current to 3 kV and13 pA, respectively.

b. Center a spherical contamination next to the trenches in the SEM at the magnification used for block face imaging.

c. Focus on the contamination and correct astigmatism either manually or by running the 'Auto-stigmator' function.

d. Center the block-face in the SEM field-of-view and focus on the edge between grid surface and block face (Figure 5C).

e. Create a selected area window (hotkey F7) on the block face and run the auto brightness-contrast function (hotkey F9) (Figure 5C).

f. Record a 3kx2k pixel image of the block face with a dwell time of 50 ns and 100 line integrations.
Note: The location of cells and organelles should be visible in the image(Figure 5D).

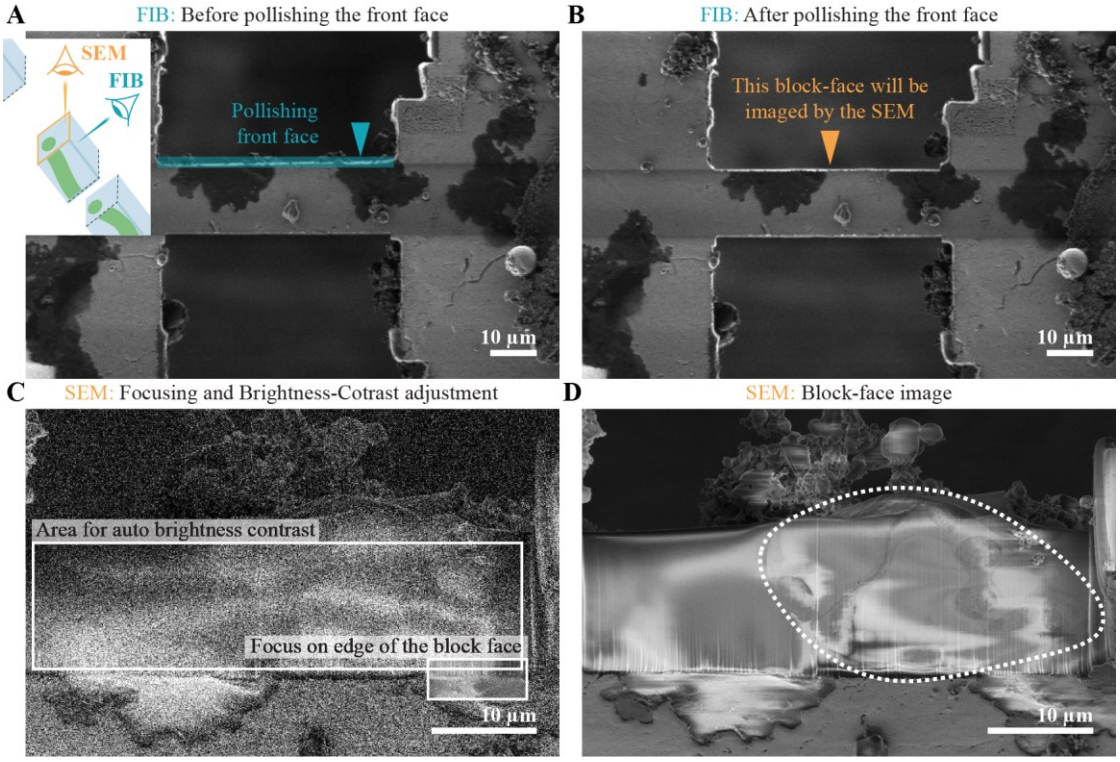


Figure 5. Axial targeting by SEM block face imaging. A. FIB image after trench milling before polishing the front face. The blue rectangle indicates the milling pattern and the blue arrowhead the milling direction. The inset

illustrates the sample surface after trench milling with respect to the imaging directions of SEM and FIB. **B.** FIB image after polishing the front surface which will be imaged by the SEM. **C.** Area for focusing and the Auto Brightness-Contrast function prior to recording the SEM block-face image. **D.** The resulting SEM block-face image. The tissue exposed at the surface is outlined by a dashed line.

2. Record FIB-view images with the int-FLM.
   Note: FIB-view images are recorded in lamella milling orientation from the same stage tilt at which lamella fine milling is performed.
   Critical: FIB-view imaging can only be performed with a high working-distance objective. If the working distance is below 10 mm, the objective may touch the shuttle before the sample can be focused. We use an Olympus LMPLFLN 50´ objective with a working distance of 10.6 mm.
   Critical: For FIB-view imaging, the optical axis of the int-FLM should be normal to the front face after trench milling (Figure 6A,B). *To achieve this, trench milling steps c-e (*Figure 4*C) are performed at a different stage tilt (see above).*

   a. Rotate the stage into lamella milling orientation (Figure 2) and set the correct stage tilt (e.g. 20° if trench milling was performed at a stage tilt of -6°).

   b. Use the reflected light channel to find the front of the trench.

   c. Acquire int-FLM FIB-view images or z-stacks recording the reflected light (excitation: 470 nm ± 10 nm; no emission filter) and cellular autofluorescence (excitation: 470 nm ± 10 nm; emission filter: 515 nm ± 15 nm, pixel size = 168 nm, 20-25 z-slices, z-step = 1 µm). An overlay of FIB and FIB-view image, both recorded in lamella milling orientation is shown Figure 6C.

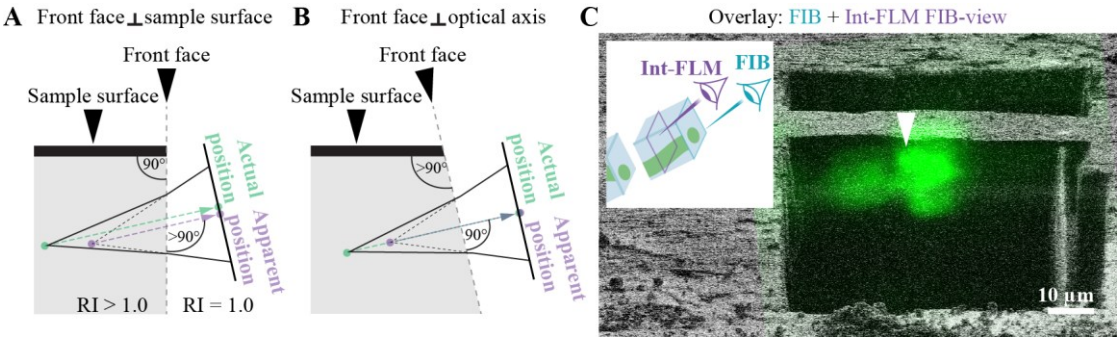


Figure 6. Axial targeting by FIB-view imaging with the int-FLM. A. If the trenches are milled at a stage tilt of 7° and a stage rotation of 180°, the exposed front face is perpendicular to the sample surface but not normal to the optical axis of the int-FLM. This would distort the axial position of a feature due to refractive index miss match at a tilted surface. **B.** If trench milling is performed that the front face in lamella milling orientation is perpendicular to the optical axis of the int-FLM, axial targeting can be performed reliably (FIB-VIEW Paper.) **C.** Overlay of a FIB (gray) and int-FLM FIB-view image recording the cellular autofluorescence (green). Both images were acquired in lamella milling orientation. The junction between cells is marked by a white arrowhead. The inset illustrates the location of the sample surface with respect to the imaging direction of FIB and int-FLM in lamella milling orientation.

B. Waffle milling

1. Apply a thick layer of metal organic platinum by opening the gas injection system (GIS) 3x20 s and 15 s in lamella milling and trench milling orientation, respectively, at the GIS working distance in z.
   Note: The GIS working distance and the thickness of the deposited layer of metal organic platinum may vary between different FIB/SEM instruments. But it can be estimated as described in the General Notes point 6.

Pause Point: After trench milling and GIS coating, grids can be unloaded and stored in grid boxes at liquid nitrogen temperature until further use.
Critical: Unloading and reloading usually changes the grid orientation slightly which may render certain regions of the target area inaccessible and may require additional milling steps. Hence, we prefer to finish Waffle milling before unloading.

2. Move the stage into lamella milling orientation at 20° stage tilt.
   Critical: If you did FIB-view imaging, this should be the angle you used for FIB-view imaging. Otherwise, the axial targeting is not reliable.
3. Find the coincidence point on the target area containing block between the trenches.
4. Remove all material below your target area by FIB milling at 3 nA.
   a. Take a FIB image. Can you see the edge at the bottom of the sample (Figure 7A)?
   b. If yes, create a cross-section with an xz-dimension of 30x2 µm covering all material below the target area but, if possible, leaving 12 µm to the surface of the sample.
   c. If not (Figure 7B), tilt the stage higher until you can see the bottom edge (Figure 7C). Remove the material with a cross-section. Tilt the stage back to 20° and check if you can see the bottom edge now. If yes, continue with (b). If not, repeat (c).
      Note: If you cannot see the bottom edge at the highest accessible tilt, rotate the stage into trench milling orientation and further elongate the trench on top. In any case, it is safer to make long enough trenches so that the lower edge is visible in shallow angles.
      Critical: It is important to remove all material below your lamella. Remaining material in the "shadow" of the actual lamella will render later TEM data acquisition impossible.

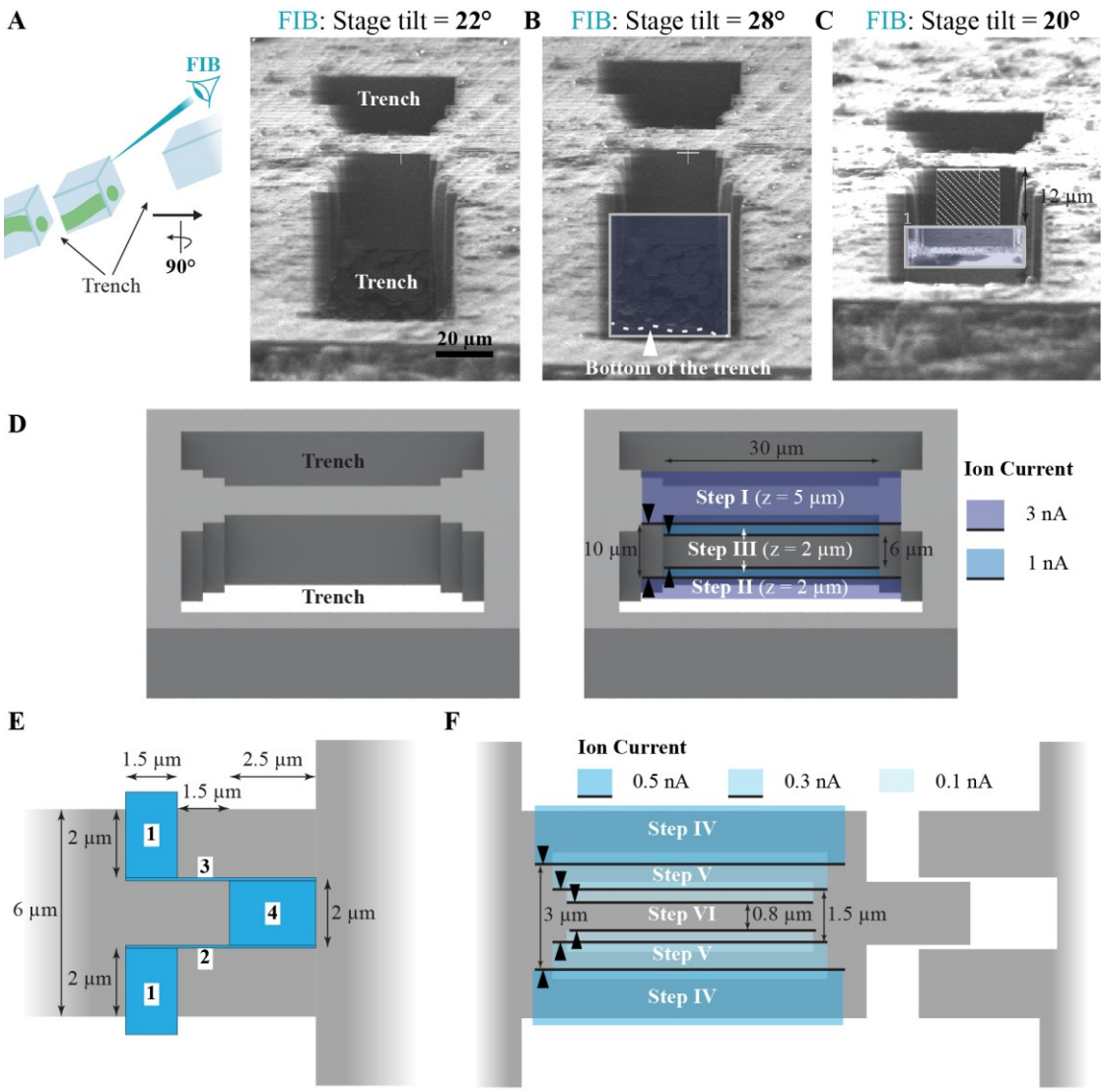


Figure 7. On-grid "waffle" milling. A-C. Removal of all material below the target area. **A**. At a stage tilt of 22°, the bottom of the trench cannot be discerned. The scheme indicates the location of the trenches with respect FIB imaging direction. **B**. At a stage tilt of 28° the bottom edge of the trench becomes visible (white dashed line). **C**. All material below the target area is removed until the bottom of the trench is visible at a stage tilt of 20° leaving a distance 12 µm to the sample surface (white rectangle). In (**B**) and (**C**), milling patterns are indicated as rectangles with blue shading. **D**. Scheme of the prepared lamella site in lamella milling orientation without and with the initial milling patterns in the left and right panel, respectively. **E**. Milling patterns for a broad notch. The numbers indicate the milling order of the rectangle patterns. **F**. Milling patterns for thinning the lamella after the preparation of the notch. The patterns in (**B**)-(**D**) and (**F**) are regular cross-sections with the milling direction towards the target area indicated by black arrow heads. The FIB milling patterns are provided in the section Supplementary information.

5. Remove the top surface of the target area containing block which is mainly composed of metal organic Platinum at I = 3 nA using a regular cross-section (z = 5 µm, Figure 7D, Step I).

6. Thin the lamella to 30x10 µm and 30x6 µm around the target area at 3 nA and 1 nA, respectively (z = 2µm, Figure 7D, Step II and III).

7. Mill a notch similar to the "Waffle" Method (Kelley et al. 2022) at current of 0.5 nA using rectangle patterns (Figure 7E).

a. Record an SEM block face image of the top of the lamella or a top view image with the int-FLM to decide if you want to mill the notch on the left or the right side. It will occupy 6-8 µm of the 30 µm wide lamella.
b. Mill the two rectangles closest to the target area in parallel (Figure 7E, patterns 1).
c. Mill the lower vertical pattern (Figure 7E, pattern2) followed by the upper one (Figure 7E, pattern 3).
d. Finish the notch by milling the rectangle furthest away from the target area (Figure 7E, pattern 4).
Note: For us, a notch allowing for lamella movements of up to 1.5 µm is necessary to prevent lamella bending during fine milling.

8. Successively thin the lamella at 0.5 nA to 3 µm (Figure 7F, Step IV), at 0.3 nA to 1.5 µm (Figure 7F, Step V) and at 0.1 nA to 0.8 µm thickness (Figure 7F, Step VI) using cross sections with xz dimensions of 18-22x2 µm.

9. Thin the lamella to a thickness of 250 nm at 50 pA using rectangle patterns milling the bottom and bottom parallelly (Figure 8A).

10. Switch to an ion current of 30 pA. Tilt the stage to 19° and 20.5-21° and polish the lamella only from bottom (Figure 8B) and the top (Figure 8C), respectively.
Note: Cross-section patterns deplete material faster and generate smoother surfaces But they typically provide a substantially slower readout than rectangle patterns. The fast readout is crucial when you thin the lamella to it's final thickness. Sometimes the lamella deforms or starts tearing. When this happens, milling must be stopped or interrupted to re-adjust patterns. Thus, we prefer to use cross-sections for initial 'course' milling steps and use rectangle patterns only for the final thinning and polishing steps.
Note: Recording low current FIB and SEM images regularly helps to understand if your lamella starts breaking. Recording a movie of FIB images (saving frames every 2-5s) during the last milling steps can be helpful for trouble shooting if something goes wrong.

11. Optional: Sputter a thin layer of metallic Platinum on the sample to increase conductivity and suppress charging-related artifacts (movement, warping) during TEM tilt-series acquisition (e.g. U = 1 kV, I = 10 mA, p = 0.2 mbar, t = 2-4 s).
Note: On our systems, this condition also deposits Platinum particles with diameters of 5-15 nm on the lamella surface. They can serve as fiducials for tilt-series alignment, generating higher-quality tomograms than patch tracking based approaches, specifically in regions devoid of high-contrast cellular features.

12. Unload the sample and store it until transfer into a transmission electron microscope.

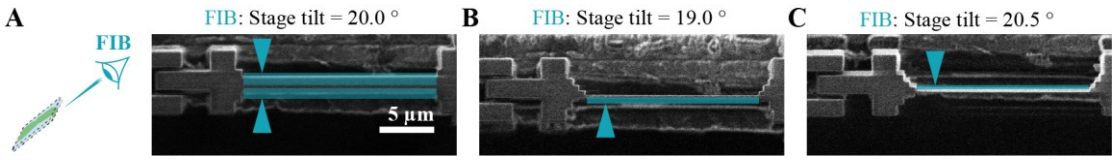


Figure 8. Fine milling of "waffle" lamellae. A. Thinning of the lamella with two rectangle patterns with a vertical distance of 250 nm milled in parallel. The scheme illustrates the location of the lamella with respect to the FIB imaging direction. **B.** Polishing of the lamella from the bottom at a stage tilt of 19°. **C.** Polishing of the lamella from the top at a stage tilt of 20.5°. Milling patterns are indicated by blue rectangles, the milling directions by blue arrowheads. The FIB milling patterns are provided in the section Supplementary information.

II. Serial Lift-Out with double sided attachment from below

Note: The redeposition milling technique used here to attach different materials works best if the surfaces of the attachment sites are smooth. This is achieved by polishing the respective surfaces with cross-sections.

A. Prepare for the lift-out session at room temperature.

1. Load a 400x100 mesh grid into the FIB.

    a. Clip the grid into a TEM cartridge without cutout for FIB milling. The shiny top of the grid must face down during clipping so that it is the top when loaded into the FIB.
    Critical: If the grid was bent during clipping, discard it. A bent grid may render the attachment later in the workflow difficult or even impossible.

    b. Label the top of the cartridge on both sides along the 100 mesh bars with two blue marks and the opposing sides along the 400 mesh bars with a black and a red mark (Figure 9A).
    Critical: Use a magnifying glass or a stereo microscope to add the marks precisely along the directions of the grid bars. The marks will help you to align the grid when loading into the FIB. Proper grid alignment is crucial for the success of lift-out with double-sided attachment.

    c. Mount the clipped 400x100 mesh grid into the FIB shuttle. The 100 mesh bars indicated by the blue markers must be aligned horizontally, the red marker should face down. Load the shuttle into the FIB at room temperature (Figure 9B).

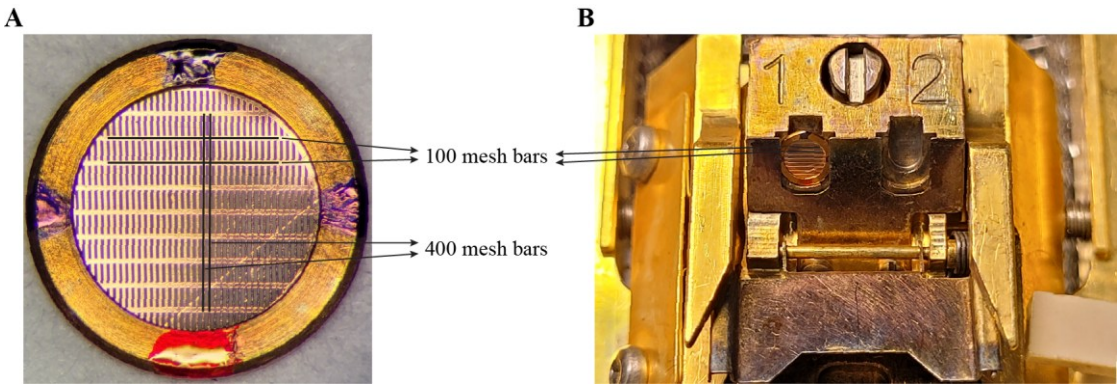


Figure 9. Labelling and mounting 400x100 mesh grids. A. Label the cartridge of a clipped 400 x 100mesh grid with two blue marks on either side along the 100 mesh bars as well as a black and a red mark on opposite sides along the 400 mesh bars. **B.** Mount the grid into the FIB shuttle with the 100 mesh bars aligned horizontally and the red mark facing down.

2. Polish the bottom edge of the needle EasyLift needle.

    a. Insert the needle to the parking position and move it into the coincidence point of FIB and SEM.

    b. Coarsely remove the remainders of previous lift-out experiments at 5-30 nA (Figure 10).
    Note: If a copper adapter with a height of at least 10 µm is attached to the needle, it can be reused as described below.

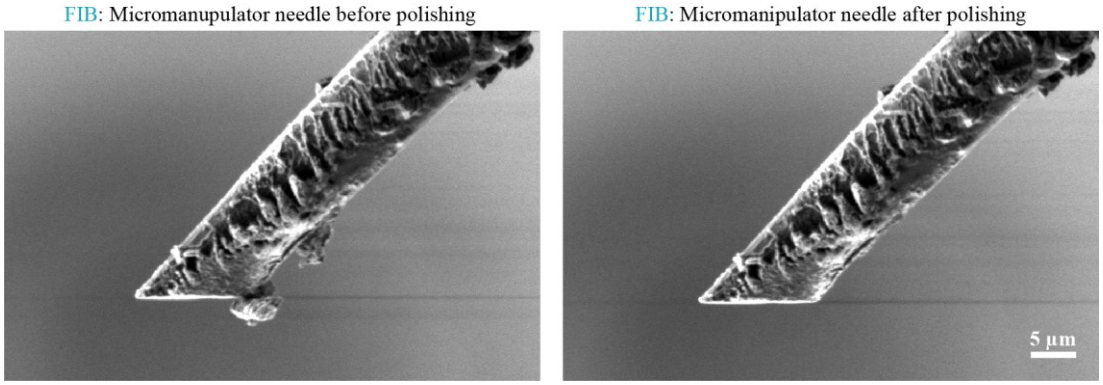


Figure 10. Polish the bottom of the needle. The needle before and after polishing its bottom in the left and right panel, respectively.

    c. Polish the bottom of the needle at 1 nA with a cross-section across the full width of the needle, milling direction towards the needle. Set the z-dimension of the cross-section to roughly the diameter of the needle at the tip.

    d. Retract the needle

3. Prepare and attach a copper adapter for the needle following the scheme in Figure 11A.

    a. Move the stage into trench milling orientation (stage tilt = 7°, relative rotation = 180°).

b. Find the coincidence point of FIB and SEM on a 100 mesh bar between two 400 mesh bars (inset in Figure 11B).

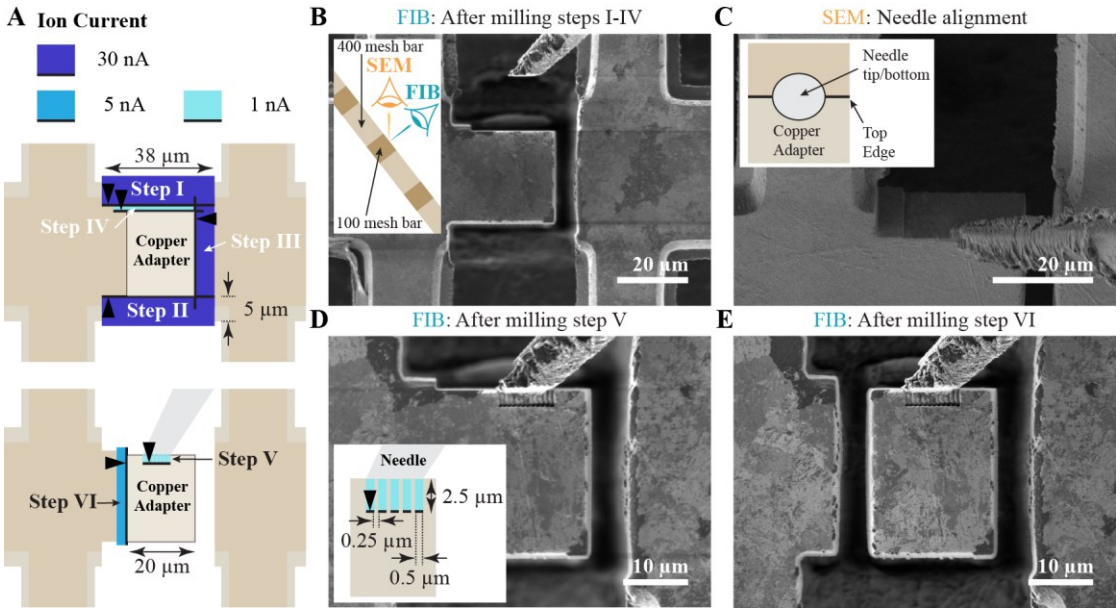


Figure 11. Preparation of a copper adapter from a 400x100 mesh grid. A. Scheme of the milling patterns. All milling patterns are Cross-sections with the black arrowheads indicating the milling direction. **B.** FIB image after milling steps I-IV. The inset illustrates the location of 400 and 100 mesh bars with respect to the FIB and SEM imaging directions. **C.** SEM image of the needle bottom centered on the top edge of the copper adapter. The inset depicts how the bottom of the needle was position with respect to the copper adapters top edge. **D.** FIB image of the needle attached to the copper adapter by redeposition milling. The inset shows the dimensions of the cross-section patterns used for redeposition milling. The "Multi pass" parameter is set to 1. The milling direction is indicated by a black arrowhead. An array of 15-25 of these cross-sections is placed along the interface between the needles bottom edge and the copper adapter. **E.** FIB image of the detached copper adapter. The FIB milling patterns are provided in the section Supplementary information.

c. Remove 4 µm on top and bottom of the grid bar using cross-sections with xyz-dimensions of 38x5x20 µm and milling direction towards the center of the grid bar at 30 nA.

d. Detach the copper adapter on one side with a 5x35x70 µm cross-section, milling towards the adapter.

e. Polish the top of the copper adapter at 1 nA (cross section, xyz size = 25x1.5x20 µm, Figure 11B).

f. Insert the polished needle.

g. In the SEM, adjust the position of the needle only in x and y so that the center of its tip aligns to the top edge of the copper adapter (Figure 11C). The polished needle face needs to form a step with the copper adapter to allow for effective redeposition and attachment.

h. In the FIB, bring the needle in contact with the upper surface of the copper adapter, moving only in z.

i. Define a horizontal array of 15-25 cross-sections with xyz-dimensions of 0.5x2.5x4 µm every 250 nm and place it along the interface between needle and adapter on the adapter with the milling direction away from the needle.
Critical: Set the "Multi pass" parameter for cross-sections used for redeposition milling to 1!.
Critical: Adjust the spacing of the patterns dependent on the alignment quality of the ion beam. Space the patterns further apart, if single attachment patterns overlap too much forming a continuous attachment groove.

j. Mill the pattern array at 1 nA to attach the needle to the copper adapter (Figure 11D).
Note: Move the needle one 500 nm step upwards in Z. You should see no movement or movement of the entire grid. If only the needle moves, the attachment was not successful.

k. Detach the copper adapter with a 5x35x70 µm cross-section at 5-30 nA resulting in a final adapter width of 15-20 µm (Figure 11E). Assure that detachment was successful by moving a 500 nm step in Z Now, only the adapter should move.

l. Polish the lower edge of the copper adapter at 1 nA (cross section, xyz-dimensions: 16-21x1.5x20 µm).
Note: Polishing the bottom of the copper adapter can also be performed after the system has been cooled down right before the lift-out experiment starts.

m. Retract the needle

4. Optional: Prepare the copper adapter for reuse (Figure 12).
Note: Copper adapters can be used for several lift-out experiments.

a. Coarsely remove the old attachment site at 5-30 nA.

b. Polish the lower edge of the adapter at 1 nA (cross section, xyz-dimensions: 16-20x1.5x20 µm).

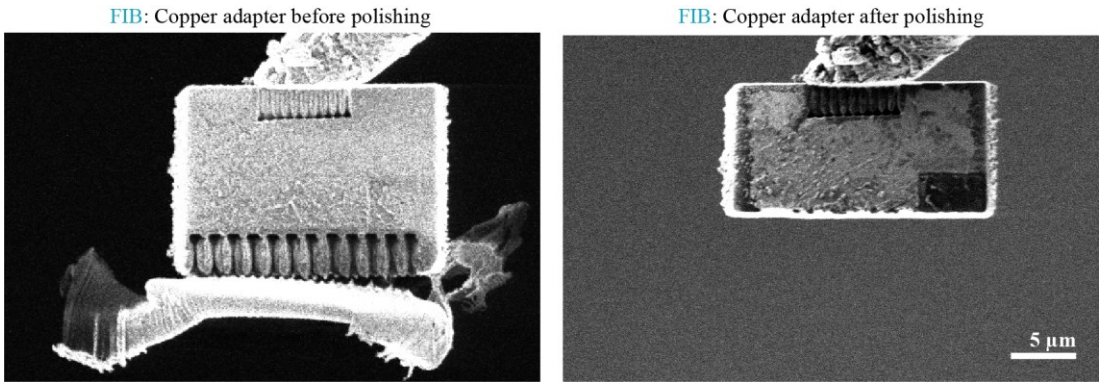


Figure 12. Reuse of the copper adapter. The copper adapter with remnants of a previous lift-out experiment before and after polishing for reuse in the left and right panel, respectively.

5. Mill cavities for the attachment from below into the receiver grid (Figure 13).
    a. If necessary, precisely align the 400 mesh bars vertically by rotating the stage.
    b. With the stage in trench milling orientation, find the coincidence point of FIB and SEM in the center of the grid.
    Critical: Only regions within about 1 µm from the grid center are accessible with the stage movement of a Titan Krios. Hence, cavities and for attachment sites must be within that range.
    c. Mill rectangular 8x90 µm cavities into neighboring 400 mesh bars at 30 nA using cross-sections with xyz-dimensions of 9x90x25 µm. The milling direction is from the mesh into the bar. The lower edge of the patterns should be in the middle of the grid rectangles (Figure 13).
    d. Unload the grid and store it until it is used for a lift-out experiment.

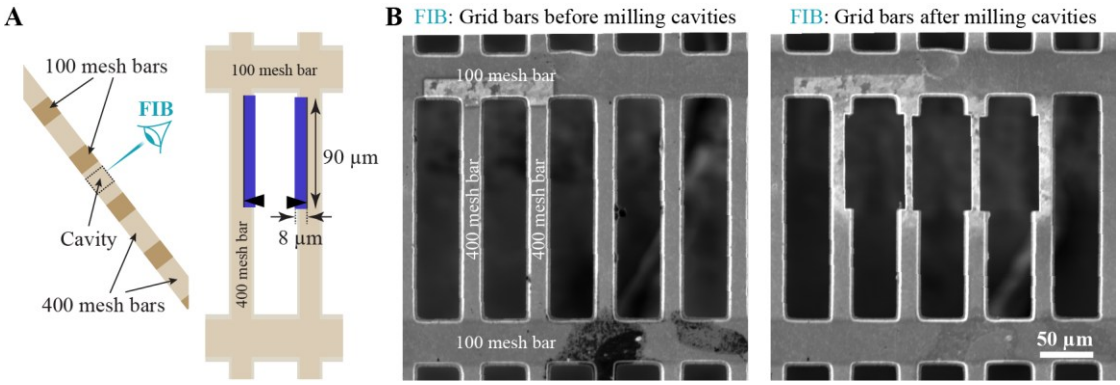


Figure 13. Preparation of cavities for attachment from below. A. Scheme illustrating the preparation of the cavities. The left scheme shows the location of cavities with respect to grid bars and the FIB imaging direction. The right scheme depicts the dimensions of the milling patterns as blue rectangles with the milling direction indicated by black arrowheads. **B.** Grid bars before and after milling the cavities in the left and right panel, respectively.

B. Perform the lift-out

1. Load the modified 400x100 mesh receiver grid and the sample for lift-out into the FIB.
    a. Mount the modified receiver grid into the FIB shuttle with the loading station at room temperature. Make sure the 100 mesh bars indicated by the blue marks are precisely aligned horizontally. Fix the grid in the shuttle by closing the shuttle clamp.
    b. Cool down the loading station.
    c. Open the shuttle clamp and load the sample for lift-out into the free slot of the shuttle. Then close the clamp again.

d. Load the shuttle into the cooled FIB.
Note: Orienting the receiver grid is much easier at room temperature than in the cold state.
Critical: The 100 mesh bars must be perfectly aligned horizontally. While for an alignment error below 10°, stage rotation may be used to compensate for remnant misalignment, the receiver grid needs to be unloaded and its rotation manually re-adjusted.

2. Perform targeted trench milling and targeting of the target area as described in the "waffle" workflow in the previous section (I. The "waffle" workflow). The final width (x-dimension) of the target area, however, must be larger than for the previously described workflow (i.e. 60-65 µm).
Critical: Extending the width of the target volume is vital for double-sided attachment. After detachment from the bulk sample, it must still be wide enough to span the mesh between the two attachment sites. For double sided attachment from below, this gap is about 55 µm wide. Another 5-10 µm are needed for the attachment. It is better to lift out a slightly too wide block as its width can always be reduced. Once the lift-out block becomes too narrow, the experiment fails.

3. Lift-out option I: with the stage in trench milling orientation similar to (Schiøtz et al. 2023) resulting in sectioning transverse to the sample surface (Figure 14A).

   a. Insert the EasyLift needle after trench milling with the stage still in trench milling orientation.

   b. If not yet done, polish the lower edge of the copper adapter at 1 nA with a cross-section (z-dimension = 10 µm).

   c. In the SEM, position the bottom face of the copper adapter in the center of the block face.

   d. In the FIB, bring the copper adapter in contact with the top block face.

   e. Define a horizontal array of cross-sections with xyz-dimensions of 0.5x2.5x4 µm every 250 nm and place it along the interface between copper adapter on target area containing block on the adapter with the milling direction away from the block (Figure 14B).
   Critical: Set "Multi pass" to 1 of the cross-sections used for redeposition milling.

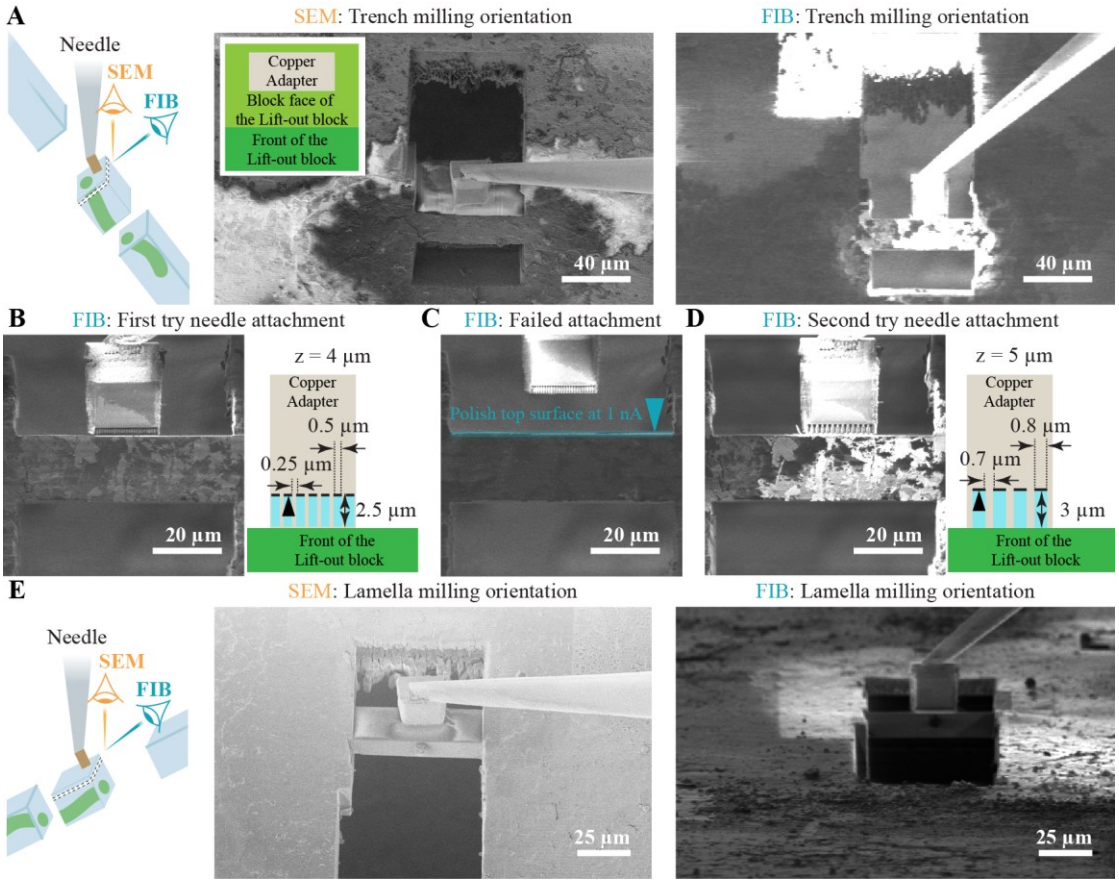


Figure 14. Lift-out in different stage orientations. The schemes on the left illustrate the orientation of sections marked by black, dashed lines with respect to the imaging directions of FIB and SEM. **A.** Lift-out in trench milling orientation. The middle panel shows an SEM image with the needle attached to the lift-out block. The inset illustrates the positioning of the copper adapter with respect to the milled front of the block. The right panel shows a FIB image. **B**. FIB image of the copper adapter attached to the lift-out block. The inset illustrates the dimensions of the cross-sections ("Multi pass" set to 1) used for the attachment. The milling direction is indicated by a black arrowhead. **C**. If the attachment fails, retract the needle and polish the top surface of the lift-out block. The milling pattern is indicated by a blue rectangle, the milling direction by a blue arrowhead. **D**. FIB image after the second attempt to attach the copper adapter. The inset shows the dimensions of the cross-sections ("Multi pass" set to 1) used for the second attachment. The milling direction is indicated by a black arrowhead. **E**. Lift-out in lamella milling orientation. SEM and FIB are shown in the middle and right panel, respectively. The copper adapter is positioned in the center of the top of the lift-out block. The FIB milling patterns are provided in the section Supplementary information.

f. Mill the pattern array at 1 nA to attach the lift-out block to the copper adapter.
*Note: Move the needle 500 nm upwards. You should see no movement **or** a movement of the entire grid. If only the needle moves, the attachment was not successful.*

g. If the attachment was not successful, retract the needle 10-20 µm.

h. Polish the top surface of the lift-out block and the bottom of the copper adapter at 1 nA with cross-sections (z = 5 µm, Figure 14C).

i. Define a horizontal array of cross-sections with xyz-dimensions of 0.8x3x5 µm every 700 nm and place it along the interface between copper adapter on target area containing block on the adapter with the milling

direction away from the lift-out block (Figure 14D).
Critical: Set "Multi pass" to 1 of the cross-sections used for redeposition milling.

j. Mill the pattern array at 1 nA to attach the block to the copper adapter.
*Note: Move the needle 500 nm upwards. You should see no movement **or** a movement of the entire grid. If only the needle moves, the attachment was not successful.*

k. Detach the lift-out block on both sides by milling cross-sections (xz-dimension = 5x5 µm) at 5 nA with the milling direction towards the lift-out block.
Critical: The distance between the two patterns determines the width of the lift-out block. For the double-sided attachment from below it must be around 55 µm.
*Note: Move the needle 500 nm upwards. You should see movement of the needle **and** the lift-out block. If only the needle moves, the attachment to the block did not hold. If nothing or the whole grid moves, the lift-out block is still attached to the bulk sample.*

l. Move the needle up in z and pay attention to not crash the lift-out block into the top edge of the trench.
Note: The movement of the needle out of the sample is neither a pure y, nor a pure x movement. Small iterative movements in both directions need to be performed to move the lift-out block out of the sample bulk. As a consequence, the movements must be controlled regularly by FIB and SEM imaging. Start with upwards movements in z (500 nm to 1 µm steps). After the volume has noticeably separated from the bulk, it may be moved forward in y.

m. Retract the needle to bring the lift-out block into a safe position and allow for stage movement.

4. Lift out option II: in lamella milling orientation resulting in sectioning nearly parallel to the sample surface (Figure 14E).

a. After trench milling, move the stage into the lamella milling orientation and find the coincidence point of FIB and SEM on the target area containing block.
Note: Locate your target area in z, if not yet done so, by SEM block face imaging or FIB-view imaging as described in the previous section I. The "waffle" workflow.
Critical: The bottom edge of the block must be discernible in FIB images in this orientation. If not, tilt the stage to a higher angle or extend the top (front) trench in trench milling orientation.

b. Apply a thick layer of metal organic platinum by moving the stage in lamella milling orientation to the GIS working distance and opening the GIS for 3x30 s.
Critical: this process will protect the front of the lift-out block that was exposed through trench milling. This layer will be continuously imaged during lift-out and subsequent sectioning. If it is too thin, the lamella front will be damaged resulting in problems during lamella preparation (see also Troubleshooting point 5).

c. Remove the uppermost layer including the rough grid surface at 3 nA using a cross-sections (z-dimension = 5 µm).

d. Coarsely remove all material above and below the target area at 3 nA (cross-sections, z-dimension = 2 µm) as determined by the target areas axial localization.

e. Polish the top edge of the block at 1 nA (cross-sections, z-dimension = 3 µm, milling direction towards the target area).
Critical: This surface must be smooth. It will be attached to the copper adapter and redeposition milling is more successful, if the attached surfaces are smooth.

f. Insert the EasyLift needle with the stage in lamella milling orientation.

g. If not yet done, polish the lower edge of the copper adapter at 1 nA with a cross-section (z-dimension = 10 µm).

h. In the SEM, position the bottom front of the copper adapter in the center of the lift-out block.

i. In the FIB, bring the copper adapter in contact with the lift-out block.

j. Define a horizontal array of cross-sections with xyz-dimensions of 0.5x2.5x4 µm every 250 nm and place it along the interface between copper adapter on target area containing block on the adapter with the milling direction away from the block.
Critical: Set "Multi pass" to 1 of the cross-sections used for redeposition milling.

k. Mill the pattern array at 1 nA to attach the block to the copper adapter.
*Note: Move the needle 500 nm upwards. You should see no movement **or** a movement of the entire grid. If only the needle moves, the attachment was not successful.*

l. Optional: If the attachment was not successful, retract the needle in z by 10 µm. polish the top of the lift-out block at 1 nA. Bring the copper adapter in contact with the lift-out block. Define a horizontal array of cross-sections

with xyz-dimensions of 0.8x3x5 µm every 700 nm. Place it along the interfaces between copper adapter and lift-out block on the copper adapter (Figure 14D). Mill at 1 nA.

m. Detach the lift-out block on both sides by milling cross-sections at (xz-dimension = 5x5 µm) at 5 nA with the milling direction towards the lift-out block.
Critical: The distance between the two patterns determines the width of the lift-out block. For the double-sided attachment from below it must be around 55 µm.
*Note: Move the needle 500 nm upwards. You should see movement of the needle **and** the lift-out block. If only the needle moves, the attachment to the block did not hold. If nothing or the whole grid moves, the lift-out block is still attached to the bulk sample*

n. Retract the needle.

C. Lift-in

1. Move the stage in lamella milling orientation (stage tilt = 15°) to the modified 400x100 mesh grid.

2. Precisely align the 100 mesh bars horizontally using the stage tilt. If the initial alignment error is larger than 10°, unload the receiver grid and adjust its orientation manually.

3. Find the coincidence point of FIB and SEM in the back of the cavities between two grid bars.

4. Prepare the plateaus for the attachment from below.

   a. FIB mill cross-sections with xyz-dimensions of 9x10x20 µm on both bars at the back of the cavity at 30 nA (milling direction top to bottom). The bottom edges of the cross-sections must be aligned to the same height. The top edge of the patterns must be at least 1 µm above the edge of the grid surface and cavity (Figure 15A).

   b. Smooth the top edge of the plateaus with two normal patterns milled in parallel on either side (I = 15 nA, xyz-dimensions = 9x1x20 µm, milling direction top to bottom, Figure 15B).
   Critical: The patterns must be milled in parallel. This assures that the plateaus have the same height on both sides even if the stage is drifting during plateau preparation (Figure 15C).
   Note: The width of the resulting attachment site on 400x100 mesh grids is between 50-55 µm. The target area containing block that is lifted out must overlap with the plateaus on both sides at least 3 µm for the attachment from below.

c. Repeat this for all cavities.

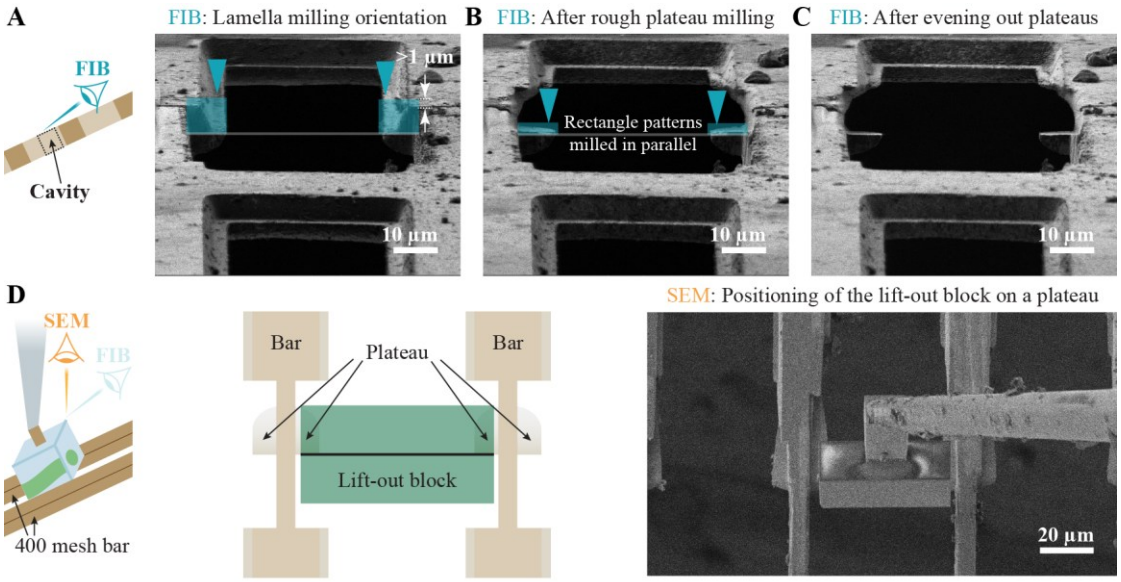


Figure 15. Preparation of plateaus for the attachment from below. A. Coarse milling of the plateaus. The scheme illustrates the location of the cavity with the stage in lamella milling orientation with respect to the FIB imaging direction. **B**. FIB image after coarse milling of plateaus. To even out height differences with between plateaus, two rectangle patterns are milled in parallel. In (**A**) and (**B**), milling patterns are indicated by blue rectangles and the milling direction by blue arrow heads. The grey line emphasizes that the lower edges of milling patterns must be aligned. **C**. FIB image after completion of the plateau preparation. **D**. Alignment of the lift-out block for the attachment from below with respect to the plateaus. The scheme in the on the left depicts the location of the lift-out block with respect to the SEM imaging direction. The scheme in the middle and the SEM image in the right show how the lift-out block is aligned with respect to the plateaus. The FIB milling patterns are provided in the section Supplementary information.

5. Insert the needle with the lift-out block attached to it.
6. In the SEM, align the center of the lift-out block to the front edge of the plateaus (Figure 15D).
7. Trim the lift-out block to fit on the plateaus.
    a. In the FIB, move the needle down until the lift-out block is 10 µm above the plateaus.
    b. If the lift-out block is wider than the plateaus, trim it on both sides (Figure 16A) with cross-sections at 1 nA (z-dimension = 2 µm, milling direction towards the lift-out block)
    Critical: The lift-out block should overlap with the plateaus at least 3 µm on either side. This assures stable attachment.
    Ciritcal: The gap between lift-out block and grid bars next to the plateaus should be larger than 500 nm on either side which prevents problems during sectioning.

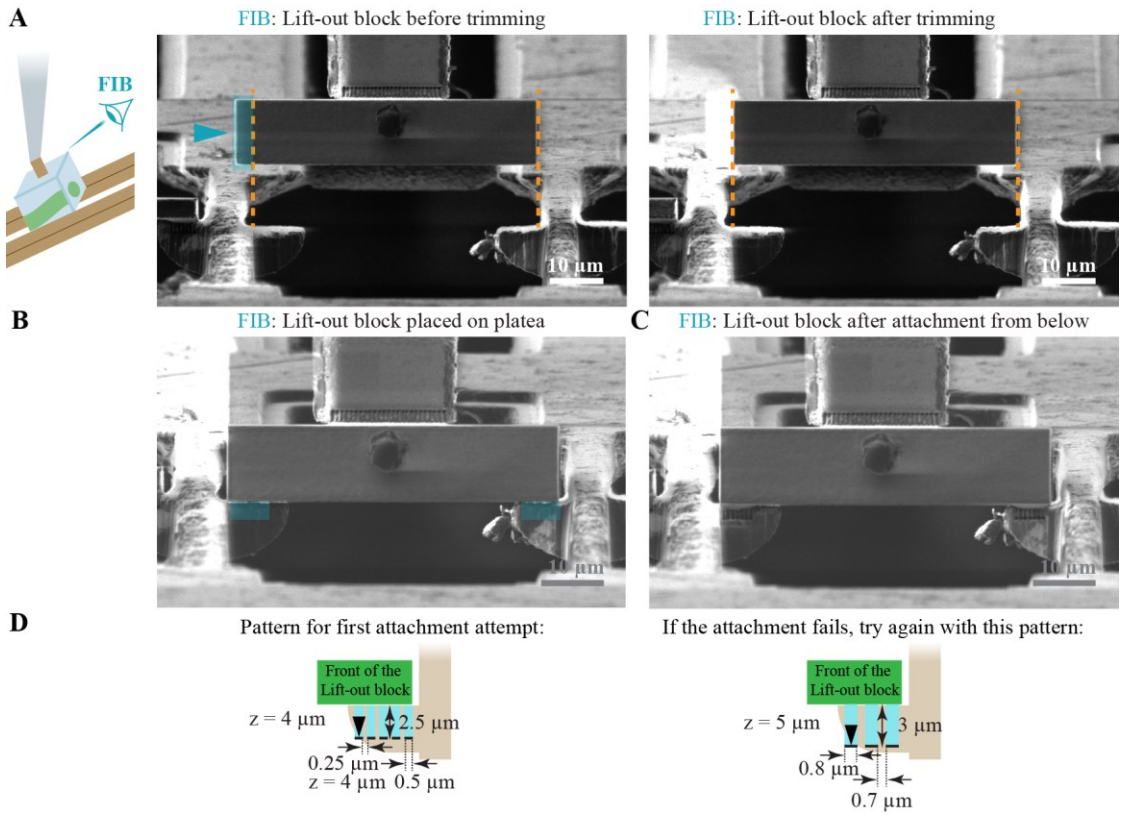


Figure 16. Attachment of Serial Lift-Out sections from below. A. The lift-out block before and after trimming to fit on the plateaus in the left and right panel, respectively. A milling pattern is indicated by a blue rectangle, its milling direction by blue arrowhead and lines used for lift-out block alignment as orange, dashed lines. The scheme on the left illustrates the location of the lift-out block with respect to the FIB imaging direction. **B.** The lift-out block placed on the two plateaus. Attachment sites are marked with blue rectangles. **C.** FIB image after the attachment from below. **D**. Scheme of the cross-section arrays ("Multi pass" set to 1) used for attachment for the first and second attempt in the left and right panel, respectively. The milling directions are indicated by black arrowheads. The FIB milling patterns are provided in the section Supplementary information.

c. Smooth the lower edge of the lift-out block at 1 nA (z-dimension = 2 µm, milling direction towards the needle).

8. Generate the serial sections.

a. Place the lift-out block on the plateaus by moving down the needle while imaging in the FIB.

b. Define two horizontal arrays of 6 cross-sections with xyz-dimensions of 0.5x2.5x4 µm every 250 nm and place them along the interfaces between the two plateaus and the lift-out block on the plateaus with the milling direction away from the block (Figure 16B).
Critical: Set "Multi pass" to 1 of the cross-sections used for redeposition milling.

c. Mill the pattern array at 1 nA to attach the lift out-block from below (Figure 16C,D).
Note: Move the needle 500 nm upwards. You should see no movement ***or*** *a*

movement of the entire grid. If only the lift-out block moves, the attachment was not successful.

d. Optional: If the attachment was not successful, define two horizontal arrays of 3 cross-sections with xyz-dimensions of 3x0.8x5 µm every 700 nm. Place them along the interfaces between the two plateaus and the lift-out block on the plateaus with the milling direction away from the block. Set the milling direction away from the block (Figure 16D). Mill at 1 nA.

e. Define a horizontal line pattern (z-dimension = 10 µm) that is 2 µm wider than the lift-out block and place it 3 µm higher than the lower edge of the lift-out block (Figure 17).
Note: The positioning of the line pattern above the lower edge of the lift-out block defines the section thickness. Thicker sections reduce the contextual information obtained by resulting in less sections. Thinner sections are possible, but that complicates the subsequent section trimming step.

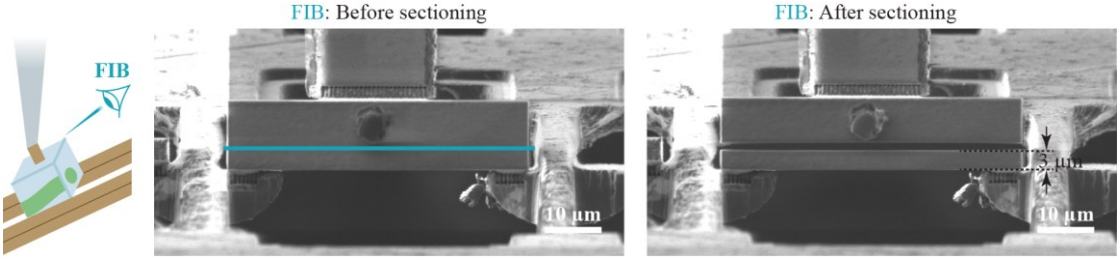


Figure 17. Sectioning of the lift-out block. The left panel illustrates the location of the lift-out block with respect to the FIB imaging direction. The lift-out block before and after sectioning is shown in the middle and right panel, respectively. The line pattern used for sectioning is indicated as blue line, the section thickness by black dashed lines. The FIB milling patterns are provided in the section Supplementary information.

f. Mill the line pattern at 1 nA.
*Note: Afterwards, move the needle 500 nm upwards. You should see movement of the needle **and** the remaining lift-out block. If nothing or the whole grid moves, the lift-out block is still attached to the section.*

g. Retract the needle and move to the next attachment site.

9. Repeat step 8 until the whole lift-out block is sliced up.

D. Trim the sections

1. Record top view images with the int-FLM of all section with the stage in trench milling orientation.

a. Use the reflected light channel to focus on the section

b. Record a z-stack with reflected light and cellular autofluorescence channel as for targeted trench milling (bin = 4, 10 z-slices, z-step = 1 µm).

2. Identify sections that do not contain the target area based on the int-FLM top views. These sections can be skipped in the next steps (Figure 18A).

3. For sections that contain the target area, identify the regions of the sections that don't contain the material of interest based on the int-FLM top views.

4. Apply a layer of metal organic platinum by opening the GIS 15 s in trench milling orientation at the GIS working distance in z.

5. For every section, remove material above and below the target area with the stage in trench milling orientation. Use cross-sections (z-dimenstion = 1 µm) milled at 3 nA with the milling direction towards the target area.

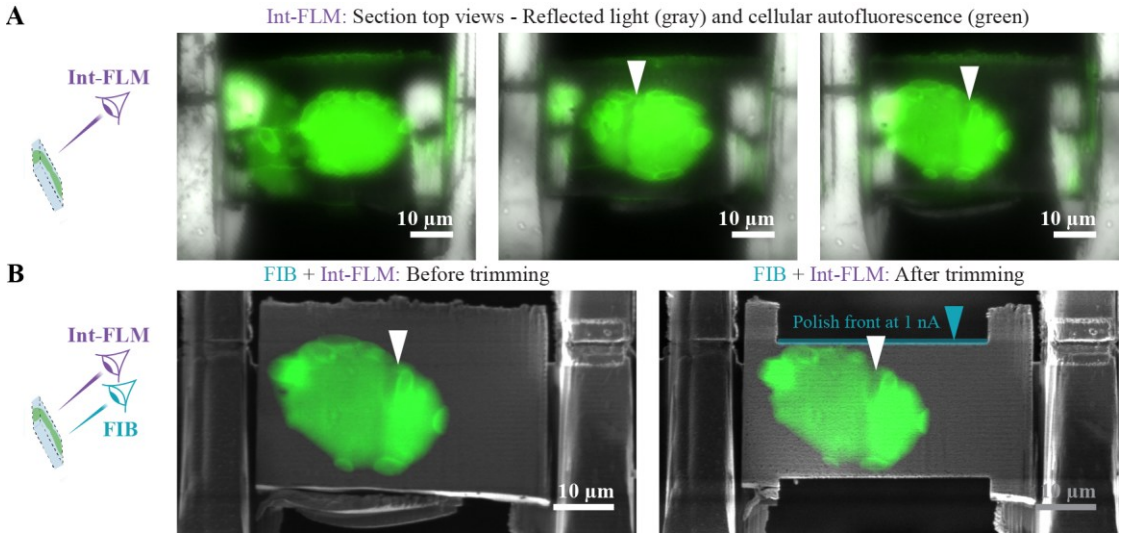


Figure 18. Trimming of Serial Lift-Out sections. The schemes on the left illustrate the orientation of sections with respect to the imaging directions of FIB and int-FLM. **A.** Top views recorded with the int-FLM of three successive Serial Lift-Out sections. Shown is the reflected light channel (gray) and cellular autofluorescence (green). The junction between cells is only contained in two of them as indicated by the white arrowheads. **B.** The section in the right panel in (**A**) before and after trimming in the left and right panel, respectively. Depicted is the overlay of a FIB image (gray) and cellular autofluorescence recorded with the int-FLM (green) both recorded in trench milling orientation. The FIB milling patterns are provided in the section Supplementary information.

6. Polish the top front at 1 nA (cross-sections, z-dimension = 2 µm, Figure 18B).
Critical: During trimming, at least 1-2 µm should be removed of the top edge. This surface was constantly exposed to the FIB during lift-out, lift-in and sectioning. Thus, it is damaged and uneven.

7. Open the GIS in trench milling and lamella milling orientation for 15 s and 3x20 s, respectively, both at the GIS working distance in z.
Note: The trimming minimizes the size of the lamella which makes fine milling faster and generates smooth surfaces covered with a thick, homogeneous layer of metal-organic platinum which is key to obtaining homogeneously thin lamellae.

8. Pause Point: Unload the grid after sectioning, section trimming and GIS coating. Store the receiver grid in a grid box and recover the lift-out sample. Store both at

liquid nitrogen temperature.
Critical: Every additional unloading and reloading step bears the risk of losing sections or even destroy them all, if mistakes occur while handling grids manually with tweezers.
Critical: If the grid is misoriented upon reloading, sections must be oriented horizontally by rotating the stage. This in turn will add an additional x-tilt to tomograms recorded on lamellae which is not desirable. If the alignment error is larger than 10°, unload the receiver grid, reorient and reload it.

E. Do the fine milling for all sections containing the target area.

1. Remove the top and bottom of the section over its whole width at 1 nA using cross-sections (top z-dimension = 5-6 µm, bottom z-dimension = 2 µm, vertical distance between patterns = 2 µm, Figure 19A).
Note: The top layer of the section is composed of metal organic platinum and requires longer milling times.

2. Optional: Record an SEM block-face image of the section surface. It can reveal the location of the target area (Figure 19B).

3. Adjust the width and position of the milling patterns to be centered around the target area.
Critical: Keep the width of the lamella for fine milling as small as possible. This speeds up the milling process and increases the success rate.

4. Thin the lamella to 1.5 µm and 0.8 µm at ion currents 0.3 nA and 0.1 nA, respectively using cross sections (similar to Figure 7F, z-dimension = 2 µm, milling direction towards the center of the lamella).

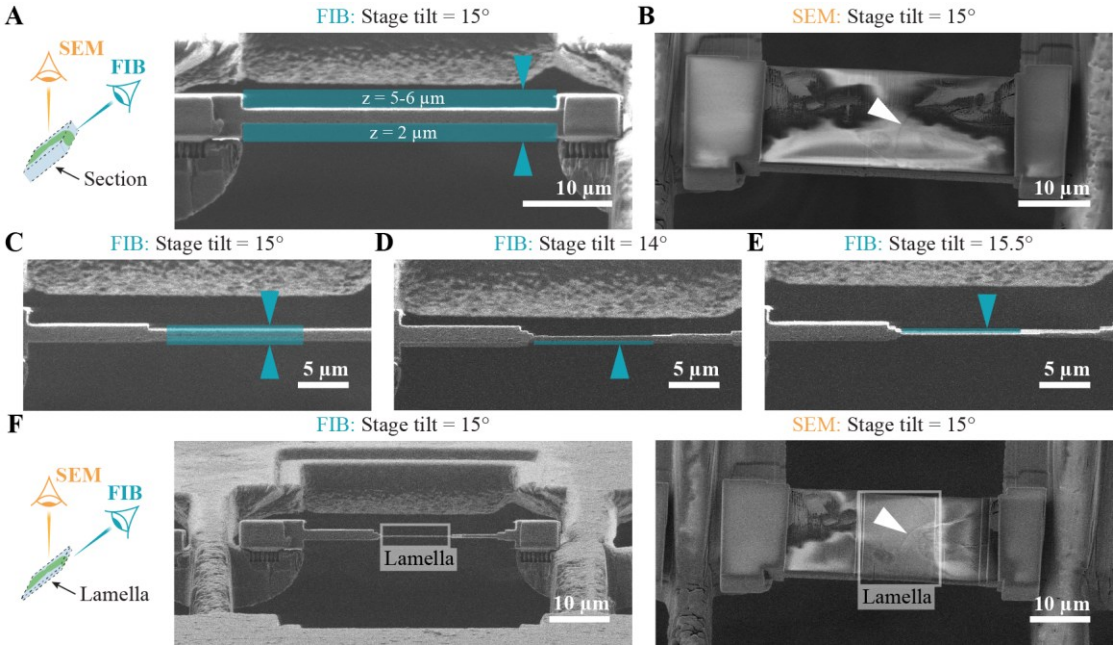


Figure 19. FIB milling of Serial Lift-Out sections. The schemes on the left illustrate the location of the section or lamella with respect to the FIB/SEM imaging direction. **A.** The first fine milling step at 1 nA. **B**. SEM block face image

after removing the thick layer of metal organic platinum on top of the section in **(A). C.** Fine milling of the section with two rectangle patterns with a vertical distance of 200 nm milled in parallel. **D.** Polishing of the lamella from the bottom at a stage tilt of 14°, **E.** Polishing of the lamella from the top at a stage tilt of 15.5°. **F.** FIB and SEM image of the final lamella in the left and right pane, respectively. Milling patterns are indicated by blue rectangles, the milling directions by blue arrowheads and the junction between cells by white arrowheads. The FIB milling patterns are provided in the section Supplementary information.

5. Thin the lamella to a thickness of 200 nm at 50 pA using rectangle patterns milled in parallel (Figure 19C).

6. Switch to an ion current of 30 pA. Tilt the stage to 14° and 15.5° and polish the lamella only from bottom (Figure 19D) and the top (Figure 19E), respectively.
Note: Cross-section deplete material faster and generate smoother surfaces But, in contrast to rectangle patterns, they don't provide an immediate readout or image. This immediate readout is crucial when you thin the lamella to its final thickness. Sometimes the lamella deforms or starts breaking and you must interrupt milling. Thus, we prefer cross-sections for all initial milling steps and use rectangle patterns only for the final thinning steps.
Note: Taking regular FIB and SEM images help to understand if your lamella starts breaking. Recording a movie in the FIB channel (saving frames every 2-5s) during the last milling steps can be beneficial for trouble shooting if something goes wrong.

7. Optional: Sputter a thin layer of metallic Platinum on your sample (U = 1 kV, I = 10 mA, p = 0.2 mbar, t = 2-4 s).
Note: On our systems, this introduces spherical Platinum particles with diameters of 5-15 nm on the lamella surface. They can be used as fiducials for tilt-series alignment. In our hands, that generates higher-quality tomograms than patch tracking based approaches.

8. Unload the sample and store it until it is imaged in a transmission electron microscope.

III. Serial Lift-Out with double sided attachment from the side

Note: The Serial Lift-Out with double-sided attachment from the side was describe previously (Schiøtz et al. 2023). *The attachment from the side has a higher throughput than the attachment from below because the time-consuming plateau preparation is omitted. It requires, however, more precision and user expertise.*

A. Prepare the lift-out session at room temperature.

1. Clip, label and load a 400x100 mesh grid and attach a copper adapter to the EasyLift needle as described in the previous section II. Serial Lift-Out with double sided attachment from below.

2. Mill marker lines for the alignment of the lift-out block (Figure 20).

    a. Move the stage into trench milling orientation.

b. Precisely align the 100 mesh bars horizontally by rotating the stage.

c. Find the coincidence point of FIB and SEM in the center of the lower grid half, three or four 100 mesh bars from the grids lower edge.

d. Define cross-sections with yz-dimensions of 2x12 µm across the center of 400 mesh bars (milling direction top to bottom) over the whole width of the grid bar.

e. Mill the marker lines at 15 nA.
Note: Milling extended cross-sections takes longer than the line patterns used in the original publication (Schiøtz et al. 2023) *but they are easier to see in SEM and FIB even if the image quality is bad which makes the experiment easier.*

f. Store the modified 400x100 mesh receiver grid until it is used for a lift-out experiment.

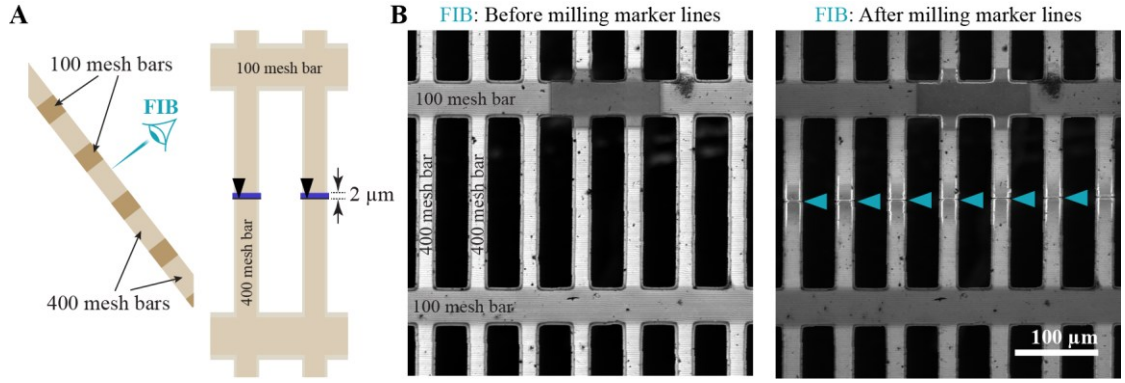


Figure 20. Milling of marker lines in trench milling orientation. A. Schemes for the preparation of marker lines in trench milling orientation. The scheme on the left illustrates the location of grid bars with respect to the FIB imaging direction. The right scheme shows the milling patterns. Cross sections are indicated by blue rectangles, the milling directions by black arrowheads. **B**. A 400x100 mesh grid before and after milling the marker lines (blue arrowheads) in the left and right panel, respectively. The FIB milling patterns are provided in the section Supplementary information.

B. Lift-out

1. Do targeted trench milling and axial targeting of the target area as it was described in the previous section I. The “waffle” workflow. Only difference is that the final width (x-dimension) of the target area containing block after trench milling is 50-55 µm.
Critical: Extending the width of the block (x-dimension with respect to FIB and SEM images) is vital for double-sided attachment. After detaching the lift-out block from the bulk sample, it must still be wide enough to bridge the gap between the two attachment sites. For double sided attachment from the side using 400x100 mesh grids, this gap is about 40 µm wide. It is better to lift out a too large block because you can always reduce its width. But once the lift-out block is too slim, the experiment fails.

C. Lift-in

1. Move the stage in lamella milling orientation (stage tilt = 15°) to the modified 400x100 mesh grid.
2. Precisely align the 100 mesh bars horizontally using the stage tilt. If the initial alignment error is larger than 10° unload the receiver grid and adjust its orientation manually.
3. Find the coincidence point of FIB and SEM in the center of a grid rectangle between two marker lines.
4. Insert the needle with the lift-out block attached to it.
5. In the SEM, align the front edge of the lift-out block to the marker line on both grid bars.
6. Trim the lift-out block to fit into the gap between grid bars.
    a. In the FIB, move the needle down until the lift-out block is 10 µm above the marker lines.
    b. Trim the lift-out block horizontally to a width that is 200 nm wider than the gap between 400 mesh bars (Figure 21A)by milling two cross-sections on either side at 1 nA (z-dimension = 2 µm, milling direction towards the lift-out block).
    Critical: Be cautious not to remove too much. If the lift-out block is a few hundred nanometers slimmer than the gap between 400 mesh bars, the experiment will fail.

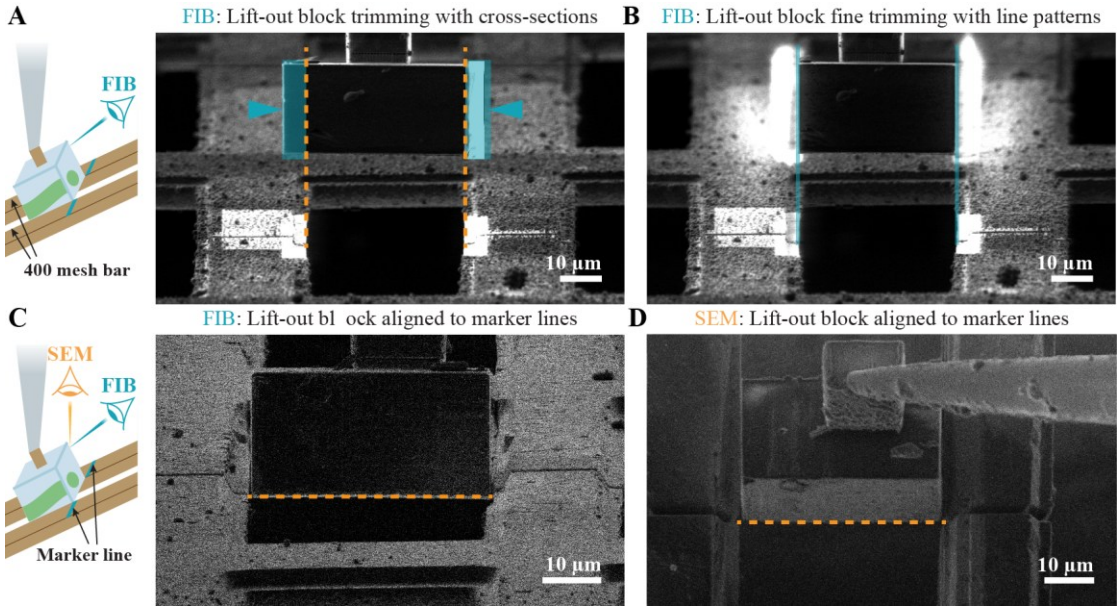


Figure 21. Trimming and alignment of the lift-out block for the attachment from the side. The schemes on the left illustrate the location of the lift-out block with respect to marker lines and the FIB/SEM imaging directions. **A.** Trimming of the lift-out block to be 200 nm wider than the gap between grid bars. Milling patterns are indicated by blue rectangles, milling directions by blue arrowheads **B.** If the lift-out block does not yet fit in between the bars, mill

line patterns (blue lines) along the outer edge of grid bars starting from the marker line and ending above the lift-out block. **C.** FIB image of the lift-out-blocks lower edge aligned to the marker lines. **D.** SEM image of the lift-out blocks lower edge aligned to the marker lines.

c. Center the lift-out block in the gap between the marker lines

d. While imaging in the FIB, carefully move down the needle and check if the block fits between the grid bars until its lower edge aligns with the marker lines.

e. If not, move the needle 10 µm up and generate two vertical line patterns on either side of the lift-out block starting from the marker line aligned to the outer edge of the grid bar, along the whole height of the lift-out block (Figure 21B).

f. Mill the line patterns (z-dimension = 3 µm) at 1 nA.

g. Repeat d-f until the lift-out block fits in between the grid bars and its lower edge aligns with the marker lines (Figure 21C).

7. In the SEM, check if the front edge is still aligned with the marker lines. If not, adjust the needle position (Figure 21D).

8. Generate the serial sections.

a. Define two vertical arrays of 6 cross-sections with xyz-dimensions of 2.5x0.5x4 µm every 250 nm. Place them along the interfaces between grid bars and lift-out block on either side on the grid bars. The lowest pattern on both sides aligns with the marker line. Set the milling direction away from the block. (Figure 22A)
Critical: Set "Multi pass" to 1 of the cross-sections used for redeposition milling.

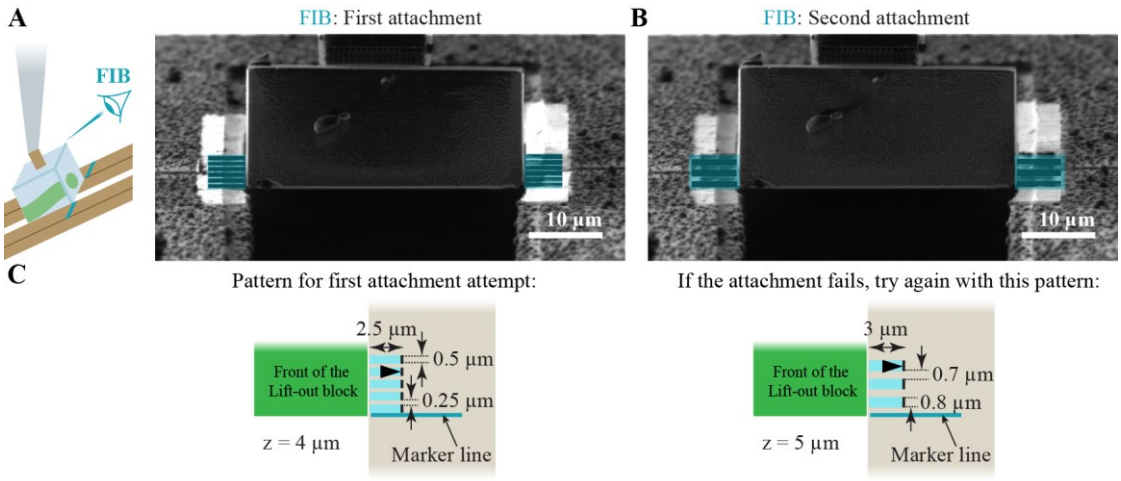


Figure 22. Attachment of Serial Lift-Out sections from both sides. A. Array of 6 cross-sections on either side used for the attachment. The scheme on the left illustrates the location of the lift-out block with respect to marker lines and the FIB imaging direction. **B.** If the attachment fails, a second array of fewer, wider and deeper patterns can be milled. **C** Scheme of the cross-section arrays ("Multi pass" set to 1) used for attachment for the first and second

attempt in the left and right panel, respectively. The black arrowheads indicate the milling direction. The FIB milling patterns are provided in the section Supplementary information.

b. Mill the pattern arrays at 1 nA to attach the lift out-block on both sides.
*Note: Move the needle 500 nm upwards. You should see no movement **or** a movement of the entire grid. If only the lift-out block moves, the attachment was not successful.*

c. Optional: If the attachment was not successful, define two vertical arrays of 3 cross-sections with xyz-dimensions of 3x0.8x5 µm every 700 nm. Place them along the interfaces between grid bars and lift-out block on either side on the grid bars. The lowest pattern on both sides aligns with the marker line. Set the milling direction away from the block (Figure 22B). Mill at 1 nA.

d. Define a horizontal line pattern (z-dimension = 10 µm) that is 2 µm wider than the lift-out block and place it 4 µm higher than the lower edge of the lift-out block (line pattern I in Figure 23).
Note: The positioning of the line pattern above the lower edge of the lift-out block defines the section thickness. Thicker sections reduce the contextual information by resulting in less sections. Thinner sections are possible, but that complicates the subsequent sectioning and trimming step.

e. Define a pair of 4 µm wide horizontal line patterns (z-dimension = 20 µm). Place them on the first line pattern centered on the interfaces between lift-out block and grid bars on both sides (line patterns II in Figure 23).
Critical. During the attachment, copper is sputtered on the sides of the lift-out block. This pair of line patterns is necessary to detach the section from the lift-out block on its sides.

f. Define a pair of vertical line patterns (z-dimension = 20 µm). Place them on the edge between lift-out block and grid bars on both sides starting at the horizontal line patterns and ending 2 µm above the topmost patterns used for the attachment (line patterns III in Figure 23).
Critical: It is possible that the lift-out block becomes attached to the grid bars above the section. This second pair of line patterns is necessary to detach the lift-out block from the grid bars.

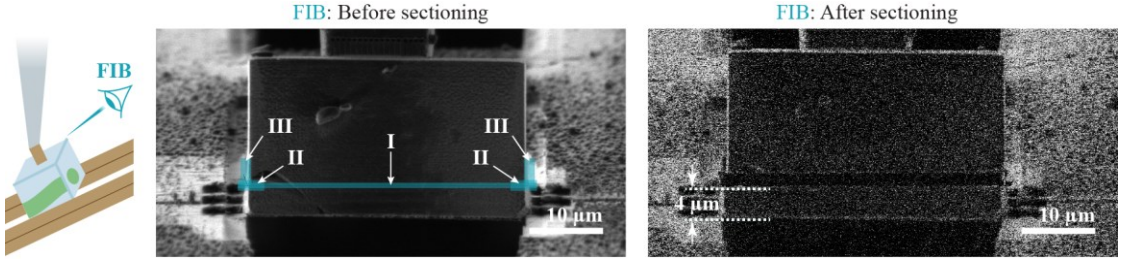


Figure 23. Sectioning of the lift-out block attached from the sides. The lift-out block before and after sectioning in the middle and right panel respectively. The Line patterns used for sectioning are indicated as blue lines in the middle panel. The scheme on the left illustrates the location of the lift-out block with respect to the FIB imaging direction.

The white dashed lines in the right panel depict the section thickness The FIB milling patterns are provided in the section Supplementary information.

g. Mill all line patterns sequentially at 1 nA.
*Note: Afterwards, move the needle 500 nm upwards. You should see movement of the needle **and** the remaining lift-out block. If nothing or the whole grid moves, the lift-out block is still attached to the section or the grid bars.*

h. Retract the needle and move to the next attachment site.

9. Repeat step 8 until the whole lift-out block is sliced up.

D. Do the section trimming and fine milling as described in the previous section II. Serial Lift-Out with double sided attachment from below and store the grid at liquid nitrogen temperatures.

IV. Serial Lift-Out with single-sided attachment

1. Prepare the lift-out session at room temperature.

a. Load a half-moon grid into the FIB.
Note: If you don't have half-moon grids, you can prepare grids with pins for single-sided attachment from a normal EM grid without support film as described in (Schiøtz et al. 2023).

i. Clip the grid into a cartridge **with** cutout for FIB milling. The half-moon grid must be clipped into the cartridge on the opposite site of the cutout.

ii. If necessary, align the half-moon grid with respect to the cutout by holding the cartridge on both sides on a flat surface. Press with sharp tweezers against the edge of the clipped halfmoon grid and rotate it with respect to the cutout.
Critical: Do not touch the half-moon grid on its central front as this may bend the pins. If you deform the half-moon grid in the process of clipping or aligning, discard it and clip a new one. A bend half-moon grid as receiver grid makes the experiment difficult or impossible.

iii. Label the cartridge with two blue marks in the 3 and 9 o'clock position as well as a red mark 6 o'clock, all with respect to the cutout 12 o'clock (Figure 24A).
Note: The marks will help you to orient the grid when loading it into microscopes.

iv. Mount the clipped half-moon grid into the FIB shuttle. The cutout must face up and the front edge of the half-moon grid must be aligned horizontally (Figure 24B). Load the shuttle into the FIB at room temperature.

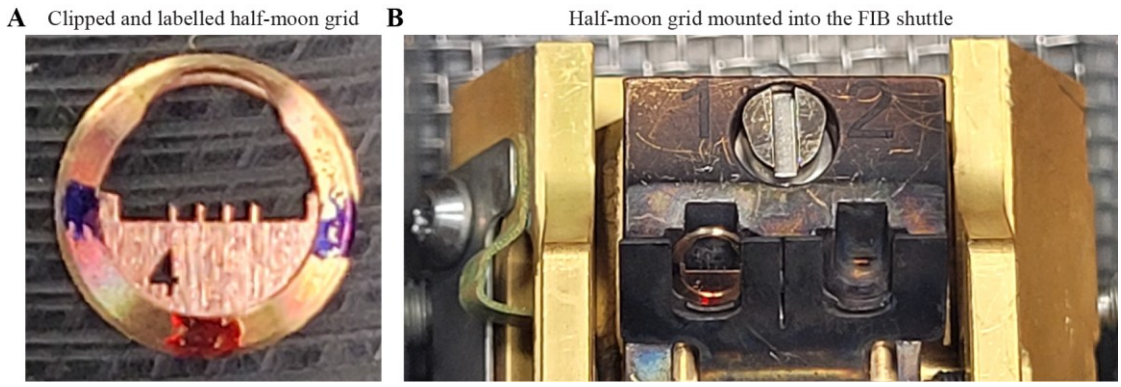


Figure 24. Labelling of the clipped half-moon grid and alignment in the FIB shuttle. A. Markers on the cartridge of a clipped half-moon grid. **B.** The half-moon grid mounted in the FIB shuttle.

b. Polish the bottom of the EasyLift needle.

   i. Inserted the needle.

   ii. Coarsely remove potential remnants of previous experiments at 5-30 nA.

   iii. polished the bottom of the needle at 1 nA with a cross-section over the whole width of the needle bottom, milling direction towards the needle. Set the z-dimension of the cross-section to the diameter of the needle at the tip.

   iv. Retract the needle.

c. Prepare and attach a copper adapter for the needle from the half-moon grid (Figure 25A).

   i. Move the stage into trench milling orientation (stage tilt = 7°, relative rotation = 180°).

   ii. Find the coincidence point of FIB and SEM on the edge of the half-moon grid next to the pins. (Figure 25B)

   iii. FIB-mill a cavity into the front edge of the grid using a cross-section with xyz-dimensions of 35x45x150 µm at 30 nA (Figure 25A step I).

   iv. Mill a 20 µm high cavity in y on the left side using a 5x20x150 µm cross section (Figure 25A step II), followed by a 35x5x200 µm trench in the back (Figure 25A step III), both at 30 nA creating the rough shape of a 30x15 µm copper adapter which is attached to the grid on only one side (Figure 25C).
   Note: the milling direction is always towards the copper adapter.
   Critical: Take a FIB image and check if the copper adapter is detached on all three sides. If not, continue FIB milling until it is detached.

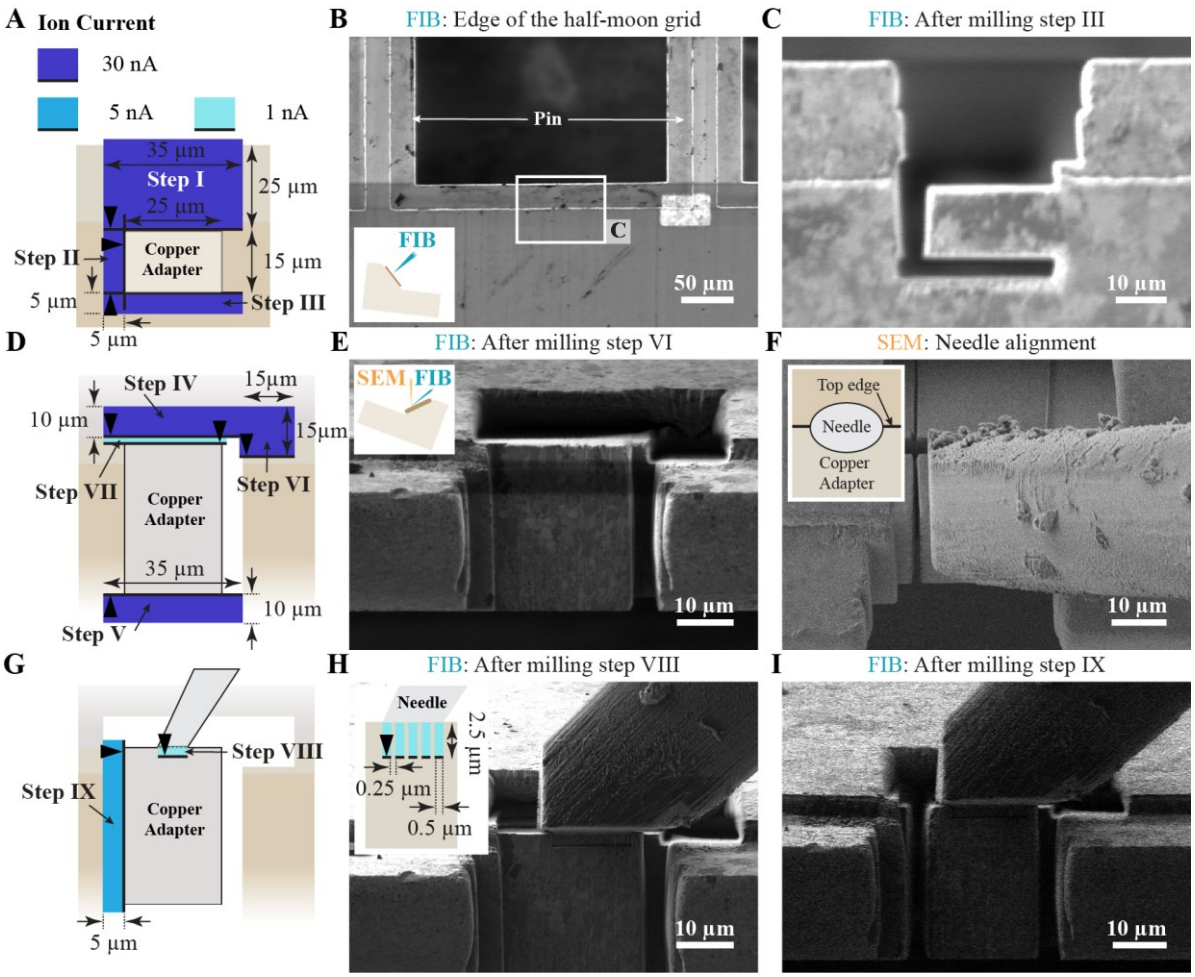


Figure 25. Preparation of a copper adapter from a half-moon grid. A. Scheme of the first set of patterns used to mill the rough shape of the copper adapter with the stage in trench milling orientation. **B**,**C**. Milling steps in trench milling orientation. **B**. Edge of the half-moon grid between two pins. The inset illustrates the shuttle in trench milling orientation with respect to the FIB imaging direction. **C**. FIB image after milling the rough shape of the copper adapter. **D**-**I**. Milling steps in lamella milling orientation. **D**. Scheme of the second set of patterns used to prepare the needle attachment site with the stage in lamella milling orientation. **E**. FIB image after milling the needle attachment site. The inset illustrates the shuttle in lamella milling orientation with respect to the FIB/SEM imaging directions. **F**. SEM image of the needle aligned above the copper adapter. The inset shows how the center of the needle bottom is positioned above the top edge of the copper adapter. **G**. Scheme of the third set of patterns required to attach the needle and detach the copper adapter from the grid milled in lamella milling orientation. **H**. Attachment of the needle to the copper adapter. The inset illustrates the dimensions of the used cross-section patterns ("Multi pass" set to 1). **I**. FIB image after detaching the copper adapter from the half-moon grid. In (A), (D), (G) and (H) black arrowheads indicate the milling directions of the cross-sections. The FIB milling patterns are provided in the section Supplementary information.

v. Rotate the stage into the lamella milling orientation and find the coincidence point of FIB and SEM on the precursor of the copper adapter.

vi. Remove 10 µm from the top and the bottom of the copper adapter using cross-sections with 35x10x30 µm in xyz at 30 nA (Figure 25D step IV and V).

vii. Extend the top trench towards the right using a cross-section with 15x15x30 µm 30 nA (Figure 25D step VI, Figure 25E).

Critical: The extension to the right is critical to allow the needle to get in contact with the top edge of the copper adapter. Otherwise, the needle may touch the surface of the grid before it comes in contact with the adapter.

viii. Polish the top front of the copper adapter 1 nA (cross-section, xyz-dimension = 20x1.5x30 µm, Figure 25D step VII).

ix. With the stage in lamella milling orientation, insert the polished needle.

x. In the SEM, adjust the position of the needle that the center of its tip aligns to the top edge of the copper adapter. This increases the surface for the redeposition (Figure 25F).

xi. While continuously imaging with the FIB move the needle down in z until it is in contact with the upper surface of the copper adapter.

i. Define a horizontal array of cross-sections with xyz-dimensions of 0.5x2.5x4 µm every 250 nm and place it along the interface between needle and adapter on the adapter with the milling direction away from the needle (Figure 25H).
Critical: Set "Multi pass" to 1 of the cross-sections used for redeposition milling.

xii. Mill the pattern array at 1 nA to attach the needle to the copper adapter (Figure 25G step VIII).
Note: Move the needle 500 nm upwards. You should see no movement or a movement of the entire grid. If only the needle moves, the attachment was not successful.

xiii. Detach the copper adapter on the remaining side. Use a cross-section with xz-dimension 5x30 µm over the whole height of the adapter milled at 5 nA (milling direction towards the adapter) resulting in a final adapter width of 15-20 µm (Figure 25G step IX ,Figure 25I).
Note: Single-sided attached lamellae are not as stable as double-sided attached lamellae. They tend to bend (Figure 29B). This tendency is reduced if the width from the attachment site is minimized and therefore if the width of the lift-out block is reduced. The width of the copper adapter must be smaller than the width of the lift-out block. The width of the copper adapter can be adjusted in this step by the position of the cross-section that detaches the adapter from the bulk grid.

xiv. If not yet done, polish the lower edge of the copper adapter at 1 nA (cross section, yz-dimensions: 1.5x30 µm over the whole width of the adapter, milling direction towards the adapter).

Note: this can be done when the system is cooled down right before the lift-out experiment starts.

xv. Retract the needle.

d. Mill marker lines into the front edges of pins for the alignment of the lift-out block.

i. In the FIB, center the tip of a pin in trench milling orientation.

ii. Align the pin vertically by adjusting stage rotation.

iii. Define cross-section with xyz-dimensions of 10x2x12 µm (milling direction top to bottom) and place them on the edge of the pin at the transition to its round tip on both sides (Figure 26).

iv. Mill the marker lines at 15 nA.

v. Repeat this for all pins.

vi. Store the modified half-moon receiver grid until it is used for a lift-out experiment.

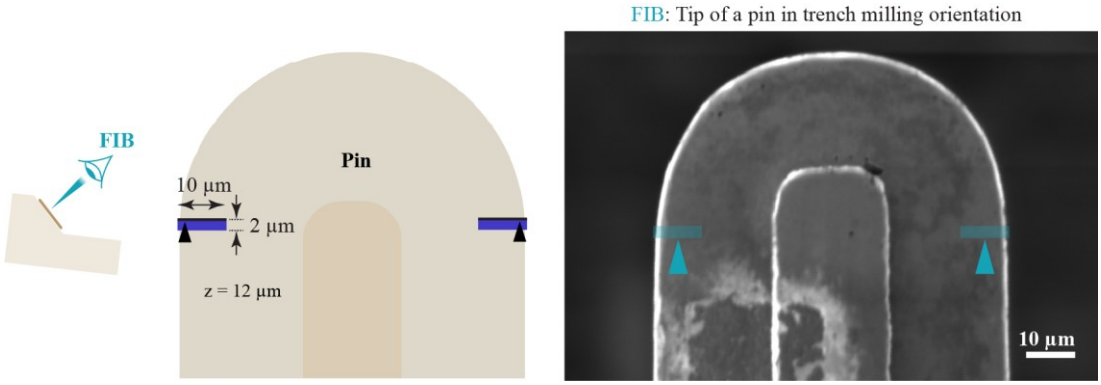


Figure 26. Marker lines for half-moon grids. The scheme on the left illustrates the stage in trench milling orientation with respect to the FIB imaging direction. The scheme in the middle and the FIB image on the right show the tip of a pin. The cross-sections used to mill marker lines are depicted as blue rectangles and. The milling direction is indicated by arrowheads. The FIB milling patterns are provided in the section Supplementary information.

2. Lift-out

a. Load the modified half-moon receiver grid and the sample for lift-out into the FIB

i. Mount the modified receiver grid into the FIB shuttle with the loading station at room temperature. Make sure the cutout for FIB milling is oriented on top and the front edge of the half-moon grid is oriented horizontally. Fix the grid in the shuttle by tightening the screw.
Note: Orienting the receiver grid is much easier at room temperature.

ii. Cool down the loading station

iii. Loosen the screw of the shuttle and load the lift-out sample into the shuttle.

iv. Load both grids into the cooled FIB after fixing them in the shuttle.

v. While imaging in the FIB, precisely align edge of the receiver grid horizontally using the stage tilt. *Critical: If the alignment error is higher than 10°, unload and manually adjust the receiver grid orientation before reloading.*

b. Do targeted trench milling and axial targeting as described in section II. The "waffle" workflow. Only difference is that the final width (x-dimension) of the target area containing block is 25-30 µm after trench milling.
Critical: Single-sided attached lamellae are not as stable as double-sided attached lamellae. They tend to bend (Figure 29B). This tendency is reduced if their width from the attachment site is minimized and therefore if the width of the lift-out block is reduced.

B. Lift-in.

1. Move to the half-moon grid with the stage in lamella milling orientation (stage tilt = 15°).
2. Find the coincidence point of FIB and SEM on a marker line at the edge of a pin.
3. Insert the needle with the lift-out block attached to it.
4. In the SEM, align the front edge of the lift-out block to the marker line with a 2 µm gap to the pin.
5. While imaging in the FIB, move down the needle until its lower edge is aligned with the marker line (Figure 27A).
6. In the SEM, check if the front edge is still aligned with the marker line. If not, adjust the needle position.
7. In the SEM, move the needle towards the pin until the lift-out block touches the pin.
8. Generate the serial sections

    a. Define a vertical array of 6 cross-sections with xyz-dimensions of 2.5x0.5x4 µm every 250 nm. Place them along the interfaces between pin and lift-out block on the pin. The lowest pattern aligns with the marker line. Set the milling direction away from the block (Figure 27B).

    b. Mill the pattern array at 1 nA to attach the lift-out block on the side.
    Note: Move the needle 500 nm upwards. You should see no movement ***or***

movement of the entire grid. If only the lift-out block moves, the attachment was not successful.

c. Optional: If the attachment was not successful, define a vertical array of 3 cross-sections with xyz-dimensions of 3x0.8x5 µm every 700 nm. Place it along the interfaces between pin and lift-out block. The lowest pattern aligns with the marker line (Figure 27D). Mill at 1 nA.

d. Define a horizontal line pattern (z-dimension = 10 µm) that is 2 µm wider than the lift-out block and place it 4 µm higher than the lower edge of the lift-out block (Line pattern I in Figure 27C).
Note: The positioning of the line pattern above the lower edge of the lift-out block defines the section thickness. Thicker sections reduce the contextual information by resulting in less sections. Thinner sections are possible, but that complicates the subsequent section trimming step.

e. Define a second horizontal line pattern (z-dimension = 20 µm) that is 4 µm wide. Place it on the first line pattern centered on the interface between lift-out block and pin (Line pattern II in Figure 27C).
Critical. During the attachment, copper is sputtered on the side of the lift-out block. This second line pattern is necessary to detach the section from the lift-out block.

f. Define a vertical line pattern (z-dimension = 20 µm). Place it on the edge between lift-out block and pin starting at the horizontal line patterns and ending 2 µm above the topmost pattern used for the attachment (Line pattern III in Figure 27C).
Critical: It is possible that the lift-out block becomes attached to the pin above the section. This third line pattern is necessary to detach the lift-out block from the pin.

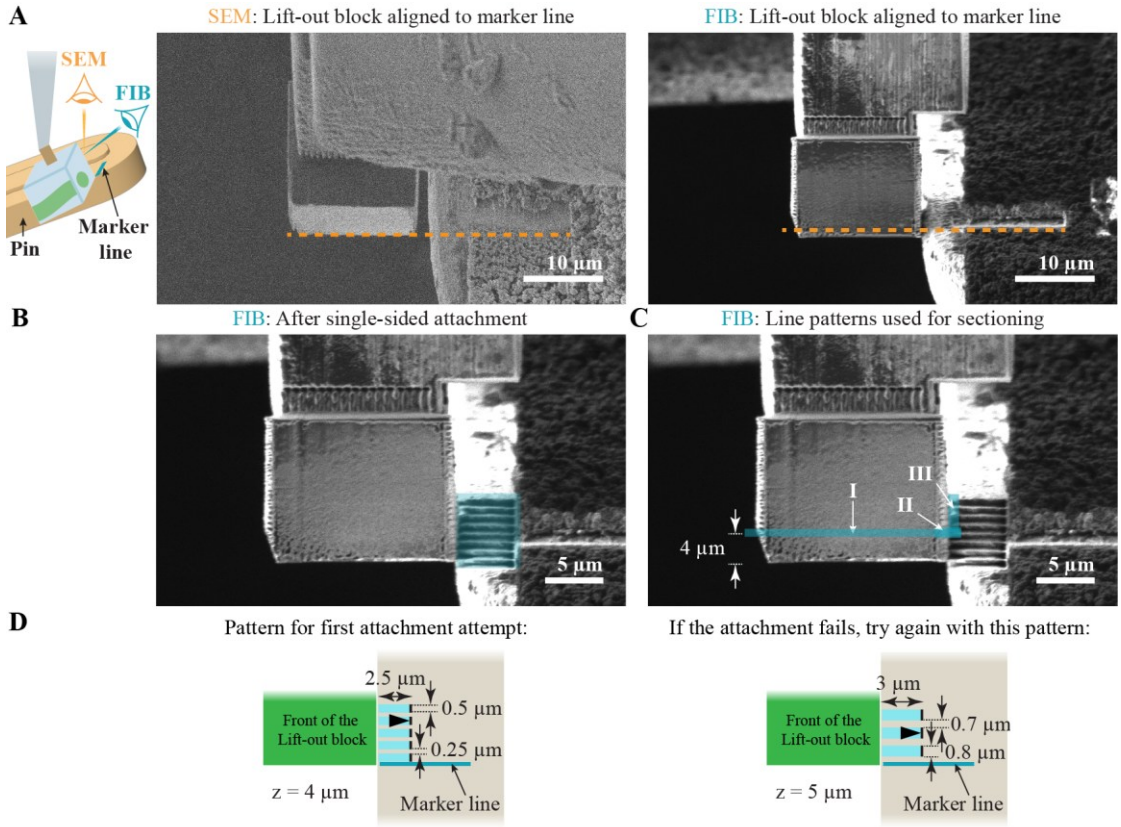


Figure 27. Alignment, attachment and sectioning of the lift-out block for single-sided attachment. A. An SEM and FIB image of the lift-out block aligned to the marker line is shown in the left and right panel, respectively. The orange dashed line indicates the alignment to the marker line. The scheme on the left illustrates the location of the lift-out block with respect to pin, marker lines and the FIB/SEM imaging directions. **B.** FIB image after the attachment from the side. **C.** Line patterns for the sectioning of the lift-out block indicated by blue lines. **D.** Scheme of the cross-section arrays ("Multi pass" set to 1) used for attachment for the first and second attempt in the left and right panel, respectively. The black arrowheads indicate the milling direction. The FIB milling patterns are provided in the section Supplementary information.

g. Mill all line patterns sequentially at 1 nA.
*Note: Afterwards, move the needle 500 nm upwards. You should see movement of the needle **and** the remaining lift-out block. If nothing or the whole grid moves, the lift-out block is still attached to the section or the pin.*

h. Retract the needle and move to the next attachment site.

9. Repeat step 8 until the whole lift-out block is sliced up.

C. Trim the sections

1. Record top view images of every section with the int-FLM with the stage in trench milling orientation.

   a. Use the reflected light channel to focus on the section.

   b. Record a z-stack with reflected light and cellular autofluorescence channel as used for targeted trench milling (bin = 4, 10 z-slices, z-step = 1 µm, see section I. The "waffle" workflow).

2. Identify sections that do not contain the target area based on the int-FLM top views. These sections can be skipped in the subsequent steps (Figure 28A).

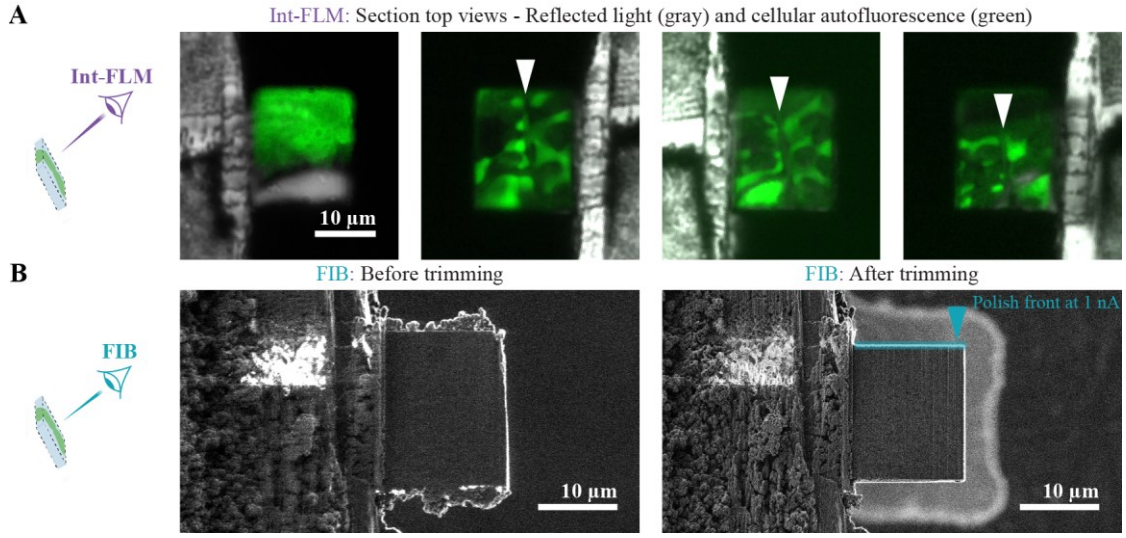


Figure 28. Trimming of single sided attached Serial Lift-Out sections. The schemes on the left illustrate the location of the section with respect to the int-FLM and FIB imaging direction. **A.** Top views recorded with the int-FLM of four successive Serial Lift-Out sections showing the reflected light channel (gray) and cellular autofluorescence (green). The junction between cells is only contained in three of them indicated by white arrowheads. **B.** FIB images of a section recorded in trench milling orientation before and after trimming in the left and right panel, respectively. Afterwards the top front is polished at 1 nA. The milling pattern is indicated by a blue rectangle and the milling direction by a blue arrowhead. The FIB milling patterns are provided in the section Supplementary information.

3. For sections that contain the target area, identify the regions of the sections that do not contain the material of interest based on the int-FLM top views.

4. Apply a layer of metal organic platinum by opening the GIS 15 s in trench milling orientation at the GIS working distance in z.

5. For every section, remove material above and below the target area as well as on the side opposite of the attachment site with the stage in trench milling orientation. Use cross-sections (z-dimenstion = 1 µm) milled at 3 nA with the milling direction towards the target area (Figure 28B).

6. Polish the top front at 1 nA (cross-sections, z-dimension = 2 µm).
Critical: During trimming, at least 1-2 µm should be removed of the top edge. This surface was constantly exposed by the FIB during lift-out, lift-in and sectioning. Thus, it is damaged and uneven.

7. Open the GIS in trench milling and lamella milling orientation for 15 s and 3x20 s, respectively, both at GIS working distance.
Note: The trimming minimizes the size of the lamella which makes fine milling faster and generates smooth surfaces covered with a thick, homogeneous layer of metal-organic platinum which is key to obtaining homogeneously thin lamellae.

D. Thin the sections by FIB milling.

1. Remove the top and bottom of the section over its whole width at 1 nA using cross-sections (top z-dimension = 5-6 µm, bottom z-dimension = 2 µm, vertical distance between patterns = 2 µm similar to Figure 19A).
   Note: The sections top layer is composed of metal organic platinum and requires longer milling times.
2. Thin the lamella to 1.5 µm at 0.3 nA using cross-sections (z-dimension = 2 µm, milling direction towards the center of the lamella).
3. Define two rectangle patterns with a vertical distance of 200 nm but leave a 1.5x1.5 µm block opposite of the attachment site (Figure 29A).
   Critical: This block prevents the lamella from folding during fine milling.
4. Mill the rectangle patterns in parallel at 50 pA.
5. Switch to an ion current of 30 pA. Tilt the stage to 14° and 15.5-16° and polish your lamella only from below and the top, respectively.
6. Optional: Sputter a thin layer of metallic Platinum on your sample (U = 1 kV, I = 10 mA, p = 0.2 mbar, t = 2-4 s).
7. Unload the sample and store it at liquid nitrogen temperatures until it is imaged in a transmission electron microscope.

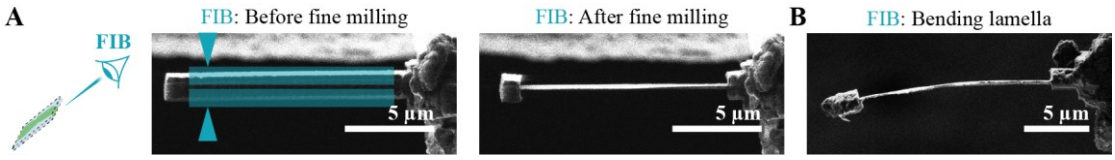


Figure 29. Fine milling of single-sided attached sections. A. Single sided attached lamella before and after fine milling in the middle and right panel, respectively. The milling patterns are indicated in blue rectangles in the middle panel, the milling directions by blue arrowheads. A 1.5x1.5 µm block opposite of the attachment site is left to prevent folding of the lamella. The left panel illustrates the location of the lamella with respect the FIB imaging direction. **B.** Single sided attached lamellae which bend after fine milling. The FIB milling patterns are provided in the section Supplementary information.

V. Workflow for in-carrier high-pressure frozen samples

A. In-carrier high-pressure freezing

1. Clean 3 mm Type A and Type B HPF carriers the day before the high-pressure freezing.
   a. Incubated carriers overnight in a 15 mL Falcon tube with cleaning solution.
   b. Wash carriers 3x with ddH_2O and 3x with acetone.
   c. Dry carriers on filter paper.
2. Coat type B carriers with cetyl palmitate.
   Note: Work under fume hood.

a. Dip the type B carriers (one 300 µm cavity and one flat side), one at a time, with tweezers into cetyl palmitate solution.

b. Removing excess of liquid by shaking it off and pushing the side of carriers against filter paper.

c. Dry carriers on filter paper with the flat side facing up.

3. Label the rim of type A carriers on the side with the 100 µm deep well with a red and a black mark in the 6 and 12 o'clock positions, respectively.
Note: Use Magnifying glasses or binocular microscopes to discern the side with the 100 µm from the 200 µm well.
Note: The label helps to identify the sample containing side of the carrier and can be used to orient the carrier when loading it into the FIB.

4. Prepare the high-pressure freezer and test the system.

a. Cool down the high-pressure freezer and the sample container. Insert the sample container and wait for the system status to change to ready.

b. Freeze two "test shots" only with two half cylinders and a middle plate without HPF carriers.

5. Place a type A carrier with the marked side facing up on a filter paper.

6. Add 2 µL freezing buffer into the 100 µm well and distribute it with the pipet tip.

7. Pick up a small patch of a *Physcomitrium patens* protonemata from a plate and place it in the droplet in the center of the carrier.
Critical: Try not to squeeze the tissue with tweezers. This will damage the cells. Lift the tissues with the tip of a single leg of the tweezers.

8. Remove air bubbles by poking them with sharp tweezers.
Critical: Air bubbles in the sample will first be compressed upon high-pressure freezing but expand again when the freezing chamber is depressurized. This can induce cracks in your sample which makes subsequent steps difficult or even impossible.

9. Remove excess of buffer until its meniscus almost vanishes. For large volumes, use 2x0.5 cm filter paper pieces. For small volumes, stick closed tweezers into the buffer, open them and take them out of the buffer.
Critical: The buffer meniscus must almost but not entirely vanish. If it vanishes, you will create a large air inclusion when you place the flat side of the type B carrier which will cause freezing problems.

10. Place a cetyl palmitate coated 3 mm type B carrier with the flat side down on top and squeeze the sandwich together.

11. Remove excess buffer with a 2x0.5 mm piece of filter paper at the gap between carriers.
12. Place the carrier sandwich in the plastic pieces of the high-pressure freezer.
13. Squeeze the sandwich for 10 s with the back side of tweezers.
14. Freeze the sample.
13. Recover the sample containing type A carriers by separating them from the type B carriers.
14. Break point: Store samples in grid boxes cooled by liquid Nitrogen until use.

E. Sample screening and targeted trench milling
Note: The 3 mm HPF carriers have a slightly smaller diameter than grids clipped into cartridges. The commercial Leica SP8 shuttles are designed for cartridges. Thus, 3 mm HPF carriers cannot be screened in the FLM as described for the "waffle" workflow in the previous sections. Record tile images with the int-FLM instead. This is sufficient to find target areas. The tissue is overall better preserved because damage due to compression by grid bars or multiple cell layers per grid square are omitted by in-carrier high-pressure freezing.

1. Load an in-carrier frozen sample and a clipped receiver grid (see previous sections) into a cooled cryo-FIB with int-FLM.
   Critical: Check at room temperature if your FIB shuttle holds both, the 3 mm carrier and the receiver grid. On some shuttles, the receiver grid falls out because the 3 mm carrier is thicker than the cartridge. If the receiver grid falls out, first only load the carrier and do the lift-out. Then unload the 3 mm carrier and load the receiver grid.
2. Remove ice contamination with the FIB (See Figure 3).
3. Optional: Sputter coat the sample (p = 0.1 mbar, U = 1 kV, I = 10-30 mA, t = 15-30 s).
   Note: The resulting Pt layer prevents charging especially for thicker samples which improves the quality of FIB and SEM images.
4. Apply a layer of metal-organic platinum by opening the GIS for 45 s in trench milling orientation at the GIS working distance in z.
5. With the stage in trench milling orientation, find the coincidence point of SEM and FIB in the center of the carrier.
6. Mill a marker (cross-section, I = 3 nA, z = 0.5 µm, Figure 30A).
   Note: An asymmetric marker can be beneficial, if FIB and int-FLM images are rotated with respect to one another. Here we used an 8x8 µm square with 6x16 µma rectangle aligned with their ipper edges at a distance of 8 µm.

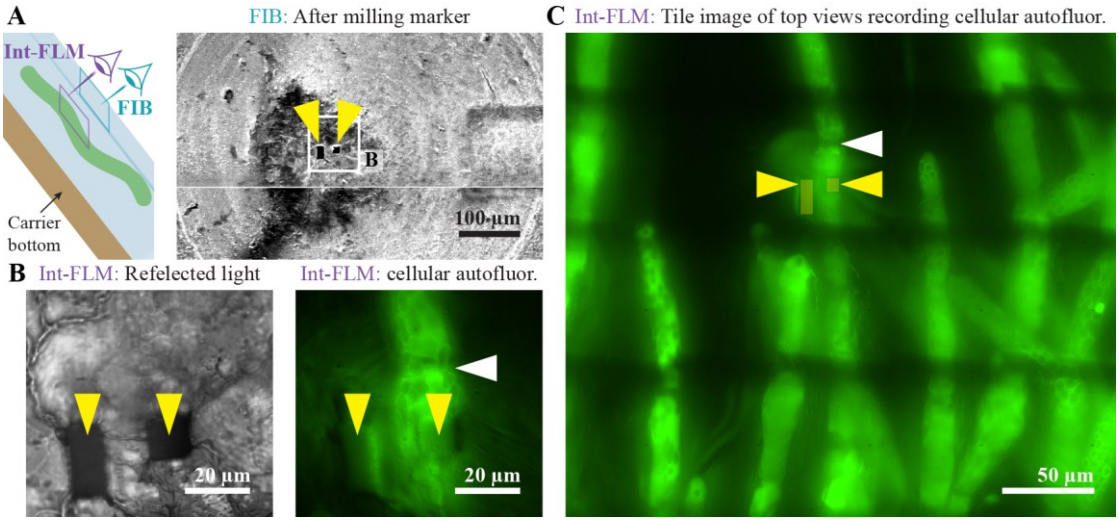


Figure 30. Screening of in-carrier frozen samples using the int-FLM. A. In-carrier frozen sample with asymmetric marker pattern milled in the center of the sample. The scheme on the left illustrates location of the sample with respect to the FIB and int-FLM imaging direction. **B.** Top views recorded with the int-FLM. The reflected light and cellular autofluorescence channels are depicted in the left and right panel, respectively. **C.** Tile image of Int-FLM top views recording cellular autofluorescence. Marker holes are indicated by yellow arrowheads, a junction between cells by a white arrowhead.

7. Use the int-FLM to screen the sample by recording tile images of top views.

    a. Focus the int-FLM on the sample surface and locate the marker pattern (Figure 30B).
    Note: This is easiest using a reflected light channel (Excitation: 470 nm ± 10 nm; no emission filter).

    b. Record tile images covering 500-1000 µm^2 as z-stacks with 5-10 z-steps and a step size of 5-10 µm using the reflected light and cellular autofluorescence (Excitation: 470 nm ± 10 nm; emission filter: 515 nm ± 15 nm, Figure 30C).
    Critical: Keep the laser power as low as possible while still being able to identify your target area. A too high laser power can devitrify your sample.
    Note: Dependent on the int-FLM system, the imaged area and the z-stack size, this can take hours.

    c. Identify a potential target area, move the stage there and record a z-stack (Figure 30B, bin = 4, 20-25 z-slices, z-step = 1 µm).
    Note: Ideally, target areas should be located close to the sample surface which can be estimated in int-FLM z-stacks. Lift-out on targets which are located tens of micrometers below the sample surface is challenging. The closer target area is located to the surface of the sample, the easier it is accessible for the lift-out.

8. Targeted trench milling was performed as described in the “waffle” workflow with two important differences:

    a. Set the z-dimension of the milling patterns to 1-1.5 µm.
    Critical: If you mill too long which is determined by the patterns z-dimension,

you will reach the metal surface at the bottom. This will sputter metal from the carrier onto the front of the target area containing block which makes the generation of a smooth front very difficult.

b. Adjust the xy-dimension of the trench milling patterns dependent on the attachment strategy for the lift-in as described in the previous sections.
Note: For the double-sided attachment, the width of the lift-out block (x-dimension with respect to FIB and SEM images) must be wide enough to bridge the gap between attachment sites.
Note: For the single sided attachment, it is beneficial if the width of the lift-out block is kept at a minimum, while the depth is increased (y-dimension with respect to FIB images recorded with the stage in trench milling orientation). This increases the area for the attachment and may prevent lamella bending.

F. Lift-out
Critical: To detach the lift-out block on in-carrier frozen samples, it is not enough to detach it on all for sides in trench milling orientation as it is the case for "waffle" samples. It requires a FIB milled "undercut" in lamella milling orientation to detach the lift-out block on the bottom from bulk sample.

1. Determine the axial location of the target area using SEM block-face imaging (Figure 31B) or FIB-view imaging with the integrated FLM (Figure 31C).
Critical: The axial localization is crucial. In-carrier HPF samples are substantially thicker than "waffle" samples. This step helps you to make sure you lift out your whole target area and not much less or more.

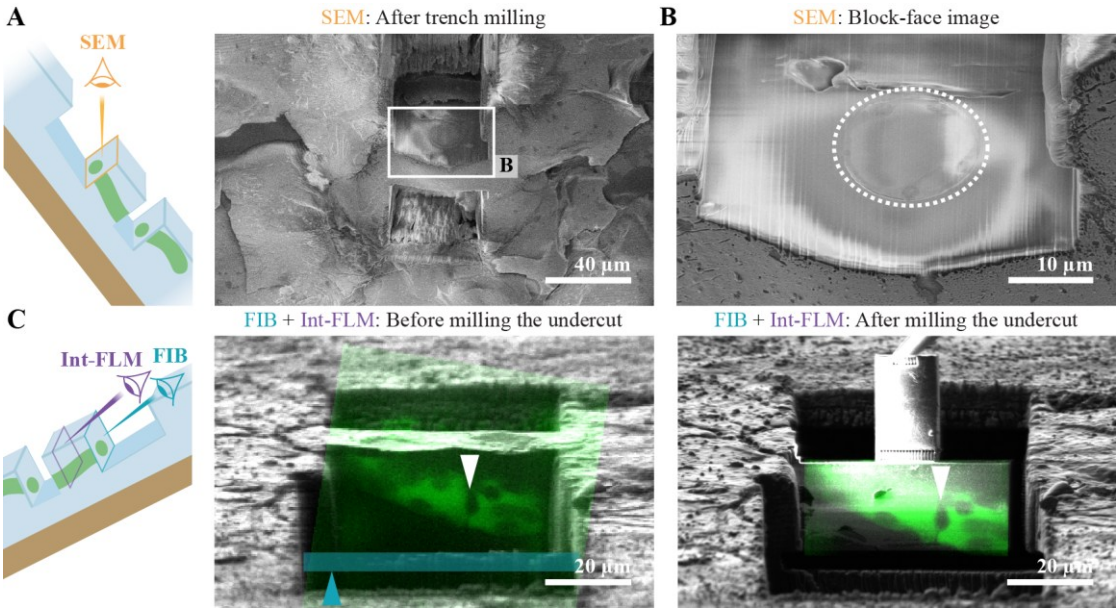


Figure 31. Lateral targeting and undercut for lift-out on in-carrier frozen samples. The schemes on the left illustrate the location of the sample with respect to the SEM, int-FLM and FIB imaging directions. **A.** SEM image of an in-carrier frozen sample after trench milling. **B.** SEM block-face image of the surface exposed through trench milling. The lateral location of a cell is indicated by a dashed white line. **C.** Overlay of FIB (gray) and FIB-view image recorded with the int-FLM (cellular autofluorescence in green) before and after milling the undercut. The undercut milling

pattern is indicated by a blue rectangle, the milling direction by a blue arrowhead and the junction between cells by white arrowheads.

2. Apply a layer of metal organic platinum
    a. Rotate the stage into lamella milling orientation and move the stage to the GIS working distance.
    b. Lift-out option I: from the side similar to (Schiøtz et al. 2023): open the GIS for 20 s.
    c. Lift out option II: from the top: open the GIS for 3x30 s.
    Critical: If you perform the lift-out in lamella milling orientation, the front of the target area containing block will be constantly exposed by imaging with the FIB. Thus, it needs a thicker protective layer.
3. Create a cross-section for the "undercut" over the whole width of the target area containing block with yz-dimensions of 3x4 µm, milling direction bottom to top. *Critical: the required z-dimension of the pattern depends on the thickness of the lift-out block in the direction of the optical axis of the FIB. It may need adjustment if the block is thicker than 30 µm.*
4. Place the undercut pattern below the target area based on its z-location and mill it at 3 nA.
5. Proceed with the lift-out as described in the section Serial Lift-Out with double sided attachment from below.

G. Lift-in, section trimming and fine milling was performed as described in the previous sections deponent on the chosen attachment strategy.

Data Analysis

Data acquisition, examples of reconstructed tomograms and a data analysis workflow based on subtomogram averaging are described in (Pöge et al. 2025).

Validation of Protocol

Over the past 3 years, we high-pressure froze 45 *P. patens* samples (Figure 32A). From 21 of these samples (47%), we obtained lamellae with vitreous tissue. The HPF results are not consistent and sample dependent. We tested the protocol on *Nicotiana benthamiana* trichomes and not a single sample was vitreous. At the same time other users high-pressure froze *Caenorhabditis elegans* L1 larvae with a success rate close to 100%.

In total, we prepared 216 lamellae. Of 74 on-grid milled "waffle" lamellae 80% survived the transfer into the TEM and could be imaged. A fraction of the non-imaged "waffle" lamellae, however, made the transfer but not all material below them was removed by FIB milling. These "shadow lamellae" prevent cryo-ET data acquisition. For single-

sided, double-sided attached lamellae from the side and double sided-attached lamellae from below we prepared 31, 49 and 99 lamellae of which 58%, 76% and 90%, respectively, could be imaged (Figure 32B). As described in (Pöge et al. 2025) from a small dataset recorded on these lamellae, we recovered subnanometer structural details by subtomogram averaging. Furthermore, we applied modified workflows to other plant tissues and species.

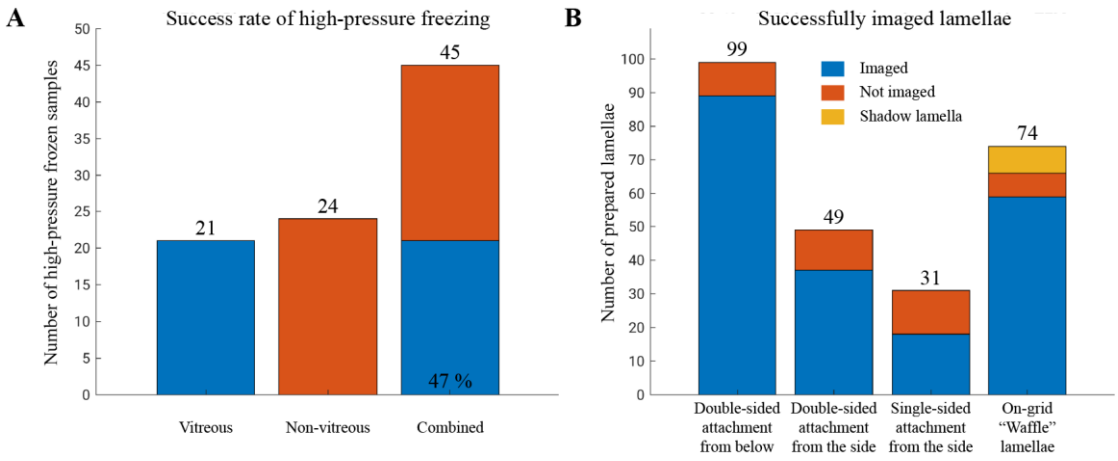


Figure 32: Success rates for high-pressure freezing and lamella preparation. A. Success rate for high-pressure freezing for *P. patens* tissue. **B.** Number of lamellae that were prepared vs the number of imaged lamellae. For on-grid milled "waffle" lamellae, the fraction "Shadow lamella" indicates lamellae where not all material was removed below the lamella which prevents the acquisition of cryo-ET data.

Acknowledgments

We thank Manuel Miras and Neda Kazemein Jasemi for their help with the *P. patens* culture. This work received funding from the European Research Council (ERC Grant agreement 'SymPore' no. 951292).

References

Arnold, J., J. Mahamid, V. Lucic, A. de Marco, J. J. Fernandez, T. Laugks, T. Mayer, A. A. Hyman, W. Baumeister, and J. M. P. 2016. "Site-Specific Cryo-Focused Ion Beam Sample Preparation Guided by 3D Correlative Microscopy." *Biophysical Journal* 110(4):860–69. doi: https://doi.org/10.1016/j.bpj.2015.10.053.

Cove, David J., Pierre François Perroud, Audra J. Charron, Stuart F. McDaniel, Abha Khandelwal, and Ralph S. Quatrano. 2009. "Culturing the Moss Physcomitrella Patens." *Cold Spring Harbor Protocols* 4(2):1–6. doi: 10.1101/pdb.prot5136.

Dobro, Megan J., Linda A. Melanson, Grant J. Jensen, and Alasdair W. McDowall. 2010. "Chapter Three - Plunge Freezing for Electron Cryomicroscopy." Pp. 63–82 in *Cryo-EM Part A Sample Preparation and Data Collection*. Vol. 481, edited by G. J. B. T.-M. in E. Jensen. Academic Press.

Dubochet, J. B. T. 2007. "The Physics of Rapid Cooling and Its Implications for Cryoimmobilization of Cells." Pp. 7–21 in *Cellular Electron Microscopy*. Vol. 79. Academic Press.

Dubochet, Jacques. 1995. “High-Pressure Freezing for Cryoelectron Microscopy.” *Trends in Cell Biology* 5(9):366–68. doi: https://doi.org/10.1016/S0962-8924(00)89071-6.

Kelley, Kotaro, Ashleigh M. Raczkowski, Oleg Klykov, Pattana Jaroenlak, Daija Bobe, Mykhailo Kopylov, Edward T. Eng, Gira Bhabha, Clinton S. Potter, Bridget Carragher, and Alex J. Noble. 2022. “Waffle Method: A General and Flexible Approach for Improving Throughput in FIB-Milling.” *Nature Communications* 13(1):1857. doi: 10.1038/s41467-022-29501-3.

Koning, R. I., A. J. Koster, and T. H. Sharp. 2018. “Advances in Cryo-Electron Tomography for Biology and Medicine.” *Annals of Anatomy - Anatomischer Anzeiger* 217:82–96. doi: https://doi.org/10.1016/j.aanat.2018.02.004.

Lučič, Vladan, Alexander Rigort, and Wolfgang Baumeister. 2013. “Cryo-Electron Tomography: The Challenge of Doing Structural Biology in Situ.” *The Journal of Cell Biology* 202(3):407–19. doi: 10.1083/jcb.201304193.

Moor, Hans. 1987. “Theory and Practice of High Pressure Freezing.” Pp. 175–91 in *Cryotechniques in Biological Electron Microscopy*, edited by R. A. Steinbrecht and K. Zierold. Berlin, Heidelberg: Springer Berlin Heidelberg.

Pöge, Matthias, Marcel Dickmanns, Peng Xu, Meijing Li, Oda H. Schiøtz, Christoph O. J. Kaiser, Jianfei Ma, Anna Bieber, Cristina Capitanio, Johann Brenner, Margot Riggi, Sven Klumpe, Manuel Miras, Neda S. Kazemein Jasemi, Waltraud X. Schulze, Rüdiger Simon, Wolf B. Frommer, Jürgen M. Plitzko, and Wolfgang Baumeister. 2025. “Making Plant Tissue Accessible for Cryo-Electron Tomography.” *BioRxiv* 2025.02.14.638237. doi: 10.1101/2025.02.14.638237.

Rensing, Stefan A., Bernard Goffinet, Rabea Meyberg, Shu Zon Wu, and Magdalena Bezanilla. 2020. “The Moss Physcomitrium (Physcomitrella) Patens: A Model Organism for Non-Seed Plants.” *Plant Cell* 32(5):1361–76. doi: 10.1105/tpc.19.00828.

Rigort, Alexander, Felix J. B. Bäuerlein, Elizabeth Villa, Matthias Eibauer, Tim Laugks, Wolfgang Baumeister, and Jürgen M. Plitzko. 2012. “Focused Ion Beam Micromachining of Eukaryotic Cells for Cryoelectron Tomography.” *Proceedings of the National Academy of Sciences* 109(12):4449–54. doi: 10.1073/pnas.1201333109.

Schiøtz, Oda Helene, Christoph J. O. Kaiser, Sven Klumpe, Dustin R. Morado, Matthias Poege, Jonathan Schneider, Florian Beck, David P. Klebl, Christopher Thompson, and Jürgen M. Plitzko. 2023. “Serial Lift-Out: Sampling the Molecular Anatomy of Whole Organisms.” *Nature Methods*. doi: 10.1038/s41592-023-02113-5.

Turk, M., and W. Baumeister. 2020. “The Promise and the Challenges of Cryo-Electron Tomography.” *FEBS Letters* 594(20):3243–61. doi: https://doi.org/10.1002/1873-3468.13948.

Yang, Jae, Veronika Vrbovská, Tilman Franke, Bryan Sibert, Matthew Larson, Alex Hall, Alex Rigort, John Mitchels, and Elizabeth R. Wright. 2023. “Integrated Fluorescence Microscopy (IFLM) for Cryo-FIB-Milling and In-Situ Cryo-ET.” *BioRxiv* 2023.07.11.548578. doi: 10.1101/2023.07.11.548578.

Chapter 7

7.1 Concluding discussion

Despite their physiological importance and more than a century of investigation, we still lack a coherent model of plasmodesmata organization and function. The molecular inventory remains incomplete and likely contains false positives, most candidate proteins are uncharacterized, and the mechanisms controlling permeability remain elusive. This chapter briefly puts the results described in this thesis into context, assesses their limitations, and outlines future steps to be taken.

To address the incomplete molecular inventory, we performed proteomic analyses of plasmodesmata-enriched cell wall fractions in *Physcomitrium patens*, identifying orthologs of known plasmodesmal proteins alongside numerous novel candidates. Because such datasets are inherently noisy, we treated proteomes not as definitive parts lists but rather as a baseline to explore new hypotheses. Selected candidates were characterized further by combining in vivo localization of fluorescent protein fusions, cell-to-cell translocation assays, phylogenetic and sequence level analysis, and protein structure prediction. This effort by necessity is incomplete, and many candidates remain to be evaluated in the future.

Among the candidates prioritized for further analysis were several components of the nuclear pore complex (NPC). Nuclear pore proteins (nucleoporins, NUPs) were identified in plasmodesmata-enriched cell wall fractions, and several fluorescently tagged NUPs showed a punctate localization pattern overlapping with aniline blue staining for callose at the cell periphery. Considering the functional analogy between nuclear pores and plasmodesmata, both being gated nanoscale pores that display selective trafficking of molecules, these observations motivated the plasmodesmal pore complex (PDPC) hypothesis: a subset of NUPs might assemble into an NPC-like scaffold at plasmodesmata, orchestrating intercellular exchange of solutes. Unlike NPCs, which are embedded in the ER-derived nuclear envelope and form a central pore, plasmodesmata contain a central ER-derived desmotubule and a peripheral cytosolic sleeve. Given that some membrane-anchoring NPC proteins show dual localization to both nuclear pores and plasmodesmata, we reasoned that a potential NUP assembly, if present at plasmodesmata, would need to be inverted; scaffolded on the desmotubule with disordered FG-NUP regions extending radially into the surrounding sleeve. This idea was further supported by the observation that cell-to-cell translocation of fluorescent tracers is impaired in some NUP mutants. However, our cryo-ET data on *P. patens* plasmodesmata did not reveal the presence of large assemblies resembling inverted NPCs. While this argues against the presence of a distinct NPC-like scaffold at plasmodesmata, it does not exclude roles for NUPs in alternative configurations, at low copy number, and/or as smaller subcomplexes whose size, heterogeneity, or

arrangement may place them below the current detection threshold of cryo-ET within the crowded plasmodesmal environment.

A related cautionary tale stems from investigations of a putative ciliary pore complex (CPC) by others (Ewerling and May-Simera 2024). Several NUPs were observed to localize to the ciliary base and some NUP mutants have been associated with ciliary defects (del Viso et al. 2016; Takao et al. 2017; Blasius et al. 2019), sparking similar ideas about NPC-like gates at cilia. Yet, cryo-ET studies of the ciliary base and transition zone could not resolve any NPC-like structures thus far, reinforcing that NUP detection at cellular pores does not necessarily imply the presence of an NPC-like scaffold (van den Hoek et al. 2022; Zhang et al. 2024). These shared observations between cilia and plasmodesmata indicate that some NUPs may carry intrinsic properties that favor their accumulation at cellular nanopores. It must also be considered that overexpression and fluorescent tagging can drive mislocalization, overaccumulation and aggregation of proteins of interest. Candidate proteins are commonly assessed for plasmodesmata localization by fluorescent tagging, evaluation of punctate patterns at the cell periphery, and quantification of the overlap with aniline blue-stained callose spots assumed to mark plasmodesmata. The resolution limit of non-super resolution light microscopy techniques lies within the 200 – 500 nm range (Huang et al. 2010). Cryo-ET and classical electron microscopy show that ER, plasma membrane, and callose-rich cell wall regions used to determine co-localization, all lie within a radius of ~50 – 200 nm around plasmodesmal apertures. Considering that the large central vacuole characteristic of plant cells pushes cytoplasmic components towards the cell periphery, plus the likely elevated expression levels in transgenic marker lines, ER-associated or cytosolic aggregates may easily appear as peripheral ‘plasmodesmata puncta’. Nevertheless, the reproducible enrichment of several NUPs in proteomics fractions and their co-localization with the plasmodesmal callose marker aniline blue seem unlikely to be random artifacts. A more conservative interpretation of the data is that at least some NUPs could be transiently retained in the vicinity of plasmodesmata without being stable components of a dedicated pore complex, as is being discussed for other plasmodesmata-associated proteins (Barr and Tilsner 2025).

The complexity of the NUP case illustrates why integrating data from different approaches is ultimately required to decode plasmodesmal composition and organization. Proximity labeling strategies (e.g. TurboID), cross-linking mass spectrometry, and super-resolution imaging (e.g. expansion microscopy) can refine the component list and report on spatial relationships, but large supramolecular assemblies remain best assessed by visualizing them directly where applicable. We therefore developed and tested cryo-ET workflows for a range of plant samples, focusing on *P. patens* in which plasmodesmata are abundant and can reliably be targeted. As far as we could determine, *P. patens* forms exclusively unbranched plasmodesmata while expressing homologs of all major plasmodesmal proteins described in flowering plants,

rendering it a compelling model system with reduced architectural complexity but representative molecular composition.

Even in this simplified context no two plasmodesmata look alike and, in a strict sense, there is no single 'structure' of the pore to be resolved. Instead, we measured and quantified a set of characteristic parameters including pore length, aperture width and cytosolic sleeve width to outline rough architectures found in different tissues and physiological states. Especially interesting was the finding that excessive deposition of cell wall material around the apertures, induced by treatment with the stress hormone abscisic acid, can fully seal plasmodesmata. Previously, only narrowing of apertures had been described where callose deposition was induced. If full closure is a moss-specific phenotype or generalizes to flowering plant plasmodesmata remains to be tested. Notably, *P. patens* and other mosses are known to enter a symplasmically isolated cyst-like state, referred to as brood cells, when exposed to cold or abscisic acid for extended periods (Arif et al. 2019; Kleist et al. 2022). While this stress-induced cyst formation is not documented in flowering plants, other arrested states with reduced cell-cell connectivity like bud dormancy, seed dormancy and floral arrest depend on abscisic acid signaling and may involve a similar plasmodesmal sealing mechanism (Tylewicz et al. 2018; Wang et al. 2020; 2023; Pan et al. 2023; Sánchez-Gerschon et al. 2024; Murata et al. 2025). In moss, abscisic acid-induced symplasmic isolation is reversible within 24h after hormone removal (Kitagawa et al. 2019), raising intriguing questions about how connectivity is reestablished. If new plasmodesmata are formed or existing ones are being reopened, and how plasmodesmal membranes are reconnected to their cellular counterparts remains to be investigated.

Besides the likely callose-dependent architectural changes involved in gating, another prominent structural feature observed in all imaged *P. patens* plasmodesmata was the desmotubule-associated protein coat. By extracting and averaging tomographic subvolumes containing several copies of these assemblies across multiple plasmodesmata we could resolve their in situ structure to ~30 Å. While this is modest compared to single-particle cryo-EM or cryo-ET analysis of highly abundant complexes, such as ribosomes or rubisco (see Chapter 4), the comparatively low throughput of cryo-ET, and the low copy number of these assemblies per tomogram at this point limit the obtainable resolution. We eventually identified Multiple C2 domain and Transmembrane Proteins (MCTPs) as the constituents of the resolved assemblies and could map their organization within the plasmodesmal pore. It should be noted that, at the achieved resolution, a given protein cannot be identified unambiguously from a density map. Instead, pinpointing MCTPs as the assembly building blocks was strongly enabled by the advent of transformer-based protein structure prediction, initiated by the release of AlphaFold2 (Jumper et al. 2021). These models enabled us to systematically assess the structure of plasmodesmata candidates identified in proteomes and compare them with the resolved assembly. In our case, identification was fortunately aided by the fact that, even among the relatively large set of proteome-derived

candidates, only a single protein family, the MCTPs, produced structure predictions compatible with the distinct geometry of the assembly; something that might not apply to less rigid, non-scaffold, or more globular proteins, for which multiple candidates likely yield comparable fits at nanometer resolution. Generally, de novo identification of previously uncharacterized proteins in cryo-ET remains a major challenge. While MCTPs are among the most abundant proteins within plasmodesmata, smaller and less abundant components that are not forming large, repetitive assemblies, may remain out of reach for subtomogram averaging as of now. Akin to the use of fluorescent protein fusions for spatial identification in light microscopy, genetically encoded cryo-ET-visible tags for targets that are too small to be detected by shape or contextual information alone have been developed. However, such tags are typically larger than the proteins that require labeling, ranging from ~5 nm (Young et al. 2025) to 30 – 40 nm (Silvester et al. 2021; Fung et al. 2023). Given that the resolved cytosolic sleeves have a diameter of only ~5 – 10 nm, these tags are expected to interfere with entry into plasmodesmal pores which would perturb native localization and function. Therefore, further progress will require label-free strategies for protein identification directly from tomograms. Here, the combination of cryo-ET and structure prediction, often guided by proteomics, is proving increasingly powerful, as demonstrated in this work and by others (McCafferty et al. 2024). To extend this approach to a broader range of targets and to advance the promise of cryo-ET-based visual proteomics, new strategies for systematic candidate screening and quantitative evaluation of agreement between predicted models and density maps will be required.

For the reasons outlined above, the resolution attainable for small and low-abundance proteins by in situ cryo-ET will likely remain in the nanometer range for the foreseeable future. Where more detail is required, individual components need to be examined in isolation. In the case of the MCTP assemblies described here, we resolved the overall geometry of the complexes and the relative arrangement of domains between subunits, but without amino acid-level information we cannot assign specific homologs to the assemblies, nor determine their molecular interactions precisely. Plant MCTPs as well as other reticulon-like proteins have been expressed in yeast, where they may rescue defects in ER tubulation and ER-plasma membrane tethering mutants (Brault et al. 2019; Xiang et al. 2023; Li et al. 2024). This indicates that functional, desmotubule-like architectures could be generated at higher density through recombinant MCTP expression, potentially allowing to achieve resolutions beyond what can currently be obtained in planta.

A general limitation of current cryo-ET is the restricted range of accessible samples. Not all biological specimens can be vitrified with the existing technology, and some may remain inaccessible to cryo-ET indefinitely. In addition to the specimens described here, we also experimented with *Arabidopsis thaliana* and *Nicotiana benthamiana* leaves, which are important and widely used model tissues in plant biology, but faced substantial challenges. The air-filled spaces in between cells of the spongy mesophyll

are problematic for vitrification by high pressure freezing. As pressure is applied, the air compresses, effectively reducing the applied pressure while also cryo-fixing the tissue under mechanical tension, increasing the likelihood of sectioned lamellae breaking during FIB-milling or sample handling with tweezers. In addition, the waxy cuticle layer covering epidermis cells frequently resulted in ice cracking at the buffer-cuticle interface, also reducing lamella stability. Overall, these issues may be mitigated by sample-specific optimization of the preparation procedure prior to freezing for some specimens. Other cell types and tissues, particularly those deeply embedded within the plants body, require dissection at room temperature to fit within the narrow sample wells of high-pressure freezing carriers (2 mm wide, 50 - 300 µm deep). Such dissection may damage a tissue to the point where it becomes questionable if, even with successful vitrification, a sample can still be considered "native". Therefore, future work should aim to extend the presented workflows to other relevant tissues while assessing biological preservation carefully.

Taken together, cryo-electron tomography represents a powerful approach for advancing plant cell biology, yet further developments are required to improve throughput, expand the accessible sample range, and enhance downstream analysis, including molecular identification of components from tomograms. In the context of plasmodesmata, cryo-ET has advanced our understanding of their native architecture and molecular organization, but future progress will depend on the continued integration of structural, biochemical, and cell biological data across scales to probe and expand the current model.

Acknowledgements

I am deeply grateful to the friends, teachers and mentors I found and who, through their encouragement, support and counsel, helped guide this work to fruition.

I thank all my current and former colleagues for making this endeavor a rewarding one. Micha M. Wudick for guidance, trust, and countless inspiring discussions; Matthias Pöge and Peng Xu for their calm, their technical mastery, and great company; Manuel Miras for getting things off the ground; Jürgen Plitzko for invaluable advice and keeping things afloat; Wolfgang Baumeister and Wolf B. Frommer for their scientific excellence and for sharing it generously; and my family and friends for their patience and support.

"We may again have reached an impasse where advances in plasmodesmal structural research are concerned. Despite many comprehensive microscopical studies that have elucidated the general structures of plasmodesmata, the finer details may not be obtainable until future breakthroughs in imaging are made" – Alison G. Roberts, 2005

"Development of new methodologies is largely driven by the biological questions being asked." – Jürgen M. Plitzko, Ringberg Retreat, 2021 (paraphrased)

References

Abedin, Monika, and Nicole King. 2010. “Diverse Evolutionary Paths to Cell Adhesion.” *Trends in Cell Biology* 20 (12): 734–42. https://doi.org/10.1016/j.tcb.2010.08.002.

Alazem, Mazen, Samantha N Nuzzi, and Tessa M Burch-Smith. 2025. “Regulation of Cell-to-Cell Trafficking by Viral Movement Proteins.” *Journal of Experimental Botany*, May 4, eraf184. https://doi.org/10.1093/jxb/eraf184.

Ansell, T. Bertie, Louis Berrios, Kabir Peay, and Peter Dahlberg. 2025. “Cryogenic Electron Tomography by the Numbers: Charting Underexplored Lineages in Structural Cell Biology.” Preprint, bioRxiv, July 13. https://doi.org/10.1101/2025.07.09.663989.

Arif, M. Asif, Manuel Hiss, Marta Tomek, et al. 2019. “ABA-Induced Vegetative Diaspore Formation in Physcomitrella Patens.” *Frontiers in Plant Science* 10 (March). https://doi.org/10.3389/fpls.2019.00315.

Badelt, K., R. G. White, R. L. Overall, and M. Vesk. 1994. “Ultrastructural Specializations of the Cell Wall Sleeve around Plasmodesmata.” *American Journal of Botany* 81 (11): 1422–27. https://doi.org/10.1002/j.1537-2197.1994.tb15628.x.

Baluška, František, Fatima Cvrčková, John Kendrick-Jones, and Dieter Volkmann. 2001. “Sink Plasmodesmata as Gateways for Phloem Unloading. Myosin VIII and Calreticulin as Molecular Determinants of Sink Strength?” *Plant Physiology* 126 (1): 39–46. https://doi.org/10.1104/pp.126.1.39.

Barr, Zoe Kathleen, and Jens Tilsner. 2025. “Should I Stay or Should I Go—Does Protein Localization to Plasmodesmata Depend on Targeting Signals?” *Journal of Experimental Botany*, June 25, eraf278. https://doi.org/10.1093/jxb/eraf278.

Baumeister, Wolfgang. 2022. “Cryo-Electron Tomography: A Long Journey to the Inner Space of Cells.” *Cell* 185 (15): 2649–52. https://doi.org/10.1016/j.cell.2022.06.034.

Bayer, Emmanuelle M., and Yoselin Benitez-Alfonso. 2024. “Plasmodesmata: Channels Under Pressure.” *Annual Review of Plant Biology* 75 (Volume 75, 2024): 291–317. https://doi.org/10.1146/annurev-arplant-070623-093110.

Beckett, A. 1981. “The Ultrastructure of Septal Pores and Associated Structures in the Ascogenous Hyphae and Asci ofSordaria Humana.” *Protoplasma* 107 (1): 127–47. https://doi.org/10.1007/BF01275613.

Benitez-Alfonso, Yoselin, Christine Faulkner, Christophe Ritzenthaler, and Andrew J. Maule. 2010. “Plasmodesmata: Gateways to Local and Systemic Virus Infection.” *Molecular Plant-Microbe Interactions®* 23 (11): 1403–12. https://doi.org/10.1094/MPMI-05-10-0116.

Bennett, Brad C., Michael D. Purdy, Kent A. Baker, et al. 2016. “An Electrostatic Mechanism for Ca2+-Mediated Regulation of Gap Junction Channels.” *Nature Communications* 7 (1): 8770. https://doi.org/10.1038/ncomms9770.

Berger, Casper, Maud Dumoux, Thomas Glen, et al. 2023. “Plasma FIB Milling for the Determination of Structures in Situ.” *Nature Communications* 14 (1): 629. https://doi.org/10.1038/s41467-023-36372-9.

Bingham, Emma P., and William C. Ratcliff. 2024. “A Nonadaptive Explanation for Macroevolutionary Patterns in the Evolution of Complex Multicellularity.” *Proceedings of the National Academy of Sciences* 121 (7): e2319840121. https://doi.org/10.1073/pnas.2319840121.

Blackman, Leila M., and Robyn L. Overall. 1998. “Immunolocalisation of the Cytoskeleton to Plasmodesmata of Chara Corallina.” *The Plant Journal* 14 (6): 733–41. https://doi.org/10.1046/j.1365-313x.1998.00161.x.

Blasius, T. Lynne, Daisuke Takao, and Kristen J. Verhey. 2019. “NPHP Proteins Are Binding Partners of Nucleoporins at the Base of the Primary Cilium.” *PLOS ONE* 14 (9): e0222924. https://doi.org/10.1371/journal.pone.0222924.

Böhm, Jochen, Achilleas S. Frangakis, Reiner Hegerl, Stephan Nickell, Dieter Typke, and Wolfgang Baumeister. 2000. “Toward Detecting and Identifying Macromolecules in a Cellular Context: Template Matching Applied to Electron Tomograms.” *Proceedings of the National Academy of Sciences* 97 (26): 14245–50. https://doi.org/10.1073/pnas.230282097.

Brault, Marie L, Jules D Petit, Françoise Immel, et al. 2019. “Multiple C2 Domains and Transmembrane Region Proteins (MCTPs) Tether Membranes at Plasmodesmata.” *EMBO Reports* 20 (8). https://doi.org/10.15252/embr.201847182.

Chaigne, Agathe, and Thibaut Brunet. 2022. “Incomplete Abscission and Cytoplasmic Bridges in the Evolution of Eukaryotic Multicellularity.” *Current Biology* 32 (8): R385–97. https://doi.org/10.1016/j.cub.2022.03.021.

Chakraborty, Ranabir, Takashi Nonaka, Masato Hasegawa, and Chiara Zurzolo. 2023. “Tunnelling Nanotubes between Neuronal and Microglial Cells Allow Bi-Directional Transfer of α-Synuclein and Mitochondria.” *Cell Death & Disease* 14 (5): 329. https://doi.org/10.1038/s41419-023-05835-8.

Chen, Chaofan, Steffen Vanneste, and Xu Chen. 2021. “Review: Membrane Tethers Control Plasmodesmal Function and Formation.” *Plant Science* 304 (March): 110800. https://doi.org/10.1016/j.plantsci.2020.110800.

Cheng, Chiu-Ping, Iris Tzafrir, B. E. L Lockhart, and Neil E Olszewski. 1998. “Tubules Containing Virions Are Present in Plant Tissues Infected with Commelina Yellow Mottle Badnavirus.” *Journal of General Virology* 79 (4): 925–29. https://doi.org/10.1099/0022-1317-79-4-925.

Choudhary, A., A. Kumar, N. Kaur, and A. Paul. 2020. “Plasmodesmata the Nano Bridges in Plant Cell: Are the Answer for All the Developmental Processes?” *Russian Journal of Plant Physiology* 67 (5): 785–96. https://doi.org/10.1134/S1021443720050039.

Claessen, Dennis, Daniel E. Rozen, Oscar P. Kuipers, Lotte Søgaard-Andersen, and Gilles P. van Wezel. 2014. “Bacterial Solutions to Multicellularity: A Tale of Biofilms, Filaments and Fruiting Bodies.” *Nature Reviews Microbiology* 12 (2): 115–24. https://doi.org/10.1038/nrmicro3178.

Cook, Martha E., Linda E. Graham, C. E. J. Botha, and Colleen A. Lavin. 1997. “Comparative Ultrastructure of Plasmodesmata of Chara and Selected Bryophytes: Toward an Elucidation of the Evolutionary Origin of Plant Plasmodesmata.” *American Journal of Botany* 84 (9): 1169–78. https://doi.org/10.2307/2446040.

Corbesier, Laurent, Coral Vincent, Seonghoe Jang, et al. 2007. “FT Protein Movement Contributes to Long-Distance Signaling in Floral Induction of Arabidopsis.” *Science* 316 (5827): 1030–33. https://doi.org/10.1126/science.1141752.

Coudert, Yoan, Wojtek Palubicki, Karin Ljung, Ondrej Novak, Ottoline Leyser, and C Jill Harrison. 2015. “Three Ancient Hormonal Cues Co-Ordinate Shoot Branching in a Moss.” *eLife* 4 (March): e06808. https://doi.org/10.7554/eLife.06808.

Cruz-León, Sergio, Tomáš Majtner, Patrick C. Hoffmann, et al. 2024. “High-Confidence 3D Template Matching for Cryo-Electron Tomography.” *Nature Communications* 15 (1): 3992. https://doi.org/10.1038/s41467-024-47839-8.

Currier, H. B., and Siegfried Strugger. 1956. “Aniline Blue and Fluorescence Microscopy of Callose in Bulb Scales ofAllium Cepa L.” *Protoplasma* 45 (4): 552–59. https://doi.org/10.1007/BF01252676.

Daum, Gabor, Anna Medzihradszky, Takuya Suzaki, and Jan U. Lohmann. 2014. “A Mechanistic Framework for Noncell Autonomous Stem Cell Induction in Arabidopsis.” *Proceedings of the National Academy of Sciences* 111 (40): 14619–24. https://doi.org/10.1073/pnas.1406446111.

Dickmanns, Marcel, Matthias Pöge, Peng Xu, et al. 2025. “In Situ Architecture of Plasmodesmata Suggests Mechanisms Controlling Intercellular Exchange.” Preprint, bioRxiv, July 25. https://doi.org/10.1101/2025.07.24.666190.

Ding, B., R. Turgeon, and M. V. Parthasarathy. 1992. “Substructure of Freeze-Substituted Plasmodesmata.” *Protoplasma* 169 (1): 28–41. https://doi.org/10.1007/BF01343367.

Ding, Biao, Myoung-Ok Kwon, and Leif Warnberg. 1996. “Evidence That Actin Filaments Are Involved in Controlling the Permeability of Plasmodesmata in Tobacco Mesophyll.” *The Plant Journal* 10 (1): 157–64. https://doi.org/10.1046/j.1365-313X.1996.10010157.x.

Dobson, Christopher M. 2019. “Biophysical Techniques in Structural Biology.” *Annual Review of Biochemistry* 88 (1): 25–33. https://doi.org/10.1146/annurev-biochem-013118-111947.

Dölger, Julia, Hanna Rademaker, Johannes Liesche, Alexander Schulz, and Tomas Bohr. 2014. “Diffusion and Bulk Flow in Phloem Loading: A Theoretical Analysis of the Polymer Trap Mechanism for Sugar Transport in Plants.” *Physical Review E* 90 (4): 042704. https://doi.org/10.1103/PhysRevE.90.042704.

Dolzmann, Peter. 1965. “Elektronenmikroskopische untersuchungen an den saughaaren von Tillandsia usneoides (Bromeliaceae).” *Planta* 64 (1): 76–80. https://doi.org/10.1007/BF00518624.

Dong, Yu, Na Liu, Gang Liu, Wen-long Li, Ai-hua Yan, and Dong-mei Wang. 2011. “Actin and Myosin Co-Localize in Plasmodesmata and Ectodesmata-Like Structure.” *Agricultural Sciences in China* 10 (6): 845–49. https://doi.org/10.1016/S1671-2927(11)60070-9.

Dym, Martin, and Don W. Fawcett. 1971. “Further Observations on the Numbers of Spermatogonia, Spermatocytes, and Spermatids Connected by Intercellular Bridges in the Mammalian Testis1.” *Biology of Reproduction* 4 (2): 195–215. https://doi.org/10.1093/biolreprod/4.2.195.

Ehlers, K., and R. Kollmann. 2001. “Primary and Secondary Plasmodesmata: Structure, Origin, and Functioning: Review Article.” *Protoplasma* 216 (1–2): 1–30. https://doi.org/10.1007/BF02680127.

Esau, Katherine, and Jennifer Thorsch. 1985. “Sieve Plate Pores and Plasmodesmata, the Communication Channels of the Symplast: Ultrastructural Aspects and Developmental Relations.” *American Journal of Botany* 72 (10): 1641–53. https://doi.org/10.1002/j.1537-2197.1985.tb08429.x.

Evert, R. F., W. Eschrich, and W. Heyser. 1977. “Distribution and Structure of the Plasmodesmata in Mesophyll and Bundle-Sheath Cells of Zea Mays L.” *Planta* 136 (1): 77–89. https://doi.org/10.1007/BF00387929.

Ewerling, Alexander, and Helen Louise May-Simera. 2024. “Evolutionary Trajectory for Nuclear Functions of Ciliary Transport Complex Proteins.” *Microbiology and Molecular Biology Reviews* 88 (3): e00006-24. https://doi.org/10.1128/mmbr.00006-24.

Fernandez-Calvino, Lourdes, Christine Faulkner, John Walshaw, et al. 2011. “Arabidopsis Plasmodesmal Proteome.” *PLOS ONE* 6 (4): e18880. https://doi.org/10.1371/journal.pone.0018880.

Franceschi, Vincent R., Biao Ding, and William J. Lucas. 1994. “Mechanism of Plasmodesmata Formation in Characean Algae in Relation to Evolution of Intercellular Communication in Higher Plants.” *Planta* 192 (3): 347–58. https://doi.org/10.1007/BF00198570.

Franklin, Rosalind E., and R. G. Gosling. 1953. “Molecular Configuration in Sodium Thymonucleate.” *Nature* 171 (4356): 740–41. https://doi.org/10.1038/171740a0.

Fung, Herman K. H., Yuki Hayashi, Veijo T. Salo, et al. 2023. “Genetically Encoded Multimeric Tags for Subcellular Protein Localization in Cryo-EM.” *Nature Methods* 20 (12): 1900–1908. https://doi.org/10.1038/s41592-023-02053-0.

Gaietta, Guido, Thomas J. Deerinck, Stephen R. Adams, et al. 2002. “Multicolor and Electron Microscopic Imaging of Connexin Trafficking.” *Science* 296 (5567): 503–7. https://doi.org/10.1126/science.1068793.

Gao, Chen, Xiangdong Liu, Nico De Storme, et al. 2020. “Directionality of Plasmodesmata-Mediated Transport in *Arabidopsis* Leaves Supports Auxin Channeling.” *Current Biology* 30 (10): 1970-1977.e4. https://doi.org/10.1016/j.cub.2020.03.014.

Gao, Peng, Pengfei Wang, Baijuan Du, Pinghua Li, and Byung-Ho Kang. 2022. “Accelerated Remodeling of the Mesophyll-Bundle Sheath Interface in the Maize C4 Cycle Mutant Leaves.” *Scientific Reports* 12 (1): 5057. https://doi.org/10.1038/s41598-022-09135-7.

Gombos, Sven, Manuel Miras, Vicky Howe, et al. 2023. “A High-Confidence Physcomitrium Patens Plasmodesmata Proteome by Iterative Scoring and Validation Reveals Diversification of Cell Wall Proteins during Evolution.” *New Phytologist* 238 (2): 637–53. https://doi.org/10.1111/nph.18730.

Greenbaum, Michael P., Lang Ma, and Martin M. Matzuk. 2007. “Conversion of Midbodies into Germ Cell Intercellular Bridges.” *Developmental Biology* 305 (2): 389–96. https://doi.org/10.1016/j.ydbio.2007.02.025.

Gunning, B. E. S., and A. W. Robards, eds. 1976. *Intercellular Communication in Plants: Studies on Plasmodesmata*. Springer. https://doi.org/10.1007/978-3-642-66294-2.

Hammerschmidt, Katrin, Giddy Landan, Fernando Domingues Kümmel Tria, Jaime Alcorta, and Tal Dagan. 2021. “The Order of Trait Emergence in the Evolution of Cyanobacterial Multicellularity.” *Genome Biology and Evolution* 13 (2): evaa249. https://doi.org/10.1093/gbe/evaa249.

Heinlein, Manfred. 2015. “Plasmodesmata: Channels for Viruses on the Move.” In *Plasmodesmata*, edited by Manfred Heinlein, vol. 1217. Methods in Molecular Biology. Springer New York. https://doi.org/10.1007/978-1-4939-1523-1_2.

Hoek, Hugo van den, Nikolai Klena, Mareike A. Jordan, et al. 2022. “In Situ Architecture of the Ciliary Base Reveals the Stepwise Assembly of Intraflagellar Transport Trains.” *Science* 377 (6605): 543–48. https://doi.org/10.1126/science.abm6704.

Howell, Alexander H., Anneline H. Christensen, Vincent James, et al. 2024. “Electric Charge Controls Plasmodesma Conductivity.” Preprint, bioRxiv, April 3. https://doi.org/10.1101/2024.04.02.587779.

Huang, Bo, Hazen Babcock, and Xiaowei Zhuang. 2010. “Breaking the Diffraction Barrier: Super-Resolution Imaging of Cells.” *Cell* 143 (7): 1047–58. https://doi.org/10.1016/j.cell.2010.12.002.

Huebinger, Jan, Hong-Mei Han, Oliver Hofnagel, Ingrid R. Vetter, Philippe I. H. Bastiaens, and Markus Grabenbauer. 2016. “Direct Measurement of Water States in Cryopreserved Cells Reveals Tolerance toward Ice Crystallization.” *Biophysical Journal* 110 (4): 840–49. https://doi.org/10.1016/j.bpj.2015.09.029.

Jackson, David, Bruce Veit, and Sarah Hake. 1994. “Expression of Maize KNOTTED1 Related Homeobox Genes in the Shoot Apical Meristem Predicts Patterns of Morphogenesis in the Vegetative Shoot.” *Development* 120 (2): 405–13. https://doi.org/10.1242/dev.120.2.405.

Johnston, Matthew G, Andrew Breakspear, Sebastian Samwald, et al. 2023. “Comparative Phyloproteomics Identifies Conserved Plasmodesmal Proteins.” *Journal of Experimental Botany* 74 (6): 1821–35. https://doi.org/10.1093/jxb/erad022.

Jumper, John, Richard Evans, Alexander Pritzel, et al. 2021. “Highly Accurate Protein Structure Prediction with AlphaFold.” *Nature* 596 (7873): 583–89. https://doi.org/10.1038/s41586-021-03819-2.

Kanno, H., R. J. Speedy, and C. A. Angell. 1975. “Supercooling of Water to -92°C under Pressure.” *Science* 189 (4206): 880–81. https://doi.org/10.1126/science.189.4206.880.

Kelley, Kotaro, Ashleigh M. Raczkowski, Oleg Klykov, et al. 2022. “Waffle Method: A General and Flexible Approach for Improving Throughput in FIB-Milling.” *Nature Communications* 13 (1): 1–13. https://doi.org/10.1038/s41467-022-29501-3.

Kitagawa, Munenori, Takumi Tomoi, Tomoki Fukushima, et al. 2019. “Abscisic Acid Acts as a Regulator of Molecular Trafficking through Plasmodesmata in the Moss Physcomitrella Patens.” *Plant and Cell Physiology* 60 (4): 738–51. https://doi.org/10.1093/pcp/pcy249.

Kleist, Thomas J., Anthony Bortolazzo, Zachary P. Keyser, et al. 2022. “Stress-Associated Developmental Reprogramming in Moss Protonemata by Synthetic Activation of the Common Symbiosis Pathway.” *iScience* 25 (2): 103754. https://doi.org/10.1016/j.isci.2022.103754.

Klumpe, Sven, Herman KH Fung, Sara K Goetz, et al. 2021. “A Modular Platform for Automated Cryo-FIB Workflows.” *eLife* 10 (December): e70506. https://doi.org/10.7554/eLife.70506.

Klumpe, Sven, Jakub Kuba, Oda H. Schioetz, Philipp S. Erdmann, Alexander Rigort, and Jürgen M. Plitzko. 2022. “Recent Advances in Gas Injection System-Free Cryo-FIB Lift-Out Transfer for Cryo-Electron Tomography of Multicellular Organisms and Tissues.” *Microscopy Today* 30 (1): 42–47. https://doi.org/10.1017/S1551929521001528.

Knoll, Andrew H. 2011. “The Multiple Origins of Complex Multicellularity.” *Annual Review of Earth and Planetary Sciences* 39 (Volume 39, 2011): 217–39. https://doi.org/10.1146/annurev.earth.031208.100209.

Köhler, Piotr, and Denis J. Carr. 2006. “Eduard Tangl (1848-1905) : Discoverer of Plasmodesmata.” *HUNTIA* 12 (2). http://ruj.uj.edu.pl/xmlui/handle/item/32303.

Kraner, Max E., Carmen Müller, and Uwe Sonnewald. 2017. “Comparative Proteomic Profiling of the Choline Transporter-Like1 (CHER1) Mutant Provides Insights into Plasmodesmata Composition of Fully Developed Arabidopsis Thaliana Leaves.” *The Plant Journal* 92 (4): 696–709. https://doi.org/10.1111/tpj.13702.

Kwiatkowska, Maria. 1991. “Autoradiographic Studies on the Role of Plasmodesmata in the Transport of Gibberellin.” *Planta* 183 (2): 294–99. https://doi.org/10.1007/BF00197801.

Kwon, Taekyung, Andrew L. Harris, Angelo Rossi, and Thaddeus A. Bargiello. 2011. “Molecular Dynamics Simulations of the Cx26 Hemichannel: Evaluation of Structural Models with Brownian Dynamics.” *Journal of General Physiology* 138 (5): 475–93. https://doi.org/10.1085/jgp.201110679.

Lai, Julian, Chuan Hock Koh, Monika Tjota, et al. 2012. “Intrinsically Disordered Proteins Aggregate at Fungal Cell-to-Cell Channels and Regulate Intercellular Connectivity.” *Proceedings of the National Academy of Sciences* 109 (39): 15781–86. https://doi.org/10.1073/pnas.1207467109.

Lamm, Lorenz, Simon Zufferey, Hanyi Zhang, et al. 2025. “MemBrain v2: An End-to-End Tool for the Analysis of Membranes in Cryo-Electron Tomography.” Preprint, bioRxiv, April 22. https://doi.org/10.1101/2024.01.05.574336.

Lampe, Paul D, and Alan F Lau. 2004. “The Effects of Connexin Phosphorylation on Gap Junctional Communication.” *The International Journal of Biochemistry & Cell Biology* 36 (7): 1171–86. https://doi.org/10.1016/S1357-2725(03)00264-4.

Leijon, Felicia, Michael Melzer, Qi Zhou, Vaibhav Srivastava, and Vincent Bulone. 2018. “Proteomic Analysis of Plasmodesmata From Populus Cell Suspension Cultures in Relation With Callose Biosynthesis.” *Frontiers in Plant Science* 9. https://www.frontiersin.org/articles/10.3389/fpls.2018.01681.

Lent, Jan van, Joan Wellink, and Rob Goldbach. 1990. “Evidence for the Involvement of the 58K and 48K Proteins in the Intercellular Movement of Cowpea Mosaic Virus.” *Journal of General Virology* 71 (1): 219–23. https://doi.org/10.1099/0022-1317-71-1-219.

Li, Chunyang, Mei Gu, Nongnong Shi, et al. 2011. “Mobile FT mRNA Contributes to the Systemic Florigen Signalling in Floral Induction.” *Scientific Reports* 1 (1): 73. https://doi.org/10.1038/srep00073.

Li, Ziqiang P., Hortense Moreau, Jules D. Petit, et al. 2024. “Plant Plasmodesmata Bridges Form through ER-Dependent Incomplete Cytokinesis.” *Science* 386 (6721): 538–45. https://doi.org/10.1126/science.adn4630.

Liu, Lu, Chang Liu, Xingliang Hou, et al. 2012. “FTIP1 Is an Essential Regulator Required for Florigen Transport.” *PLOS Biology* 10 (4): e1001313. https://doi.org/10.1371/journal.pbio.1001313.

López-Sáez, J. F., G. Giménez-Martin, and M. C. Risueño. 1966. “Fine Structure of the Plasmodesm.” *Protoplasma* 61 (1): 81–84. https://doi.org/10.1007/BF01247912.

Lu, Kuan-Ju, Nien-Chen Huang, Yu-Shan Liu, Chung-An Lu, and Tien-Shin Yu. 2012. “Long-Distance Movement of Arabidopsis FLOWERING LOCUS T RNA Participates in Systemic Floral Regulation.” *RNA Biology* 9 (5): 653–62. https://doi.org/10.4161/rna.19965.

Lucas, William J., Sabine Bouché-Pillon, David P. Jackson, et al. 1995. “Selective Trafficking of KNOTTED1 Homeodomain Protein and Its mRNA Through Plasmodesmata.” *Science* 270 (5244): 1980–83. https://doi.org/10.1126/science.270.5244.1980.

Luo, Kai-Ren, Nien-Chen Huang, Yu-Hsin Chang, Yu-Wen Jan, and Tien-Shin Yu. 2024. “Arabidopsis Cyclophilins Direct Intracellular Transport of Mobile mRNA via Organelle Hitchhiking.” *Nature Plants* 10 (1): 161–71. https://doi.org/10.1038/s41477-023-01597-5.

Maeda, Shoji, So Nakagawa, Michihiro Suga, et al. 2009. “Structure of the Connexin 26 Gap Junction Channel at 3.5 Å Resolution.” *Nature* 458 (7238): 597–602. https://doi.org/10.1038/nature07869.

Mangin, M. Louis. 1892. “Observations Sur La Présence De La Callose Chez Les Phanérogames.” *Bulletin de La Société Botanique de France* 39 (6): 260–67. https://doi.org/10.1080/00378941.1892.10828658.

McCafferty, Caitlyn L., Sven Klumpe, Rommie E. Amaro, Wanda Kukulski, Lucy Collinson, and Benjamin D. Engel. 2024. “Integrating Cellular Electron Microscopy with Multimodal Data to Explore Biology across Space and Time.” *Cell* 187 (3): 563–84. https://doi.org/10.1016/j.cell.2024.01.005.

McLean, Peter F., and Lynn Cooley. 2013. “Protein Equilibration Through Somatic Ring Canals in Drosophila.” *Science* 340 (6139): 1445–47. https://doi.org/10.1126/science.1234887.

Mehra, Poonam, Bipin K. Pandey, Dalia Melebari, et al. 2022. “Hydraulic Flux–Responsive Hormone Redistribution Determines Root Branching.” *Science* 378 (6621): 762–68. https://doi.org/10.1126/science.add3771.

Mellor, Nathan L., Ute Voß, George Janes, Malcolm J. Bennett, Darren M. Wells, and Leah R. Band. 2020. “Auxin Fluxes through Plasmodesmata Modify Root-Tip Auxin Distribution.” *Development* 147 (6): dev181669. https://doi.org/10.1242/dev.181669.

Miao, Lianjie, Yangyang Lu, Anika Nusrat, et al. 2025. “Tunneling Nanotube–like Structures Regulate Distant Cellular Interactions during Heart Formation.” *Science* 387 (6739): eadd3417. https://doi.org/10.1126/science.add3417.

Michod, Richard E. 2007. “Evolution of Individuality during the Transition from Unicellular to Multicellular Life.” *Proceedings of the National Academy of Sciences* 104 (suppl_1): 8613–18. https://doi.org/10.1073/pnas.0701489104.

Miras, Manuel, Mathieu Pottier, T. Moritz Schladt, et al. 2022. “Plasmodesmata and Their Role in Assimilate Translocation.” *Journal of Plant Physiology*, February 3, 153633. https://doi.org/10.1016/J.JPLPH.2022.153633.

Moor, Hans. 1987. “Theory and Practice of High Pressure Freezing.” In *Cryotechniques in Biological Electron Microscopy*. Springer Berlin Heidelberg. https://doi.org/10.1007/978-3-642-72815-0_8.

Murata, Yusuke, Kenji Nagata, and Mitsutomo Abe. 2025. “Cell-to-Cell Translocation of Florigen Is Inhibited by Low Ambient Temperature through Abscisic Acid Signaling in Arabidopsis Thaliana.” *Proceedings of the National Academy of Sciences* 122 (28): e2507987122. https://doi.org/10.1073/pnas.2507987122.

Musil, Linda S., Anh-Chi N. Le, Judy K. VanSlyke, and Lori M. Roberts. 2000. “Regulation of Connexin Degradation as a Mechanism to Increase Gap Junction Assembly and Function*.” *Journal of Biological Chemistry* 275 (33): 25207–15. https://doi.org/10.1074/jbc.275.33.25207.

Nakajima, K., G. Sena, T. Nawy, and P. N. Benfey. 2001. “Intercellular Movement of the Putative Transcription Factor SHR in Root Patterning.” *Nature* 413 (6853): 307–11. https://doi.org/10.1038/35095061.

Nandakumar, Shyama, and Deepika Vasudevan. 2025. “Ring Canals in the Larval Adipose of Drosophila Buffer Stress Response.” Preprint, bioRxiv, June 11. https://doi.org/10.1101/2025.06.11.658881.

Nguyen, Ho Thuy Dung, Gaia Perone, Nikolai Klena, et al. 2024. “Serialized On-Grid Lift-in Sectioning for Tomography (SOLIST) Enables a Biopsy at the Nanoscale.” *Nature Methods* 21 (9): 1693–701. https://doi.org/10.1038/s41592-024-02384-6.

Nicolas, William J., Magali S. Grison, Sylvain Trépout, et al. 2017. “Architecture and Permeability of Post-Cytokinesis Plasmodesmata Lacking Cytoplasmic Sleeves.” *Nature Plants* 3 (7): 17082. https://doi.org/10.1038/nplants.2017.82.

Northcote, D. H., Robin Davey, and Jim Lay. 1989. “Use of Antisera to Localize Callose, Xylan and Arabinogalactan in the Cell-Plate, Primary and Secondary Walls of Plant Cells.” *Planta* 178 (3): 353–66. https://doi.org/10.1007/BF00391863.

Olatunji, Damilola, Natalie M. Clark, and Dior R. Kelley. 2023. “The Class VIII Myosin ATM1 Is Required for Root Apical Meristem Function.” *Development (Cambridge, England)* 150 (20): dev201762. https://doi.org/10.1242/dev.201762.

Olesen, P. 1979. “The Neck Constriction in Plasmodesmata : Evidence for a Peripheral Sphincter-like Structure Revealed by Fixation with Tannic Acid.” *Planta* 144 (4): 349–58. https://doi.org/10.1007/BF00391578.

Ostermeyer, Grayson P., Kaare H. Jensen, Aslak R. Franzen, Winfried S. Peters, and Michael Knoblauch. 2022. “Diversity of Funnel Plasmodesmata in Angiosperms: The Impact of Geometry on Plasmodesmal Resistance.” *The Plant Journal: For Cell and Molecular Biology* 110 (3): 707–19. https://doi.org/10.1111/tpj.15697.

Overall, Robyn L., Rosemary G. White, Leila M. Blackman, and Janine E. Radford. 2000. “Actin and Myosin in Plasmodesmata.” In *Actin: A Dynamic Framework for Multiple Plant Cell Functions*, edited by C. J. Staiger, F. Baluška, D. Volkmann, and P. W. Barlow. Springer Netherlands. https://doi.org/10.1007/978-94-015-9460-8_28.

Pan, Wenqiang, Jingru Li, Yunpeng Du, et al. 2023. “Epigenetic Silencing of Callose Synthase by VIL1 Promotes Bud-Growth Transition in Lily Bulbs.” *Nature Plants* 9 (9): 1451–67. https://doi.org/10.1038/s41477-023-01492-z.

Park, Sang-Ho, Fangfang Li, Justin Renaud, et al. 2017. “NbEXPA1, an α-Expansin, Is Plasmodesmata-Specific and a Novel Host Factor for Potyviral Infection.” *The Plant Journal* 92 (5): 846–61. https://doi.org/10.1111/tpj.13723.

Penesyan, Anahit, Ian T. Paulsen, Staffan Kjelleberg, and Michael R. Gillings. 2021. “Three Faces of Biofilms: A Microbial Lifestyle, a Nascent Multicellular Organism, and an Incubator for Diversity.” *Npj Biofilms and Microbiomes* 7 (1): 80. https://doi.org/10.1038/s41522-021-00251-2.

Pentz, Jennifer T, Kathryn MacGillivray, James G DuBose, et al. 2023. “Evolutionary Consequences of Nascent Multicellular Life Cycles.” *eLife* 12 (October): e84336. https://doi.org/10.7554/eLife.84336.

Pérez-Sancho, Jessica, Marija Smokvarska, Gwennogan Dubois, et al. 2025. “Plasmodesmata Act as Unconventional Membrane Contact Sites Regulating Intercellular Molecular Exchange in Plants.” *Cell* 188 (4): 958-977.e23. https://doi.org/10.1016/j.cell.2024.11.034.

Peters, Winfried S., Kaare H. Jensen, Howard A. Stone, and Michael Knoblauch. 2021. “Plasmodesmata and the Problems with Size: Interpreting the Confusion.” *Journal of Plant Physiology* 257 (February): 153341. https://doi.org/10.1016/j.jplph.2020.153341.

Plitzko, Jürgen, and Wolfgang P. Baumeister. 2019. “Cryo-Electron Tomography.” In *Springer Handbook of Microscopy*, edited by Peter W. Hawkes and John C. H. Spence. Springer International Publishing. https://doi.org/10.1007/978-3-030-00069-1_4.

Radford, Janine E., and Rosemary G. White. 1998. “Localization of a Myosin-like Protein to Plasmodesmata.” *The Plant Journal* 14 (6): 743–50. https://doi.org/10.1046/j.1365-313x.1998.00162.x.

Ramus, J. 1969. “Pit Connection Formation in the Red Alga Pseudogloiophloea.” *Journal of Phycology* 5 (1): 57–63. https://doi.org/10.1111/j.1529-8817.1969.tb02577.x.

Raven, J. A. 2003. “Long-Distance Transport in Non-Vascular Plants.” *Plant, Cell & Environment* 26 (1): 73–85. https://doi.org/10.1046/j.1365-3040.2003.00920.x.

Raven, John A. 1987. “The Role of Vacuoles.” *New Phytologist* 106 (3): 357–422. https://doi.org/10.1111/j.1469-8137.1987.tb00149.x.

Reagan, Brandon C., and Tessa M. Burch-Smith. 2020. “Viruses Reveal the Secrets of Plasmodesmal Cell Biology.” *Molecular Plant-Microbe Interactions®* 33 (1): 26–39. https://doi.org/10.1094/MPMI-07-19-0212-FI.

Reichelt, Stefanie, Alex E. Knight, Tony P. Hodge, et al. 1999. “Characterization of the Unconventional Myosin VIII in Plant Cells and Its Localization at the Post-Cytokinetic Cell Wall.” *The Plant Journal* 19 (5): 555–67. https://doi.org/10.1046/j.1365-313X.1999.00553.x.

Ritzenthaler, Christophe, Monique Pinck, and Lothaire Pinck. 1995. “Grapevine Fanleaf Nepovirus P38 Putative Movement Protein Is Not Transiently Expressed and Is a Stable Final Maturation Product in Vivo.” *Journal of General Virology* 76 (4): 907–15. https://doi.org/10.1099/0022-1317-76-4-907.

Robards, A. W. 1968. “Desmotubule—a Plasmodesmatal Substructure.” *Nature* 218 (5143): 784–784. https://doi.org/10.1038/218784a0.

Roberts, Alison G. 2005. “Plasmodesmal Structure and Development.” In *Plasmodesmata*. John Wiley & Sons, Ltd. https://doi.org/10.1002/9780470988572.ch1.

Rustom, Amin, Rainer Saffrich, Ivanka Markovic, Paul Walther, and Hans-Hermann Gerdes. 2004. “Nanotubular Highways for Intercellular Organelle Transport.” *Science* 303 (5660): 1007–10. https://doi.org/10.1126/science.1093133.

Sager, Ross E., and Jung-Youn Lee. 2018. “Plasmodesmata at a Glance.” *Journal of Cell Science* 131 (11): jcs209346. https://doi.org/10.1242/jcs.209346.

Sánchez-Gerschon, Verónica, Irene Martínez-Fernández, María R González-Bermúdez, et al. 2024. “Transcription Factors HB21/40/53 Trigger Inflorescence Arrest through Abscisic Acid Accumulation at the End of Flowering.” *Plant Physiology* 195 (4): 2743–56. https://doi.org/10.1093/plphys/kiae234.

Sartori, N., K. Richter, and J. Dubochet. 1993. “Vitrification Depth Can Be Increased More than 10-Fold by High-Pressure Freezing.” *Journal of Microscopy* 172 (1): 55–61. https://doi.org/10.1111/j.1365-2818.1993.tb03393.x.

Sartori-Rupp, Anna, Diégo Cordero Cervantes, Anna Pepe, et al. 2019. “Correlative Cryo-Electron Microscopy Reveals the Structure of TNTs in Neuronal Cells.” *Nature Communications* 10 (1): 342. https://doi.org/10.1038/s41467-018-08178-7.

Schaffer, Miroslava, Julia Mahamid, Benjamin D. Engel, Tim Laugks, Wolfgang Baumeister, and Jürgen M. Plitzko. 2017. “Optimized Cryo-Focused Ion Beam Sample Preparation Aimed at in Situ Structural Studies of Membrane Proteins.” *Journal of Structural Biology* 197 (2): 73–82. https://doi.org/10.1016/j.jsb.2016.07.010.

Schiøtz, Oda Helene, Christoph J. O. Kaiser, Sven Klumpe, et al. 2024. “Serial Lift-Out: Sampling the Molecular Anatomy of Whole Organisms.” *Nature Methods* 21 (9): 1684–92. https://doi.org/10.1038/s41592-023-02113-5.

Schladt, T. Moritz, Manuel Miras, Jona Obinna Ejike, et al. 2025. “Identification of Nuclear Pore Proteins at Plasmodesmata: Potential Role in Intercellular Transport?” *eLife* 14 (September). https://doi.org/10.7554/eLife.108676.1.

Schnepf, E., and Th. Sawidis. 1991. “Filament Disruption in Funaria Protonemata: Occlusion of Plasmodesmata.” *Botanica Acta* 104 (2): 98–102. https://doi.org/10.1111/j.1438-8677.1991.tb00203.x.

Sessions, Allen, Martin F. Yanofsky, and Detlef Weigel. 2000. “Cell-Cell Signaling and Movement by the Floral Transcription Factors LEAFY and APETALA1.” *Science* 289 (5480): 779–81. https://doi.org/10.1126/science.289.5480.779.

Silvester, Emma, Benjamin Vollmer, Vojtěch Pražák, et al. 2021. “DNA Origami Signposts for Identifying Proteins on Cell Membranes by Electron Cryotomography.” *Cell* 184 (4): 1110-1121.e16. https://doi.org/10.1016/j.cell.2021.01.033.

Skerrett, I. Martha, and Jamal B. Williams. 2017. “A Structural and Functional Comparison of Gap Junction Channels Composed of Connexins and Innexins.” *Developmental Neurobiology* 77 (5): 522–47. https://doi.org/10.1002/dneu.22447.

Söhl, Goran, and Klaus Willecke. 2004. “Gap Junctions and the Connexin Protein Family.” *Cardiovascular Research* 62 (2): 228–32. https://doi.org/10.1016/j.cardiores.2003.11.013.

Strasburger, Eduard. 1901. "Ueber Plasmaverbindungen Pflanzlicher Zellen." *Sonderabdruck Jahrb. Wiss. Bot*, Band XXXVI, Heft 3.

Strugger, S. 1957. “Der elektronenmikroskopische Nachweis von Plasmodesmen mit Hilfe der Uranylimprägnierung an Wurzelmeristemen.” *Protoplasma* 48 (2): 231–36. https://doi.org/10.1007/BF01252659.

Su, Shengzhong, Zhaohui Liu, Cheng Chen, et al. 2010. “Cucumber Mosaic Virus Movement Protein Severs Actin Filaments to Increase the Plasmodesmal Size Exclusion Limit in Tobacco.” *The Plant Cell* 22 (4): 1373–87. https://doi.org/10.1105/tpc.108.064212.

Su, Vivian, and Alan F. Lau. 2014. “Connexins: Mechanisms Regulating Protein Levels and Intercellular Communication.” *FEBS Letters* 588 (8): 1212–20. https://doi.org/10.1016/j.febslet.2014.01.013.

Takao, Daisuke, Liang Wang, Allison Boss, and Kristen J. Verhey. 2017. “Protein Interaction Analysis Provides a Map of the Spatial and Temporal Organization of the Ciliary Gating Zone.” *Current Biology* 27 (15): 2296-2306.e3. https://doi.org/10.1016/j.cub.2017.06.044.

Tangl, Eduard. 1880. “Ueber Offene Communicationen Zwischen Den Zellen Des Endosperms Einiger Samen.” *Jahrb. Wiss. Bot.* 12: 170–90.

Tee, Estee E., and Christine Faulkner. 2024. “Plasmodesmata and Intercellular Molecular Traffic Control.” *New Phytologist* 243 (1): 32–47. https://doi.org/10.1111/nph.19666.

Terauchi, Makoto, Chikako Nagasato, and Taizo Motomura. 2014. “Plasmodesmata of Brown Algae.” *Journal of Plant Research* 128 (1): 7–15. https://doi.org/10.1007/s10265-014-0677-4.

Terry, B. R., and A. W. Robards. 1987. “Hydrodynamic Radius Alone Governs the Mobility of Molecules through Plasmodesmata.” *Planta* 171 (2): 145–57. https://doi.org/10.1007/BF00391090.

Tuijtel, Maarten W., Sergio Cruz-León, Jan Philipp Kreysing, et al. 2024. “Thinner Is Not Always Better: Optimizing Cryo-Lamellae for Subtomogram Averaging.” *Science Advances* 10 (17): eadk6285. https://doi.org/10.1126/sciadv.adk6285.

Tylewicz, S., A. Petterle, S. Marttila, et al. 2018. “Photoperiodic Control of Seasonal Growth Is Mediated by ABA Acting on Cell-Cell Communication.” *Science* 360 (6385): 212–15. https://doi.org/10.1126/science.aan8576.

Vaddepalli, Prasad, Anja Herrmann, Lynette Fulton, et al. 2014. “The C2-Domain Protein QUIRKY and the Receptor-like Kinase STRUBBELIG Localize to Plasmodesmata and Mediate Tissue Morphogenesis in Arabidopsis Thaliana.” *Development* 141 (21): 4139–48. https://doi.org/10.1242/dev.113878.

Vatén, Anne, Jan Dettmer, Shuang Wu, et al. 2011. “Callose Biosynthesis Regulates Symplastic Trafficking during Root Development.” *Developmental Cell* 21 (6): 1144–55. https://doi.org/10.1016/j.devcel.2011.10.006.

Viso, Florencia del, Fang Huang, Jordan Myers, et al. 2016. “Congenital Heart Disease Genetics Uncovers Context-Dependent Organization and Function of Nucleoporins at Cilia.” *Developmental Cell* 38 (5): 478–92. https://doi.org/10.1016/j.devcel.2016.08.002.

Wan, W., and J.A.G. Briggs. 2016. “Cryo-Electron Tomography and Subtomogram Averaging.” In *Methods in Enzymology*, vol. 579. Elsevier. https://doi.org/10.1016/bs.mie.2016.04.014.

Wang, Chengliang, Yuanyuan Lyu, Qi Zhang, Hongye Guo, Defu Chen, and Xiwen Chen. 2023. “Disruption of BG14 Results in Enhanced Callose Deposition in Developing Seeds and Decreases Seed Longevity and Seed Dormancy in Arabidopsis.” *The Plant Journal* 113 (5): 1080–94. https://doi.org/10.1111/tpj.16102.

Wang, Haiting, Yuman Zhang, Na Xiao, et al. 2020. “Rice GERMIN-LIKE PROTEIN 2-1 Functions in Seed Dormancy under the Control of Abscisic Acid and Gibberellic Acid Signaling Pathways1.” *Plant Physiology* 183 (3): 1157–70. https://doi.org/10.1104/pp.20.00253.

Watson, J. D., and F. H.C. Crick. 1953. “Molecular Structure of Nucleic Acids: A Structure for Deoxyribose Nucleic Acid.” *Nature* 171 (4356): 737–38. https://doi.org/10.1038/171737a0.

Weber, Paul A., Hou-Chien Chang, Kris E. Spaeth, Johannes M. Nitsche, and Bruce J. Nicholson. 2004. “The Permeability of Gap Junction Channels to Probes of Different Size Is Dependent on Connexin Composition and Permeant-Pore Affinities.” *Biophysical Journal* 87 (2): 958–73. https://doi.org/10.1529/biophysj.103.036350.

Welling, F. 1965. “Zur Feinstruktur der Plasmodesmen und Plasmakanäle bei Pollenmutterzellen.” *Planta* 64 (2): 97–118. https://doi.org/10.1007/BF00396004.

White, R. G., K. Badelt, R. L. Overall, and M. Vesk. 1994. “Actin Associated with Plasmodesmata.” *Protoplasma* 180 (3): 169–84. https://doi.org/10.1007/BF01507853.

Wilkins, M. H.F., A. R. Stokes, and H. R. Wilson. 1953. “Molecular Structure of Nucleic Acids: Molecular Structure of Deoxypentose Nucleic Acids.” *Nature* 171 (4356): 738–40. https://doi.org/10.1038/171738a0.

Wowk, Brian. 2010. “Thermodynamic Aspects of Vitrification.” *Cryobiology*, Special Issue: Thermodynamic aspects of Cryobiology, vol. 60 (1): 11–22. https://doi.org/10.1016/j.cryobiol.2009.05.007.

Wu, Shu-Zon, Julie A. Ritchie, Ai-Hong Pan, Ralph S. Quatrano, and Magdalena Bezanilla. 2011. “Myosin VIII Regulates Protonemal Patterning and Developmental Timing in the Moss *Physcomitrella Patens*.” *Molecular Plant* 4 (5): 909–21. https://doi.org/10.1093/mp/ssr068.

Wu, Xuelin, José R. Dinneny, Katrina M. Crawford, et al. 2003. “Modes of Intercellular Transcription Factor Movement in the Arabidopsis Apex.” *Development* 130 (16): 3735–45. https://doi.org/10.1242/dev.00577.

Xiang, Yun, Rui Lyu, and Junjie Hu. 2023. “Oligomeric Scaffolding for Curvature Generation by ER Tubule-Forming Proteins.” *Nature Communications* 14 (1): 2617. https://doi.org/10.1038/s41467-023-38294-y.

Young, Lindsey N., Alice Sherrard, Huabin Zhou, et al. 2025. “ExoSloNano: Multimodal Nanogold Labels for Identification of Macromolecules in Live Cells and Cryo-Electron Tomograms.” *Nature Methods*, November 28, 1–12. https://doi.org/10.1038/s41592-025-02928-4.

Zhang, Zhixian, Abigail R. Moye, Feng He, Muyuan Chen, Melina A. Agosto, and Theodore G. Wensel. 2024. “Centriole and Transition Zone Structures in Photoreceptor Cilia Revealed by Cryo-Electron Tomography.” Research Articles. *Life Science Alliance* 7 (3). https://doi.org/10.26508/lsa.202302409.